

國立交通大學

電子物理學系

博士論文

利用量子球檯介觀波函數類比研究大面積面射型雷射
之橫向模態

Analogous Investigations on the Transverse Modes of Broad-Area
Vertical-Cavity Surface-Emitting Lasers by Mesoscopic Wave
Functions of Quantum Billiards

研究生：陳建誠

指導教授：陳永富 教授

中華民國九十八年六月

利用量子球檯介觀波函數類比研究大面積面射型雷射之橫向模態
Analogous Investigations on the Transverse Modes of Broad-Area Vertical-Cavity
Surface-Emitting Lasers by Mesoscopic Wave Functions of Quantum Billiards

研 究 生：陳建誠

Student : Chien-Cheng Chen

指 導 教 授：陳永富

Advisor : Yung-Fu Chen

國 立 交 通 大 學

電 子 物 理 學 系

博 士 論 文

A Dissertation

Submitted to Department of Electrophysics

College of Science

National Chiao Tung University

in partial Fulfillment of the Requirements

for the Degree of

Doctor of Philosophy

in

Electrophysics

June 2009

Hsinchu, Taiwan, Republic of China

中華民國九十八年六月

利用量子球檯介觀波函數類比研究大面積面射型雷射之橫向模態

學生：陳建誠

指導教授：陳永富

國立交通大學電子物理學系博士班

摘 要

近軸近似光學與二維量子力學之間的類比性是本篇論文的核心概念。基於 Helmholtz 方程式與非時變 Schrödinger 方程式之間的相似性，我們可以用量子球檯的介觀波函數解釋大面積面射型雷射的高階近場橫向模態。相反地，非可積量子球檯的波函數雖然沒有解析解，但我們可以利用混沌形狀的面射型雷射做類比觀察。除此之外，同調波突然從量子球檯釋放出來之後的演變也可以透過面射型雷射之橫向模態的傳遞做類比觀察。由於二維量子系統與近軸光學的類比性不僅止於波函數與橫向模態，還包括它們的軌道角動量，所以藉由計算同調波從量子球檯釋放出來之後的軌道角動量可以類比分析面射型雷射光束的軌道角動量。更有趣的是，面射型雷射的模態除了線性偏振之外，還可以形成一種偏振與空間糾纏的向量場。既然光的偏振乃是對應於量子波的自旋，分析面射型雷射之中的向量場可以提供重要的資訊給考慮電子自旋的量子球檯系統。

Analogous Investigations on the Transverse Modes of Broad-Area Vertical-Cavity Surface-Emitting Lasers by Mesoscopic Wave Functions of Quantum Billiards

Student : Chien-Cheng Chen

Advisor : Yung-Fu Chen

Department of Electrophysics
National Chiao Tung University

ABSTRACT

The analogies between paraxial optics and two-dimensional (2-D) quantum mechanics lie in the heart of this thesis. Based on the similarity between Helmholtz equation and time-independent Schrödinger equation, mesoscopic wave functions of quantum billiards are used to interpret the high-order transverse modes of broad-area Vertical-Cavity Surface-Emitting Lasers (VCSELs). Reversely, chaotic-shaped VCSELs can be employed to analogously observe the wave functions of non-integrable billiards which have no analytic solutions. In addition, the free-time evolution of coherent waves suddenly released from quantum billiards can be analogously observed from the free-space propagation of lasing modes emitted from VCSELs. Furthermore, the analogies are not restricted to quantum wave functions and optical transverse modes, the orbital angular momentum (OAM) density carried by a light beam emitted from VCSELs can be analogously analyzed by calculating the OAM of coherent waves abruptly set free from quantum billiards. More interestingly, the lasing modes of VCSELs are not only linearly-polarized but can form the vector fields, in which the polarization is spatially dependent. Since the polarization of light corresponds to the spin of quantum wave, the analyses of the vector fields in VCSELs can provide important information for quantum-billiard systems (such as ballistic quantum dots) with consideration on electronic spin.

誌謝

Acknowledgement

首先要感謝我的指導教授陳永富老師。以前每當有人問起誰是影響自己最多的人時，心裡總是沒有明確的答案。但現在我可以肯定的說，是陳永富教授。讀大學時候的我根本沒想過會攻讀博士，但機緣之下陳老師讓我得以一窺科學的美妙。從一開始用挖洞的方法重建 Chaotic Patterns 我就已經著迷於這神奇的世界，後來種種的實驗發現與理論計算重建都一次一次的撼動我的心，我也常常為了這些發現而興奮好幾天。雖然我在研究過程中常常讓老師失望，但老師還是一直很有耐心的指引我，把我導向正途。陳老師讓我成長的並不僅止於學識，老師的言教身教也歷歷在在影響我的人生觀，讓原本避世的我也想要成為跟老師一樣熱血有抱負的人。能夠讓我完成博士學業的另一隻推手是跟陳老師共同指導我的黃凱風教授，黃老師提供了世界一流的實驗設備及元件，讓我可以無憂無慮的做研究。此外，黃老師淵博的學識與對科學的熱誠是我所景仰的，每當碰到瓶頸黃老師總是可以用指點我明確的方向找到出口。除此之外，聽黃老師講故事是非常享受的。在這段日子有兩位良師可以一起教導我、帶我探索充滿驚奇的科學世界讓我感到萬分幸福。往後的日子裡，我將效法兩位恩師的精神，孜孜不倦地為科學貢獻一己之力。

除了老師之外，首先要感謝蘇冠暉老大帶我做研究，你的認真、細心、及觀察力一直是我的學習指標。在實驗器材上，要感謝洪天河先生不厭其煩的鼎力相助。另一方面要感謝劉春鞠學姊帶我整理研究工作，跟你的討論使我受益良多。感謝陸亭樺學姊，黃哲彥、黃仕璋、王偉立學長，有你們做為學習的榜樣，我才能真正融入研究生活。當然還有一起奮鬥成長的興弛、依萍、雅婷、恩毓，有你們一起修課、討論作業、互相砥礪，讓我享受跟朋友一起學習的愉快。此外彥廷、建至、阿仁，跟你們討論幫助我釐清很多觀念。另外，蔡玲意及古美玲學姊、黃國欽及林伯祥學長、阿龍哥、黃文政、紀暉、李易純、陳毅帆、莊威哲、龔家禎、林毓捷雖然跟大家只有短暫的相處，但我感覺得出來你們都是好人。還要額外感謝一起打球的好伙伴梁興弛、偉立哥、彥廷、阿仁，雖然我打球只有一千零一招，但有你們的強大支援還是可以讓我在短短的時間內有充足的運動量。除了實驗室的夥伴之外，我要感謝光環科技公司提供各種雷射元件，也感謝口試委員的指正與建議。

感謝跟我同甘苦共患難的老婆宸聿這麼多年來的陪伴，你跟宣竹是我認真向上的動力。還有感謝哥哥姊姊們對我從小的照顧與疼愛。最後，僅以此文獻給我摯愛的雙親，特別感謝你們的養育之恩。

Contents

Abstract (Chinese)	i
Abstract	ii
Acknowledgement	iii
Contents	iv
List of Figures	vi
Chapter1	Introduction.....	1
1.1	Quantum Billiards.....	2
1.2	Diffraction in Time.....	6
1.3	Singularities in Optical Waves.....	10
1.4	Vertical-Cavity Surface-Emitting Lasers.....	18
1.5	Overview of Thesis.....	24
Chapter2	Wave Functions of Quantum Billiards.....	26
2.1	The Square Billiard.....	27
2.2	The Equilateral-Triangular Billiard.....	36
2.3	The Chaotic Billiards.....	47
Chapter3	Analogous Observation on Quantum-Billiard Wave Functions from VCSELs.....	56
3.1	The Analogy between VCSELs and Quantum Billiard.....	58
3.2	Experimental Sutup.....	61
3.3	Typical Lasing Modes of Square VCSEL.....	64
3.4	Chaotic Wave Function in Rippled-Square VCSEL.....	73
3.5	Typical Lasing Modes in Equilateral-Triangular VCSEL.....	86

Chapter4	Transient Dynamics of Coherent Waves Released from Quantum Billiard: Analogous Studies on the Propagation of Lasing Modes Emitted from VCSELs.....	98
4.1	Stationary States Suddenly Released from 1-D Infinite Potential Well.....	100
4.2	Transient Dynamics of Coherent Waves Released from Quantum Billiard.....	104
4.3	Analogous Observations on Coherent Waves Released from Quantum Billiard by Free-Space Propagating Transverse Modes of VCSELs.....	112
4.4	Probability Current and Angular Momentum Densities of Coherent Waves Released from Quantum Billiard: Optical Vortices Generated by VCSEL.....	118
Chapter5	Vector Fields and Vector Singularities in VCSELs.....	145
5.1	Vector Field in Square VCSEL.....	147
5.2	Chaotic Vector Field in VCSEL.....	156
Chapter6	Summary and Future Work.....	167
6.1	Summary.....	168
6.2	Future Work.....	171
Appendix A	Diffraction in Time: Moshinsky's Shutter Problem.....	172
Appendix B	Angular Momentum Density of a Light Beam.....	176
References	182
Curriculum Vitae	201
Publication List	202

List of Figures

Chapter1

Fig. 1.1-1. Schematic diagram for a 2D flat billiard. The particle in the billiard goes in straight lines. The incidence angle on the wall equals the reflection angle. The energy of the particle is constant.

Fig. 1.2-1. (a) Demonstration of the shutter problem. (b) Red curve displays the temporary interference pattern and blue dash line indicates a classical result. (See Appendix A for a more detailed discussion.)

Fig. 1.3-1. A color wheel. At the center the color becomes undefined.

Fig. 1.3-2. (a)-(b) Vector fields with vortex, saddle, and source, respectively; (a')-(b') The corresponding orientation angle function of vector fields shown in (a)-(b).

Fig. 1.3-3. (a)-(c) The phase structures of singularities, saddle, and maximum (extremum). The gradient of these phases will result in the vector fields shown in Fig. 1.3-2 (a)-(c), respectively.

Fig. 1.4-1. Schematic diagram of an edge-emitting laser. The laser output is parallel to the semiconductor layers. The out put beam is highly diverged due to the thin emission region.

Fig. 1.4-2. Schematic diagram of a VCSEL. The laser output is perpendicular to the wafer. The isotropic aperture results in a good beam quality.

Chapter2

Fig.2.1-1. Some classical periodic orbits denoted by (p, q, ϕ) , where p and q are two positive integers describing the number of collisions with horizontal and vertical walls, and the parameter ϕ ($-\pi \leq \phi \leq \pi$) that is related to the wall positions of specular reflection points.

- Fig.2.1-2.** First some eigenstates and the one of $(n_1, n_2) = (30, 30)$. We can expect that conventional eigenstates do not manifest the properties of classical periodic orbits even in the correspondence limit of large quantum numbers.
- Fig.2.1-3.** Stationary coherent states $\Psi_{50,20}^{p,q,\phi}(x, y)$ associated with classical periodic orbits (p, q, ϕ) .
- Fig.2.1-4.** The N dependence of the wave pattern $|C_{N,5}^{1,1,0,6\pi}(x, y)|^2$. It can be seen that N is related to the mode order.
- Fig.2.1-5.** The M dependence of the wave patterns $|C_{30,M}^{1,1,0,6\pi}(x, y)|^2$. It can be seen that M is related to the localization of the patterns.
- Fig.2.2-1.** Some classical periodic orbits (p, q, ϕ) , where p and q are two positive integers with restriction $p \geq q$, and the parameter ϕ ($-\pi \leq \phi \leq \pi$) is related to the initial point of the billiard ball.
- Fig.2.2-2.** Some eigenstate of equilateral-triangular billiard $\Phi_{m,n}^{(C)}(x, y)$.
- Fig.2.2-3.** Some eigenstate of equilateral-triangular billiard $\Phi_{m,n}^{(S)}(x, y)$. Notice that $\Phi_{2n,n}^{(S)}(x, y) = 0$.
- Fig.2.2-4.** Stationary coherent states $|\Psi_{50,15}^{Tri}(x, y; p, q, \phi)|^2$ associated with classical periodic orbits (p, q, ϕ) .
- Fig.2.2-5.** The N dependence of the wave pattern $|C_{N,10}^{Tri}(x, y; 1, 0, \pi/3)|^2$. It can be seen that N is related to the mode order.
- Fig.2.2-6.** The M dependence of the wave patterns $|C_{40,M}^{Tri}(x, y; 1, 0, \pi/3)|^2$. It can be seen that M is related to the localization of the patterns.
- Fig. 2.3-1.** The stadium billiard. The trajectory in chaotic billiard is generally ergodic.
- Fig. 2.3-2.** Some unstable periodic orbits in the stadium billiard.
- Fig. 2.3-3.** First eight eigenstates of the stadium billiard. The result is similar to rectangular billiard.

- Fig. 2.3-4.** (a)-(d) The 152nd, 165th, 175th, and 208th excited states of a slightly asymmetric stadium billiard are shown to exhibit random patterns that do not exist in regular billiard.
- Fig. 2.3-5.** (a) A random superposition of several eigenstates with quantum number satisfying $54 \leq \sqrt{n_1^2 + n_2^2} \leq 55$, as illustrated in (b)
- Fig. 2.3-6.** (a)-(b) The statistics for the amplitude and intensity of the random wave shown in the previous figure. The fitting curves are Gaussian and Porter-Thomas distributions, respectively.
- Fig. 2.3-7.** (a)-(d) The scars appear in the 122nd, 132nd, 207th, and 258th excited states of the slightly asymmetric stadium billiard. The highlighted lines indicate the unstable periodic orbits.

Chapter3

- Fig.3.1-1.** (a) The schematic diagrams for vertical-cavity surface-emitting laser. The separability of the wave function in the VCSEL device enables the wave vectors to be decomposed into k_z and k_t . (b) The illustration of a wave incident upon the current-guiding oxide boundary would undergo total internal reflection for $k_t \ll k_z$.
- Fig.3.2-1.** The schematic diagrams for the experimental setup.
- Fig.3.2-2.** (a) The VCSEL mounted on the copper holder. (b) Side view of the cryogenic system. (c) The objective lens with NA=0.9 (d) Face view of the cryogenic system.
- Fig. 3.3-1.** The SEM image of square VCSEL device
- Fig. 3.3-2.** Optical microscope image view from the aperture of the VCSEL. The bright region displays the spontaneous emission to manifest the details on the square boundary.
- Fig. 3.3-3.** (a) The temperature dependence of the threshold current and the lasing modes observed at temperatures of (b) 295K (room temperature) (c) 285K (d) 250K (e) 230K.

- Fig. 3.3-4.** (a)-(c) The bouncing ball modes observed in different square VCSEL devices. (a')-(c') The theoretical explanations of (a)-(c), which are expressed by Eq. (3.3.2)-(3.3.4), respectively.
- Fig. 3.3-5.** a)-(c) Various superscar modes observed in different square VCSEL devices. (a')-(c') Theoretical interpretation of (a)-(c) by SU(2) coherent states $C_{36,10}^{1,1,0.57\pi}(x, y)$, $C_{38,6}^{1,1,0.46\pi}(x, y)$, and $C_{40,25}^{1,1,0.8\pi}(x, y)$ respectively
- Fig. 3.3-6.** (a)-(c) Various multi-POs superscar modes observed in different square VCSEL devices. (a')-(c') Theoretical patterns of (a)-(c) given by Eq. (3.3.6)-(3.3.8), respectively.
- Fig. 3.4-1.** Experimental pattern of the spontaneous emission to manifest the details on the ripple boundary.
- Fig. 3.4-2.** Near-threshold lasing patterns of the rippled VCSEL at temperatures of (a) $T = 260K$ and (b) $T = 220K$.
- Fig. 3.4-3.** (a) An unknown wave function (b) The intensity distribution (c) Square Root of intensity distribution (d) Positive part of the wave function (e) Demonstration of $2\psi_p(x) - |\psi(x)|$ (f) The result of $2\psi_p(x) - |\psi(x)|$.
- Fig. 3.4-4.** (a) and (b) The intensity plots of the positive wave functions $|\psi_p(x_i, y_j)|$ for experimental results shown in Figs. 3.4-2 (a) and (b), respectively.
- Fig. 3.4-5.** (a) and (b) Distribution of the coefficients $|C_{m,n}|$ obtained by Eq. (3.4.6) for experimental results shown in Figs. 3.4-1 (a) and (b).
- Fig. 3.4-6.** (a) and (b) The reconstructed patterns with the eigenfunction expansion method for experimental results.
- Fig. 3.4-7.** (a) and (b) The amplitude distributions of the wave functions shown in Fig. 3.4-6 (a) and (b), respectively.
- Fig. 3.4-8.** (a) and (b) The intensity distributions of the patterns shown in Fig. 3.4-6 (a) and (b), respectively.
- Fig. 3.5-1.** (a) Optical microscope image of the VCSEL device. (b) Zoom-in view of (a) and is operated with an electric current under threshold current at room

temperature. (c) The spontaneous emission to manifest the details on the triangular boundary temperature.

Fig. 3.5-2. Temperature dependence of the threshold current of the equilateral triangular VCSEL.

Fig. 3.5-3. (a)-(i) The near-threshold lasing patterns of triangular VCSEL at temperatures labeled by A-I in Fig 3.5-2, respectively.

Fig. 3.5-4. (a) Experimental pattern observe at 195K. (b) Numerical wave pattern of eigenstate $|\Phi_{5,55}^{(S)}(x, y)|^2$.

Fig. 3.5-5. Experimental pattern observe at (a)275K and (b)135K; Numerical wave pattern of coherent state (c) $|C_{36,9}^{Tri}(x, y; 1, 0, 0.23\pi)|^2$ and (d) $|C_{20,6}^{Tri}(x, y; 1, 1, 0.35\pi)|^2$; The classical periodic orbits that the wave functions localized on are depicted in the insets of (c) and (d).

Fig. 3.5-6. The intensity plots of the positive wave functions $|\psi_p(x_i, y_j)|$ for experimental results shown in Figs. 3.5-3 (f).

Fig. 3.5-7. (a) Experimental pattern observe at 175K. (b) Reconstructed pattern of (a). (c) Intensity statistics of (b) with fitting curve to be Porter-Thomas intensity distribution.

Chapter4

Fig. 4.1-1. (a)-(k) Intensity plots of $\psi^S(x, t; 10)$ at $t = 0T - T$, respectively, with equal time interval $\Delta t = 0.1T$. (l) Intensity plots of $\psi_{10}(x, t)$ at $t = 1.5T$. The intensity pattern preserves its shape after $t = 1.5T$.

Fig. 4.2-1. Numerical patterns to illustrate the wave patterns $|\psi_{15,15}(x, y, t)|^2$ at $t =$ (a) $0T$, (b) $0.1T$, (c) $0.2T$, (d) $0.3T$, (e) $0.4T$, (f) $0.5T$, (g) $1.0T$, (h) $2.0T$, and (i) ∞ .

Fig. 4.2-2. Numerical patterns to illustrate the wave patterns $|\Psi_{35,13}^{1,1,0,6}(x, y, t)|^2$ at $t =$ (a) $0T$, (b) $0.1T$, (c) $0.2T$, (d) $0.3T$, (e) $0.4T$, (f) $0.5T$, (g) $1.0T$, (h) $2.0T$, and (i) ∞ .

- Fig. 4.2-3.** Numerical patterns to illustrate the wave patterns $|C_{35,13}^{1,1,0.6}(x, y, t)|^2$ at $t =$ (a) $0T$, (b) $0.1T$, (c) $0.2T$, (d) $0.3T$, (e) $0.4T$, (f) $0.7T$, (g) $1.0T$, (h) $2.0T$, and (i) ∞ .
- Fig. 4.2-4.** Numerical patterns to illustrate the wave patterns $|\psi_{chaos}(x, y, t)|^2$ at $t =$ (a) $0T$, (b) $0.1T$, (c) $0.2T$, (d) $0.4T$, (e) $0.55T$, (f) $0.8T$, (g) $1.5T$, (h) $3.0T$, and (i) ∞ .
- Fig. 4.3-1.** Experimental patterns of a superscar mode with propagation distance at $z =$ (a) $0z_d$, (b) $0.1z_d$, (c) $0.2z_d$, (d) $0.3z_d$, (e) $0.4z_d$, (f) $0.7z_d$, (g) $1.0z_d$, (h) $2.0z_d$, and (i) 20cm , where $z_d \sim 72\mu\text{m}$.
- Fig. 4.3-2.** Experimental patterns of a chaotic mode with propagation distance at $z =$ (a) $0z_d$, (b) $0.1z_d$, (c) $0.2z_d$, (d) $0.4z_d$, (e) $0.55z_d$, (f) $0.8z_d$, (g) $1.5z_d$, (h) $3.0z_d$, and (i) 20cm , where $z_d \sim 138\mu\text{m}$.
- Fig. 4.4-1.** (a)-(f) The vector plot of $\vec{J}_{15,15}(x, y, t)$ at $t = 0.1T$, $0.2T$, $0.3T$, $0.4T$, $0.5T$, and $1.0T$, respectively.
- Fig. 4.4-2.** (a)-(f) show the density plots of $\bar{l}_{15,15}(x, y, t)$ at $t = 0.1T$, $0.2T$, $0.3T$, $0.4T$, $0.5T$, and $1.0T$, respectively.
- Fig. 4.4-3.** The OAM spectrum of $\psi_{15,15}(x, y, t)$.
- Fig. 4.4-4.** (a)-(f) The vector plot of $\vec{J}_{35,13}^{1,1,0.6\pi}(x, y, t)$ at $t = 0.1T$, $0.2T$, $0.3T$, $0.4T$, $0.5T$, and $1.0T$, respectively.
- Fig. 4.4-5.** (a)-(f) The density plots of $\bar{L}_{35,13}^{1,1,0.6\pi}(x, y, t)$ at $t = 0.1T$, $0.2T$, $0.3T$, $0.4T$, $0.5T$, and $1.0T$ are presented in Fig. 4.3-9 (a)-(f), respectively.
- Fig. 4.4-6.** The OAM spectrum of $\Psi_{35,13}^{1,1,0.6\pi}(x, y, t)$.
- Fig. 4.4-7.** (a)-(c) The intensity patterns of $\Psi_{35,13}^{1,1,\phi}(x, y, t)$ with $\phi = 0$, 0.25π , and 0.5π , respectively; (a')-(c') The OAM spectra of the coherent states shown in (a)-(c), respectively.

- Fig. 4.4-8.** (a)-(f)The vector plot of $\vec{J}_{35,13}^{1,1,0,6\pi}(x, y, t)$ at $t = 0.1T$, $0.2T$, $0.3T$, $0.4T$, $0.7T$, and $1.0T$, respectively.
- Fig. 4.4-9.** (a)-(f)The density plots of $\bar{L}C_{35,13}^{1,1,0,6\pi}(x, y, t)$ at $t = 0.1T$, $0.2T$, $0.3T$, $0.4T$, $0.7T$, and $1.0T$, respectively.
- Fig. 4.4-10.** The OAM spectrum of $C_{35,13}^{1,1,0,6\pi}(x, y, t)$.
- Fig. 4.4-11.** (a)-(f) The vector plot of $\vec{j}_{chaos}(x, y, t)$ at $t = 0.1T$, $0.2T$, $0.4T$, $0.55T$, $0.8T$, and $1.55T$, respectively.
- Fig. 4.4-12.** (a) The vector plot of $\vec{j}_{chaos}(x, y, 0.1T)$. (b)-(d) Zoom-in views of small regions marked by the hollow squares in (a). Backgrounds are the corresponding contour plots of phase functions.
- Fig. 4.4-13.** (a) The vector plot of $\vec{j}_{chaos}(x, y, 0.2T)$. (b)-(d) Zoom-in views of small regions marked by the hollow squares in (a). Backgrounds are the corresponding contour plots of phase functions.
- Fig. 4.4-14.** (a) The vector plot of $\vec{j}_{chaos}(x, y, 0.4T)$. (b)-(d) Zoom-in views of small regions marked by the hollow squares in (a). Backgrounds are the corresponding contour plots of phase functions.
- Fig. 4.4-15.** (a)-(f) The density plot of $\bar{l}_{chaos}(x, y, t)$ at $t = 0.1T$, $0.2T$, $0.4T$, $0.55T$, $0.8T$, and $1.55T$, respectively.
- Fig. 4.4-16.** The OAM spectrum of $\psi_{chaos}(x, y, t)$.

Chapter5

- Fig. 5.1-1.** (a) Reference of the polarization angle (b) The threshold currents of the two polarizations. Simultaneous lasings occur at temperatures around $295K$ and $255K$.
- Fig. 5.1-2.** (a)-(d) The lasing patterns in 0° , 45° , 90° , and -45° and (e) The total intensity pattern observed at $295K$.
- Fig. 5.1-3.** (a)-(d) The lasing patterns in 0° , 45° , 90° , and -45° and (e) The total

intensity pattern observed at $255K$.

- Fig. 5.1-4.** (a)-(d) The reconstructed patterns of Fig. 5.2-3(a)-(d), respectively.
- Fig. 5.1-5.** (a) The contour plot of the angle function $\Theta(x, y)$. (b) Zoom-in view of the small regions highlighted by the white square. (c) The vector plot of the polarization vector with vortices and saddles labeled by “+” and “-” signs, respectively.
- Fig. 5.2-1.** Experimental polarization-resolved near-field patterns observed at the operating temperature of $T=265$ K with polarization in (a) 0° (perpendicular) (b) 90° (horizontal) (c) 45° (d) 135° .
- Fig. 5.2-2.** (a) and (b) Intensity plots of the positive wave functions $|\psi_p(x_i, y_j)|$ for experimental results shown in Figs. 5.2-1(a) and 5.2-1(b), respectively.
- Fig. 5.2-3.** (a) and (b) Distribution of the coefficients $|C_{m,n}|$ obtained by Eq. (3.4.6) for experimental results shown in Figs. 5.2-1(a) and (b), respectively.
- Fig. 5.2-4.** (a)-(d): Reconstructed patterns with the eigenfunction expansion method for experimental results shown in Fig. 5.2-1(a)-(d), respectively.
- Fig. 5.2-5.** Amplitude distributions of the polarization-resolved wave functions (blue step lines) for experimental results shown in Fig. 5.2-1(a)-(d), respectively. Red lines: Gaussian distributions (Eq. (2.3.2)).
- Fig. 5.2-6.** Intensity distributions of the polarization-resolved wave functions (blue step lines) for experimental results shown in Fig. 5.2-1(a)-(d), respectively. Red lines: Porter-Thomas distributions (Eq. (2.3.3)).
- Fig. 5.3-7.** (a) The contour plot of the angle function $\Theta_c(x, y)$. (b)-(c) Zoom-in view of the two small regions with the hollow circles on the singularities.

Chapter 1

Introduction



1.1 Quantum Billiards

Billiards is known as a dynamical system in which a particle goes in straight line and elastically reflects from the hard-wall boundary, as illustrated in Fig. 1.1-1. In general the region enclosed by the boundary of the billiards can be multi-dimensional and even in non-Euclidean space [KL91], but here subject is restricted to the billiards in two-dimensional (2D) plane. Depending on the initial conditions, initial position and velocity, there are infinitely possible trajectories and they are all deterministic, i. e. they can be traced. Besides, the Poincare map of the billiards can be easily obtained by calculating particle's incident angle on the circumference. As a result, billiards is often used as a paradigm in study chaos [Sina70, Buni79].

Quantum billiards [Stöc99], a quantum analogue of classical dynamic billiards, is actually a 2D infinite potential well in arbitrary shape. According to Bohr-Sommerfeld quantization rule, the eigenenergies of the quantum billiards can be calculated from the classical periodic orbits (POs). In 1917 Einstein suggested that the close integral in Bohr-Sommerfeld quantization rule can be evaluated in phase space in which the energy surface of an integrable system forms a torus [Enge97, Ston05]. Meanwhile, Einstein raised a question: how to quantize a classically nonintegrable system, since there is no close loop in phase space. The survey concerns the quantum manifestation of classical chaos was then termed quantum chaos [BÅ00, Stöc99] or quantum chaology [Berr87].

Even though quantum mechanics has been well developed in 1920s, Einstein's question was not answered until Gutzwiller used trace formula to connect the quantum mechanical energy density with classical POs of chaotic systems in 1970s [Gutz71, Gutz80, Gutz90]. The periodic-orbit theory has been experimentally tested by microwave billiards [SS90, Rich01]. Furthermore, the periodic-orbit theory was utilized to show that the statistics of nearest-neighbor energy spacing of chaotic system should obey Wigner distribution, in contrast to Poisson distribution of regular

system [Berr83]. This level statistics is often used as a signature of quantum chaos and has been intensively studied in quantum billiards [MK79,SS90] as well as in other various systems [DG86, Haak91, Wint87, WKL+89].

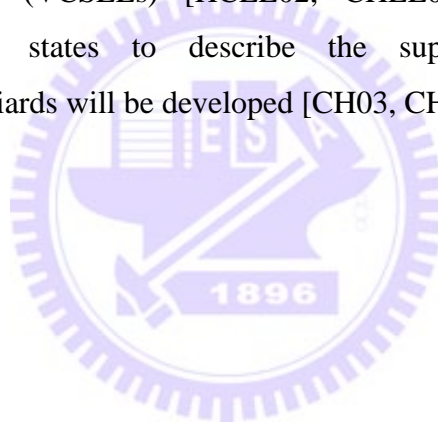
On the other hand, the wave-function aspect, Berry used semiclassical approach to show that the autocorrelation function of chaotic wave function is Bessel-type and suggested that chaotic wave function should be Gaussian random waves [Berr77]. With the numerical computation, this conjecture was validated by McDonald and Kaufman who showed that the eigenfunction of stadium billiard indeed exhibits random pattern [MK79, MK88]. Although the chaotic eigenfunctions were shown to be generally ergodic, Heller showed that high-order eigenfunctions of stadium billiard would concentrate on the classical unstable periodic orbits [Hell84]. Such a localized wave function has been called the “scar [Hell84].”

The scar has been shown to play a vital role in a wide variety of physical systems. For examples, the lasing mechanism of high-power directional emission in deformed microdisk lasers has been analogously interpreted with the scar effect in chaotic billiards [GCN+98, LLHZ06, LLZ+07, NS97, NSC94, RTS+]; the conductance fluctuations of quantum dots, in which electronic motion is predominately ballistic in nature, have also been shown to be closely related the scarred wave functions [BAF+99]; the efficiency of fiber laser can be enhanced by selectively amplification of scarred optical wave [MDLM07].

Even if the scar has been shown to be very important, direct experimental observation of scarred matter wave is very few [CSG+03] since the wave function of 2D system is very difficult to measure. The observations of the scar were mostly performed in analogous experiments. Due to the analogy between 2D Helmholtz equation and 2D time-independent Schrödinger equation, the first experimental visualization of scars was realized in the microwave cavity [KKS95, Srid91, SS92]. As well as microwave cavity, scar modes were also manifested in acoustic wave cavity [CH96, KAG01,]. Besides, the scarred optical patterns were also shown to appear in the transverse mode of optical fiber [DLM01].

In addition to scars, the other significant high-order states are the so-called

superscars [BS04, BDF+06]. The terminology “superscar” was originally used by Heller [Hell84] to refer the wave functions localized on stable periodic orbits in stadium billiard and to make a difference with scar. Recently its meaning was extended to wave function localized on stable periodic orbits in pseudointegrable billiard [BS04, BDF+06]. Superscar has also been shown to closely relate to the conductance fluctuation of quantum dots [AF99, CLO+97, LMH+06] and the mode characteristics of microdisk lasers with regular shapes [AYL+06, CKH+00, HGW00, HGYL01, LCG+04, PCC01, YAK+07]. However the analogous observations of the superscars are much fewer than that of scars [BDF+06, HCLL02]. The main aim of this thesis is to analogously observe the superscar mode by broad-area vertical-cavity surface emitting lasers (VCSELs) [HCLL02, CHLL03a, CLS+07, CSCH08]. Besides, the coherent states to describe the superscars in square and equilateral-triangular billiards will be developed [CH03, CHL02].



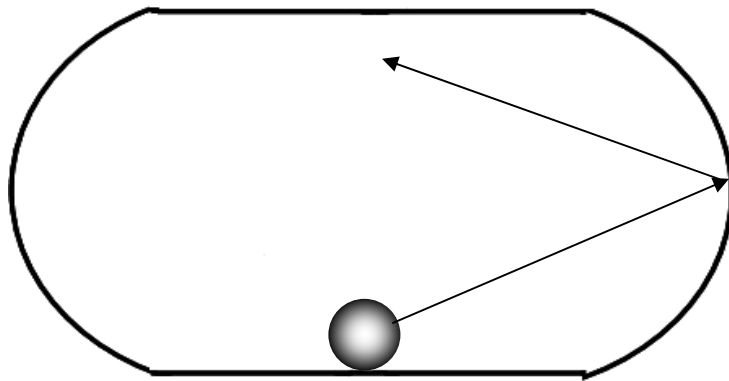


Fig. 1.1-1. Schematic diagram for a 2D flat billiard. The particle in the billiard goes in straight lines. The incidence angle on the wall equals the reflection angle. The energy of the particle is constant.

1.2 Diffraction in Time

Diffraction is a particular behavior of waves, which occurs when propagating waves encounter obstructions. It may result in a digression from the geometrical path including deflection into geometrically forbidden regimes. As well as classical waves (such as light, sound, or water waves), matters (such as electron, neutron, or proton) can also be diffracted due to wave-particle duality [DG27, SWMD48, WS48]. The diffraction mentioned above are spatial, while Moshinsky showed that matter wave can be also diffracted in time [Mosh52], i. e. waves can be deflected into a time zone which is classically prohibited. Consider the following shutter problem proposed by Moshinsky: A monochromatic non-relativistic particle beam, moving parallel to the x -axis, incidents on a completely absorbing shutter placed at $x = 0$, as illustrated in Fig. 1.2-1 (a). If the shutter is suddenly opened, what will be the transient particle current observed at a distance behind the shutter? By the analogy between paraxial optics and non-relativistic quantum mechanics [DD04], it was showed that the transient wave function has remarkable temporary interference pattern (as shown in Fig. 1.2-1 (b)) analogous to the spatial interference pattern of light diffracted by a sharp edge [Mosh52] (See Appendix A for a more detailed discussion). Since Moshinsky first put forward this idea, diffraction in time has received considerable attentions. The time evolution of various bound states [Godo02, Godo03] and even arbitrary initial conditions [GM05] have been investigated for an abrupt potential change. Besides, the transient dynamics has also been studied for potentials with different time modulations [dCMM07]. Moreover, the case of matter wave diffraction simultaneously in space and time has also been considered [BZ97]. The experimental test for this diffraction-in-time effect was indeed hard to reach at the time of the first introduction. However, due to the development in ultrafast laser [PLW+03], atom cooling, and optical trapping [WPW99], the transient dynamics has been recently observed in wide variety of

systems including neutrons [HFG+98], ultracold atoms [SSDD95], electrons [LSW+05], and Bose-Einstein condensates [CMPL05].

The explorations of diffraction in time are not only for scientific interests but also have some potential applications, as the transient response to abrupt changes of the confined potential in semiconductor structures and quantum dots would exhibit diffraction-in-time effect [DCM02, DMA+05]. As indicated in previous section, semiconductor quantum dots have been widely used as 2-D quantum billiards to explore the properties of quantum chaos [NH04]. Understanding the time evolution of suddenly released quantum-billiard waves can provide the nanostructure transport properties for developing novel ultrahigh-speed semiconductor devices [DCM02, DMA+05]. Moreover, it is closely related to atom laser dynamics from a tight wave guide whose boundary shape can be modified with the laser-trapping beam [dCL+08]. However the presented theoretical analysis only focuses on 1D potential barrier, the diffraction in time of 2D quantum-billiard wave functions has never been explored. In 1-D systems the current flow is monotonous since it is linear and can only flow to two direction, $+x$ or $-x$ axes. However, the 2-D probability current density becomes much complicated because its multi directionalities. Moreover, orbital angular momentum (OAM), which is an important physical quantity both in classical- [GPS02] and quantum-mechanical [BVD65] systems, will naturally arise due to the 2D current flow.

In this dissertation, the time evolutions, probability currents, and OAM densities of eigenstate, coherent state, and chaotic state released from 2D square billiard are theoretically investigated. Besides, the evolution of the time-diffracted wave functions are analogously observed by the free space propagation of lasing modes of VCSEL based on the similarities between paraxial optics and non-relativistic quantum mechanics. However, the analogies between paraxial optics and 2-D quantum system are not only restricted to the correspondence between amplitude distribution and wave function but also consist in the similarity between optical and quantum OAM densities [ZB06, ZB07]. Recent years have been increased attention being given to optical OAM [ABSW92, FAAP08] for its wide applications in atom trapping

[KTS+97], optical tweezers [MRS+99], and optical spanner [SADP97]. Furthermore, OAM of light beam can be encoded as qudit and has great potential applications in quantum information [MVWZ01]. Therefore, the analysis on quantum OAM of wave functions released from 2D billiard can be served as an analogous investigation on optical OAM of lasing modes emitted from VCSEL.



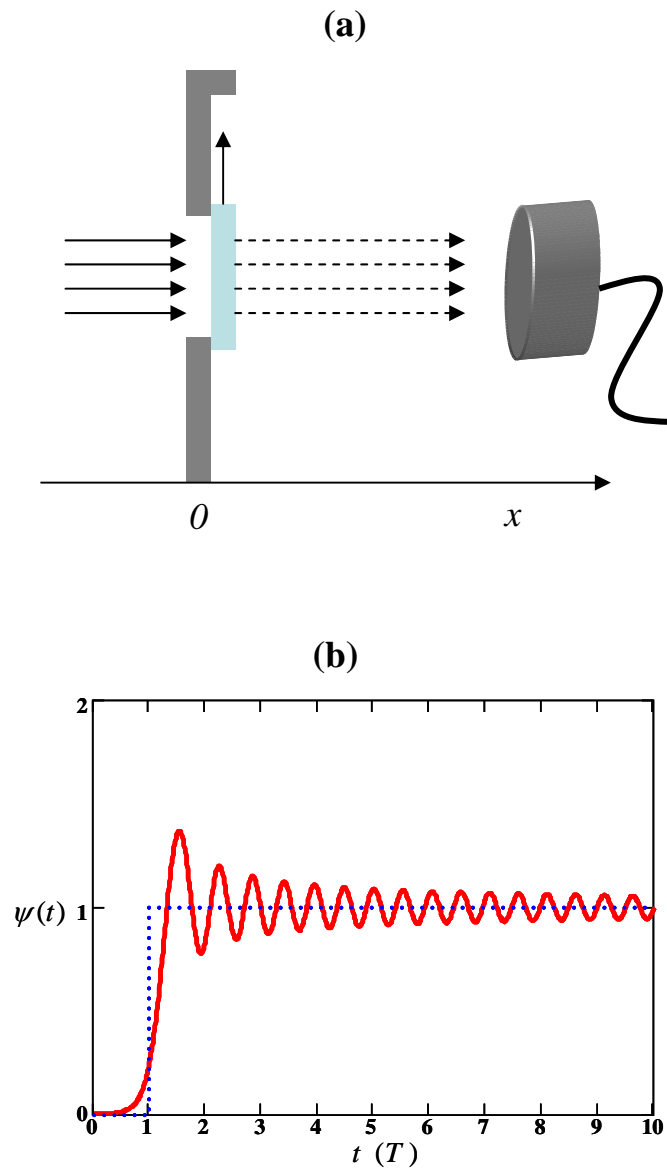


Fig. 1.2-1. (a) Demonstration of the shutter problem. (b) Red curve displays the temporary interference pattern and blue dash line indicates a classical result. (See Appendix A for a more detailed discussion.)

1.3 Singularities in Optical Waves

Singularities are places at which some quantities become undefined. For example, as shown in Fig. 1.3-1, the center of a color wheel is a color singularity at which the color becomes undefined. The basic reasons study singularities is because of their ubiquity and structural stability [Berr80]. For optical waves, there are mainly two kinds of singularities being concerned: phase singularities and polarization singularities [Nye99]. The survey of these singularities has become a very modern area of interest in contemporary physics and is named singular optics [SV01].

Generally, phase singularities [Berr98] are points in plane and lines in space at which intensity vanishes and the phase of complex scalar wave field become undefined. In this work only 2D complex scalar field is concerned, which stand either for 2-D quantum wave function or for transverse modulus of light beam. It is convenient to introduce the mathematical form

$$\psi(x, y) = R(x, y) + i I(x, y). \quad (1.3.1)$$

with $R(x, y)$ and $I(x, y)$ to be real. By defining $\rho(x, y) = R^2(x, y) + I^2(x, y)$ and $\theta(x, y) = \arg[\psi(x, y)]$, the scalar field can rewrite as

$$\psi(x, y) = \sqrt{\rho(x, y)} \exp[i\theta(x, y)]. \quad (1.3.2)$$

The positions at which $R(x, y)$ and $I(x, y)$ simultaneously equal to zero such that the amplitude $\sqrt{\rho(x, y)}$ vanishes and the phase $\theta(x, y)$ becomes undefined are the phase singularities. These nodal points in 2D plane are analogous to crystal dislocation and are also referred as phase dislocation [NB74].

Another important quantity related to the phase is the probability current density

which is generally given by

$$\vec{j}(x, y) = \frac{\hbar}{m} \text{Im}[\psi^*(x, y) \nabla \psi(x, y)]. \quad (1.3.3)$$

Substituting Eq. (1.3.2) in to Eq. (1.3.3), the probability current density can be alternatively expressed as the gradient of the phase $\theta(x, y)$

$$\vec{j}(x, y) = \frac{\hbar}{m} \rho(x, y) \nabla \theta(x, y). \quad (1.3.4)$$

According to fundamental calculus, the curl of \vec{j} will be zero at all positions except for the phase singularities. Hence, phase singularity is also termed as vortex for the circulating current density around it. The vortices have been involved in a wide variety of coherent phenomena such as superconducting films [MFDM03], superfluid [MFDM03], Bose-Einstein condensate [MAH+99], microwave billiards [ŠHK+97], quantum ballistic transport [BSS02], and liquid crystal films [dGP93].

One important characteristic of a phase singularity is its topology charge (also named as winding number or dislocation strength) defined by

$$s = \frac{1}{2\pi} \oint_C d\theta = \frac{1}{2\pi} \oint_C \nabla \theta(x, y) \cdot (dx \hat{a}_x + dy \hat{a}_y) \quad (1.3.5)$$

, where C is arbitrary closed loop containing only one singularity inside. The charge is positive (negative) if the phase circulates counterclockwise (clockwise). A crucial topological property of singularities is the sign rule which indicates that the charge of the neighboring singularities on a constant phase contour must have opposite signs [Freu95].

Due to the underlying analogy between optical momentum density and the probability current density (See Appendix B for a more detailed discussion), the phase singularity of the amplitude distribution of light beam manifest itself as optical vortex

[VS99]. Consequently, optical vortices is intimately related to optical OAM [SGV+97]. As revealed in last section, optical OAM has attracted much interest because of the wide applications, such as atom trapping [KTS+97], optical tweezers [MRS+99], optical spanner [SADP97], and quantum information [MVWZ01].

In singular optics to generate optical vortex is one of the predominant topics. Typically, optical vortices can be generated by passing a fundamental-mode Gaussian beam through such as cylindrical-lens mode converters [BAv+93], holograms [HMS+92], spiral phase plates [BCKW94], axicons [KKS+07], uniaxial crystals [VSF+06], and glass wedges [YAC+07]. Besides, spontaneous formations of optical vortices in laser system have also been reported in solid-state lasers [CL01, OC09], Na₂ laser [BBL+91] and proton-implanted vertical-cavity surface-emitting laser (VCSEL) [SO99]. The mechanism of the vortex formation in proton-implanted VCSEL is due to transverse mode locking, assisted by the laser nonlinearity, of nearly degenerate Laguerre-Gaussian modes [SO99]. Different from proton-implanted VCSEL, the near-field transverse modes of oxide-confined VCSELs were shown to be analogous to closed-quantum-billiard wave functions [HCLL02, CHLL03a, CLS+07, CSCH08], which are purely real and contain only zero phases. However, transverse field becomes complex as soon as it propagates out of the VCSEL cavity [CYC+09] and contains intricate vortex structure, as will be shown in chapter4.

In addition to phase singularity of complex scalar waves, the singularities at which the orientations of a real vector field become undefined are the so-called vector field singularities [Denn01], or vector singularities [Freu01] in brief. In terms of mathematical expression, a 2-D real vector field can be written as

$$\vec{V}(x, y) = V_x(x, y) \hat{a}_x + V_y(x, y) \hat{a}_y . \quad (1.3.6)$$

The vector singularities are the positions at which $V_x(x, y)$ and $V_y(x, y)$ equal to zero simultaneously such that the orientation angle determined by the angle function

$$\Theta(x, y) = \text{angle}[V_x(x, y), V_y(x, y)] \quad (1.3.7)$$

becomes undefined. The topological charge of a vector singularity given by

$$I_p = \frac{1}{2\pi} \oint_C d\Theta = \frac{1}{2\pi} \oint_C \nabla\Theta(x, y) \cdot (dx \hat{a}_x + dy \hat{a}_y) \quad (1.3.8)$$

is called Poincaré index of zero [Denn01], where the contour C should be a very small path around the singularity. The vector singularities with Poincaré index to be ± 1 can be categorized into vortices, sources and sinks, and saddles. Fig. 1.3-2 (a)-(c) show the distributions of the real vector field around a vortex, saddle, and source, respectively. The contour plots of orientation angles functions of the vector fields shown in Fig. 1.3-2 (a)-(c) are depicted in Fig. 1.3-2 (a')-(c'). It can be seen that both vortex and source have their Poincaré indices to be 1 and the Poincaré index of a saddle is -1 . In fact the probability current density is one kind of the most familiar vector fields. The locations in phase function $\theta(x, y)$ correspond to the vector singularities of current density $\vec{j}(x, y)$ are called critical points. The critical points of phase giving rise to vortices, sources and sinks, and saddles in current density are singularities, extrema, and saddle. Assume the vector fields shown in Fig. 1.3-2 (a)-(c) are probability current densities of some wave functions. We depict the corresponding phase structures of the wave functions, which containing phase singularity, maximum, and saddle, in Fig. 1.3-3 (a)-(c), respectively. In conclusion, these critical points of scalar function become crucial as some vector field is expressed as the gradient of the scalar function.

Vector singularities have also been involved in a wide variety of physics. For optical waves, vector singularities are isolated, stationary points in a plane at which the orientation of the electric vector of a linearly polarized real vector field becomes undefined [Freu01]. The features of the vector singularities have been experimentally observed in laser modes with the interrelated behavior of spatial

structures and polarization states [Gil93, VKMR01, LCH07, Erdo92, PTMA97]. In this work, the vector singularities embedded in the near field patterns of VCSELs will be analyzed in an unambiguous way [CHLL03b, CSL+07].



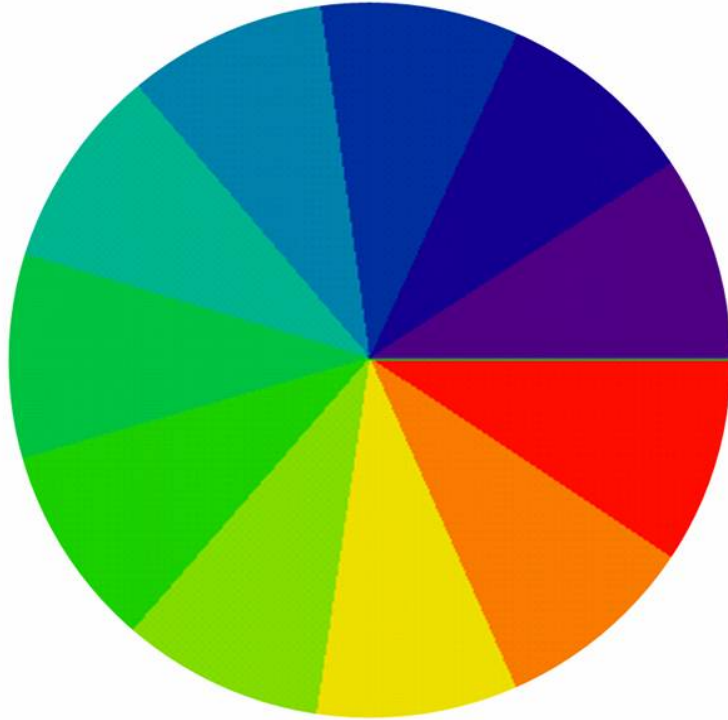


Fig. 1.3-1. A color wheel. At the center the color becomes undefined.

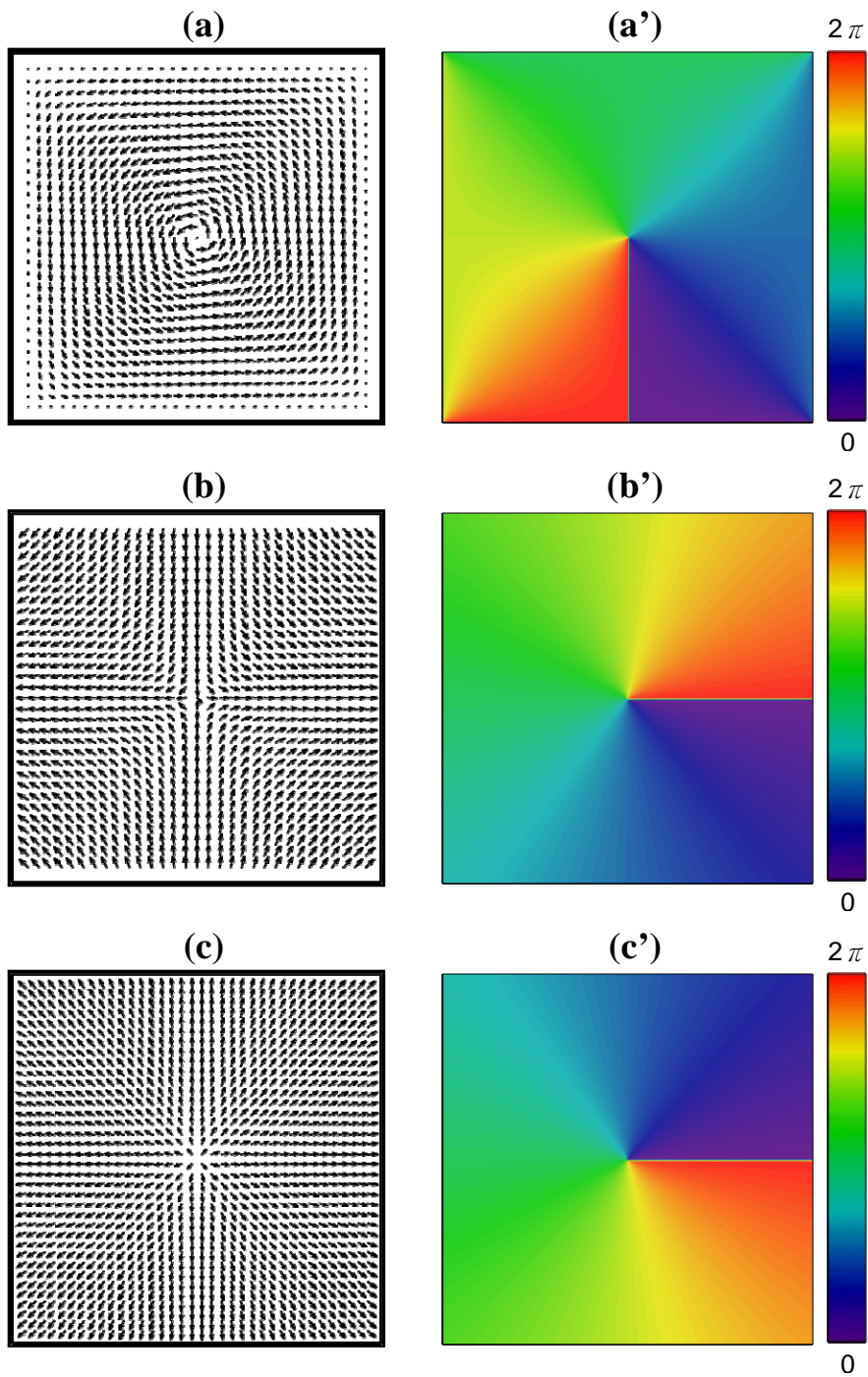


Fig. 1.3-2. (a)-(b) Vector fields with vortex, saddle, and source, respectively; (a')-(b') The corresponding orientation angle function of vector fields shown in (a)-(b).

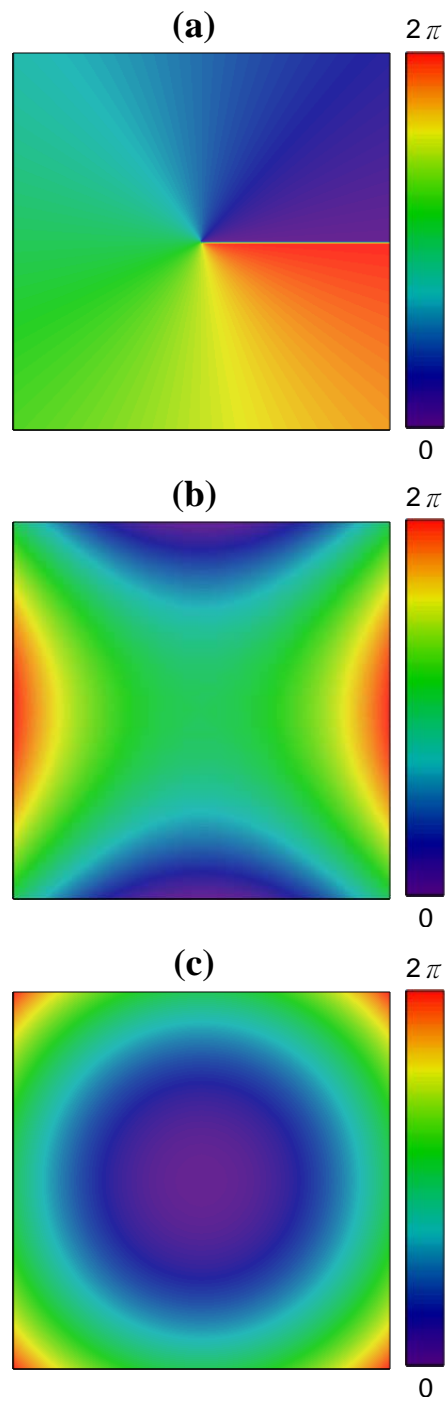


Fig. 1.3-3. (a)-(c) The phase structures of singularities, saddle, and extremum. The gradient of these phases will result in the vector fields shown in Fig. 1.3-2 (a)-(c), respectively.

1.4 Vertical-Cavity Surface-Emitting Lasers

Stimulated emission is one of basic interactions between light and matter. During this process an excited electron is perturbed by an incident photon with specifying energy and then jumps to a lower energy level accompanied with emission of another photon with the same energy, polarization, phase, and direction as the incident photon. Coherent amplification of radiation by stimulated emission was first realized with microwave by Townes et al in 1954 [GZT54]. Four years later Schawlow and Townes proposed that coherent amplification can be applied to infrared and optical wave [ST58]. In 1960 Maiman first demonstrated laser, light amplification by stimulated emission of radiation, operation with a ruby crystal [Maim60]. The superiors of laser over other light source, such as light bulbs and neon tubes, consist in the high directionality and intensity, coherence, and monochromatism of the output light. Based on these advantages, laser has had great applications in many fields of science and influenced people's life in various aspects.

Laser is mainly composed by gain medium, optical cavity, and pumping source [Sieg86]. One way to catalog lasers is in accordance with the types of the gain medium: For example, solid-state and gas lasers have solid crystal and gas as their gain medium, respectively. Among all types of lasers, semiconductor lasers have the greatest impact on human's everyday life: they are applied to the CD-ROM, DVD-player, laser printer, etc.

The first semiconductor laser was demonstrated with a p-n junction by Nathan et al at IBM in 1962 [NDB+62]. However, a simple p-n junction laser is not efficient and a great improvement by using heterostructure was proposed by Kroemer [Kroe63]. The device structure of a typical hetero-structure laser diode is depicted in Fig. 1.4-1. The electrons in the valence band of active medium are electrically pumped to conduction band to achieve population inversion. The resonator cavity is formed by the cleaved facets which have a reflectivity of about 30% due to the large

discontinuity of refraction indices between semiconductor and air. The laser output is parallel to the epitaxial layers and emitting from the edge of the device. As a result such laser diodes are commonly referred as edge-emitting lasers (EELs).

There are many advantages of semiconductor laser over other types of lasers: They are compatible with modern electronics and are easy to use; the whole device is manufactured by traditional semiconductor process such that they are compact and low-cost; their lasing wave length can be engineered for special purposes. However, due to the extremely narrow emitting region, the beam profile of an EEL is elliptical with high divergence in one direction and is detrimental for coupling into optical fiber. Besides, EEL is typically under multi-mode operation because of the long cavity length and this would induce longitudinal mode hopping that is undesirable for application. These critical drawbacks motivated the invention of VCSEL.

The device structure of a modern VCSEL structure is schematically shown in Fig. 1.4-2 to make a comparison with an EEL. As indicated by its name, the directions of laser oscillation and output are perpendicular to the semiconductor wafer. The first VCSEL is invented by Iga and co-workers in 1979 [SIKS79], while only pulsed operation is permitted at cryogenic temperature. With usage of distributed Bragg reflector (DBR) as cavity mirror [OHKY83], room-temperature continuous wave (CW) lasing of VCSEL was achieved by the inventors in 1989 [KKI89]. On the other hand, the efficiency of VCSEL has a big breakthrough with the introduction of quantum wells as active medium [JHT+89]. The efficiency is also closely related to the lateral electric current confinement, which also guides the optical field. There are four types of electrical and optical confinement, air-post, ion-implanted, regrown, and oxide-confined structures, for the modern VCSEL devices [CC+97]. Among these, oxide-confined VCSEL has the highest efficiency and lowest threshold and the devices used in this work are of this type.

Resulted from the symmetric transverse optical confinement, VCSEL has good beam quality as was expected. The cavity length of VCSEL is consequently designed to be about one wavelength and permits single longitudinal mode lasing. Due to the thin active layer, VCSEL can be modulated with an ultra-high speed

[STB+93]. Since the reflected mirrors of VCSELs are fabricated during epitaxial growth, batch processing and on-wafer testing make VCSEL more cost-efficient. Meanwhile, VCSELs can be arranged to high-fill-factor 2D laser arrays [GMJ+99] and can be monolithically integrated with photodetector [HTW+91], waveguide [LLP+05], modulator [GGK+96], and mirror [KDR+08], etc. Owing to these advantages, VCSEL has been widely used in optical communication [EFM+96, GAL98].

Despite that VCSEL is superior to EEL in many aspects VCSEL still has two shortcomings that do not exist in EEL. First, the output power of VCSEL is limited by the thin active medium. In contrast, high output power can be achieved by enhancing the length of the laser diode. Though high output power of VCSEL can be realized by enlarging the aperture, this will simultaneously result in high divergence angle since the Fresnel number of a cavity is proportional to the transverse area. Second, the polarization of EEL is fixed due to the extremely asymmetric emission region; while the polarization of VCSEL is unstable because its transverse aperture is isotropic. There is much effort to deal with these two problems: High-power fundamental-mode operation of broad-area VCSEL can be attained by manufacturing a photonic crystal on the surface [KSL+08] and integrating with monolithic micromirror [KDR+08]; the polarization of VCSEL can be controlled by several way [BCSR99, VdS+06]. However, our goal here is not to overcome the two problems but base on the two characteristics to explore interesting pattern formations in VCSELs.

Pattern formation [Lam98, CH99] is the spontaneous development of spatial (-temporal) nonuniformities of non-equilibrium systems under homogeneous external condition and has attracted much interest in chemistry [POS97], biology [LLM06], and physics [GL99]. Recently, Hegarty *et al.* have reported interesting pattern formations in the transverse mode of large-aperture oxide-confined VCSELs [HHMC99, HHP+99]. Besides, optical vortices have also been shown to spontaneously form in implanted VCSEL [SO99]. More recently, broad-area VCSELs have been shown to maintain cavity solitons [BTB+02, TAFJ08]. Most

importantly, it has also shown that the near-field transverse patterns of broad-area oxide-confined VCSEL are analogous to the mesoscopic wave functions of quantum billiards [HCLL02, CHLL03a, CLS+07, CSCH08]. The main idea of this dissertation is based on this interesting analogy.

As mentioned above, the polarization of VCSEL is unstable due to the isotropic gain region and birefringence. Generally, VCSEL emits linearly polarized light field in one direction at near-threshold current. As the injection current increases, the polarization behaviors of VCSEL becomes more complicated. One general condition is that two orthogonal linear polarization states independently coexist. Another interesting phenomenon is the polarization switching, in the process the lasing polarization state switches to the perpendicular one [AS01, MFM95, vEWW98]. Here a third case in which the transverse pattern has different morphology at different polarization angles is concerned [Erdo92, PTMA97]. In fact, this condition corresponds to the formation of vector field [CHLL03b], which also has been studied in various laser systems [Gil93, VKMR01, CLH06, LCH07]. Final part of this dissertation is to analyze the vector singularities embedded in the vector field emitted from VCSEL.

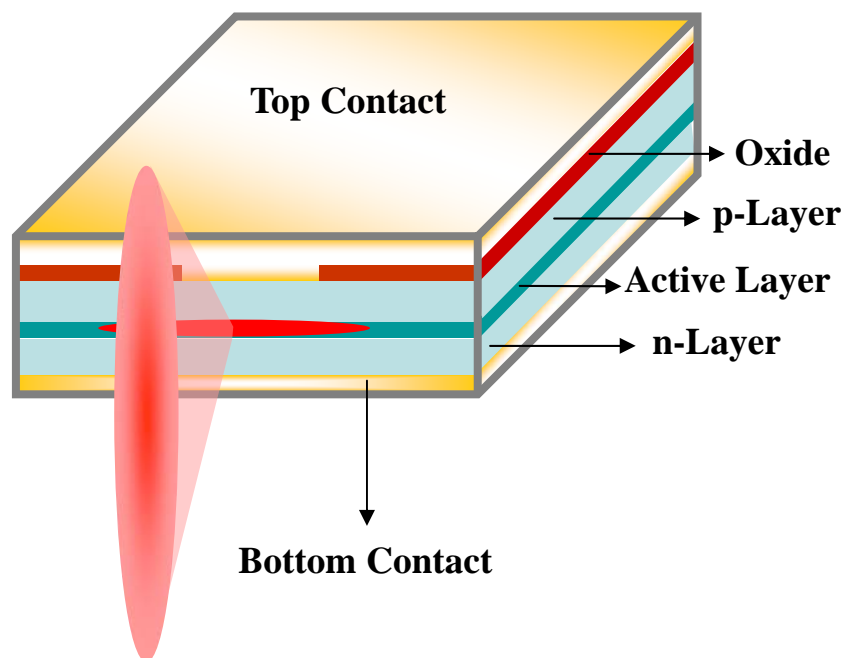


Fig. 1.4-1. Schematic diagram of an edge-emitting laser. The laser output is parallel to the semiconductor layers. The output beam is highly divergent due to the thin emission region.

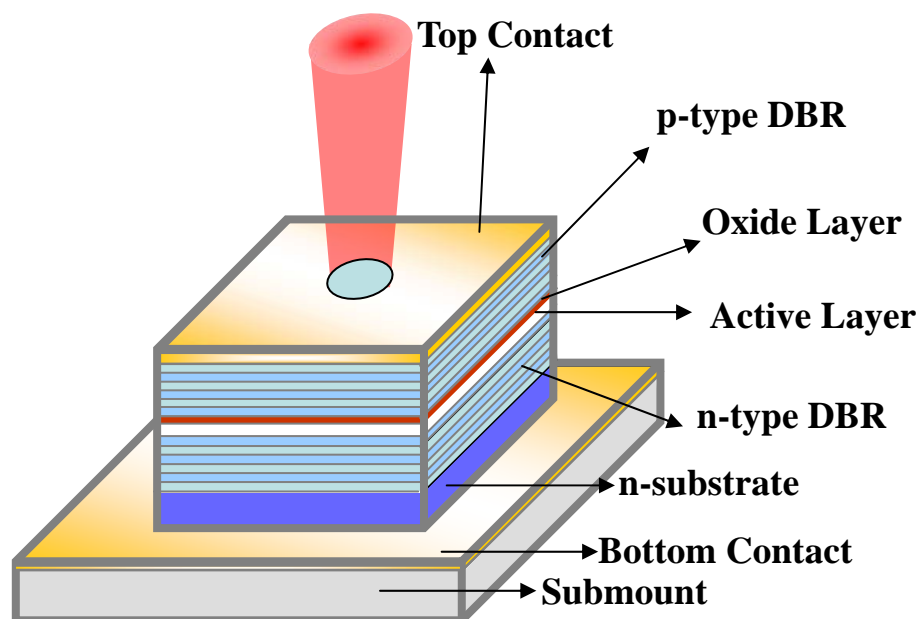


Fig. 1.4-2. Schematic diagram of a VCSEL. The laser output is perpendicular to the wafer. The isotropic aperture results in a good beam quality.

1.5 Overview of Thesis

The main text of this dissertation is structured as follow:

In chapter2 quantum billiards is employed to explore the classical-quantum correspondence of regular and chaotic systems. In Sec. 2.1 the classical POs and quantum eigenstates of square are reviewed and then the coherent states with wave functions localized on classical POs will be introduced. Similar process is done for an equilateral-triangular billiard in Sec. 2.2. In the final section of chapter2, the stadium billiard is used to demonstrate the quantum properties of chaotic systems.

In chapter3 the analogous observations on various quantum-billiard wave functions from transverse modes VCSELs are presented. The first section of this chapter justifies the analogy between the transverse mode of VCSELs and the wave functions of quantum billiards. After which the experimental setup will be shown. The typical lasing modes of the square billiard are presented in Sec. 3.3. What follows is the chaotic modes generated by a rippled-square VCSEL. Finally, equilateral-triangular shaped VCSEL are shown to exhibit mixed properties of regular and chaotic system.

In chapter4, we investigate the time evolutions, probability currents, and OAM densities of eigenstate, coherent state, and chaotic state released of 2D square billiard. The time evolution of a stationary wave function abruptly released from 1-D infinite potential is first reviewed in the opening section. In Sec. 4.2, we extend to study the transient dynamics of various wave functions with a suddenly removal of 2-D square billiards. In third section of chapter4, we utilize the similarity between paraxial optics and 2-D non-relativistic quantum mechanics to analogously observe the time evolutions of coherent waves released from quantum billiards by free-space propagation of transverse modes of VCSELs. In final part of chapter4 we are to analyze the linear and angular momentum densities of the light beam emitted from VCSELs by analogously calculating the probability current and angular momentum

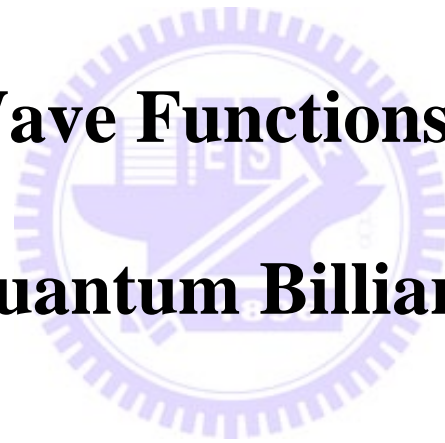
densities of coherent waves released from quantum billiard.

From chapter1 to chapter4, the observed patterns are all lasing in unipolarization and have their phasor amplitudes to be scalar field. In chapter5, we will consider the vector field formation in the transverse modes of VCSELs. In first section of chapter5 we present a polarization-entangled pattern associated with two superscars modes in a square shaped VCSEL. We reconstruct the patterns in two orthogonal polarization states by $SU(2)$ coherent states to manifest the vector field and vector singularities. Similar experimental method as that in Sec. 5.1 is applied to originally generate a chaotic vector in Sec. 5.2. By using the eigenfunction expansion technique, the vector field is reconstructed to unambiguously analyze the vector singularities embedded in a chaotic vector field.



Chapter 2

Wave Functions of Quantum Billiards



As revealed in Sec. 1.1, the eigenenergy of a regular quantum system can be determined by the old quantum theory with the help of the classical POs. On the other hand, the behavior of the quantum particle was not understood until Schrodinger particle was not understood until Schrodinger put developed the wave mechanics and Born interpreted the wave function by probability density. With Schrodinger equation, the wave function of integrable system can be analytically solved. In contrary, the wave function of chaotic system is still mysterious until Berry conjectured that chaotic wave function should be Gaussian random wave [Berr77]. With numerical calculation, the morphology of chaotic wave function was visualized [MK79, MK88]. More importantly, Heller showed that in addition to random phase filed some eigenstates of chaotic system will localize on the unstable PO [Hell84]s. Such kind of wave functions were called scar [Hell84]. For a chaotic system, both types of high-order wave functions, random wave or scar exhibit classical behaviors, as indicated by Bohr's correspondence principle. Nevertheless, the highly-excited eigenstate of regular system do not reveal classical properties even with quantum number approaching to infinity.

In this chapter quantum billiards, which is one of the standard models (the other two are harmonic oscillator and Hydrogen atom) for studying quantum physics, is employed to explore the classical-quantum correspondence of regular and chaotic systems. In first section the classical POs and quantum eigenstates of square are reviewed and then the wave functions of superscar will be introduced. In Sec. 2.2 similar process is done for an equilateral-triangular billiard. Finally, the stadium billiard is used to demonstrate the quantum properties of chaotic systems.

2.1 The Square Billiard

The square billiard is one of the simplest billiards that is completely integrable in classical mechanics [Wier01, dSF01]. In a square billiard each family of periodic orbits can be denoted by three parameters (p, q, ϕ) , where p and q are two positive integers describing the number of collisions with horizontal and vertical walls, and the parameter ϕ ($-\pi \leq \phi \leq \pi$) that is related to the wall positions of specular reflection points [BB97, vonO94, Robi97]. Some examples of orbit families are shown in Fig. 2.1-1. It can be seen that the trajectory constitute a single, nonrepeated orbit provided that p and q are relatively prime. On the other hand, if p and q have a common factor f , the orbit family can be recast as the primitive periodic orbit $(p/f, q/f, \phi/f)$ and f is the number of repetitions of the primitive periodic orbit.

Since the square billiard is separable, the quantum eigenstates of square billiard are just the multiplication of the eigenstates of 1-D infinite potential well with variables in x and y

$$\Psi_{n_1, n_2}(x, y) = \frac{2}{a} \sin\left(\frac{n_1 \pi x}{a}\right) \sin\left(\frac{n_2 \pi y}{a}\right) \quad (2.1.1)$$

Fig. 2.1-2 displays some of the eigenstates with their quantum numbers labeled below the figures. We can see that conventional eigenstates of a square billiard do not manifest the properties of classical periodic orbits even in the correspondence limit of large quantum numbers.

To construct the wave functions associated with periodic orbits, the SU(2) coherent state are extended to the square billiard [CHL02, CHLL03a]

$$\begin{aligned} \Psi_{N, M}^{p, q, \phi}(x, y) &= \frac{1}{\sqrt{2^M}} \sum_{K=0}^{M-1} \sqrt{C_K^M} e^{iK\phi} \Psi_{qN+pK, pN+q(M-1-K)}(x, y) \\ &= \frac{2}{a\sqrt{2^M}} \sum_{K=0}^{M-1} \sqrt{C_K^M} e^{iK\phi} \sin\left[\frac{(qN+pK)\pi x}{a}\right] \sin\left[\frac{(pN+q(M-1-K))\pi y}{a}\right] \end{aligned} \quad (2.1.2)$$

In order to understand the properties of the stationary coherent, we rewrite it as

$$\begin{aligned}
 \Psi_{N,M}^{p,q,\phi}(x,y) &= \frac{-1}{2a\sqrt{M}} \left\{ e^{i[qN\frac{\pi}{a}x + pN\frac{\pi}{a}y]} e^{iq(M-1)\frac{\pi}{a}y} \sum_{K=0}^{M-1} e^{[iK(\frac{p\pi}{a}x - \frac{q\pi}{a}y + \phi)]} \right. \\
 &\quad + e^{-i[qN\frac{\pi}{a}x + pN\frac{\pi}{a}y]} e^{-iq(M-1)\frac{\pi}{a}y} \sum_{K=0}^{M-1} e^{[-iK(\frac{p\pi}{a}x - \frac{q\pi}{a}y - \phi)]} \\
 &\quad - e^{i[qN\frac{\pi}{a}x - pN\frac{\pi}{a}y]} e^{-iq(M-1)\frac{\pi}{a}y} \sum_{K=0}^{M-1} e^{[iK(\frac{p\pi}{a}x + \frac{q\pi}{a}y + \phi)]} \\
 &\quad \left. - e^{-i[qN\frac{\pi}{a}x - pN\frac{\pi}{a}y]} e^{iq(M-1)\frac{\pi}{a}y} \sum_{K=0}^{M-1} e^{[-iK(\frac{p\pi}{a}x + \frac{q\pi}{a}y - \phi)]} \right\} \\
 &= \frac{-1}{2a\sqrt{M}} \{ e^{i\Theta_+(x,y)} F_+(x,y;\phi) + e^{-i\Theta_+(x,y)} F_-(x,y;\phi) \\
 &\quad - e^{i\Theta_-(x,y)} G_+(x,y;\phi) - e^{-i\Theta_-(x,y)} G_-(x,y;\phi) \}
 \end{aligned} \tag{2.1.3}$$

, where

$$\begin{aligned}
 F_{\pm}(x,y;\phi) &= \sum_{K=0}^{M-1} e^{[\pm iK(\frac{p\pi}{a}x - \frac{q\pi}{a}y \pm \phi)]}, \\
 G_{\pm}(x,y;\phi) &= \sum_{K=0}^{M-1} e^{[\pm iK(\frac{p\pi}{a}x + \frac{q\pi}{a}y \pm \phi)]},
 \end{aligned}$$

and $\Theta_{\pm}(x,y) = [qN\frac{\pi}{a}x + pN\frac{\pi}{a}y] \pm q(M-1)\frac{\pi}{a}y$. Since the property of the functions $F_{\pm}(x,y;\phi)$ and $G_{\pm}(x,y;\phi)$ is similar to the Dirichelet kernel, the stationary coherent state has maximum value whenever

$$\frac{p\pi}{a}x \pm \frac{q\pi}{a}y \pm \phi = 2n\pi \tag{2.1.4}$$

, which coincide with the classical trajectories of periodic orbits labeled as (p,q,ϕ) .

Fig. 2.1-3 displays the stationary coherent states $\Psi_{50,20}^{p,q,\phi}(x,y)$ associated with the periodic orbits shown in Fig. 2.1-1. It can be seen that the wave functions of $\Psi_{N,M}^{p,q,\phi}(x,y)$ well localize on the periodic orbits (p,q,ϕ) . Furthermore, the distribution of $|\Psi_{N,M}^{p,q,\phi}(x,y)|^2$ illustrates Bohr's correspondence principle: the

velocity of classical particle is at minimum at the specular reflection points and therefore $|\Psi_{N,M}^{p,q,\phi}(x,y)|^2$ becomes extremely large at these points.

The wave given in (2.1.2) represents a traveling-wave property. The standing-wave representation can be obtained by using $\Psi_{N,M}^{p,q,\phi}(x,y) + \Psi_{N,M}^{*p,q,\phi}(x,y)$.

Including the normalization constant, the standing-wave forms can be expressed as

$$C_{N,M}^{p,q,\phi}(x,y) = \frac{2/a}{\sqrt{\sum_{K=0}^{M-1} C_K^M \cos^2(K\phi)}} \sum_{K=0}^{M-1} \sqrt{C_K^M} \cos(K\phi) \sin\left[\frac{(qN + pK)\pi x}{a}\right] \times \sin\left[\frac{(pN + q(M-1-K)\pi y)}{a}\right] \quad (2.1.5)$$

and

$$S_{N,M}^{p,q,\phi}(x,y) = \frac{2/a}{\sqrt{\sum_{K=0}^{M-1} C_K^M \sin^2(K\phi)}} \sum_{K=0}^{M-1} \sqrt{C_K^M} \sin(K\phi) \sin\left[\frac{(qN + pK)\pi x}{a}\right] \times \sin\left[\frac{(pN + q(M-1-K)\pi y)}{a}\right] \quad (2.1.6).$$

Here we only show the wave pattern $|C_{N,M}^{p,q,\phi}(x,y)|^2$ because the wave pattern $|S_{N,M}^{p,q,\phi}(x,y)|^2$ generally has the same properties. The N dependence of the wave pattern $|C_{N,M}^{p,q,\phi}(x,y)|^2$ is presented in Fig. 2.1-4. We can see that large value of N naturally results in high mode order, since (qN, pN) stands for the central quantum number in the expansion. The M dependence of the wave pattern $|C_{N,M}^{p,q,\phi}(x,y)|^2$ is presented in Fig. 2.1-5. It can be seen that the larger the value of M is, the more strongly the wave pattern localize. This fact can be understood from the expressions of $F_{\pm}(x,y;\phi)$ and $G_{\pm}(x,y;\phi)$, which are similar to Dirichlet kernel having narrower width for larger M .

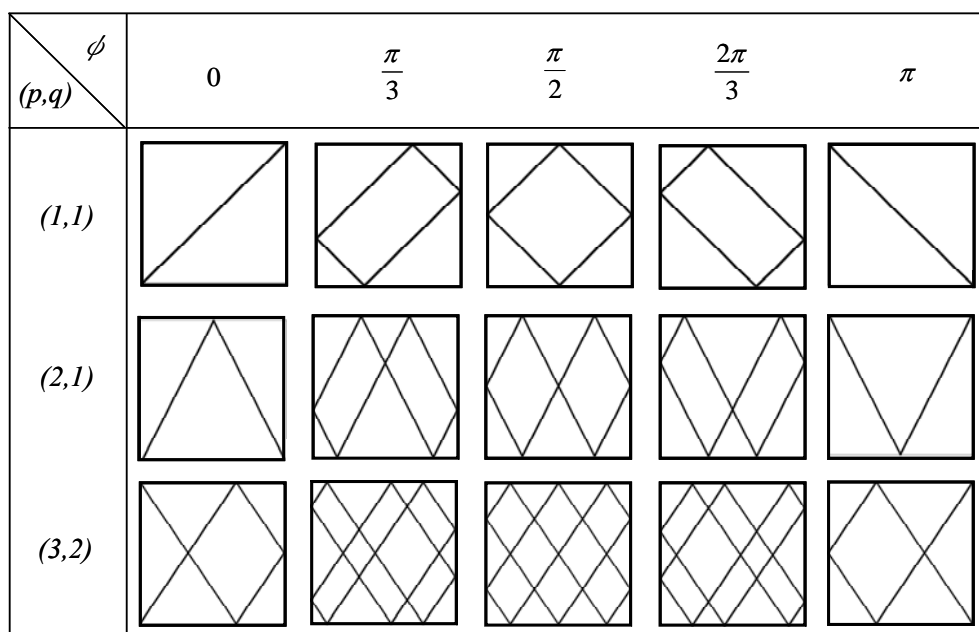


Fig.2.1-1. Some classical periodic orbits denoted by (p, q, ϕ) , where p and q are two positive integers describing the number of collisions with horizontal and vertical walls, and the parameter ϕ ($-\pi \leq \phi \leq \pi$) that is related to the wall positions of specular reflection points.

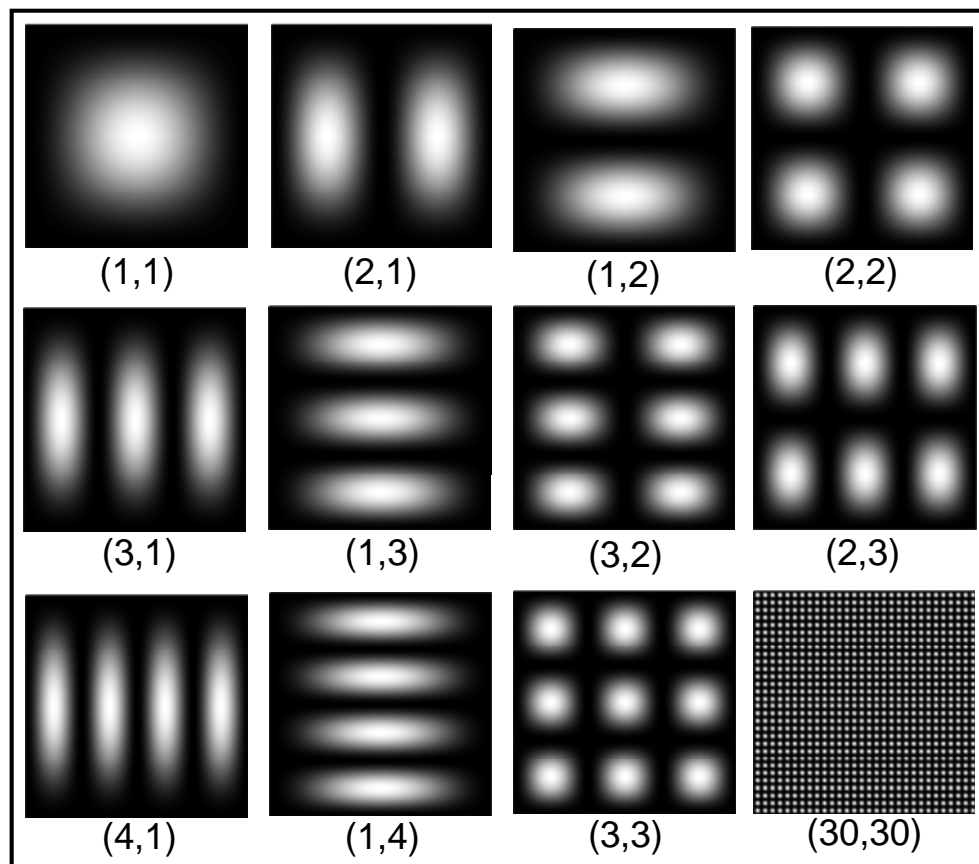


Fig.2.1-2. First some eigenstates and the one of $(n_1, n_2) = (30, 30)$. We can expect that conventional eigenstates do not manifest the properties of classical periodic orbits even in the correspondence limit of large quantum numbers.

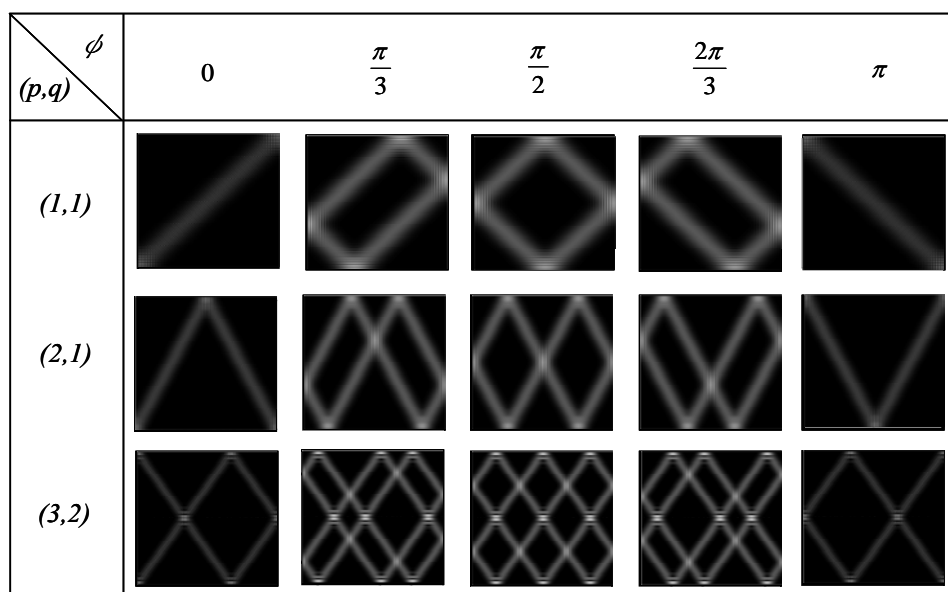
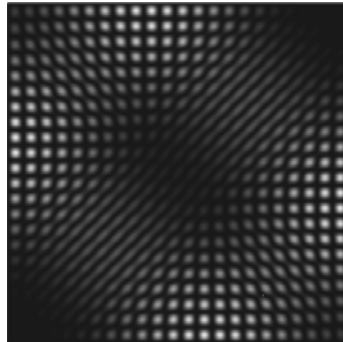
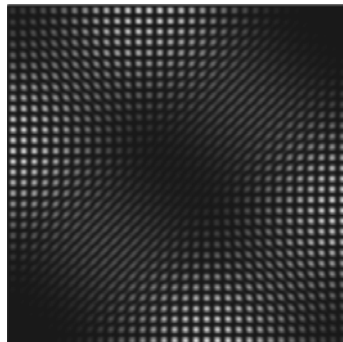


Fig.2.1-3. Stationary coherent states $\Psi_{50,20}^{p,q,\phi}(x,y)$ associated with classical periodic orbits (p,q,ϕ) .

$$|C_{20,5}^{1,1,0.6\pi}(x,y)|^2$$



$$|C_{30,5}^{1,1,0.6\pi}(x,y)|^2$$



$$|C_{40,5}^{1,1,0.6\pi}(x,y)|^2$$

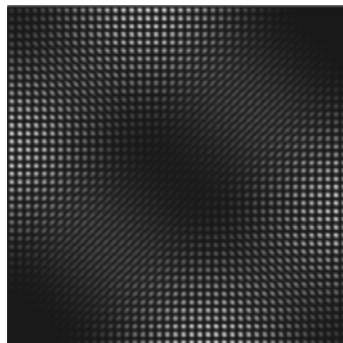


Fig.2.1-4. The N dependence of the wave pattern $|C_{N,5}^{1,1,0.6\pi}(x,y)|^2$. It can be seen that N is related to the mode order.

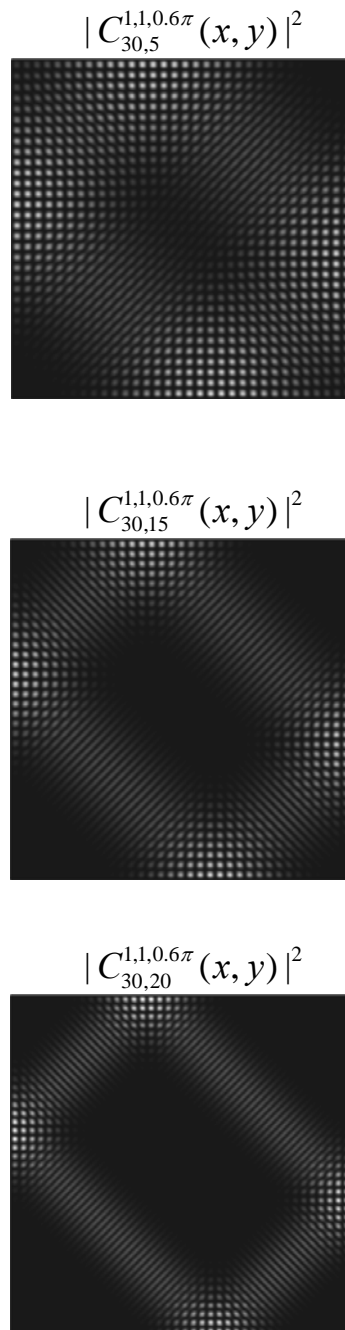


Fig.2.1-5. The M dependence of the wave patterns $|C_{30,M}^{1,1,0.6\pi}(x,y)|^2$. It can be seen that M is related to the localization of the patterns.

2.2 The Equilateral-Triangular Billiard

The equilateral-triangular billiard is a classically integrable but non-separable system. Let three vertices of an equilateral-triangular billiard to be set at $(0,0)$, $(a/2, \sqrt{3}a/2)$, and $(-a/2, \sqrt{3}a/2)$. The formation of classical periodic orbits can be also denoted by three parameter (p, q, ϕ) , where the parameter p and q are nonnegative integers with the restriction that $p \geq q$; the parameter ϕ is in the range of $-\pi$ to π . The sign of ϕ and the parameter p and q correspond to the initial angle of the billiard ball by [DB02, CH03]

$$\tan(\theta) = \text{sgn}(\phi) \frac{1}{\sqrt{3}} \frac{p-q}{p+q} \quad (2.2,1)$$

, where the initial angle θ is with respect to horizontal. Assuming the initial position to be on y axis, the parameter ϕ can be related to the initial position by

$$y_0 = \frac{1}{p+q} \frac{\sqrt{3}a}{2} \frac{|\phi|}{\pi}. \quad (2.2.2)$$

Some sample orbit families are given in Fig. 2.2-1. In terms of p and q , the path length can be written as

$$L_{p,q} = \sqrt{3}a \sqrt{p^2 + q^2 + pq}, \quad (2.2.3)$$

except for the isolated orbits such as $(1,1, \pi)$ [DB02].

The eigenstates in an equilateral triangular quantum billiard have been derived by several groups [Shaw74, RB81, LB85]. The wave function for the two degenerate stationary states can be expressed as

$$\begin{aligned}
 \Phi_{m,n}^{(C)}(x, y) = \sqrt{\frac{16}{a^2 3\sqrt{3}}} \left\{ \cos \left[(m+n) \frac{2\pi}{3a} x \right] \sin \left[(m-n) \frac{2\pi}{\sqrt{3}a} y \right] \right. \\
 + \cos \left[(2m-n) \frac{2\pi}{3a} x \right] \sin \left[n \frac{2\pi}{\sqrt{3}a} y \right] \\
 \left. - \cos \left[(2n-m) \frac{2\pi}{3a} x \right] \sin \left[m \frac{2\pi}{\sqrt{3}a} y \right] \right\}
 \end{aligned} \tag{2.2.4}$$

and

$$\begin{aligned}
 \Phi_{m,n}^{(S)}(x, y) = \sqrt{\frac{16}{a^2 3\sqrt{3}}} \left\{ -\sin \left[(m+n) \frac{2\pi}{3a} x \right] \sin \left[(m-n) \frac{2\pi}{\sqrt{3}a} y \right] \right. \\
 + \sin \left[(2m-n) \frac{2\pi}{3a} x \right] \sin \left[n \frac{2\pi}{\sqrt{3}a} y \right] \\
 \left. - \sin \left[(2n-m) \frac{2\pi}{3a} x \right] \sin \left[m \frac{2\pi}{\sqrt{3}a} y \right] \right\}
 \end{aligned} \tag{2.2.5}$$

$\Phi_{m,n}^{(C)}(x, y)$ and $\Phi_{m,n}^{(S)}(x, y)$ have the following characteristics:

$$\begin{aligned}
 \Phi_{m,m}^{(C)}(x, y) = 0, \quad \Phi_{m,m}^{(S)}(x, y) = 0, \quad \Phi_{m,n}^{(C)}(x, y) = -\Phi_{n,m}^{(C)}(x, y), \quad \Phi_{m,n}^{(S)}(x, y) = -\Phi_{n,m}^{(S)}(x, y), \\
 \Phi_{m,m-n}^{(C)}(x, y) = \Phi_{m,n}^{(C)}(x, y), \quad \text{and} \quad \Phi_{m,m-n}^{(S)}(x, y) = -\Phi_{m,n}^{(S)}(x, y).
 \end{aligned} \tag{2.2.6}$$

Hence, the condition of $m > 2n$ is required to keep all eigenstates to be linearly independent to each other. Figures 2.2-2 and 2.2-3 show some of the $\Phi_{m,n}^{(C)}(x, y)$ and $\Phi_{m,n}^{(S)}(x, y)$ with their quantum number labeled below the pictures. Notice that the conventional eigenstates do not manifest the properties of classical periodic orbits even in the limit of large quantum number.

For the construction of the coherent states associated with the periodic, it is mandatory to use the traveling wave states from linear combination of eigenstates in Eq. (2.2.4) and (2.2.5):

$$\begin{aligned}
 \Phi_{m,n}^{\pm}(x, y) &= \Phi_{m,n}^{(C)}(x, y) \pm i\Phi_{m,n}^{(S)}(x, y) \\
 &= \sqrt{\frac{16}{a^2 3\sqrt{3}}} \left\{ \exp\left[\pm i(m+n)\frac{2\pi}{3a}x\right] \sin\left[(m-n)\frac{2\pi}{\sqrt{3}a}y\right] \right. \\
 &\quad + \exp\left[\mp i(2m-n)\frac{2\pi}{3a}x\right] \sin\left[n\frac{2\pi}{\sqrt{3}a}y\right] \\
 &\quad \left. - \exp\left[\mp i(2n-m)\frac{2\pi}{3a}x\right] \sin\left[m\frac{2\pi}{\sqrt{3}a}y\right] \right\} \quad (2.2.7)
 \end{aligned}$$

Similar to stationary coherent state in square billiard, the stationary coherent state associated with periodic orbit denoted by (p, q, ϕ) in equilateral-triangular billiard can be expressed as [CH03]

$$\Psi_{N,M}^{Tri}(x, y; p, q, \phi) = \frac{1}{\sqrt{2^M}} \sum_{K=0}^{M-1} \sqrt{C_K^M} e^{iK\phi} \Phi_{m_0+pK, n_0+q(M-1-K)}^+(x, y), \quad (2.2.8)$$

with $m_0 = (2q + p)N$ and $n_0 = (2p + q)N$, where M stands for the number of eigenstates that are involved in the superposition and N is related to the mode order. To show the stationary coherent state will indeed localize on the classical periodic orbits, we rewrite (2.2.8) as

$$\begin{aligned}
 \Psi_{N,M}^{Tri}(x, y; p, q, \phi) &= \frac{1}{\sqrt{M}} \sqrt{\frac{16}{a^2 3\sqrt{3}}} \frac{1}{2i} \times \\
 &\left\{ e^{i\{-[m_0+n_0+q(M-1)]\frac{2\pi}{3a}x+[m_0-n_0-q(M-1)]\frac{2\pi}{\sqrt{3}a}y\}} \sum_{K=0}^{M-1} e^{iK\{-(p-q)\frac{2\pi}{3a}x+(p+q)\frac{2\pi}{\sqrt{3}a}y+\phi\}} \right. \\
 &+ e^{i\{-[m_0+n_0+q(M-1)]\frac{2\pi}{3a}x-[m_0-n_0-q(M-1)]\frac{2\pi}{\sqrt{3}a}y\}} \sum_{K=0}^{M-1} e^{iK\{-(p-q)\frac{2\pi}{3a}x-(p+q)\frac{2\pi}{\sqrt{3}a}y+\phi\}} \\
 &+ e^{i\{[2m_0-n_0-q(M-1)]\frac{2\pi}{3a}x+[n_0+q(M-1)]\frac{2\pi}{\sqrt{3}a}y\}} \sum_{K=0}^{M-1} e^{iK\{(2p+q)\frac{2\pi}{3a}x-q\frac{2\pi}{\sqrt{3}a}y+\phi\}} \\
 &+ e^{i\{[2m_0-n_0-q(M-1)]\frac{2\pi}{3a}x-[n_0+q(M-1)]\frac{2\pi}{\sqrt{3}a}y\}} \sum_{K=0}^{M-1} e^{iK\{(2p+q)\frac{2\pi}{3a}x+q\frac{2\pi}{\sqrt{3}a}y+\phi\}} \\
 &+ e^{i\{[2n_0-m_0+2q(M-1)]\frac{2\pi}{3a}x+m_0\frac{2\pi}{\sqrt{3}a}y\}} \sum_{K=0}^{M-1} e^{iK\{-(2q+p)\frac{2\pi}{3a}x+p\frac{2\pi}{\sqrt{3}a}y+\phi\}} \\
 &\left. + e^{i\{[2n_0-m_0+2q(M-1)]\frac{2\pi}{3a}x-m_0\frac{2\pi}{\sqrt{3}a}y\}} \sum_{K=0}^{M-1} e^{iK\{-(2q+p)\frac{2\pi}{3a}x-p\frac{2\pi}{\sqrt{3}a}y+\phi\}} \right\} \quad (2.2.9)
 \end{aligned}$$

Similar to (2.1.3), the stationary coherent state $\Psi_{N,M}^{Tri}(x, y; p, q, \phi)$ will localize on the six families of lines,

$$\left\{ \begin{aligned}
 -(p-q)\frac{2\pi}{3a}x + (p+q)\frac{2\pi}{\sqrt{3}a}y + \phi &= 2n\pi \\
 -(p-q)\frac{2\pi}{3a}x - (p+q)\frac{2\pi}{\sqrt{3}a}y + \phi &= 2n\pi \\
 (2p+q)\frac{2\pi}{3a}x - q\frac{2\pi}{\sqrt{3}a}y + \phi &= 2n\pi \\
 (2p+q)\frac{2\pi}{3a}x + q\frac{2\pi}{\sqrt{3}a}y + \phi &= 2n\pi \\
 -(2q+p)\frac{2\pi}{3a}x + p\frac{2\pi}{\sqrt{3}a}y + \phi &= 2n\pi \\
 -(2q+p)\frac{2\pi}{3a}x - p\frac{2\pi}{\sqrt{3}a}y + \phi &= 2n\pi
 \end{aligned} \right. \quad (2.2.10)$$

, which make up the classical periodic orbits that have been presented in Fig.2.2-1.

Fig. 2.2-4 display the stationary coherent states $|\Psi_{50,15}^{Tri}(x, y; p, q, \phi)|^2$ associated with

the periodic orbits shown in Fig. 2.2-1. It can be seen that the wave functions of $|\Psi_{50,15}^{Tri}(x, y; p, q, \phi)|^2$ indeed localize on the periodic orbits (p, q, ϕ) . Similar to the stationary coherent state in square billiard, the distribution of $|\Psi_{50,15}^{Tri}(x, y; p, q, \phi)|^2$ has a peak at specular reflection points.

As we can see, $\Psi_{N,M}^{Tri}(x, y; p, q, \phi)$ represents the traveling wave and the expression for the standing wave can be given by

$$C_{N,M}^{Tri}(x, y, p, q, \phi) = \Psi_{N,M}^{Tri}(x, y, p, q, \phi) + \Psi_{N,M}^{*Tri}(x, y, p, q, \phi) \quad (2.2.11)$$

and

$$S_{N,M}^{Tri}(x, y, p, q, \phi) = \Psi_{N,M}^{Tri}(x, y, p, q, \phi) - \Psi_{N,M}^{*Tri}(x, y, p, q, \phi) \quad (2.2.12)$$

Here we only show the wave pattern $|C_{N,M}^{Tri}(x, y; p, q, \phi)|^2$, because the wave pattern $|S_{N,M}^{Tri}(x, y; p, q, \phi)|^2$ have similar characteristics. Figs. 2.2-5 and 2.2-6 demonstrate the N and M dependences of the wave pattern $|C_{N,M}^{Tri}(x, y; p, q, \phi)|^2$, respectively. The results are the same as that of square billiard.

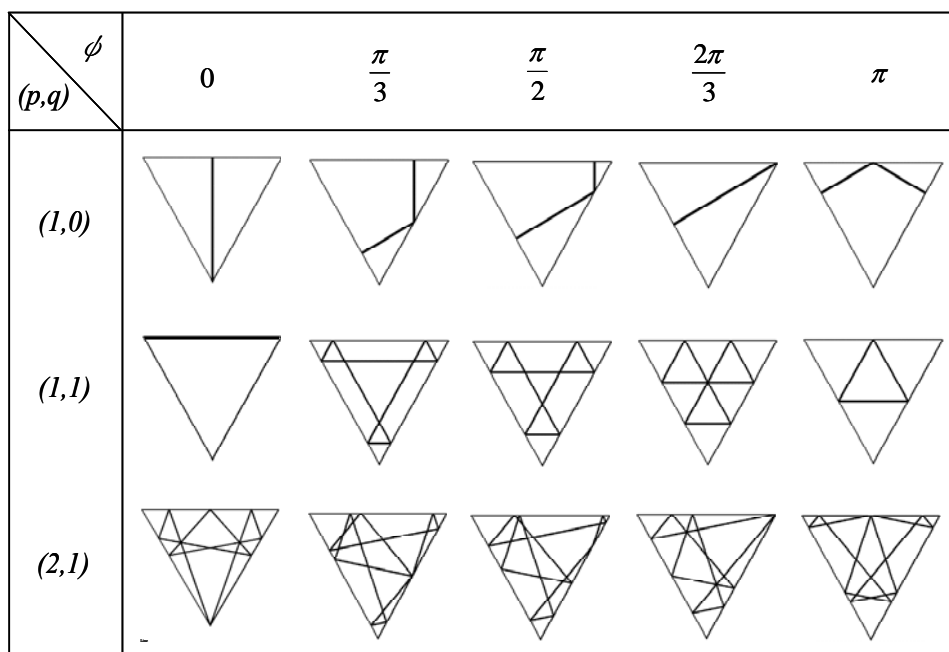


Fig.2.2-1. Some classical periodic orbits (p,q,ϕ) , where p and q are two positive integers with restriction $p \geq q$, and the parameter ϕ ($-\pi \leq \phi \leq \pi$) is related to the initial point of the billiard ball.

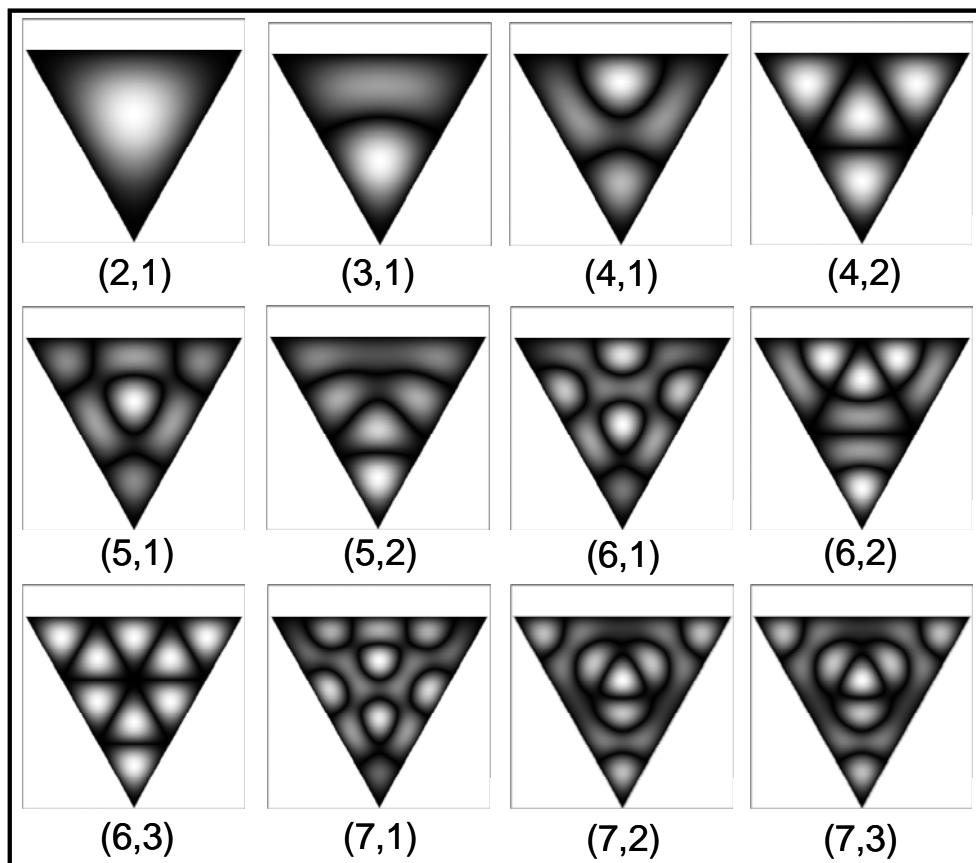


Fig.2.2-2. Some eigenstate of equilateral-triangular billiard $\Phi_{m,n}^{(C)}(x,y)$.

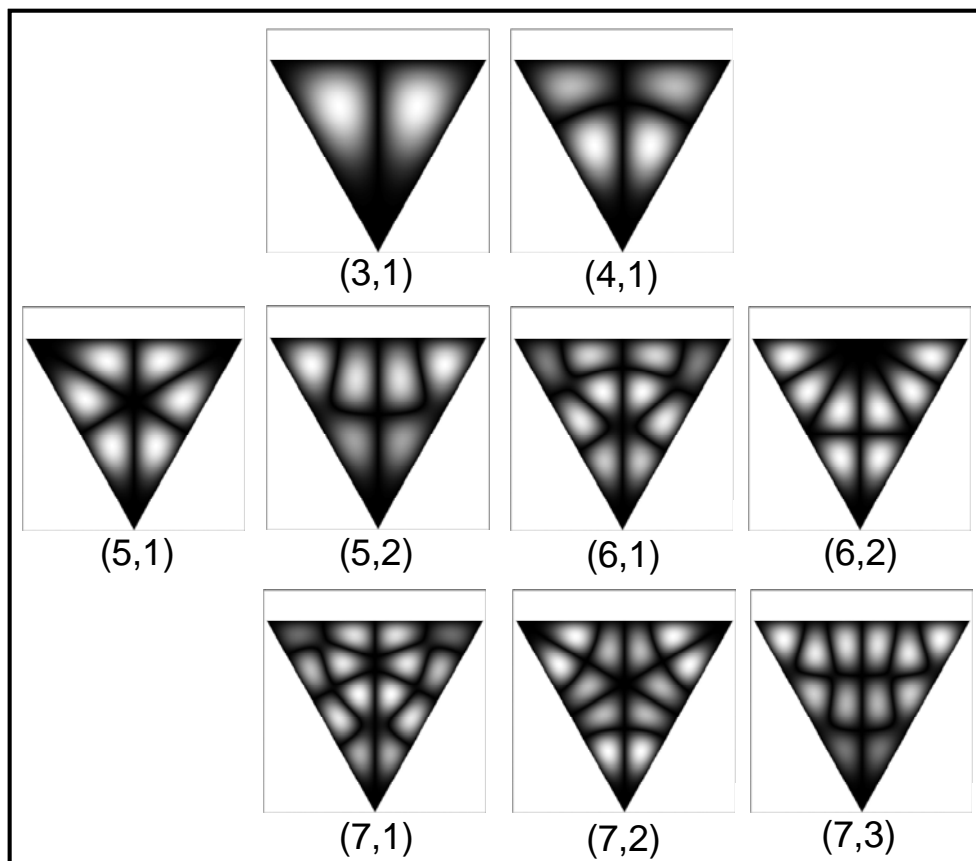


Fig.2.2-3. Some eigenstate of equilateral-triangular billiard $\Phi_{m,n}^{(S)}(x, y)$. Notice that $\Phi_{2n,n}^{(S)}(x, y) = 0$.

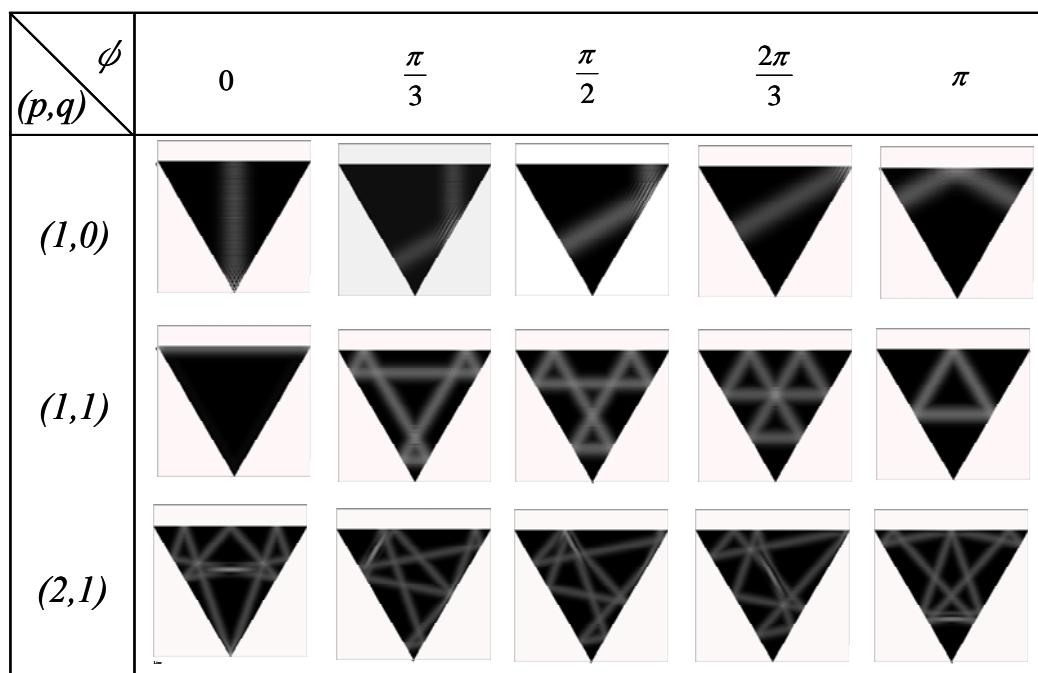
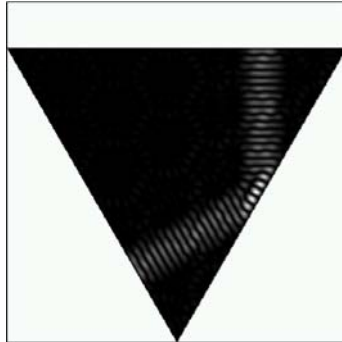
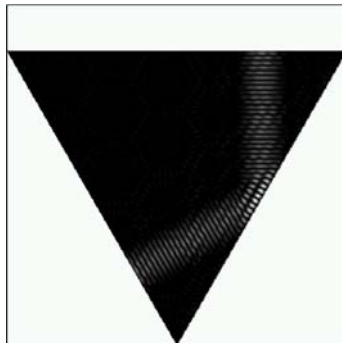


Fig.2.2-4. Stationary coherent states $|\Psi_{50,15}^{Tri}(x, y; p, q, \phi)|^2$ associated with classical periodic orbits (p, q, ϕ) .

$$|C_{20,10}^{Tri}(x, y; 1, 0, \pi/3)|^2$$



$$|C_{30,10}^{Tri}(x, y; 1, 0, \pi/3)|^2$$



$$|C_{40,10}^{Tri}(x, y; 1, 0, \pi/3)|^2$$

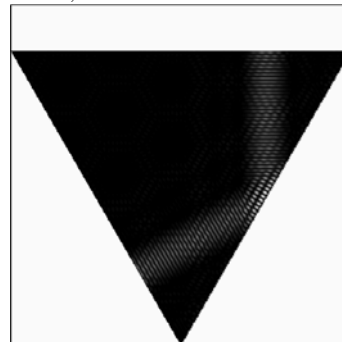


Fig.2.2-5. The N dependence of the wave pattern $|C_{N,10}^{Tri}(x, y; 1, 0, \pi/3)|^2$. It can be seen that N is related to the mode order.

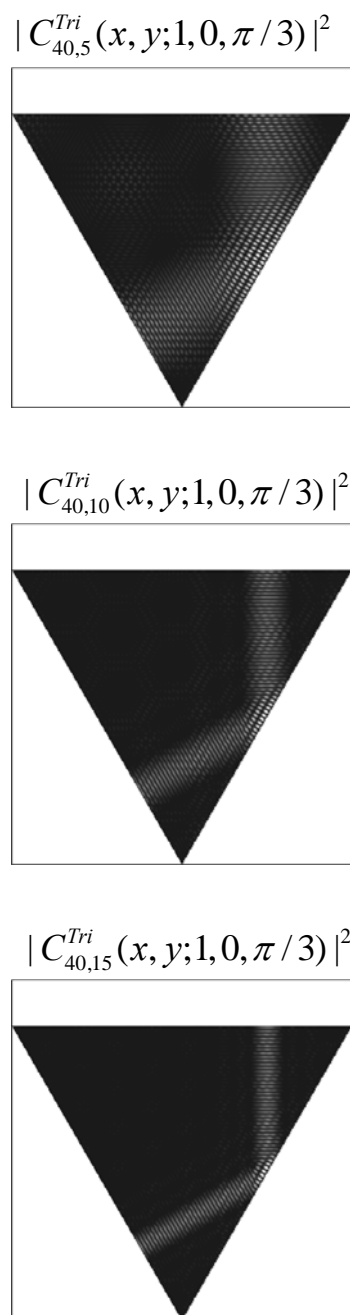


Fig.2.2-6. The M dependence of the wave patterns $|C_{40,M}^{Tri}(x, y; 1, 0, \pi/3)|^2$. It can be seen that M is related to the localization of the patterns.

2.3 The Chaotic Billiards

Chaotic billiards has long been used as a paradigm to study the classical and quantum chaos [Stöc99]. Among all kinds of chaotic billiards, stadium billiard (as shown in Fig. 2.3-1) is the most popular model for which is a strong chaotic system [Hell84]. The trajectories in stadium billiard are generally ergodic, they spread all over the phase space. In addition to ergodic trajectories, Fig. 2.3-2 displays some of the unstable POs which are intimately related to the quantum energy density [Gutz91]. Unlike integrable billiards, the quantum eigenstates of stadium billiard have no analytic forms and can only be obtained by numerical computation. In this section the expansion method [KKS99] is utilized to investigate the wave functions of stadium billiard.

The first eight eigenstates of stadium billiard are depicted in Fig. 2.3-3. As we can see that the low-order wave function behaves like that of regular billiard. Fig. 2.3-4 (a)-(d) present the 152nd, 165th, 175th, and 208th eigenstates, respectively. Notice that symmetry has been intentionally broken in this calculation. Unlike regular billiard, high order wave function exhibits random patterns. The morphology of such chaotic waves can be mimicked by a random superposition of plane waves with fixed wave-vector magnitude but uncorrelated amplitudes, directions, and phases [Berr77]. Fig. 2.3-5 (a) shows the random wave of

$$\psi^{chaos}(x, y) = \frac{2}{a} \sum_{n_1} \sum_{n_2} \cos(\phi_{n_1, n_2}) \sin\left(\frac{n_1 \pi x}{a}\right) \sin\left(\frac{n_2 \pi y}{a}\right) \quad (2.3-1)$$

with random phase factors ϕ_{n_1, n_2} and quantum numbers satisfying $54 \leq \sqrt{n_1^2 + n_2^2} \leq 55$, as illustrated in Fig. 2.3-5 (b). The signatures of such chaotic quantum wave functions consist in [Stöc99] the Gaussian distribution for amplitudes

$$P(\psi) = \frac{1}{\sigma\sqrt{2\pi}} \exp\left(-\frac{\psi^2}{2\sigma^2}\right) \quad (2.3-2)$$

where σ is the standard deviation given by $\sigma = 1/\sqrt{A}$ with A denotes the area of the billiard, and Porter-Thomas distribution for intensities

$$P(I) = \frac{1}{\sqrt{2\pi I}} \exp\left(-\frac{I}{2}\right), \quad (2.3-3)$$

, where $I = |\psi|^2$. The histograms in Fig. 2.3-6 (a) and (b) validate the statistics of wave function and intensity of $\psi^{md}(x,y)$ are actually in Gaussian and Porter-Thomas distributions, respectively.

In addition to these chaotic wave functions, some scar modes are also found in the calculation. Fig. 2.3-7 (a)-(d) depicts the 122nd, 132nd, 207th, and 258th eigenstate, respectively. The classical POs on which the scars localize on are highlighted by orange lines. In consistence with Bohr's correspondence principle, the highly-excited eigenstates of stadium billiard, random waves or scars, exhibit the properties of classical trajectories.

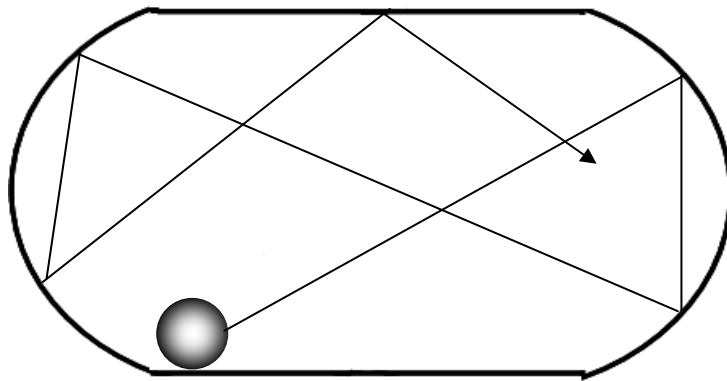


Fig. 2.3-1. The stadium billiard. The trajectory in chaotic billiard is generally ergodic.

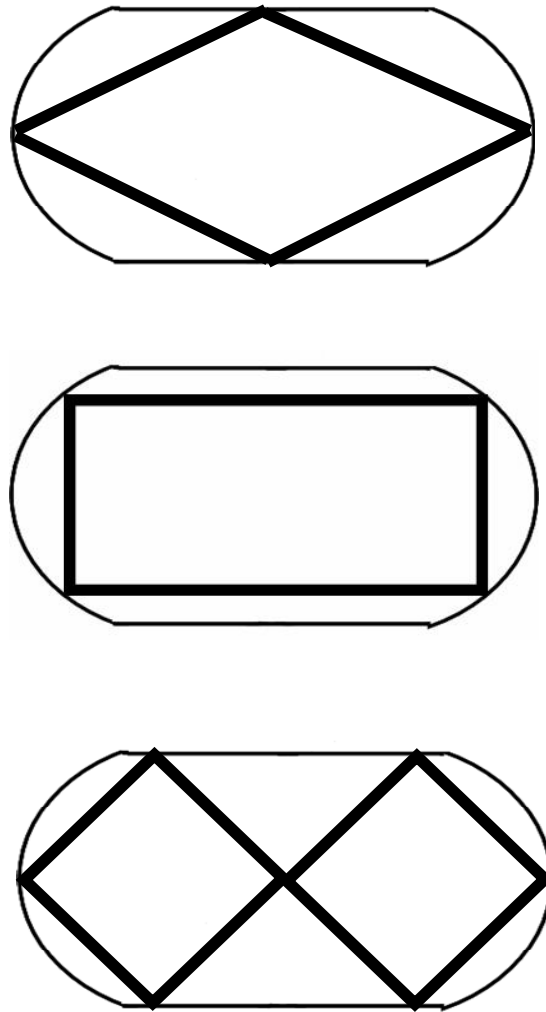


Fig. 2.3-2. Some unstable periodic orbits in the stadium billiard.

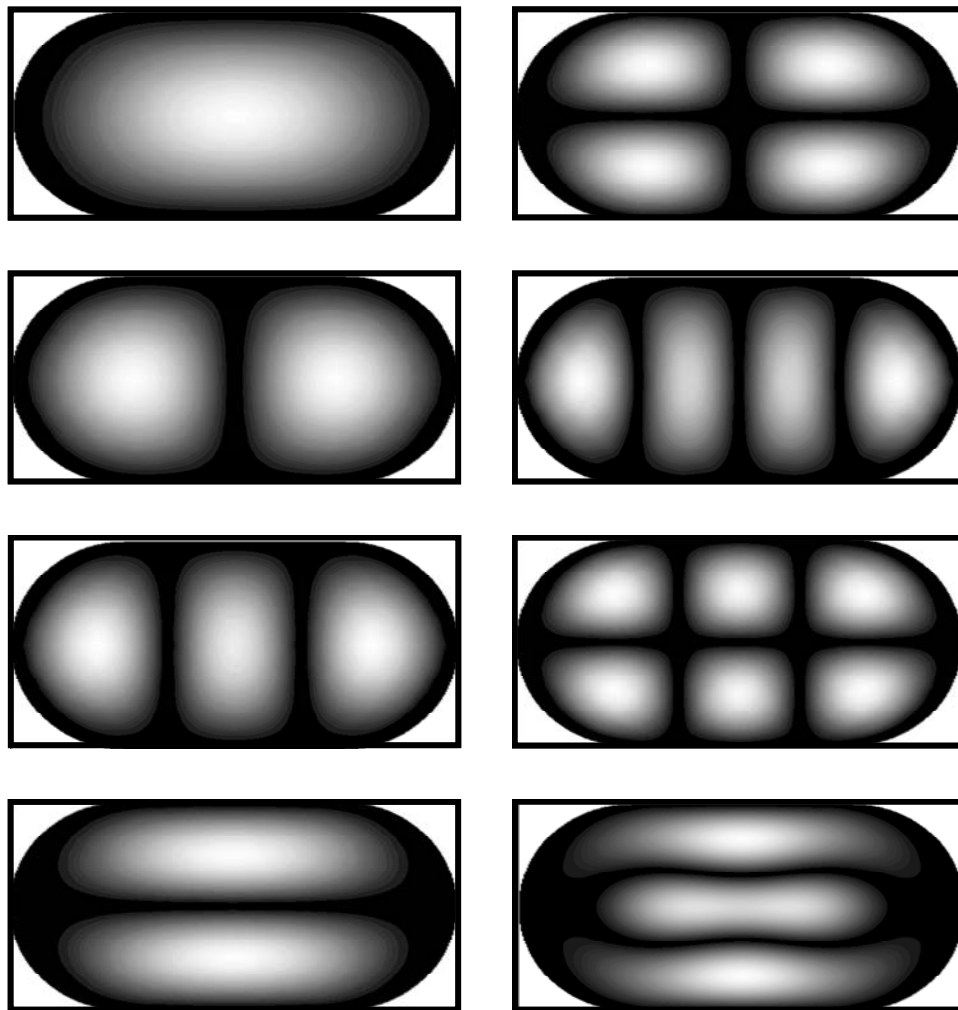


Fig. 2.3-3. First eight eigenstates of the stadium billiard. The result is similar to rectangular billiard.

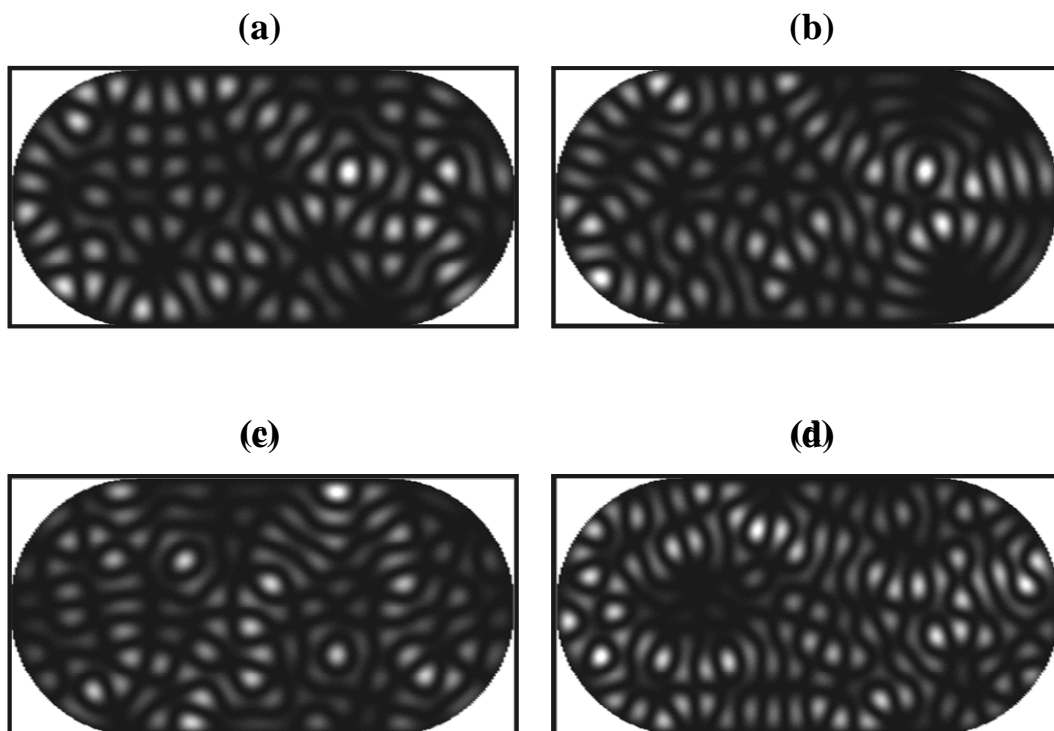
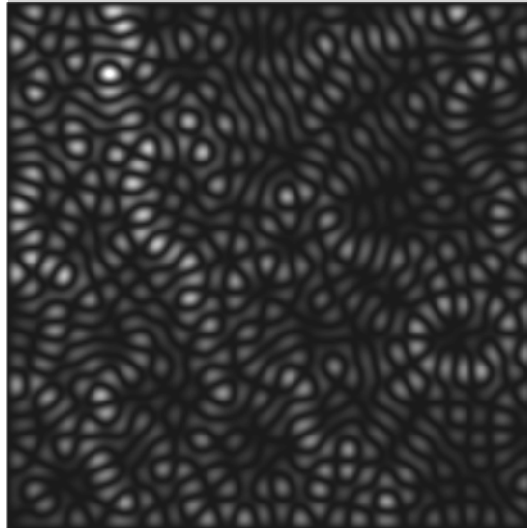


Fig. 2.3-4. (a)-(d) The 152nd, 165th, 175th, and 208th excited states of a slightly asymmetric stadium billiard are shown to exhibit random patterns that do not exist in regular billiard.

(a)



(b)

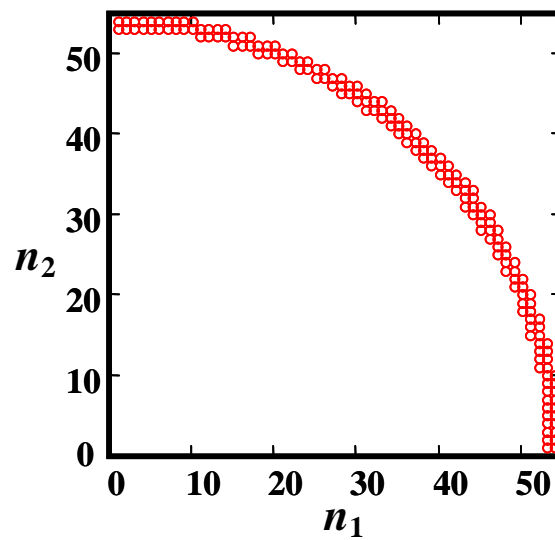


Fig. 2.3-5. (a) A random superposition of several eigenstates with quantum number satisfying $54 \leq \sqrt{n_1^2 + n_2^2} \leq 55$, as illustrated in (b)

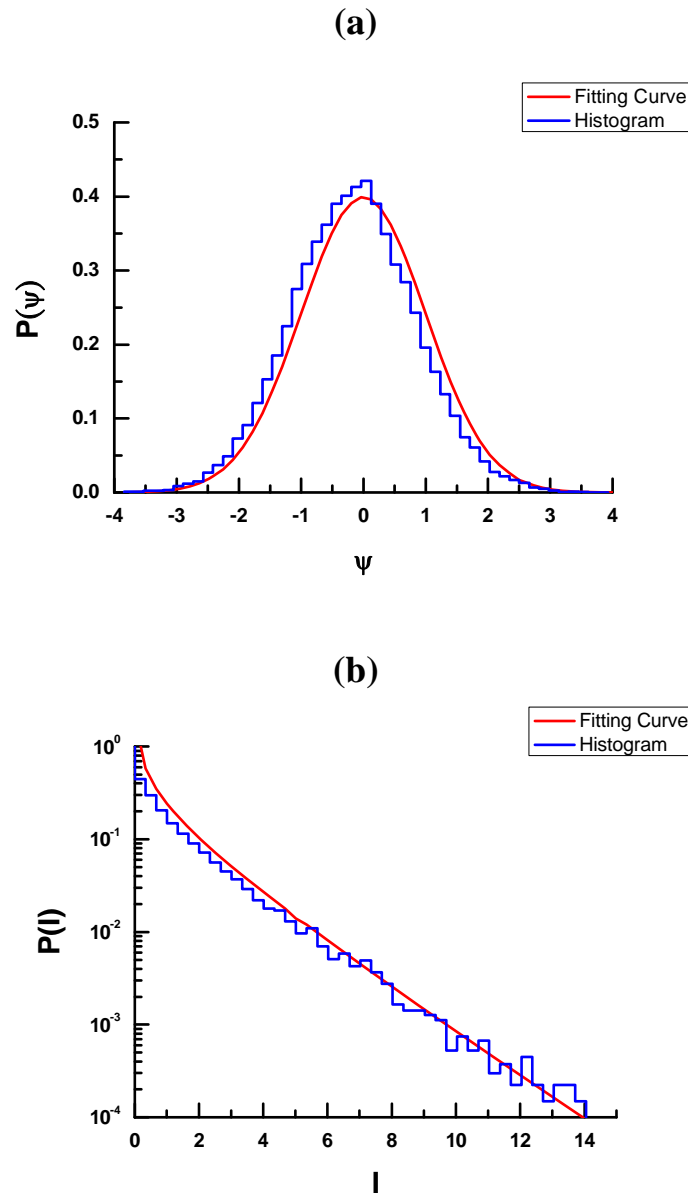


Fig. 2.3-6. (a)-(b) The statistics for the amplitude and intensity of the random wave shown in the previous figure. The fitting curves are Gaussian and Porter-Thomas distributions, respectively.

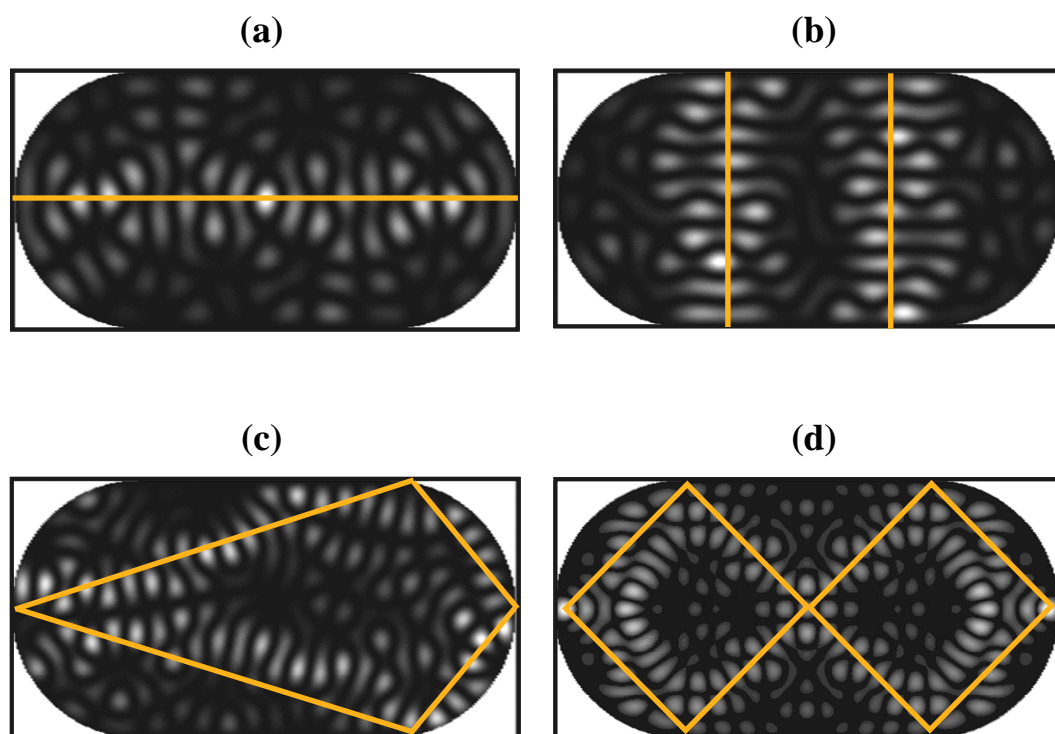



Fig. 2.3-7. (a)-(d) The scars appear in the 122nd, 132nd, 207th, and 258th excited states of the slightly asymmetric stadium billiard. The highlighted lines indicate the unstable periodic orbits.

Chapter 3

Analogous Observation on Quantum-Billiard Wave Functions from VCSELs



In Sec. 1.1 the significance of quantum-billiard wave functions corresponding to classical POs has been introduced and their formations have also been theoretically demonstrated in chapter 2. Since 2D wave function is difficult to directly visualize, the experimental observations on quantum-billiard wave functions are mostly performed in an analogous way. In this chapter VCSELs are employed to analogously observe the wave function of quantum billiards.

VCSELs inherently emit in single longitudinal mode due to their extremely short cavity length, but broad-area VCSELs can exhibit complex high-order transverse mode structures. Hegarty *et al.* reported interesting transverse mode patterns from square-shaped large-aperture (VCSELs) [HHMC99, HHP+99]. Their experimental results revealed that a wave incident upon the current-guiding oxide boundary would undergo total internal reflection because of large index discontinuities between oxide layer and the surrounding semiconductor material. That is, VCSEL can be considered as a planar wave guide with a dominant wave vector along the vertical direction. Because of the analogy between the Helmholtz equation and Schrödinger equation, it is essentially feasible to use the oxide-confined VCSEL cavity to present quantum mechanical potential wells. In this case, the transverse patterns can reveal the probability density of the corresponding wave functions to the 2D quantum billiards. Most importantly, the superiority of oxide-confined VCSELs consists in their longitudinal wave vector k_z that can bring out the near-field patterns to be directly reimaged with simple optics.

In this chapter the analogous observations of various quantum-billiard wave functions are presented. The remainder of this chapter is structured as follows: The first section explains why the transverse mode of VCSELs can be analogous to the wave functions of quantum billiards. After which the experimental setup will be shown. The typical lasing modes of the square billiard are presented in Sec. 3.3. What follows is the chaotic modes generated by a rippled-square VCSEL. Finally, equilateral-triangular shaped VCSEL are shown to exhibit mixed properties of regular and chaotic system.

3.1 The Analogy between VCSELs and Quantum Billiard

The function of 2D wave-billiard wall in the VCSEL device comes from the fact that the large index discontinuity between the oxide layer and surrounding semiconductor leads to a total internal reflection of a wave incident upon the boundary. As shown in Fig. 3.1-1 (a), the separability of the wave function in the VCSEL device enables the wave vectors to be decomposed into k_z and k_t , where k_z is the wave-vector component along the direction of vertical emission and k_t is the transverse wave-vector component. The vertical dimension of the cavity is designed to have a large k_z component and a relatively small transverse component k_t , generally $k_t < 0.12 k_z$. The angle between the photon-velocity vector and the normal vector of the boundary surface, $\tan^{-1}(k_z/k_t)$, can be calculated to be greater than 1.45 rad. On the other hand, the critical angle for the total reflection is given by $\sin^{-1}(n_{ox}/n_{GaAs})$, where n_{ox} is the effective refractive index of the oxide layer and n_{GaAs} is the effective refractive index of the semiconductor cavity. With $n_{ox} \approx 1.5$ and $n_{GaAs} \approx 3.5$, it can be confirmed that the angle between the photon-velocity vector and the normal vector of the boundary surface is certainly greater than the critical angle for the total reflection, as illustrated in Fig. 3.1-1 (b). As a consequence, the lateral oxide boundaries can be modeled as rigid walls and the losses through the wall boundaries are extremely low.

Under the circumstance of paraxial optics, $k_t \ll k_z$, the longitudinal field is significantly small in comparison with the transverse field. Therefore, the electric field can be approximated to have only transverse components and no longitudinal component, i.e. so-called quasi-TEM waves. After separating the z component in the wave equation, we are left with a two-dimensional Helmholtz equation:

$(\nabla_t^2 + k_t^2)\psi(x, y) = 0$, where ∇_t^2 means the Laplacian operator operating on the coordinates in the transverse plane and $\psi(x, y)$ is a scalar wave function that describes the transverse distribution of the laser mode. As a result, the transverse eigenfunctions of the oxide-confined VCSEL device are equivalent to the eigenfunctions of the 2D Schrodinger equation with hard wall boundaries of the same geometry.



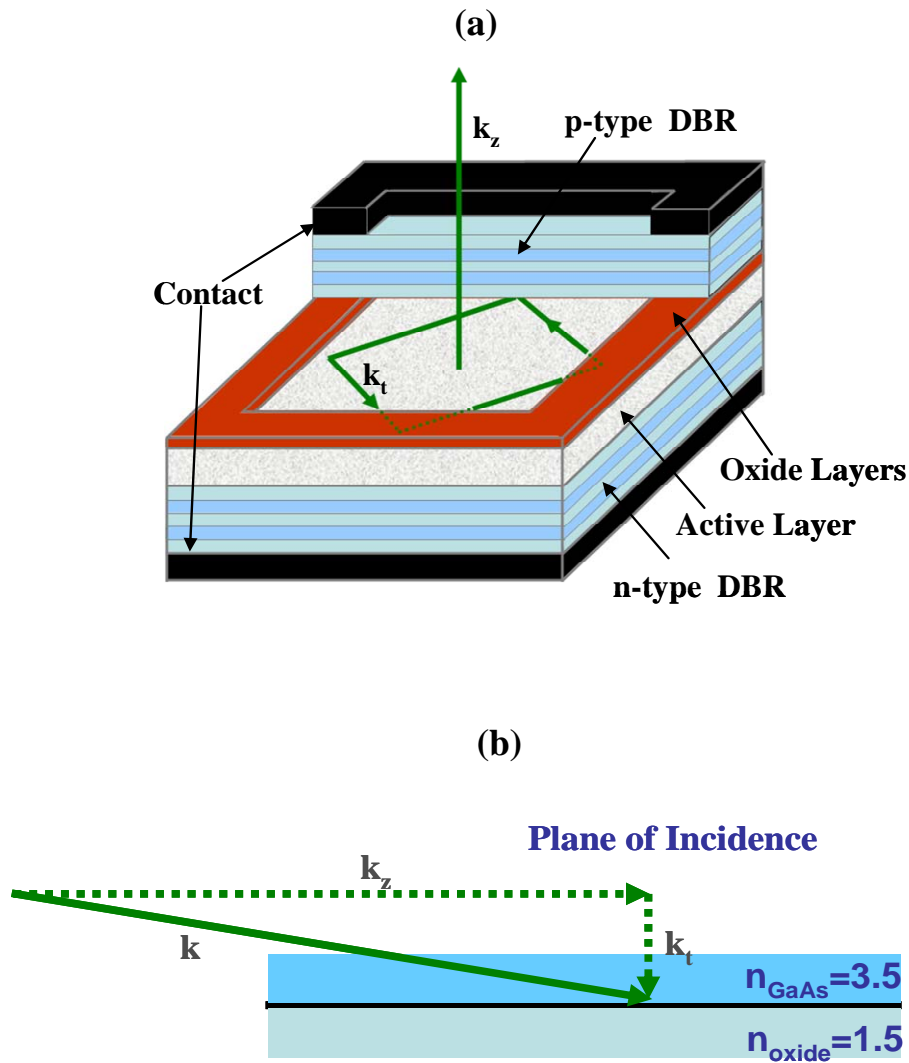


Fig.3.1-1. (a) The schematic diagrams for vertical-cavity surface-emitting laser. The separability of the wave function in the VCSEL device enables the wave vectors to be decomposed into k_z and k_t . (b) The illustration of a wave incident upon the current-guiding oxide boundary would undergo total internal reflection for $k_t \ll k_z$.

3.2 Experimental Setup

The experimental setup is schematically depicted in Fig. 3.2-1 and Fig. 3.2-2 present the detailed photos of the equipments. The VCSEL devices are mounted on a cooper holder (Fig. 3.2-2 (a)) with good thermal conductance and placed in the cryogenic system (Janis, VPF-100, Fig. 3.2-2 (b)) that is operating with liquid nitrogen. The temperature is controlled by a temperature controller (Neocera, LTC-11) with a temperature stability of 0.1 K at the range of 80-300 K. The VCSEL is driven by a DC power supplier (KEITHLEY 2400) with a precision of 0.005 mA.

The near-field patterns were re-imaged into a CCD camera (Coherent, Beam-Code) with a microscope objective lens (Mitsutoyo, M Plan Apo, NA=0.9, Fig.3.2-2 (c)). The objective lens is placed in a tube that is connected with the cryogenic system and can be tilted by the seven valves (Fig.3.2-2 (d)). A polarizer was used to obtain polarization-resolved near field patterns. The spectral information of the laser output was measured by a Fourier optical spectrum analyzer (ADVANTEST Q8347) with a Michelson interferometer.

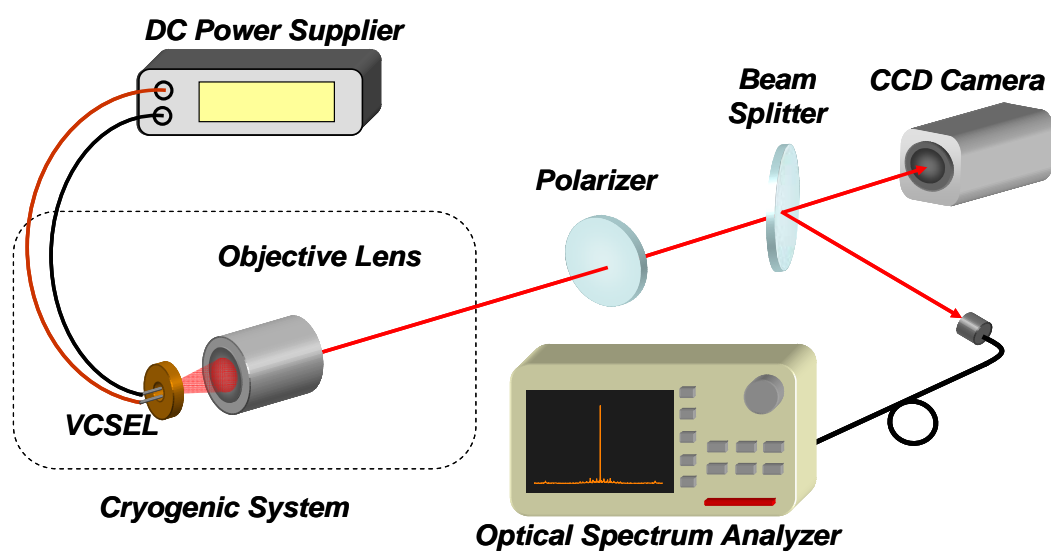


Fig.3.2-1. The schematic diagrams for the experimental setup.

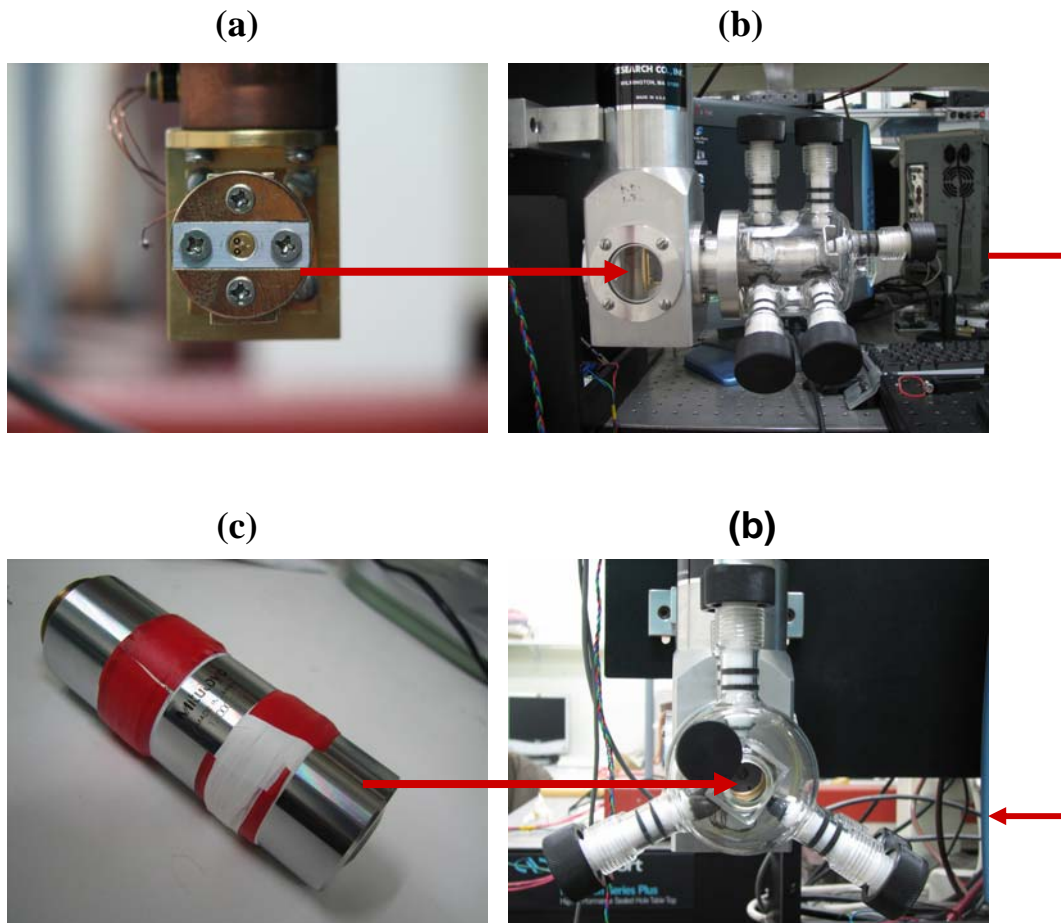


Fig.3.2-2. (a) The VCSEL mounted on the copper holder. (b) Side view of the cryogenic system. (c) The objective lens with NA=0.9 (d) Face view of the cryogenic system.

3.3 Typical Lasing Modes of Square VCSEL

The SEM image and the optical microscope image of the square VCSEL device used in this work are shown in Fig. 3.3-1 and Fig. 3.3-2, respectively. The bright region in Fig. 3.3-2 displays the spontaneous emission to manifest the details on the square boundary. The edge length of the aperture is measured to be about $40 \mu\text{m}$. The control parameters of this experiment are the device temperature and pumping currents. Since the lasing patterns will become multi modes, we only focus on the lasing modes at near-threshold currents. The temperature dependence of threshold current is shown in Fig. 3.3-3 (a) and Fig. 3.3-3 (b)-(d) depicts the experimental near-field patterns of one of our square VCSEL devices at temperatures as indicated. These patterns are robust; they remain unchanged for the durations of at least 1.0mA, and can be reproduced under the same experimental circumstances. The lasing pattern shown in Fig. 3.3-3(b) is obtained at room temperature. The lasing patterns of VCSEL are typically multi-mode emission because of the thermal fluctuations. The lasing state at the operating temperature of 285K becomes a bouncing-ball mode, as seen in Fig. 3.3-3(c). When the operating temperature further decreases to 250K, the near-field pattern dramatically changes to a multi-diamond pattern hat is a superscar mode associated with several POs, as shown in Fig. 3.3-3(d). For the operating temperature below 230K, the experimental pattern shown in Fig. 3.3-3(e) corresponds to another superscar mode that is localized on a single PO. The behaviors of each VCSEL devices are different but their characteristics are generally the same. In conclusion, the temperatures at which the bouncing-ball or superscar modes appear are not all the same for all devices, but it can be sure that the bouncing-ball mode appears at a higher temperature than that for the superscar mode. The multi-POs superscar mode does not always exist, but the temperature at which it appears is higher than the temperature for a single-PO superscar mode if it ppears. Most devices lase with single-PO superscar mode at low temperatures.

These lasing patterns can be analogously interpreted by the quantum-billiard model. The eigenstates of square billiard are given by (2.1.1)

$$\psi_{n_1, n_2}(x, y) = \frac{2}{a} \sin\left(\frac{n_1 \pi x}{a}\right) \sin\left(\frac{n_2 \pi y}{a}\right). \quad (3.3.1)$$

We find that the bouncing-ball mode shown in Fig. 3.3-3(c) is not merely an eigenstate but more like a linear combination of two eigenstates

$$\psi_{43,11}(x, y) \sin(0.6\pi) + \psi_{42,16}(x, y) \cos(0.6\pi) \quad (3.3.2)$$

The experimental result and theoretical simulation are depicted in Fig. 3.3-4 (a) and (a'), respectively, for convenient comparison. Such kind of bouncing-ball modes are prevalent in square VCSEL; we show some other two cases in Fig. 3.3-4 (b) and (c). The corresponding mathematical expressions of Fig. 3.3-4 (b') and (c') are

$$\psi_{40,11}(x, y) \sin(0.35\pi) + \psi_{39,14}(x, y) \cos(0.35\pi) \quad (3.3.3)$$

and

$$\psi_{11,44}(x, y) \sin(0.7\pi) + \psi_{14,43}(x, y) \cos(0.7\pi) \quad (3.3.4)$$

, respectively.

The other representative lasing pattern is the superscar mode that localized on the diamond-shaped PO. As discussed in chapter 2, the superscar can be expressed as

$$C_{N,M}^{p,q,\phi}(x, y) = \frac{2/a}{\sqrt{\sum_{K=0}^{M-1} C_K^M \cos^2(K\phi)}} \sum_{K=0}^{M-1} \sqrt{C_K^M} \cos(K\phi) \sin\left[\frac{(qN + pK)\pi x}{a}\right] \times \sin\left[\frac{(pN + q(M-1-K))\pi y}{a}\right] \quad (3.3.5)$$

It can be found that the superscar mode shown in Fig. 3.3-3 (e) can be interpreted by $C_{36,10}^{1,1,0.57\pi}(x, y)$. We can compare the experimental and theoretical patterns from Fig. 3.3-5(a) and Fig. 3.3-5(a'). The low-temperature lasing modes of most square VCSELs are dominated by the superscar modes. Fig. 3.3-5 (b) and (c) display two other similar superscar modes observed from the other devices. The corresponding theoretical results are also shown in Fig. 3.3-5 (b') and (c') for comparisons.

We can also reconstruct the multi-POs superscar mode by superposing SU(2) coherent states. Based on thorough numerical analysis, the experimental multi-POs superscar modes can be found to be well reconstructed by

$$C_{32,20}^{1,1,0.25\pi}(x, y) + 0.7C_{32,30}^{1,1,0.57\pi}(x, y) + 0.9C_{32,20}^{1,1,0.8\pi}(x, y) \quad (3.3.6)$$

Fig. 3.3-6 (a) and (a') depict the experimental and theoretical results. Although the multi-POs mode is not as prevalent as the bouncing-ball and single-POs superscar mode, it also commonly appears in the transition regime between the two popular modes. Fig. 3.3-6 (b) and (c) show the other two paradigmatic multi-POs superscar modes. The two typical multi-POs modes can be reconstructed by

$$C_{40,18}^{1,1,0.28\pi}(x, y) + C_{40,15}^{1,1,0.64\pi}(x, y) \quad (3.3.7)$$

and

$$C_{40,30}^{1,1,0.3\pi}(x, y) + C_{40,30}^{1,1,0.55\pi}(x, y) + C_{40,30}^{1,1,0.8\pi}(x, y) \quad (3.3.8)$$

and are shown in Fig. 3.3-6 (b') and (c'), respectively. As we have demonstrated, the transverse mode of square VCSELs can be well reconstructed by quantum-billiard wave functions.

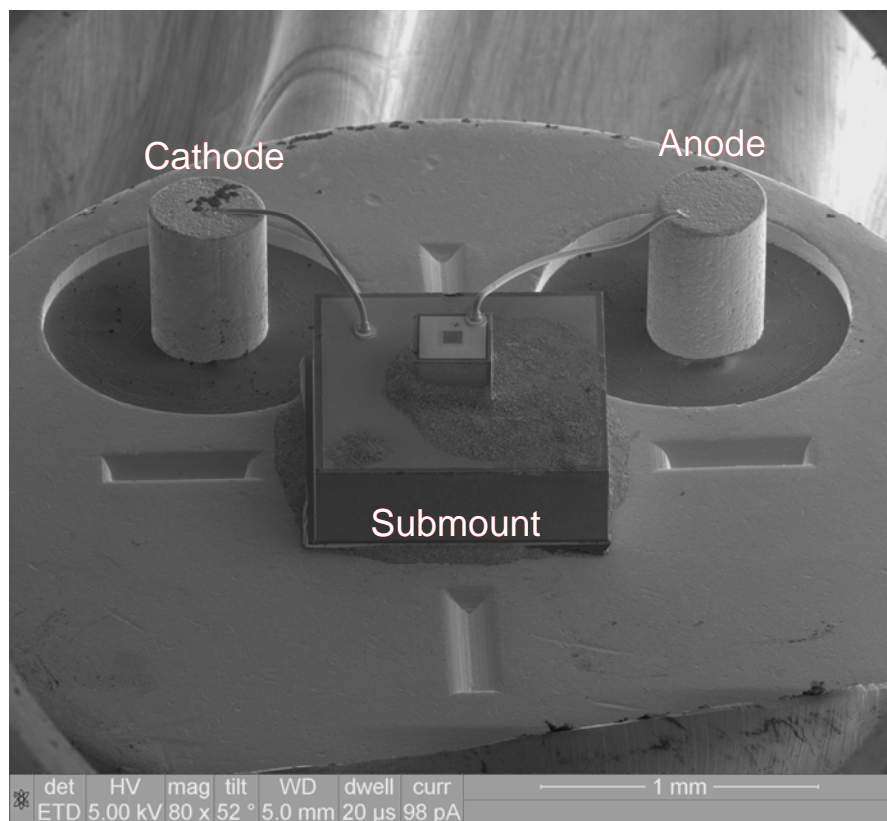


Fig. 3.3-1. The SEM image of square VCSEL device

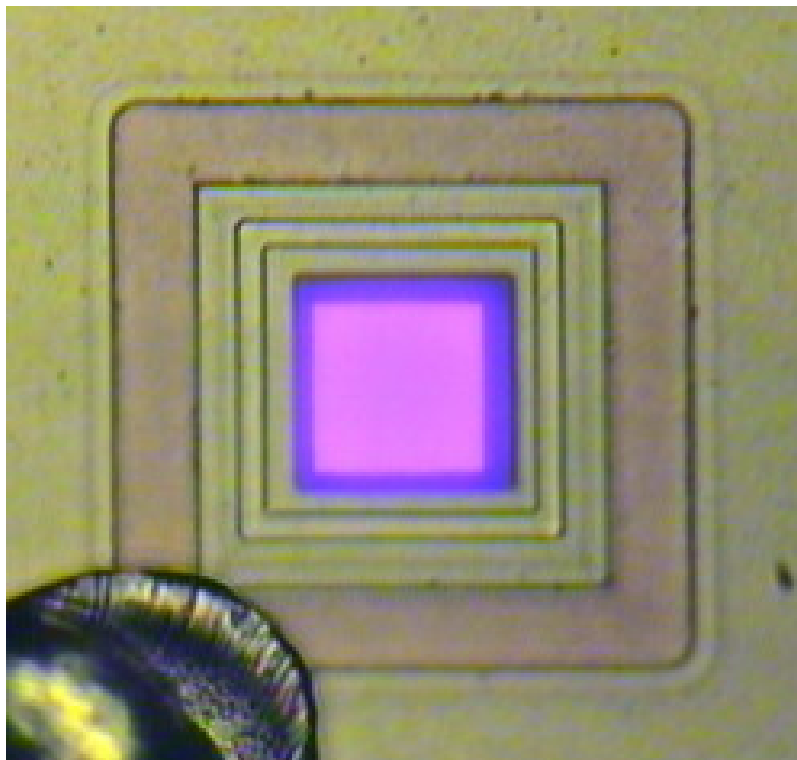


Fig. 3.3-2. Optical microscope image view from the aperture of the VCSEL. The bright region display the spontaneous emission to manifest the details on the square boundary.

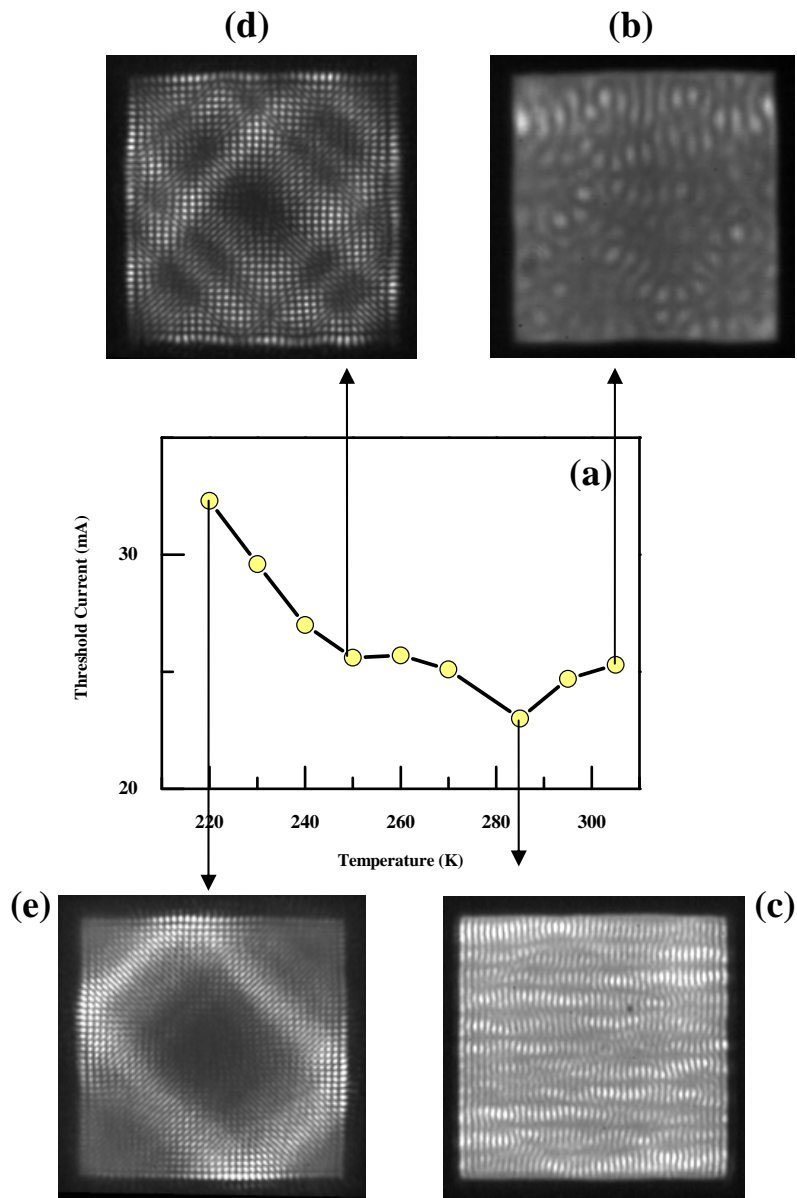


Fig. 3.3-3. (a) The temperature dependence of the threshold current and the lasing modes observed at temperatures of (b) 295K (room temperature) (c) 285K (d) 250K (e) 230K.

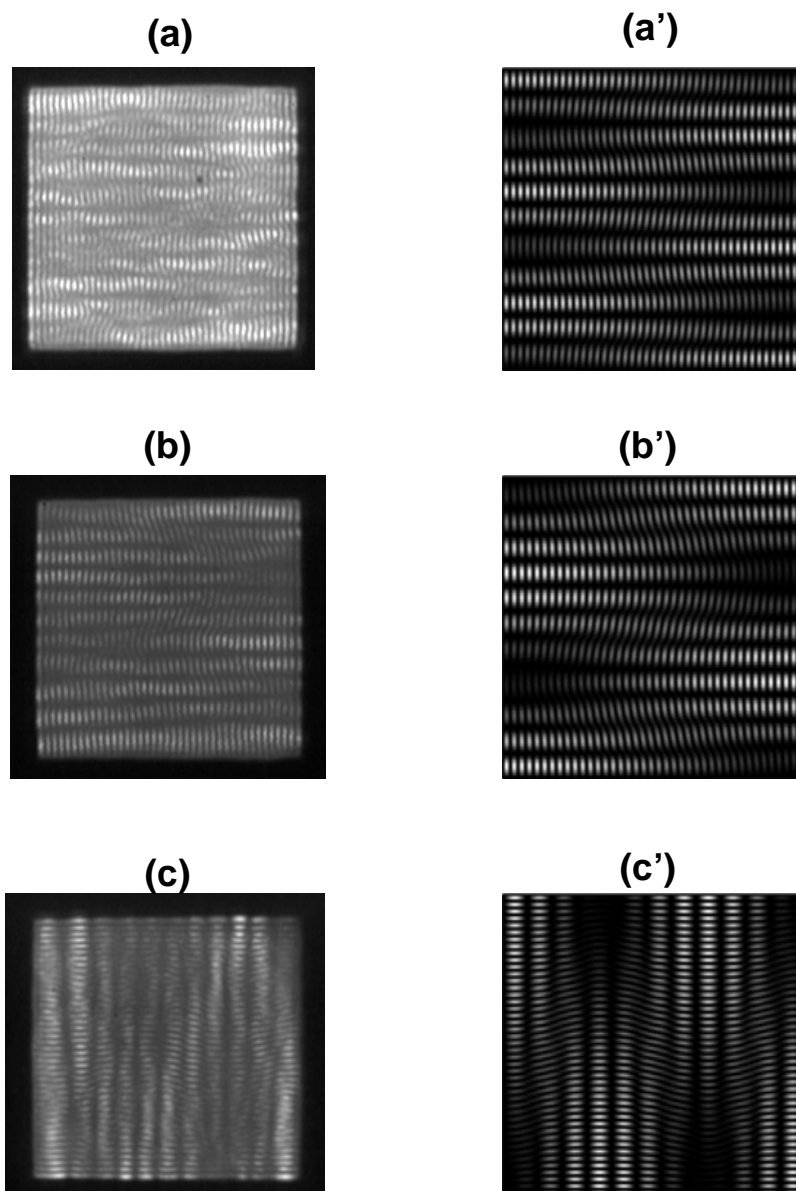


Fig. 3.3-4. (a)-(c) The bouncing ball modes observed in different square VCSEL devices. (a')-(c') The theoretical explanations of (a)-(c), which are expressed by Eq. (3.3.2)-(3.3.4), respectively.

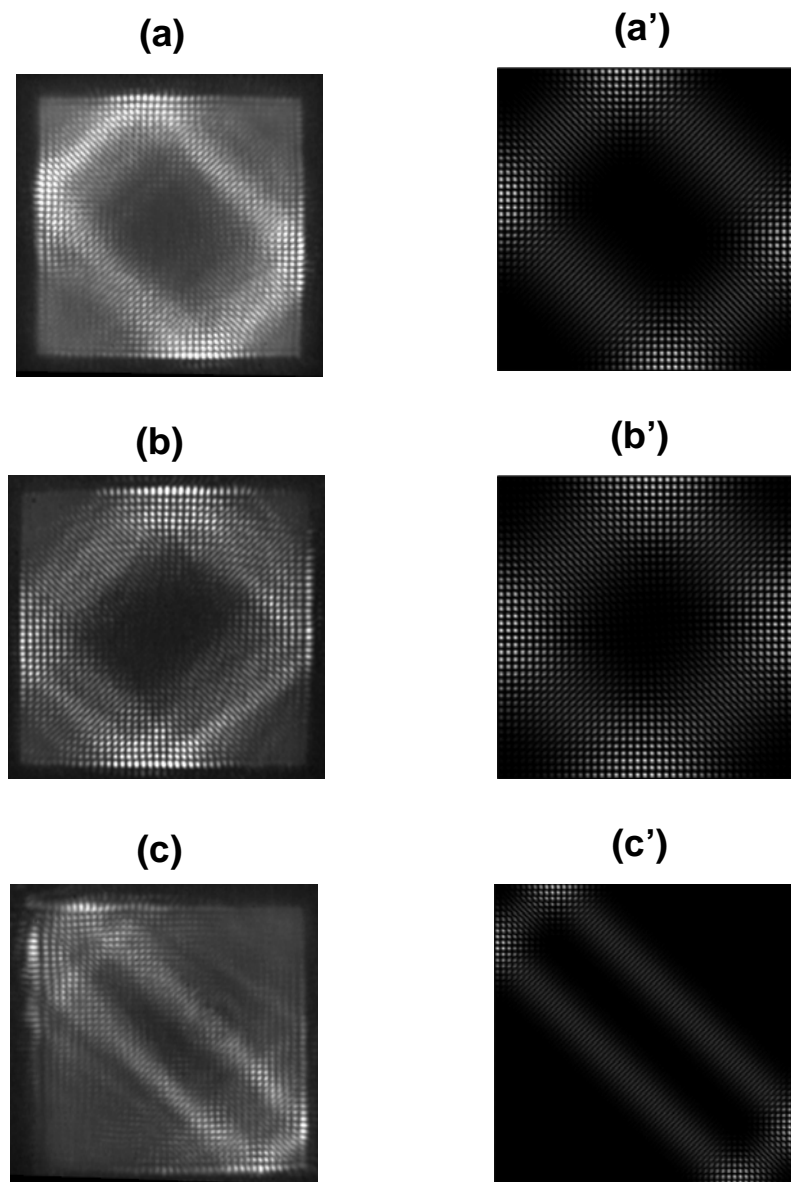


Fig. 3.3-5. (a)-(c) Various superscar modes observed in different square VCSEL devices. (a')-(c') Theoretical interpretation of (a)-(c) by SU(2) coherent states $C_{36,10}^{1,1,0.57\pi}(x,y)$, $C_{38,6}^{1,1,0.46\pi}(x,y)$, and $C_{40,25}^{1,1,0.8\pi}(x,y)$ respectively.

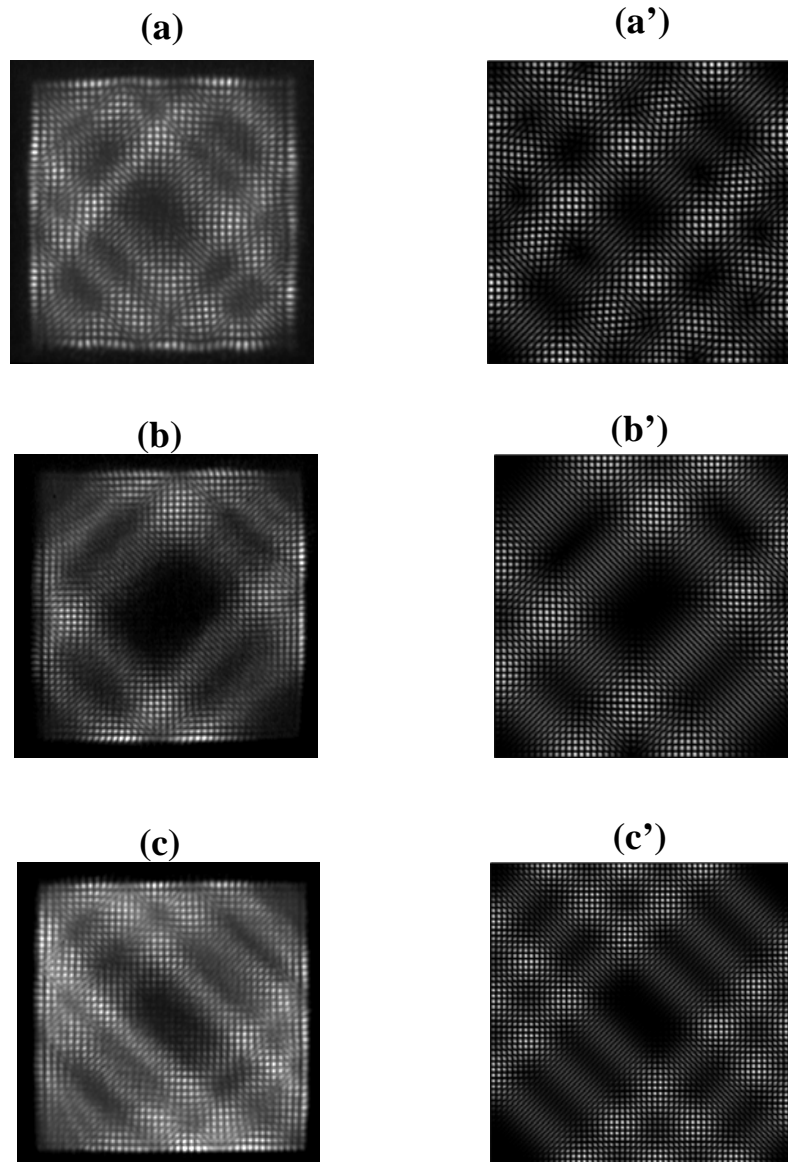


Fig. 3.3-6. (a)-(c) Various multi-POs superscar modes observed in different square VCSEL devices. (a')-(c') Theoretical patterns of (a)-(c) given by Eq. (3.3.6)-(3.3.8), respectively.

3.4 Chaotic Wave Function in Rippled-Square VCSEL

Recently, Li *et al.* reported interesting quantum chaotic phenomena in ripple billiard [LRW02]. In last section we have confirmed that transverse mode of VCSEL is equivalent to the wave function of quantum billiard. Hence, we can analogously observe the quantum chaotic wave function and experimentally investigate the statistical properties of the chaotic wave functions. Although the statistical properties of chaotic wave function have been theoretically well studied [MK88], the experimental wave functions are interfered in the measuring processes. It is known that microwave cavities have been used to obtain the statistics of chaotic wave state [KKS95, ŠHK+97, SHS04]. However, the statistical properties of the chaotic wave functions emitted from VCSELS have never been studied.

Fig. 3.4-1 shows the pattern of the spontaneous emission that manifests the details on the ripple boundary. The forms for the bottom and top walls of the ripple are approximately expressed as

$$Y(x) = \begin{cases} 0.044 a \left[1 - \exp\left(-13.5 \left| \frac{x}{a} - \frac{1}{2} \right| \right) \right] & \text{for the bottom wall} \\ a - 0.044 a \left[1 - \exp\left(-13.5 \left| \frac{x}{a} - \frac{1}{2} \right| \right) \right] & \text{for the top wall} \end{cases}, \quad (3.4.1)$$

where a is the central length of the ripple boundary. The right and left walls of the ripple are described with the same functional form. The size of the oxide aperture is $45 \times 45 \mu\text{m}^2$. Figures 3.4-2 (a) and (b) show the near-threshold lasing patterns of the rippled VCSEL at temperatures of $T = 260\text{K}$ and $T = 220\text{K}$, respectively. It can be seen that the two patterns exhibit similar morphology as a chaotic wave function as shown in Ref. [OGH87]. We can validate that the two patterns are chaotic wave

functions or not by testing its statistical properties. Since the intensity patterns do not contain sufficient information, the reconstruction of the wave functions is practically useful for studying the statistical properties of the chaotic modes.

We first demonstrate the logic of the method for reconstructing the wave function before going on. As demonstrated in Fig. 3.4-3, consider an unknown function $\psi(x)$ which is the stationary wave function of the system. Experimentally, one can only observed its intensity distribution $|\psi(x)|^2$. How can we obtain $\psi(x)$ from the experimental result $|\psi(x)|^2$? Firstly, we have to find the square root of $|\psi(x)|^2$, i. e. $|\psi(x)|$. Then we can see that $|\psi(x)|$ is formed by many nodal domains which are separated by the nodes. In $|\psi(x)|$ these nodal domains are all positive but they actually may be negative in $\psi(x)$ and the signs of the neighboring two nodal domains are different. We set the nodal domains with minus signs to be zero and obtain the positive part of $\psi(x)$ denoted as $\psi_p(x)$. Finally, $\psi(x)$ can be obtained by

$$\psi(x) = 2\psi_p(x) - |\psi(x)| \quad (3.4.2)$$

Extending to 2D case, the patterns shown in Fig. 3.4-2 (a) and (b) are the experimentally observed intensity distributions and we are going to obtain the corresponding wave function. In order to reconstruct the wave functions, we need to deduce the field point matrix $\psi(x_i, y_j)$ from the experimental intensity point matrix $|\psi(x_i, y_j)|^2$, where the indices (i, j) denote the pixel positions of the CCD camera and the total pixel number of the experimental data is 200×200 . Since the nodal lines separate the positive and negative domains of the wave function, a so-called positive wave distribution $|\psi_p(x_i, y_j)|$ can be obtained by preserving the wave amplitude $|\psi(x_i, y_j)|$ for the domains with the same sign and setting the wave amplitude to be zero for the domains with the opposite sign [SHS04].

Figures 3.4-4(a) and (b) depict the patterns of $|\psi_p(x_i, y_j)|$ for two chaotic modes shown in Figures 3.4-2 (a) and (b), respectively. With the positive wave distribution $|\psi_p(x_i, y_j)|$, the experimental wave function $\psi(x_i, y_j)$ can be determined by

$$\psi(x_i, y_j) = 2 \cdot |\psi_p(x_i, y_j)| - |\psi(x_i, y_j)| \quad (3.4.3)$$

Since the experimental wave functions are too coarse to explore the statistical properties completely, the eigenfunction expansion technique is utilized to find analytical expressions for $\psi(x_i, y_j)$. With the eigenstates of 2D square billiards as a basis, the experimental chaotic wave function can be expressed as

$$\psi(x, y) = \sum_{n_1} \sum_{n_2} C_{n_1, n_2} \sin\left(\frac{n_1 \pi}{a} x\right) \sin\left(\frac{n_2 \pi}{a} y\right) \quad (3.4.4)$$

where a is the length of the square boundary, n_1 and n_2 are the quantum number in the x and y direction, respectively, and C_{n_1, n_2} denote the expansion coefficients. Even though some other bases can be chosen for the expansion, the simple analytical form of the eigenstates of 2D square billiards leads to the calculation to be extremely straightforward. The orthogonality relation leads $C_{m, n}$ to be

$$C_{n_1, n_2} = \int_0^a \int_0^a \psi(x, y) \sin\left(\frac{n_1 \pi}{a} x\right) \sin\left(\frac{n_2 \pi}{a} y\right) dx dy, \quad (3.4.5)$$

With the experimental wave function $\psi(x_i, y_j)$, the integral in Eq. (3.4.5) can be numerically calculated by a summation:

$$C_{n_1, n_2} = \sum_{i=1}^N \sum_{j=1}^N \psi(x_i, y_j) \sin\left(\frac{n_1 \pi}{a} x_i\right) \sin\left(\frac{n_2 \pi}{a} y_j\right) \Delta x_i \Delta y_j \quad . \quad (3.4.6)$$

Figures 3.4-5(a) and (b) show the intensity plots of $|C_{n_1, n_2}|$ corresponding to Figures 3.4-2 (a) and 3.4-2(b), respectively. These ring areas signify the random directional distribution of transverse wave vectors \mathbf{k} , since $|C_{n_1, n_2}|$ corresponds to the weighting in k -space. The distribution of $|C_{n_1, n_2}|$ in Figure 3.4-5(a) has a mean radius $\bar{R}_{260} = 60.14$ and standard deviation $\sigma_{260}^r = 1.62$, while in Figure 3.4-5(b) $\bar{R}_{220} = 60.92$ and $\sigma_{220}^r = 1.35$. Here the mean radius \bar{R} and standard deviation σ^r are defined as

$$\bar{R} = \sum_{n_1, n_2} |C_{n_1, n_2}|^2 \cdot r_{n_1, n_2} \quad \text{and} \quad \sigma^r = \left[\sum_{n_1, n_2} |C_{n_1, n_2}|^2 \cdot (r_{n_1, n_2} - \bar{R})^2 \right]^{1/2} \quad (3.4.7)$$

, where the radius r_{n_1, n_2} is given by $r_{n_1, n_2} = \sqrt{n_1^2 + n_2^2}$. Naturally \bar{R}_{260} is smaller than \bar{R}_{220} because the detuning at $T=260K$ is smaller than that at $T=220K$. On the other hand, σ_{260}^r is larger than σ_{220}^r because the thermal fluctuation at $T=260K$ is larger than that at $T=220K$.

With the expansion coefficients $|C_{n_1, n_2}|$ the experimental wave functions can be reconstruct by inserting $|C_{n_1, n_2}|$ into Eq. (3.4.4). The reconstructed intensity patterns for Fig. 3.4-2 (a) and (b) are displayed in Fig. 3.4-6 (a) and (b), respectively. We can see that it is very successful in reconstructing the experimentally observed chaotic modes. The statistical properties of the two chaotic modes can now be precisely studied. As discussed in Sec. 2.3, one obtains chaotic wave function in the form of a Gaussian distribution for amplitude,

$$P(\psi) = \frac{1}{\sigma\sqrt{2\pi}} \exp\left(-\frac{\psi^2}{2\sigma^2}\right) \quad (3.4.8)$$

, where σ is the standard deviation given by $\sigma = 1/\sqrt{A}$ with A denotes the area of the billiard. Fig. 3.4-7 (a) and (b) depict the amplitude distributions of the wave functions shown in Fig. 3.4-8 (a) and (b), respectively, with the fitting curves described by Eq. (3.4.8). In addition to Gaussian amplitude distribution, the intensity distribution of a chaotic wave function is shown to be Porter-Thomas distribution

$$P(I) = \frac{1}{\sqrt{2\pi I}} \exp\left(-\frac{I}{2}\right). \quad (3.4.9)$$

Figs. 3.4-9 (a) and (b) illustrate the intensity distributions of the reconstructed patterns Figs. 3.4-7 (a) and (b), respectively.

It can be seen that there are slight variations between our statistical results and theoretical predictions, especially for the case of $T = 260K$. This phenomena may be caused by the thermal fluctuation that results in a broadening of the deviation (σ') of the nearly degenerate modes in experiment.

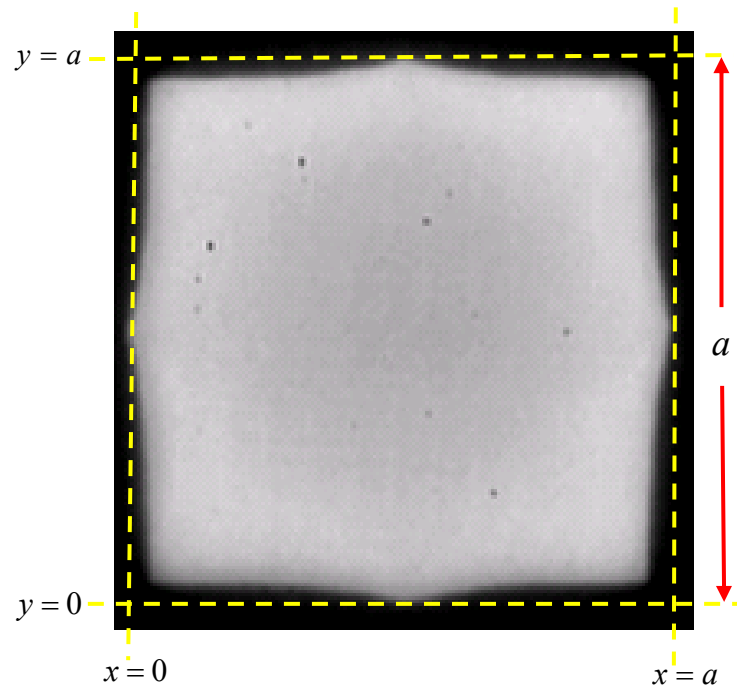


Fig. 3.4-1. Experimental pattern of the spontaneous emission to manifest the details on the ripple boundary.

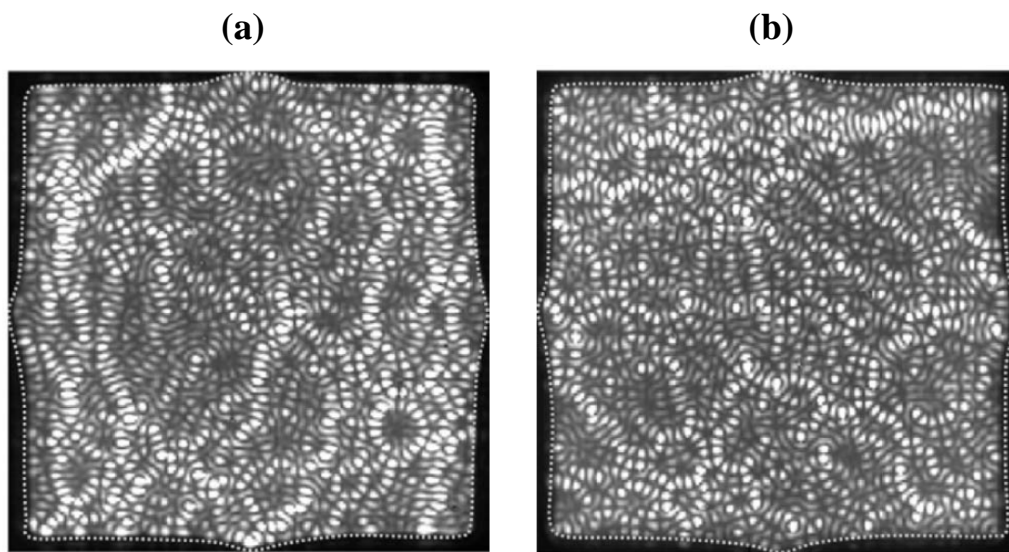


Fig. 3.4-2. Near-threshold lasing patterns of the rippled VCSEL at temperatures of (a) $T = 260K$ and (b) $T = 220K$.

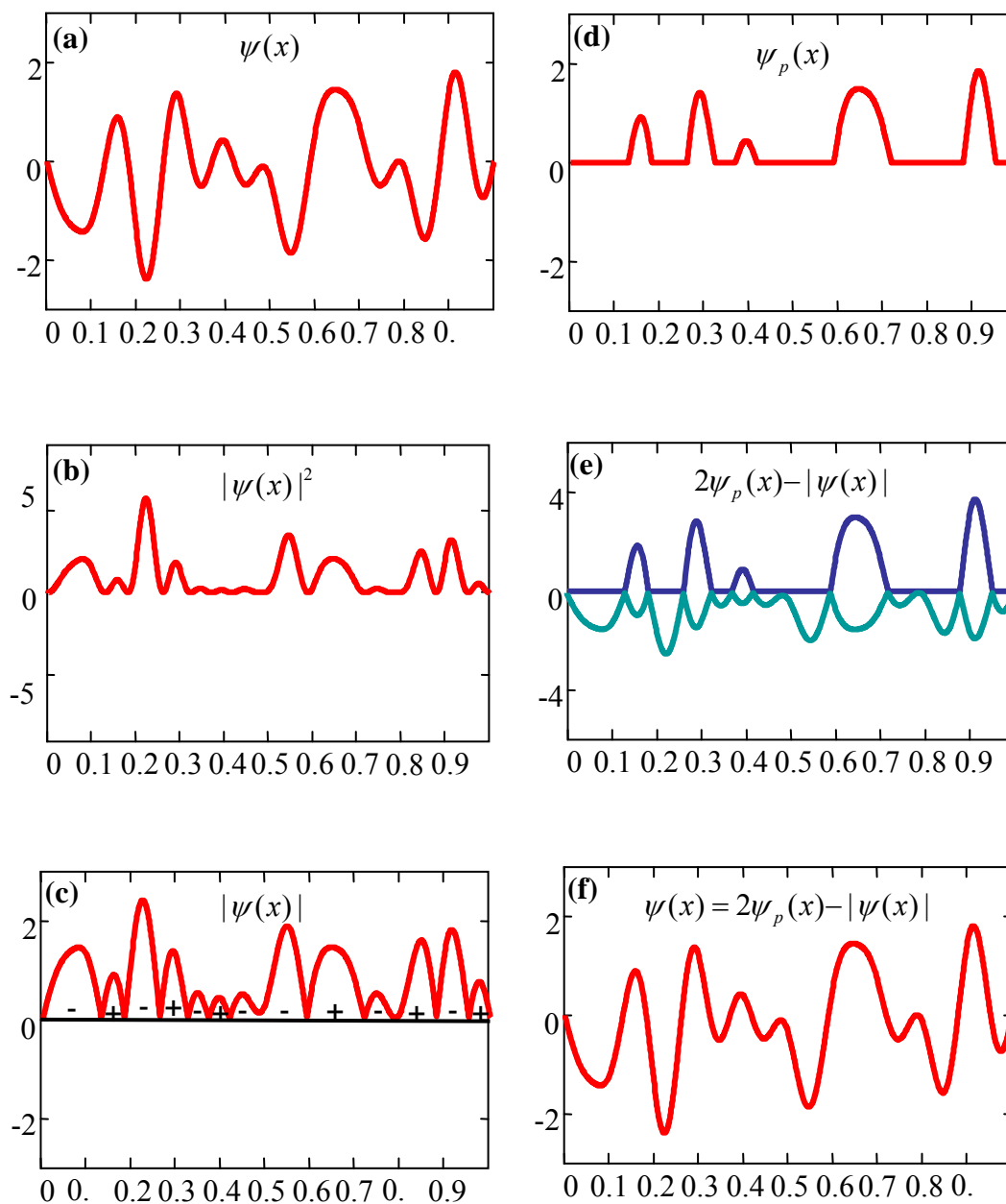


Fig. 3.4-3. (a) An unknown wave function (b) The intensity distribution (c) Square Root of intensity distribution (d) Positive part of the wave function (e) Demonstration of $2\psi_p(x) - |\psi(x)|$ (f) The result of $2\psi_p(x) - |\psi(x)|$.

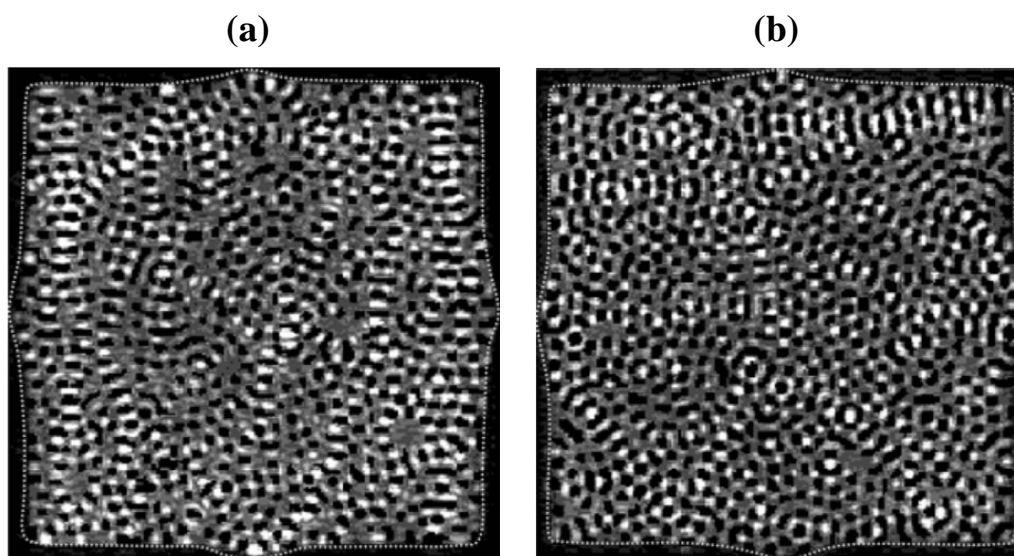


Fig. 3.4-4. (a) and (b) The intensity plots of the positive wave functions $|\psi_p(x_i, y_j)|$ for experimental results shown in Figs. 3.4-2 (a) and (b), respectively.

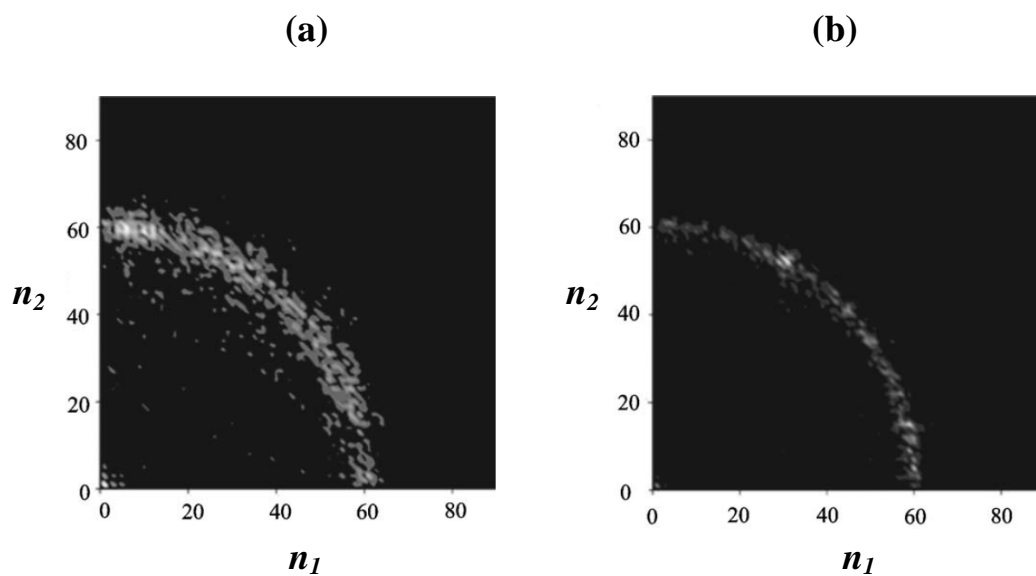


Fig. 3.4-5. (a) and (b) Distribution of the coefficients $|C_{m,n}|$ obtained by Eq. (3.4.6) for experimental results shown in Figs. 3.4-1 (a) and (b).

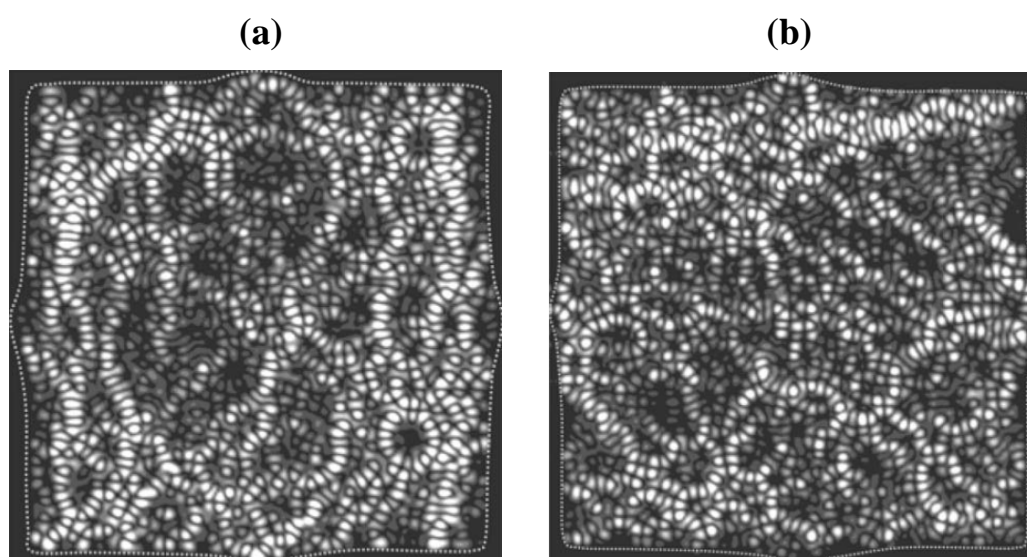


Fig. 3.4-6. (a) and (b) The reconstructed patterns with the eigenfunction expansion method for experimental results.

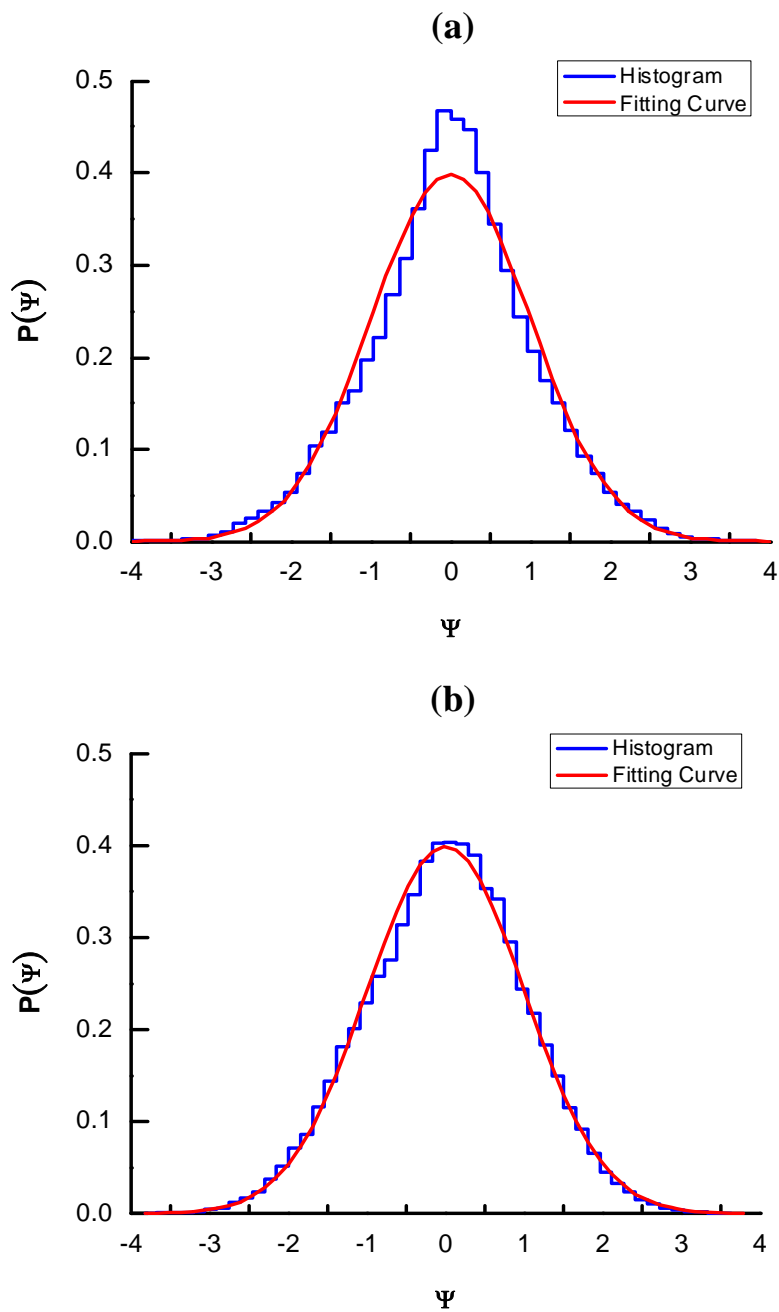


Fig. 3.4-7. (a) and (b) The amplitude distributions of the wave functions shown in Fig. 3.4-6 (a) and (b), respectively.

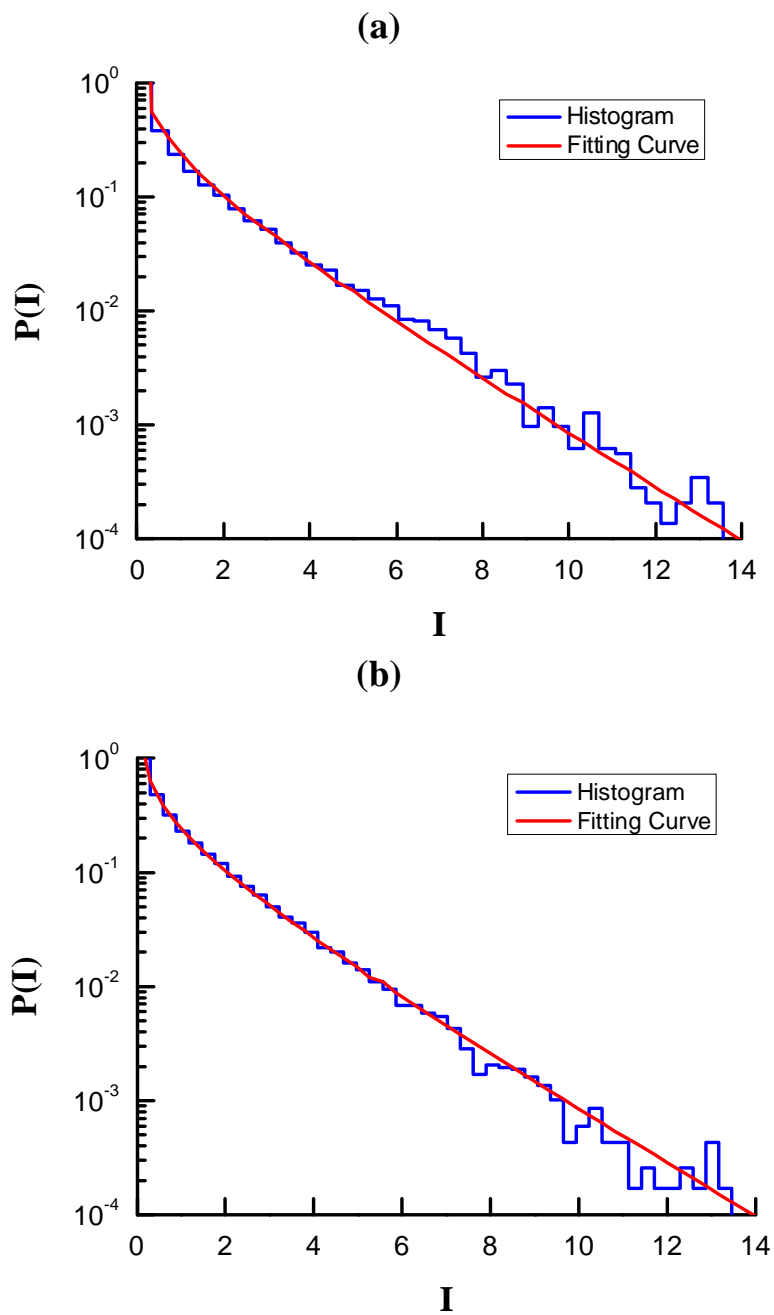


Fig. 3.4-8. (a) and (b) The intensity distributions of the patterns shown in Fig. 3.4-6 (a) and (b), respectively.

3.5 Typical Lasing Modes in Equilateral-Triangular VCSEL

Equilateral triangular billiard is a special polygonal billiard, which is classically nonseparable but integrable system [DR02]. The experimental observation of the lasing modes in equilateral triangular VCSEL may provide useful information for the microdisk lasers experiments with equilateral triangular resonators [CKL+00, HGL00, HGYL01, LCG+04, YAK+07,] and electron transport phenomena in equilateral triangular quantum dots [CLO+97].

Fig. 3.5-1(a) and (b) show the optical microscope image of the device operated with an electric current under threshold current at room temperature. The bright region indicates the equilateral triangular pattern of spontaneous emission, which can be more clearly visualized in CCD camera as shown in Fig. 3.5-1(c). The edge length of the oxide aperture was measured to be approximately 66.8 μm .

Similarly, we only focus on the lasing patterns at near threshold current. Fig. 3.5-2 shows the temperature dependence of the threshold current in the range from 300K to 120K. Figures 3.5-3(a)-(i) depict the experimental near-field patterns that are characteristically observed at different device temperatures. It is found that the lasing patterns are generally robust and reproducibly observed under the same experimental circumstances. The lasing pattern shown in Fig. 3.5-3(a) is obtained at the operating temperature of 295K and the optical spectrum indicates it to be a multi-mode emission. The lasing state at the operating temperature of 275K is found to dramatically change to a superscar mode that is similar to Fabry-Pérot modes impinging on lateral sides vertically [MMN64], as seen in Fig. 3.5-3(b). When the operating temperature decreases to 195K, the lasing pattern shown in Fig. 3.5-3(e) exhibits a honeycomb structure. As discussed later, the honeycomb morphology corresponds to the pattern of an eigenstate. When the operating temperature further decreases to 175K, the near-field pattern shown in Fig. 3.5-3(f) behaves like a chaotic wave state that can be described as a random superposition of plane waves [OGH87].

For the operating temperature below 135K, the experimental pattern shown in Fig. 3.5-3(i) corresponds to another superscar mode that is related to a geometrical PO [DR02]. This superscar mode is found to be unchanged when the temperature decreases from 135K to 80K. Intriguingly, the lasing pattern displays the transition and coexistence of the chaotic and superscar modes at the other operating temperature. As shown in Fig. 3.5-3(c), the lasing mode at 255K is a superscar mode like Fig. 3.5-3(b) but with a background of random wave. Fig. 3.5-3(d) is a mixing of honey-comb eigenstate and random wave. The transition from chaotic wave function to superscar mode is clearly displayed from Fig. 3.5-3(f)-(i). The lasing patterns of each VCSEL devices are different but their characteristics are generally the same.

The analogy between the electromagnetic wave equation in paraxial approximation and the Schrödinger equation enables us to make a detailed connection between the quantum wave functions and the experimental patterns. As discussed in Sec. 2.2, the quantum eigenstates of the equilateral triangular billiard are given by

$$\Phi_{m,n}^{\pm}(x,y) = \sqrt{\frac{16}{a^2 3\sqrt{3}}} \left\{ e^{\pm i(m+n)\frac{2\pi}{3a}x} \sin\left[(m-n)\frac{2\pi}{\sqrt{3}a}y\right] + e^{\mp i(2m-n)\frac{2\pi}{3a}x} \sin\left[n\frac{2\pi}{\sqrt{3}a}y\right] - e^{\mp i(2n-m)\frac{2\pi}{3a}x} \sin\left[m\frac{2\pi}{\sqrt{3}a}y\right] \right\}, \quad (3.5.1)$$

with $2n \geq m$. The eigenstates $\Phi_{m,n}^{\pm}(x,y)$ are the representation of traveling waves. The standing-wave wave representation of $\Phi_{m,n}^{\pm}(x,y)$ can be expressed as $\Phi_{m,n}^{(S)}(x,y) = \Phi_{m,n}^{+}(x,y) - \Phi_{m,n}^{-}(x,y)$. The experimental honeycomb pattern shown in Fig. 3.5-3 (e) can be numerically confirmed to correspond to the wave intensity of $|\Phi_{5,5}^{(S)}(x,y)|^2$, as depicted in Fig. 3.5-4 (b). Superscar modes that are associated

with classical POs can be analytically expressed with the representation of quantum coherent states

$$\Psi_{N,M}^{Tri}(x, y; p, q, \phi) = \frac{1}{\sqrt{2^M}} \sum_{K=0}^{M-1} \sqrt{C_K^M} e^{iK\phi} \Phi_{m_0+pK, n_0+q(M-1-K)}^+(x, y) \quad (3.5.2)$$

Similarly, $\Psi_{N,M}^{Tri}(x, y; p, q, \phi)$ represents the traveling wave and the expression for the standing wave can be given by

$$C_{N,M}^{Tri}(x, y, p, q, \phi) = \Psi_{N,M}^{Tri}(x, y, p, q, \phi) + \Psi_{N,M}^{*Tri}(x, y, p, q, \phi). \quad (3.5.3)$$

Based on thorough numerical analysis, the experimental superscar modes can be found to be well reconstructed with the coherent states of $C_{36,9}^{Tri}(x, y; 1, 0, 0.23\pi)$ and $C_{22,6}^{Tri}(x, y; 1, 1, 0.35\pi)$. Figures 3.5-5(c) and (d) depict the numerical wave patterns of $|C_{36,9}^+(x, y; 1, 0, 0.23\pi)|^2$ and $|C_{20,6}^-(x, y; 1, 1, 0.35\pi)|^2$ corresponding to the experimental patterns shown in Fig. 3.5-5 (a) and (b), respectively. The excellent agreement between the experimental and numerical patterns confirms that the quantum formalism is of great importance in describing distinct branches of physics because of the underlying structural similarity. Conversely, the present analysis also provides a further indication that laser resonators can be designed to demonstrate the quantum phenomenon in mesoscopic physics.

Although an ideal equilateral triangular billiard is integrable, some experimental patterns reveal the property of quantum chaotic modes, as seen in Fig. 3.5-6(a). To prove this pattern is chaotic, the method used in last section is employed to reconstruct this experimental result. Since the eigenstates of equilateral-triangular form a complete set of basis, the wave function can be spanned by [DB02]

$$\begin{aligned} \psi(x, y) = & \sum_{m \geq 2n}^{\infty} \sum_{n=0}^{\infty} c1_{m,n} \Phi_{m,n}^{(C)}(x, y) \\ & + \sum_{m > 2n}^{\infty} \sum_{n=0}^{\infty} c2_{m,n} \Phi_{m,n}^{(S)}(x, y) \end{aligned} \quad (3.5.4)$$

Based on the orthogonality of the eigenstates, the expansion coefficients can be obtained by

$$c1_{m,n} = \iint_S \psi(x, y) \Phi_{m,n}^{(C)}(x, y) dx dy \quad (3.5.5)$$

and

$$c2_{m,n} = \iint_S \psi(x, y) \Phi_{m,n}^{(S)}(x, y) dx dy \quad (3.5.6)$$

, where the integration area S is the entire equilateral-triangle billiard. Similarly, the experimental wave function $\psi(x_i, y_j)$ can be found by

$$2 \cdot |\psi_p(x_i, y_j)| - |\psi(x_i, y_j)| \quad (3.5.7)$$

, where $\psi_p(x_i, y_j)$ shown in Fig. 3.5-6 is the positive wave distribution. With the experimental wave function $\psi(x_i, y_j)$, the integrals in Eq. (3.5.5) and (3.5.6) can be numerically calculated by summations:

$$c1_{m,n} = \sum_i \sum_j \psi(x_i, y_j) \Phi_{m,n}^{(C)}(x_i, y_j) \Delta x_i \Delta y_j \quad (3.5.8)$$

and

$$c2_{m,n} = \sum_i \sum_j \psi(x_i, y_j) \Phi_{m,n}^{(S)}(x_i, y_j) \Delta x_i \Delta y_j \quad (3.5.9)$$

, with the indices (i, j) satisfying $x_i > -\sqrt{3}y_j \wedge x_i < \sqrt{3}y_j \wedge y_j < \frac{\sqrt{3}}{2}a$. Inserting the expansion coefficients $c1_{m,n}$ and $c2_{m,n}$ into Eq. (3.5.4), we can obtain the reconstructed wave function as shown in Fig. 3.5-7(b). Besides, it has been discussed that the intensity statistics of the chaotic wave functions obey the Porter-Thomas distribution $P(I) = \left(1/\sqrt{2\pi I}\right)e^{-I/2}$. We evaluate the intensity statistics for the reconstructed wave function, as shown in Fig. 3.5-7(c). The good agreement validates that the wave pattern corresponds to a chaotic wave function. The origin of stationary chaotic modes is inspected to arise from spontaneous imperfections, such as roughness on boundary or unequal of the three internal angles. In other words, the spontaneous symmetry breaking may cause the real devices with idealized integrable confinements to exhibit the characteristics of nonintegrable systems. As discussed in Ref. [BU94], although a triangular billiard with internal angles to be slightly different from $\pi/3$ is intrinsically chaotic, the wave functions can still be scarred by families of POs. Briefly, tiny symmetry breaking can lead to the emergence of superscar as well as chaotic modes in the almost integrable systems. Our experimental results are utterly consistent with the theoretical findings.

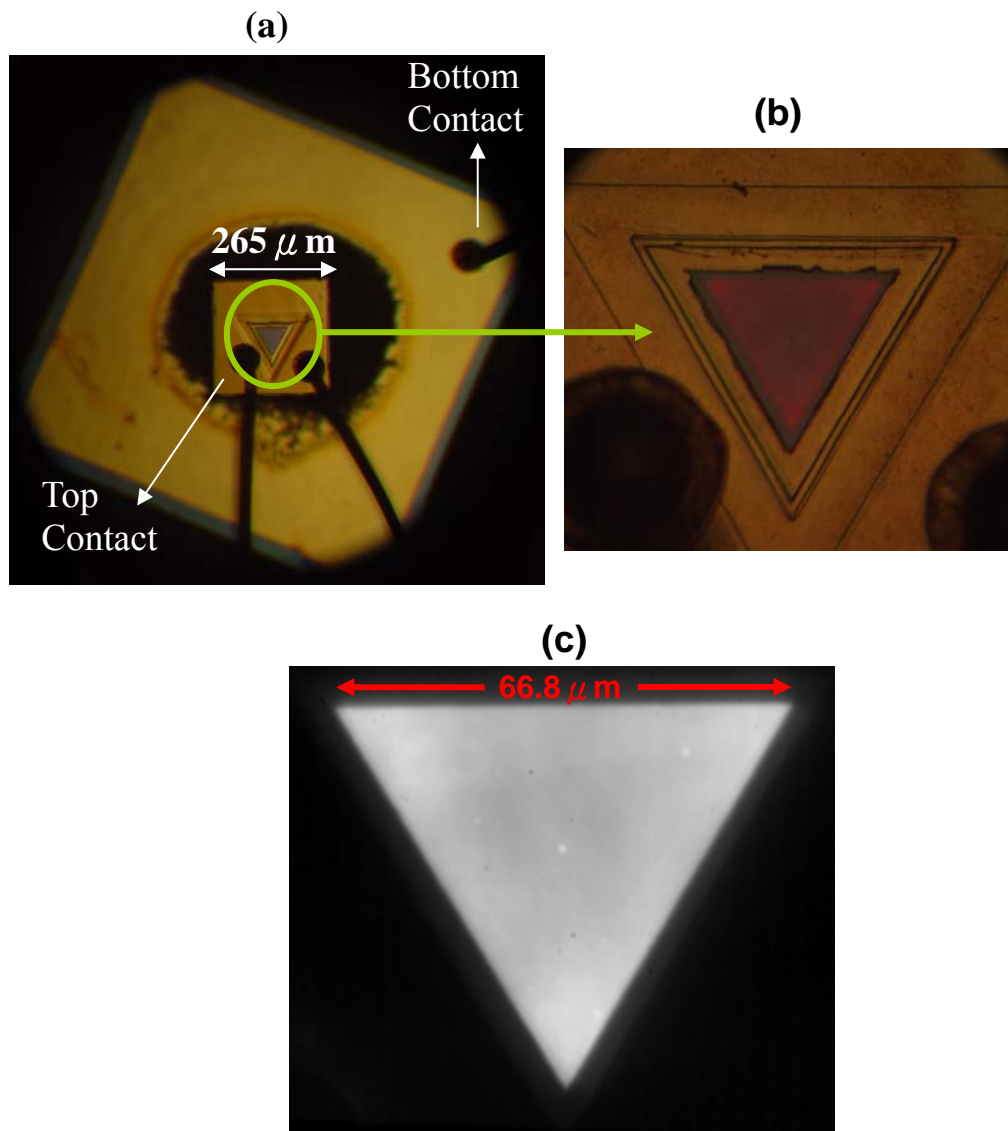


Fig. 3.5-1. (a) Optical microscope image of the VCSEL device. (b) Zoom-in view of (a) and is operated with an electric current under threshold current at room temperature. (c) The spontaneous emission to manifest the details on the triangular boundary temperature.

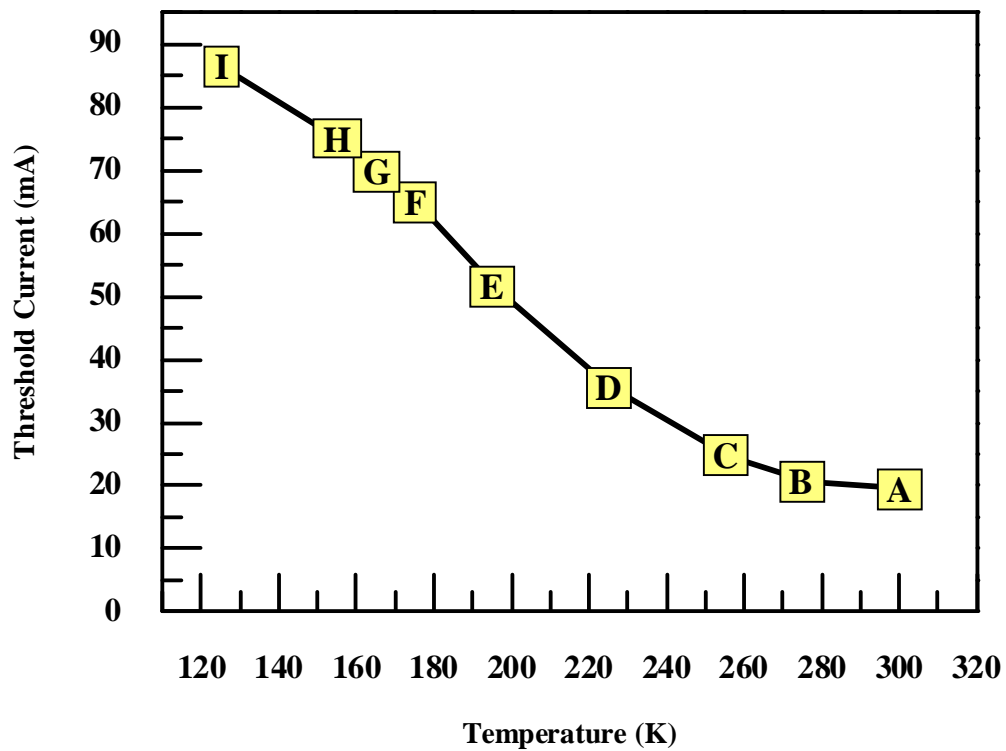


Fig. 3.5-2. Temperature dependence of the threshold current of the equilateral triangular VCSEL.

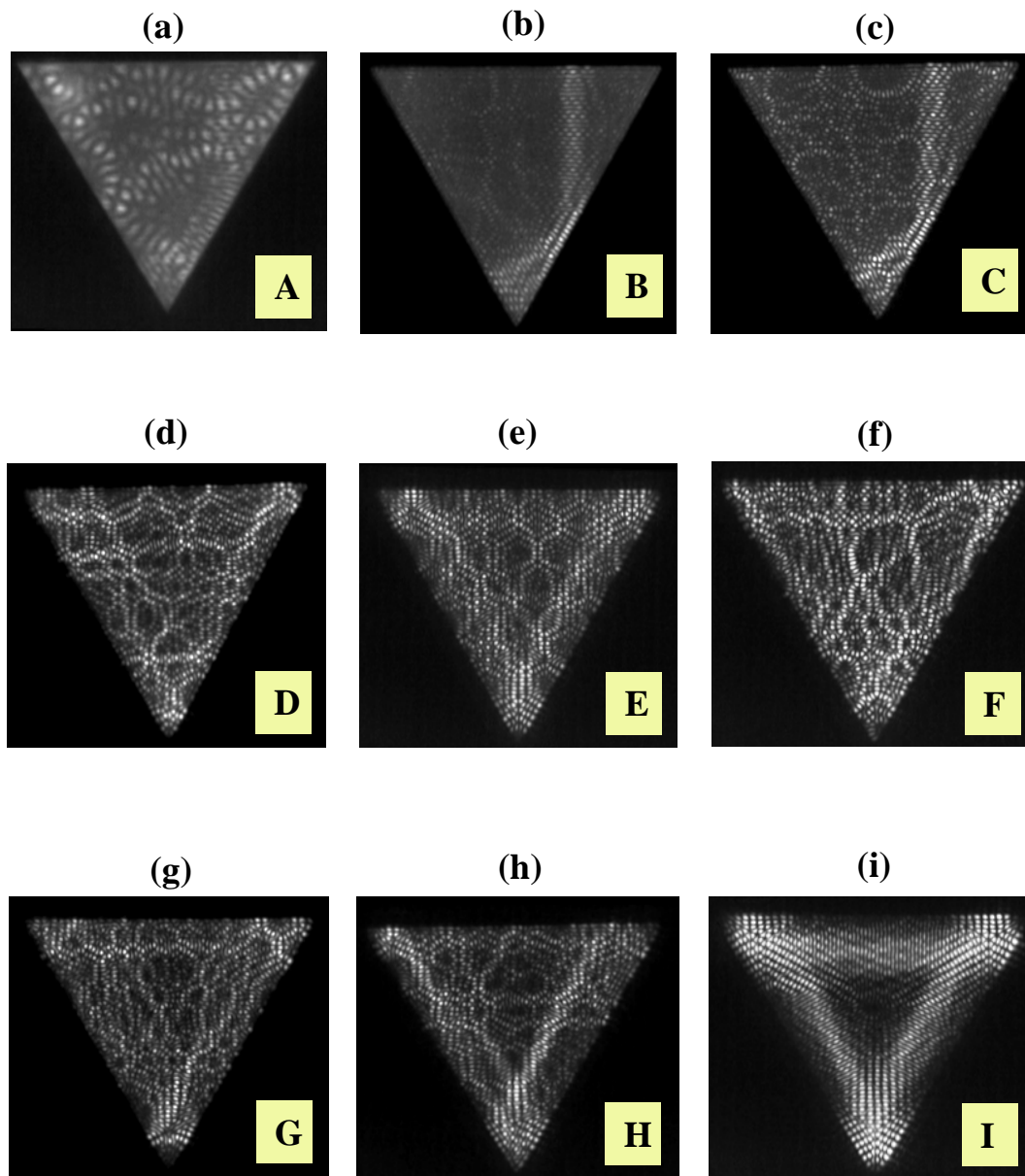


Fig. 3.5-3. (a)-(i) The near-threshold lasing patterns of triangular VCSEL at temperatures labeled by A-I in Fig 3.5-2, respectively.

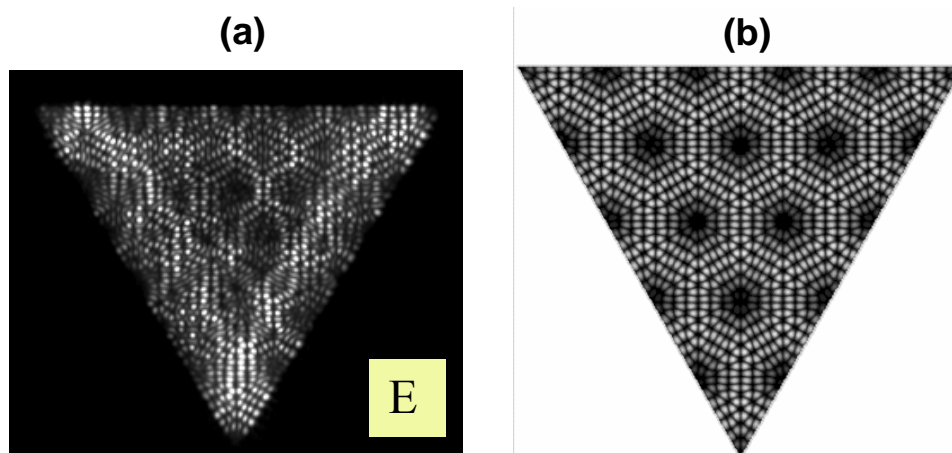


Fig. 3.5-4. (a) Experimental pattern observe at 195K. (b) Numerical wave pattern of eigenstate $|\Phi_{5,55}^{(S)}(x, y)|^2$.

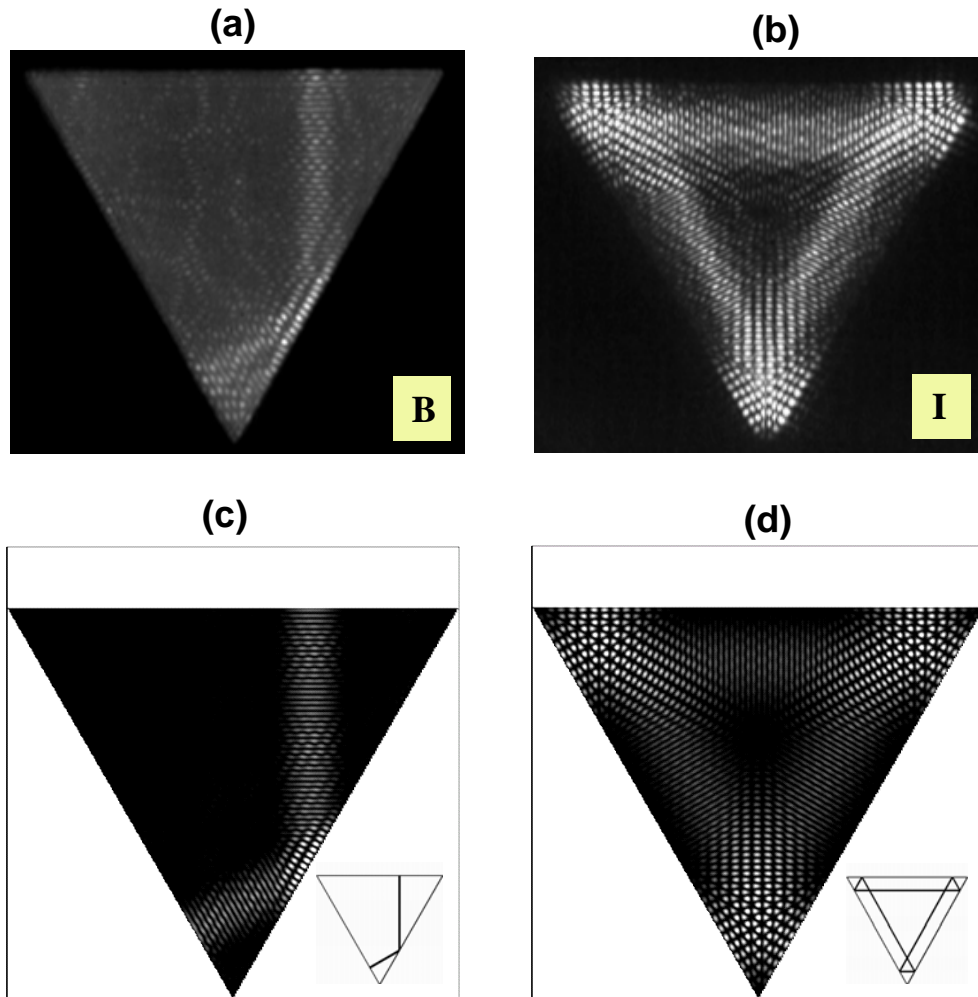


Fig. 3.5-5. Experimental pattern observe at (a)275K and (b)135K; Numerical wave pattern of coherent state (c) $|C_{36,9}^{Tri}(x, y; 1, 0, 0.23\pi)|^2$ and (d) $|C_{20,6}^{Tri}(x, y; 1, 1, 0.35\pi)|^2$; The classical periodic orbits that the wave functions localized on are depicted in the insets of (c) and (d).

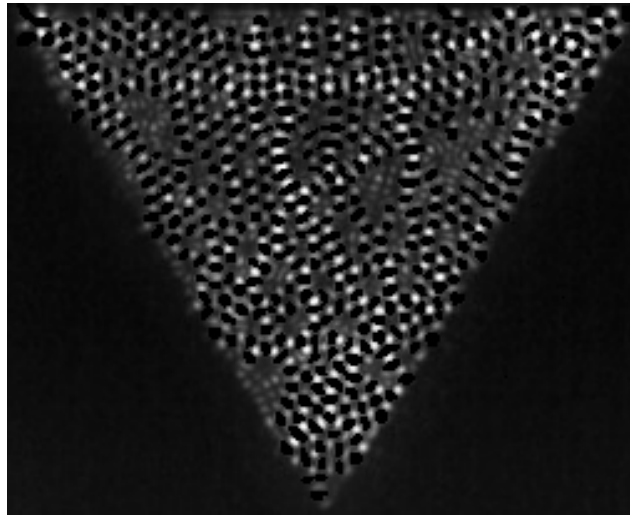


Fig. 3.5-6. The intensity plots of the positive wave functions $|\psi_p(x_i, y_j)|$ for experimental results shown in Figs. 3.5-3 (f).

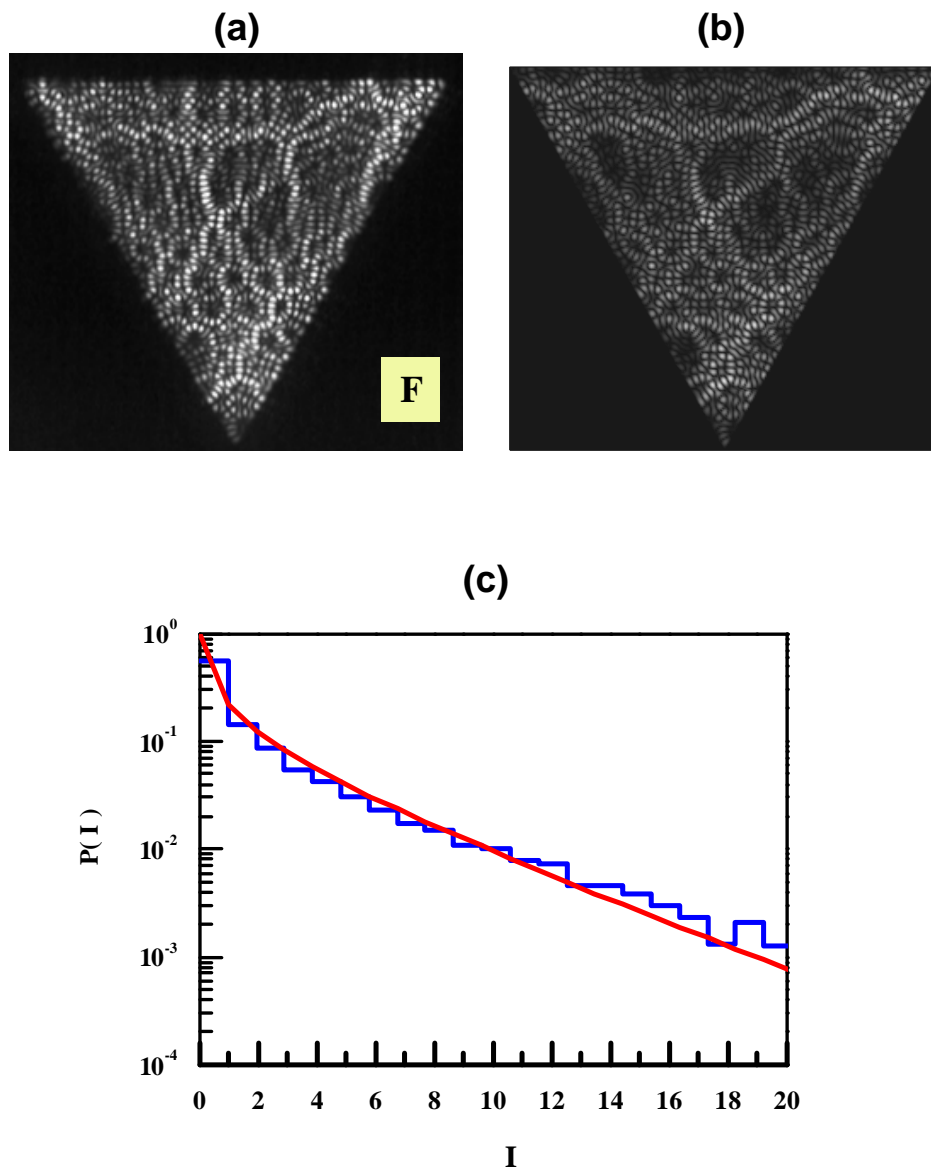
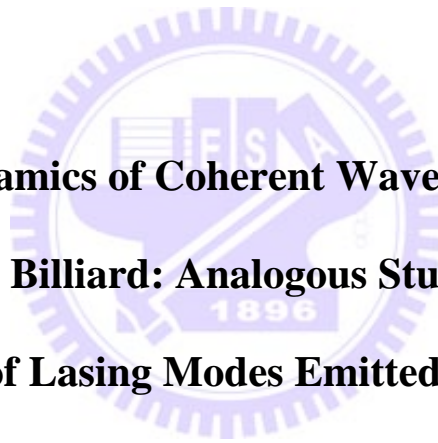


Fig. 3.5-7. (a) Experimental pattern observe at 175K. (b) Reconstructed pattern of (a). (c) Intensity statistics of (b) with fitting curve to be Porter-Thomas intensity distribution.

Chapter 4

**Transient Dynamics of Coherent Waves Released from
Quantum Billiard: Analogous Studies on the
Propagation of Lasing Modes Emitted from VCSELs**



Ch4 Transient Dynamics of Coherent Waves Released from Quantum Billiard:
Analogous Studies on the Propagation of Lasing Modes Emitted from VCSELs

One of the most relevant quantum transient phenomena in matter waves is the diffraction-in-time effect for a suddenly released coherent beam, which appears to have first been introduced by Moshinsky in 1952 [Mosh52]. The hallmark feature of the diffraction-in-time effect is the temporal quantum interference patterns, by analogy with the spatial interference patterns of light diffracted by a sharp edge [MMS99, Godo02, GM05, dCMM07]. The experimental test for this effect was indeed hard to reach at the time of the first introduction. However, due to the development in ultrafast laser [PLW+03], atom cooling, and optical trapping [WPW99], the transient dynamics has been recently observed in wide variety of systems including neutrons [HFG+98], ultracold atoms [SSDD95], electrons [LSW+05], and Bose-Einstein condensates [CMPL05].

Another physical connection to the diffraction-in-time effect would be the transient response to abrupt changes of the confined potential in semiconductor structures and quantum dots [DCM02, DMA+05]. Semiconductor quantum dots, in which electronic motion is predominately ballistic in nature, have been widely used as two-dimensional (2D) quantum billiards to explore the properties of quantum chaos [AF99, ZB97, BAF+99]. Understanding the time evolution of suddenly released quantum-billiard waves has some important applications, as it can provide the nanostructure transport properties for developing novel ultrahigh-speed semiconductor devices [DCM02]. Moreover, it is closely related to atom laser dynamics from a tight waveguide whose boundary shape can be modified with the laser trapping-beam [DMA+05, dCL+08]. Nevertheless, the investigation for the transient dynamics of 2D quantum-billiard coherent waves has not been performed as yet.

This chapter is structured as follow: The time evolution of a stationary wave function abruptly released from 1-D infinite potential is quickly reviewed in the opening section. Secondly, similar problem will be extended to various wave functions with a suddenly removal of 2-D square billiards. In third section, we utilize the similarity between paraxial optics and 2-D non-relativistic quantum

mechanics to analogously observe the time evolutions of coherent waves released from quantum billiards by free-space propagation of transverse modes of VCSELs. In final section our aim is to analyze the linear and angular momentum densities of the light beam emitted from VCSELs by analogously calculating the probability current and angular momentum densities of coherent waves released from quantum billiard.

4.1 Stationary States Suddenly Released from 1-D Infinite Potential Well

Since Moshinsky first proposed the shutter problem in 1952 [Mosh52], diffraction in time has received considerable attentions. Recently, the transient dynamics of an initially bounded stationary state suddenly released from 1-D infinite potential well has been studied by Godoy [Godo02]. Before investigating the transient dynamics of a particle suddenly released from 2D quantum billiard, we first reviewed the work done by Godoy.

Consider that a particle is confined in a 1-D box as $t < 0$, and then the box is abruptly removed at $t = 0$. What will be the time evolution of this particle? The problem implies to solve the Schrödinger equation

$$i\hbar \frac{\partial}{\partial t} \psi(x, t) = -\frac{\hbar^2}{2m} \frac{\partial^2}{\partial x^2} \psi(x, t) \quad (4.1.1)$$

with initial condition

$$\psi_n(x, 0) = \begin{cases} \sin\left[\frac{n\pi}{a}\left(x + \frac{a}{2}\right)\right] & \text{if } -a/2 < x < a/2 \\ 0 & \text{otherwise} \end{cases} \quad (4.1.2)$$

In terms of the free propagator (Appendix A), the free time evolution of the initial

Ch4 Transient Dynamics of Coherent Waves Released from Quantum Billiard:
Analogous Studies on the Propagation of Lasing Modes Emitted from VCSELs

wave function is given by

$$\psi(x, t) = \sqrt{\frac{m}{i2\pi\hbar t}} \int_{-a/2}^{a/2} \psi(x, 0) \exp\left[\frac{im(x-x')^2}{2\hbar t}\right] dx' \quad (4.1.3)$$

Substituting Eq. (4.1.2) into Eq. (4.1.3), after some algebra (a process similar to that done in Appendix A), $\psi_n(x, t)$ is expressed as follow

$$\psi_n(x, t) = \frac{e^{-\frac{i}{\hbar} E_n t}}{\sqrt{4i^3 a}} [G(x, t; k_n, a) - G(x, t; -k_n, a)] \quad (4.1.4)$$

, where $k_n = n\pi/a$, $E_n = \hbar^2 k_n^2 / 2m$, and

$$G(x, t; k_n, a) = e^{ik_n(x+a/2)} [F(\xi(x-a/2, t; k_n)) - F(\xi(x+a/2, t; k_n))] \quad (4.1.5)$$

with $F(\xi) = C(\xi) + iS(\xi)$ denoting the complex Fresnel's integral. Fig. 4.1-1 (a)-(k) display the intensity of $\psi^S(x, t; 10)$ at $t = 0T - T$ with equal time interval $\Delta t = 0.1T$, where $T = 2ma/\hbar k_n$ corresponds to the round-trip time of the wave. The complicated interference patterns at $t < T$ is a quantum-mechanical phenomenon, since a classical particle released from a box will simply go in $+x$ or $-x$ directions with equal probability. Notice that this solution corresponds to the diffraction of optical wave from sinusoidal grating [Good05].

As the time satisfies the condition of $t \gg ma^2/\hbar$, Eq. (4.1.3) can be approximated to

$$\psi(x, t) = \sqrt{\frac{m}{i2\pi\hbar t}} e^{i\frac{mx^2}{2\hbar t}} \int_{-\infty}^{\infty} \psi(x', 0) \exp\left(-\frac{imxx'}{\hbar t}\right) dx' \quad (4.1.6)$$

, which is an analogy of Fraunhofer's diffraction in optics and is just a Fourier

Ch4 Transient Dynamics of Coherent Waves Released from Quantum Billiard:
Analogous Studies on the Propagation of Lasing Modes Emitted from VCSELs

transform. In other words, $\psi(x,t)$ with $t \gg ma^2/\hbar$ essentially corresponds to the momentum-space wave function of $\psi(x,0)$

$$\phi(p_x) = \frac{1}{\sqrt{2\pi}} \int_{-\infty}^{\infty} \psi(x',0) \exp(-\frac{ip_x x'}{\hbar}) dx'. \quad (4.1.7)$$

Neglecting the phase factor, we have the correspondence $p_x \leftrightarrow mv_x$ with $v_x = x/t$ denoting the average velocity to arrive x . Therefore, the momentum-space wave function can be alternatively interpreted as free time evolution of the real-space wave function with time approaches to infinity.

For the case of sine function released from 1-D box, Eq. (4.1.6) becomes

$$\psi_n^F(x,t) \approx \begin{cases} \frac{2n\pi}{a} \frac{\sin(\frac{max}{2\hbar t})}{(\frac{mx}{\hbar t})^2 - (\frac{n\pi}{a})^2} & \text{if } n \in \text{even} \\ -i \frac{2n\pi}{a} \frac{\cos(\frac{max}{2\hbar t})}{(\frac{mx}{\hbar t})^2 - (\frac{n\pi}{a})^2} & \text{if } n \in \text{odd} \end{cases} \quad (4.1.8)$$

Hence, as the time satisfies the condition that $t \gg ma^2/\hbar$, the wave function preserves its form as shown in Fig. 4.1-1 (l).

Ch4 Transient Dynamics of Coherent Waves Released from Quantum Billiard:
Analogous Studies on the Propagation of Lasing Modes Emitted from VCSELs

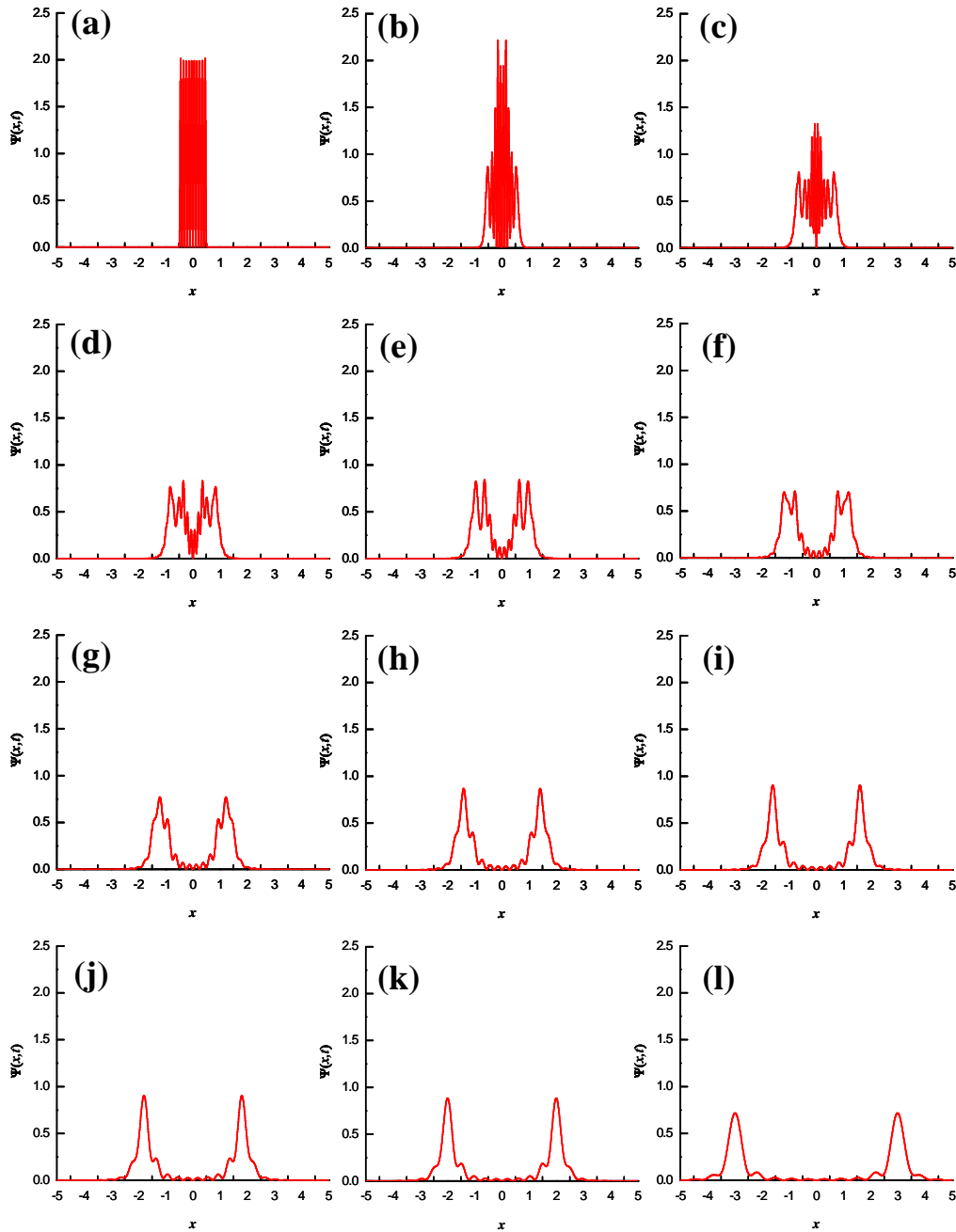


Fig. 4.1-1. (a)-(k) Intensity plots of $\psi^S(x,t;10)$ at $t = 0T - T$, respectively, with equal time interval $\Delta t = 0.1T$. (l) Intensity plots of $\psi_{10}(x,t)$ at $t = 1.5T$. The intensity pattern preserves its shape after $t = 1.5T$.

4.2 Transient Dynamics of Coherent Waves Released from Quantum Billiard

In Sec. 4.1 we have discussed the time evolution of a stationary wave function abruptly released from 1-D infinite potential well and similar problem will be extended to 2-D square billiards in this section.

The 2-D square billiard is one of the simplest billiards that is completely integrable in classical mechanics [Wier01, CHL02]. The quantum eigenstates $\psi_{n_1, n_2}(x, y)$ for the vertices are at $(\pm a/2, \pm a/2)$ and $(\pm a/2, \mp a/2)$ are given by

$$\psi_{n_1, n_2}(x, y) = (2/a) \sin[k_{n_1}(x + a/2)] \sin[k_{n_2}(y + a/2)], \quad (4.2.1)$$

where $k_n = n\pi/a$ ($n=1,2,3,\dots$) and a is the length of the square boundary. Extending Eq. (4.1.3) to 2D, the free time evolution of the eigenstates $\psi_{n_1, n_2}(x, y)$ suddenly released at time $t=0$ is given by

$$\psi_{n_1, n_2}(x, y, t) = \frac{m}{2\pi i \hbar t} \times \int_{-a/2}^{a/2} \int_{-a/2}^{a/2} \exp\left[\frac{im[(x-x')^2 + (y-y')^2]}{2\hbar t}\right] \psi_{n_1, n_2}(x', y') dx' dy' \quad (4.2.2)$$

The wave function $\psi_{n_1, n_2}(x, y, t)$ is just a 2-D extension of Eq. (4.1.4)

$$\psi_{n_1, n_2}(x, y, t) = \frac{e^{-\frac{i}{\hbar} E_{n_1, n_2} t}}{4i^3 a} \left[G(x, t; k_{n_1}, a) - G(x, t; -k_{n_1}, a) \right] \times \left[G(y, t; k_{n_2}, a) - G(y, t; -k_{n_2}, a) \right] \quad (4.2.3)$$

Ch4 Transient Dynamics of Coherent Waves Released from Quantum Billiard:
Analogous Studies on the Propagation of Lasing Modes Emitted from VCSELs

, where $E_{n_1, n_2} = \hbar^2(k_{n_1}^2 + k_{n_2}^2)/(2m)$ and $G(x, t; k_n, a)$, $F(\xi)$, and $\xi(x, t; k)$ are the same as those have been defined in last section.

Fig. 4.2-1(a)-(i) depict the numerical results calculated with Eq. (4.2.3) and the parameters of $(n_1, n_2) = (15, 15)$ to illustrate the wave patterns $|\psi_{n_1, n_2}(x, y, t)|^2$ at $t = 0T$, $0.1T$, $0.2T$, $0.3T$, $0.4T$, $0.5T$, $1.0T$, $2.0T$, and ∞ , respectively, where T defined as $T = 2ma/\hbar k_{n_1}$ corresponds to the roundtrip time of the wave in the x -direction. In these presentations, the spatial range S of these figures varies with t in the relation of $S = a + 2\frac{\hbar k_{15}}{m}t$ to fit the dimension of the patterns. The time-evolution wave distributions clearly exhibit strong interference patterns in the time interval between $0.1T$ and T . Note that the wave function $\psi_{n_1, n_2}(x, y, t)$ in an infinite time is just the Fourier transform of the initial wave function. In 2-D case, $\psi_{n_1, n_2}(x, y, t)$ with $t \gg ma^2/\hbar$ can be approximated to

$$\psi_{n_1, n_2}^F(x, y, t) = \psi_{n_1}^F(x, t)\psi_{n_2}^F(y, t). \quad (4.2.4)$$

Therefore, the four-lobed beam pattern in Fig. 4.2-1(i) reveals the momentum distribution.

The results of recent studies of open square quantum dots show that the wave functions localized on classical periodic orbits are not only the persistent states but also are associated with the striking phenomena of conductance fluctuations [AF99, ZB97, BAF+99]. As discussed in chapter 2, the wave functions associated with periodic orbits (p, q, ϕ) is analytically expressed as

$$\Psi_{N, M}^{p, q, \phi}(x, y) = \frac{1}{\sqrt{2^M}} \sum_{K=0}^{M-1} \sqrt{C_K^M} e^{iK\phi} \psi_{qN+pK, pN+q(M-1-K)}(x, y) \quad (4.2.5)$$

Note that the asymptotic property indicates that the coherent states $\Psi_{N, M}^{p, q, \phi}(x, y)$ are stationary states in the classical limit, i.e., $N \rightarrow \infty$. Since the Fresnel's transform is a linear operation, the free time evolution of the coherent states $\Psi_{N, M}^{p, q, \phi}(x, y)$

Ch4 Transient Dynamics of Coherent Waves Released from Quantum Billiard:
Analogous Studies on the Propagation of Lasing Modes Emitted from VCSELs

suddenly released at time $t = 0$ can be directly expressed as

$$\Psi_{N,M}^{p,q,\phi}(x, y, t) = \frac{1}{\sqrt{2^M}} \sum_{K=0}^{M-1} \sqrt{C_K^M} e^{iK\phi} \Psi_{qN+pK, pN+q(M-1-K)}(x, y, t). \quad (4.2.6)$$

Fig. 4.2-2 (a)-(i) presents the intensity distributions of $\Psi_{35,13}^{1,1,0.6\pi}(x, y, t)$ at $t = 0T$, $0.1T$, $0.2T$, $0.3T$, $0.4T$, $0.5T$, $1.0T$, $2.0T$, and ∞ , respectively. In this case $T = 2ma/\hbar k_{qN}$ corresponds to the round-trip time of the PO. This transient dynamics can be well connected with the classical picture of an orbiting particle suddenly released from a box. After the billiard is removed the particle may go in the four ways along the moving directions on the four segments of the PO. Besides, the probabilities of the four directions in which the particle may go are proportional to the length of the four segments and this fact can be observed from the asymmetry of the four spots in Fig. 4.2-2(i). Actually this picture nicely demonstrates the formation of directional emission in microdisk laser [GCN+98, LLHZ06, LLZ+07, NS97, NSC94, RTS+].

Note that the coherent states $\Psi_{N,M}^{p,q,\phi}(x, y)$ behave as the traveling waves in the billiards, while the superscar mode in VCSEL is associated with the standing-wave representation

$$C_{N,M}^{p,q,\phi}(x, y) = \left[\Psi_{N,M}^{p,q,\phi}(x, y) + \Psi_{N,M}^{p,q,-\phi}(x, y) \right] / \sqrt{2}. \quad (4.2.7)$$

As a result, the time evolution of the coherent states $C_{N,M}^{p,q,\phi}(x, y)$ suddenly released at time $t = 0$ can be given by

$$C_{N,M}^{p,q,\phi}(x, y, t) = \left[\Psi_{N,M}^{p,q,\phi}(x, y, t) + \Psi_{N,M}^{p,q,-\phi}(x, y, t) \right] / \sqrt{2}. \quad (4.2.8)$$

Figures 4.2(a)-(i) illustrate the numerical patterns for the wave patterns $\left| C_{N,M}^{p,q,\phi}(x, y, t) \right|^2$ with the parameters of $(p, q) = (1, 1)$, $(N, M) = (35, 13)$, and

Ch4 Transient Dynamics of Coherent Waves Released from Quantum Billiard:
Analogous Studies on the Propagation of Lasing Modes Emitted from VCSELs

$\phi = 0.6\pi$ at $t = 0T, 0.1T, 0.2T, 0.3T, 0.4T, 0.7T, 1.0T, 2.0T$, and ∞ , respectively. It can be seen that the transient dynamics of the coherent state displays not only the feature of classical flow but also the salient interference patterns, especially in the regime of $t < T$. From Eq. (4.2.4) we can figure out that $C_{N,M}^{p,q,\phi}(x, y, \infty)$ is also purely real or imaginary.

In contrast to the eigenstate $\psi_{n_1, n_2}(x, y)$ and superscar $\Psi_{N,M}^{p,q,\phi}(x, y)$, the third type of wave function to be concerned is the chaotic wave function $\psi_{chaos}(x, y)$ that presents an irregular pattern. It has been shown that the universal features of stationary chaotic wave functions in quantum billiards can be manifested with a superposition of plane waves of fixed wave-vector magnitude with random amplitude, phase, and direction [Berr77]. As revealed in Sec. 2.3, the standing-wave chaotic wave functions in a square-shaped quantum billiard can be described as

$$\psi_{chaos}(x, y) = \sum_{n_1} \sum_{n_2} C_{n_1, n_2} \psi_{n_1, n_2}(x, y) \quad (4.2.9)$$

, where the eigenstates $\psi_{n_1, n_2}(x, y)$ in the summation are subject to the condition that the values $\sqrt{k_{n_1}^2 + k_{n_2}^2}$ are nearly constant and the phase factors C_{n_1, n_2} are random. With the superposition principle, the free time evolution of the chaotic wave $\Psi(x, y)$ is then given by $\psi_{chaos}(x, y, t) = \sum_{n_1, n_2} C_{n_1, n_2} \psi_{n_1, n_2}(x, y, t)$. To connect with our experiment, we demonstrate this transient dynamics by a chaotic mode reconstructed from experimental result shown in next section. With the expansion coefficients C_{n_1, n_2} found by the same method as that used in Sec. 3.4, we display the intensity patterns of $\psi_{chaos}(x, y, t)$ at $t = 0T, 0.1T, 0.2T, 0.4T, 0.55T, 0.8T, 1.5T, 3.0T$, and ∞ in Fig. 4.2-4(a)-(i), respectively. Unlike the regular wave functions (shown in Figures 4.2-1, 4.2-2, and 4.2-3) exhibiting high directionality, the chaotic patterns at time interval of $0.1 < t < 1T$ display a striking feature of random branching behavior with the appearance of intricate interference fringes.

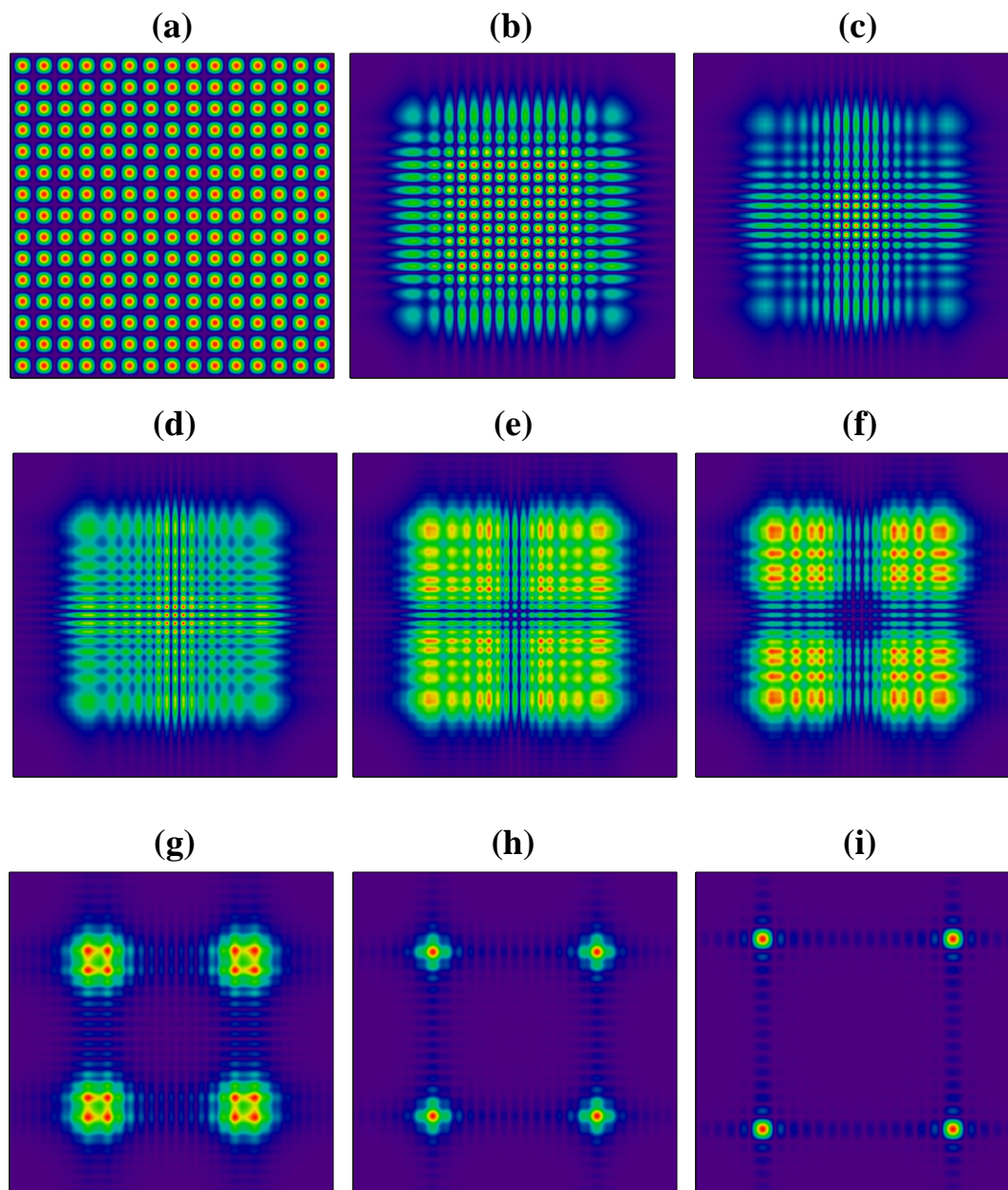


Fig. 4.2-1. Numerical patterns to illustrate the wave patterns $|\psi_{15,15}(x, y, t)|^2$ at $t =$ (a) $0T$, (b) $0.1T$, (c) $0.2T$, (d) $0.3T$, (e) $0.4T$, (f) $0.5T$, (g) $1.0T$, (h) $2.0T$, and (i) ∞ .

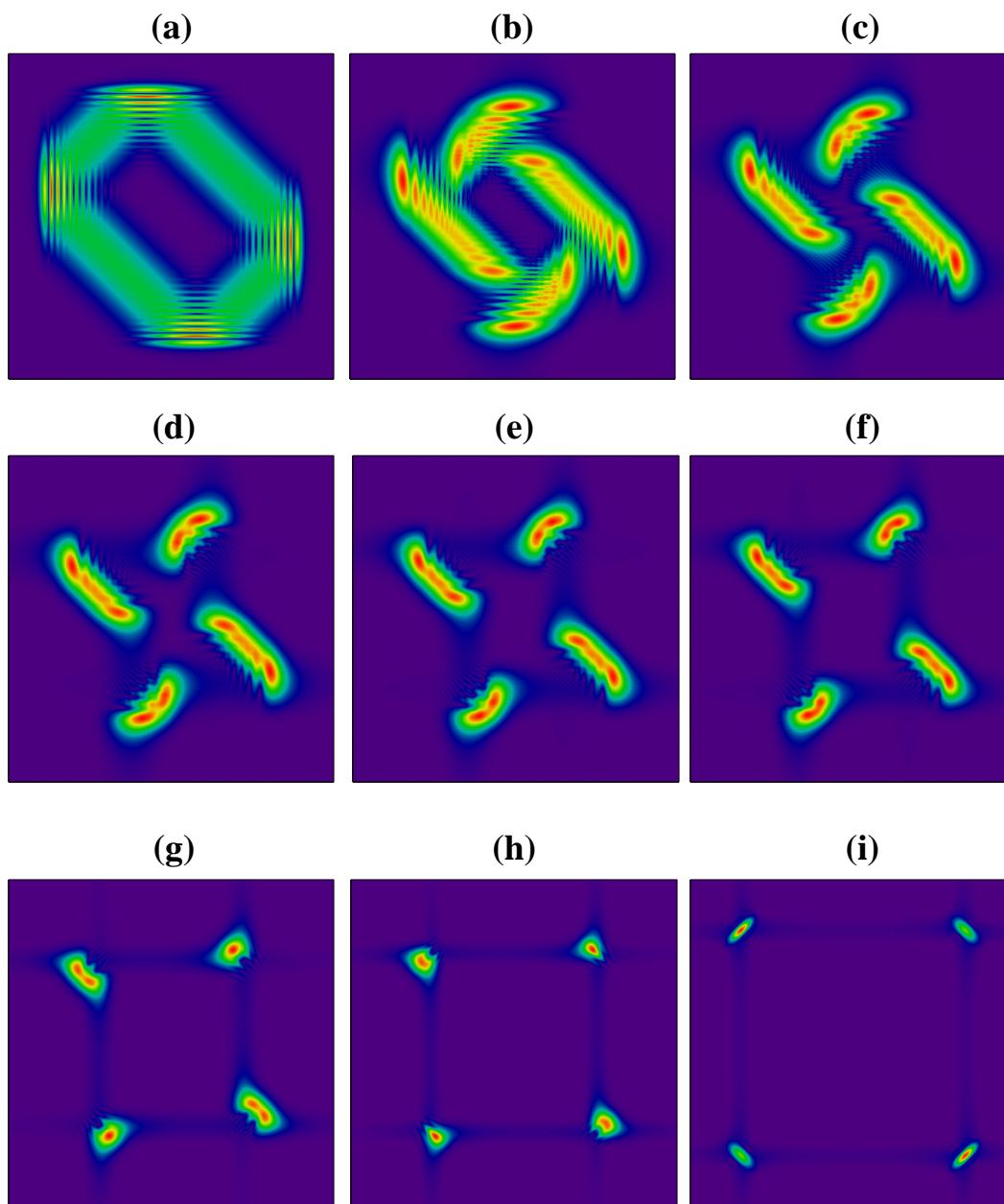


Fig. 4.2-2. Numerical patterns to illustrate the wave patterns $|\Psi_{35,13}^{1,1,0,6}(x, y, t)|^2$ at $t =$ (a) $0T$, (b) $0.1T$, (c) $0.2T$, (d) $0.3T$, (e) $0.4T$, (f) $0.5T$, (g) $1.0T$, (h) $2.0T$, and (i) ∞ .

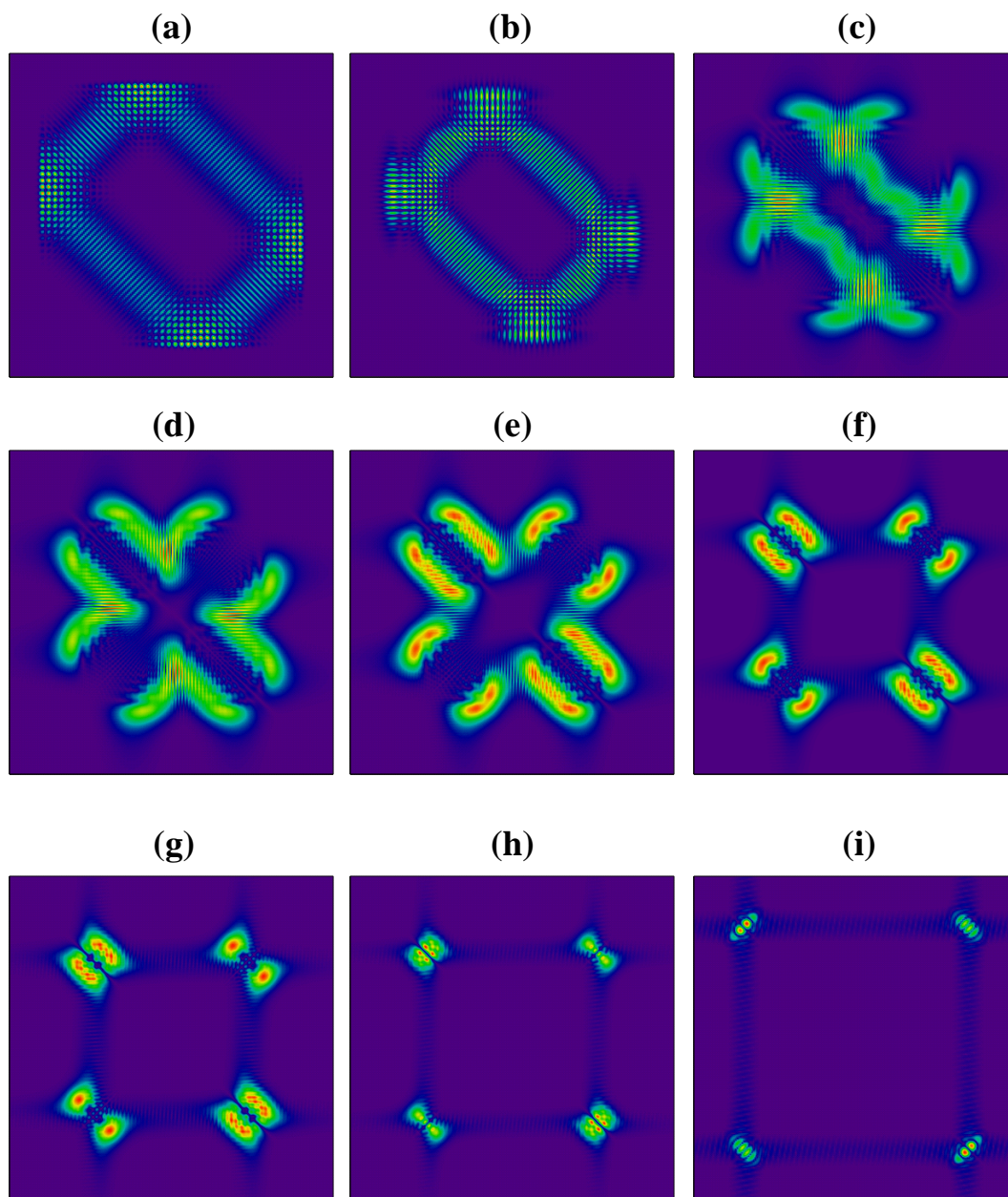


Fig. 4.2-3. Numerical patterns to illustrate the wave patterns $\left| C_{35,13}^{1,0,6}(x, y, t) \right|^2$ at $t =$ (a) $0T$, (b) $0.1T$, (c) $0.2T$, (d) $0.3T$, (e) $0.4T$, (f) $0.7T$, (g) $1.0T$, (h) $2.0T$, and (i) ∞ .

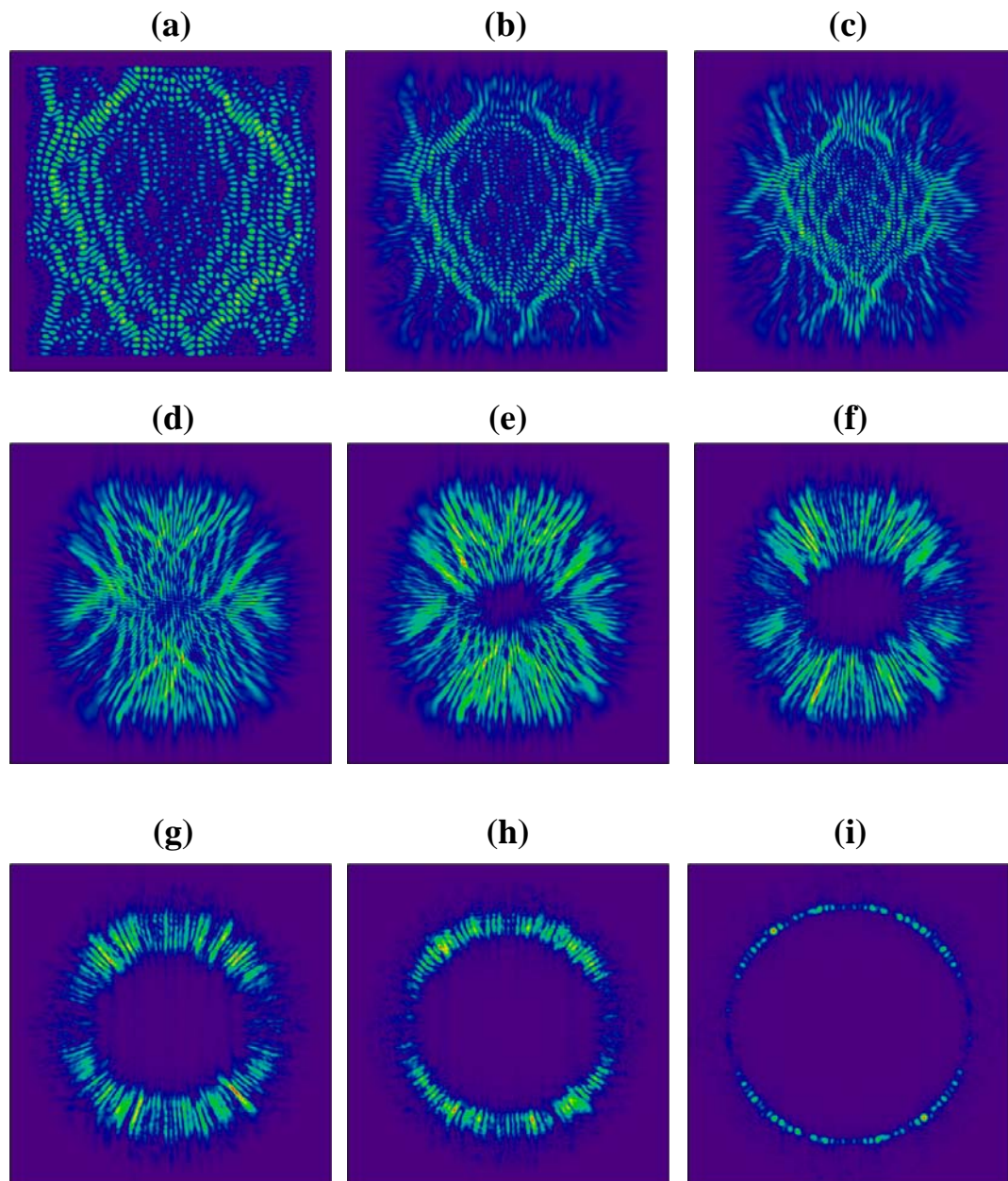


Fig. 4.2-4. Numerical patterns to illustrate the wave patterns $|\psi_{chaos}(x, y, t)|^2$ at $t =$ (a) $0T$, (b) $0.1T$, (c) $0.2T$, (d) $0.4T$, (e) $0.55T$, (f) $0.8T$, (g) $1.5T$, (h) $3.0T$, and (i) ∞ .

4.3 Analogous Observations on Coherent Waves Released from Quantum Billiard by Free-Space Propagating Transverse Modes of VCSELs

The time evolutions of coherent waves released from quantum billiards have been shown in Sec. 4.2. Our theoretical analysis can provide useful information for developing ultra-fast semiconductor device. However, the transient dynamics are very difficult to be experimentally observed. In this section, we utilize the similarity between paraxial optics and 2-D non-relativistic quantum mechanics to analogously observe the time evolutions of coherent waves released from quantum billiards by free-space propagation of transverse modes of VCSELs.

For a time-harmonic electromagnetic wave in free space, the phasor amplitude of the emission field distribution $E(x, y, z)$ would obey Helmholtz equation

$$\nabla^2 E(x, y, z) + k^2 E(x, y, z) = 0 \quad (4.3.1)$$

, where k is the wave number. Since the vertical emission through the top DBR represents the coupling of the wave field from the inside cavity to the outside environment, the phasor amplitude $E(x, y, z)$ of a light beam satisfies the paraxial approximation

$$E(x, y, z) = u(x, y, z) e^{-ikz} \quad (4.3.2)$$

, where $u(x, y, z)$ is the amplitude distribution. Substituting Eq. (4.3.2) into Eq. (4.3.1), we can find that the amplitude distribution $u(x, y, z)$ satisfies the paraxial wave equation [Haus84]

Ch4 Transient Dynamics of Coherent Waves Released from Quantum Billiard:
Analogous Studies on the Propagation of Lasing Modes Emitted from VCSELs

$$i \frac{\partial}{\partial z} u(x, y, z) = -\frac{1}{2k} \nabla_t^2 u(x, y, z) \quad (4.3.3)$$

, where $\nabla_t^2 = \partial^2 / \partial x^2 + \partial^2 / \partial y^2$ is the Laplacian operator for the transverse coordinate. This paraxial wave equation completely has the same mathematical form as Schrödinger equation (Eq (4.1.1)) for 2-D systems with the analogies $t \leftrightarrow z$ and $m/\hbar \leftrightarrow k$. Hence, the amplitude distribution $u(x, y, z)$ can be shown to relate with the amplitude distribution at $z=0$ by the similar process from Eq. (A.3) to Eq. (A.9)

$$u(x, y, z) = \frac{-i}{2\pi} \frac{k}{z} \iint u(x, y, 0) \cdot e^{i \frac{k}{2z} [(x-x_0)^2 + (y-y_0)^2]} dx_0 dy_0. \quad (4.3.4)$$

Combining Equations (4.3.2) and (4.3.4), the phasor amplitude $E(x, y, z)$ can be shown to relate with $E(x, y, 0)$ by the Fresnel transform [Good05]

$$E(x, y, z) = \frac{e^{ikz}}{i\lambda z} \iint E(x, y, 0) \cdot e^{i \frac{k}{2z} [(x-x_0)^2 + (y-y_0)^2]} dx_0 dy_0 \quad (4.3.5)$$

In brief, the time evolution of a 2D quantum state is equivalent to the Fresnel transformation of a near-field optical wave. For VCSELs, in chapter3 we have demonstrated that the near-field transverse modes $E(x, y, 0)$ are analogous to the wave functions of quantum billiard with the same geometry. Therefore, the free space propagation of coherent modes emitted from VCSELs is analogous to the time evolution of quantum-billiard wave functions.

The experimental set up is similar to that described in Sec. 3.2. The device first used is a square-shaped VCSEL with aperture size to be about $40 \times 40 \mu m^2$. It was operated at a temperature of $T = 220 K$ and near threshold current of $I = 38.3 mA$ to generate a linearly polarized superscar mode similar to that shown in Fig. 4.2-3(a),

Ch4 Transient Dynamics of Coherent Waves Released from Quantum Billiard:
Analogous Studies on the Propagation of Lasing Modes Emitted from VCSELs

as shown in Fig. 4.3-1(a). The measurement of the optical spectrum indicates that the pattern is a single mode with its wavelength to be 804.06 nm. To observe propagation from near field to far field, we defocus the large-NA objective lens by translating the stage. Figures 4.3-1(b)-1(g) are the experimental transverse patterns observed at propagation distances of $0.1 z_d$, $0.2 z_d$, $0.3 z_d$, $0.4 z_d$, $0.7 z_d$, $1.0 z_d$, and $2.0 z_d$, respectively, where $z_d = 2ak_z / k_t$ is the characteristic length that is analogous to characteristic time T in Sec. 4.2. The transverse and longitudinal wave vectors, k_t and k_z , can be found by the half angle of diffraction α . In this experiment the angle α is measured to be 24° and such that z_d can be evaluated to be about $72 \mu m$. The far-field pattern was directly projected to a paper screen at a distance of $\sim 20 cm$ from the laser device and the scattered light was captured by a digital camera. Figure 4.3-1(f) depicts the far-field pattern with the central bright region to be the background luminescence. The good agreement between Figs. 4.3-1 and 4.2-3 validates that the free space propagation of coherent modes emitted from VCSELs can be employed as an analogous observation of the time evolution of quantum-billiard wave functions.

Next we exploit a deformed-square-shaped VCSEL with a ripple boundary to experimentally study the transient dynamics of the wave functions released from 2D chaotic billiard systems. The same experimental method was applied to this chaotic-shaped VCSEL to obtain a linearly polarized chaotic wave state, as shown in Fig. 4.3-2(a), with the operating temperature at $T = 295K$ and threshold current $I = 56.0mA$. The measurement of the optical spectrum also shows that the pattern is a single mode with its wavelength to be 827.08 nm. Figures 4.3-2(b)-(g) display the experimental transverse patterns observed at propagation distances of $0.1 z_d$, $0.2 z_d$, $0.4 z_d$, $0.55 z_d$, $0.8 z_d$, $1.5 z_d$, and $3.0 z_d$, respectively. The half angle of diffraction was measured to be 30° and z_d is about $138 \mu m$. In fact, the experimental near-field pattern has been employed to study the transient dynamics of a suddenly released chaotic wave in Sec. 4.2. Comparing Figs. 4.3-2 and 4.3-4, it

Ch4 Transient Dynamics of Coherent Waves Released from Quantum Billiard:
Analogous Studies on the Propagation of Lasing Modes Emitted from VCSELs

can be seen that our reconstruction of chaotic modes not only match the experimental results in near field but for the whole propagation process. This agreement further confirms the method for reconstructing the chaotic mode and the presented analysis.



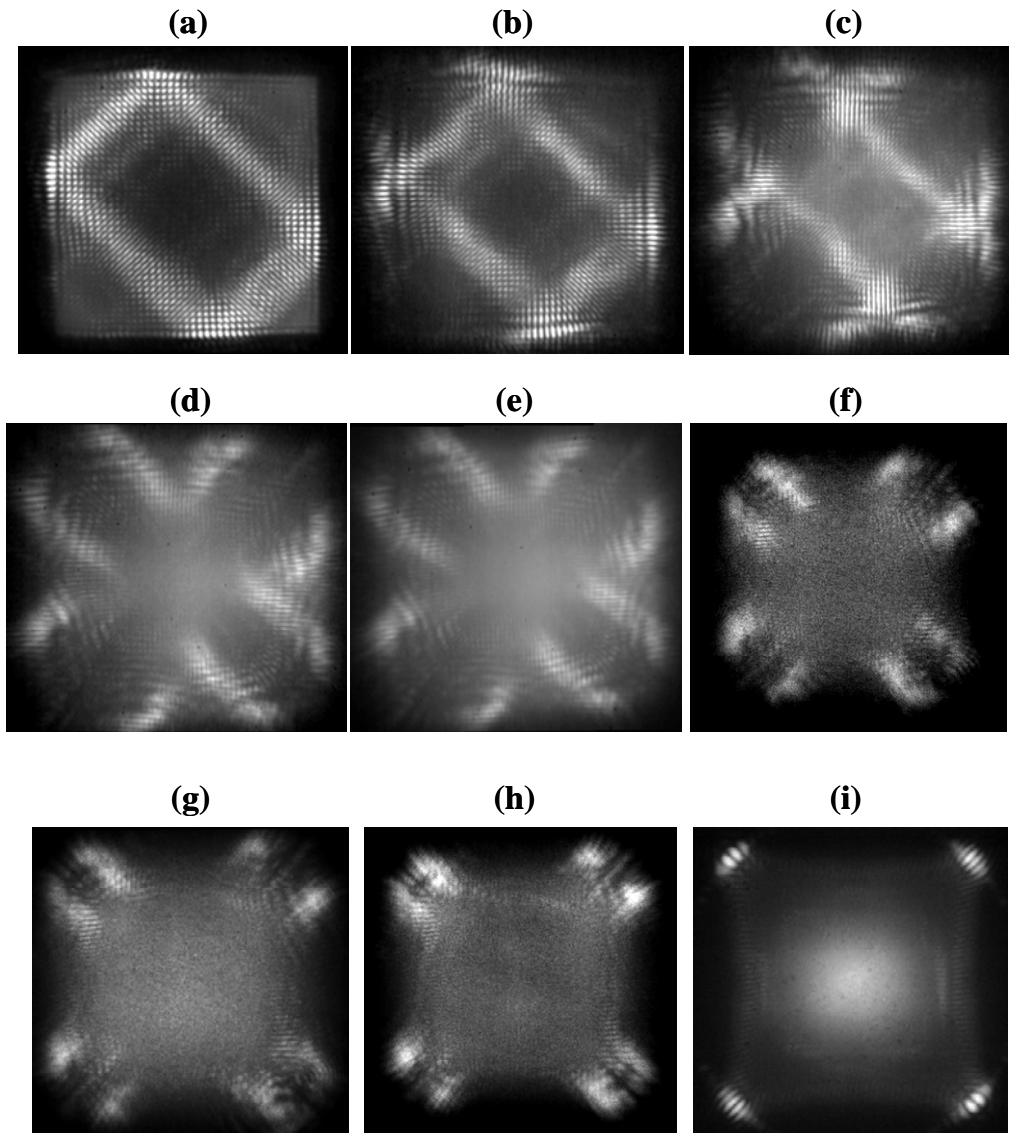


Fig. 4.3-1. Experimental patterns of a superscar mode with propagation distance at $z =$ (a) $0z_d$, (b) $0.1z_d$, (c) $0.2z_d$, (d) $0.3z_d$, (e) $0.4z_d$, (f) $0.7z_d$, (g) $1.0z_d$, (h) $2.0z_d$, and (i) 20cm , where $z_d \sim 72\mu\text{m}$.

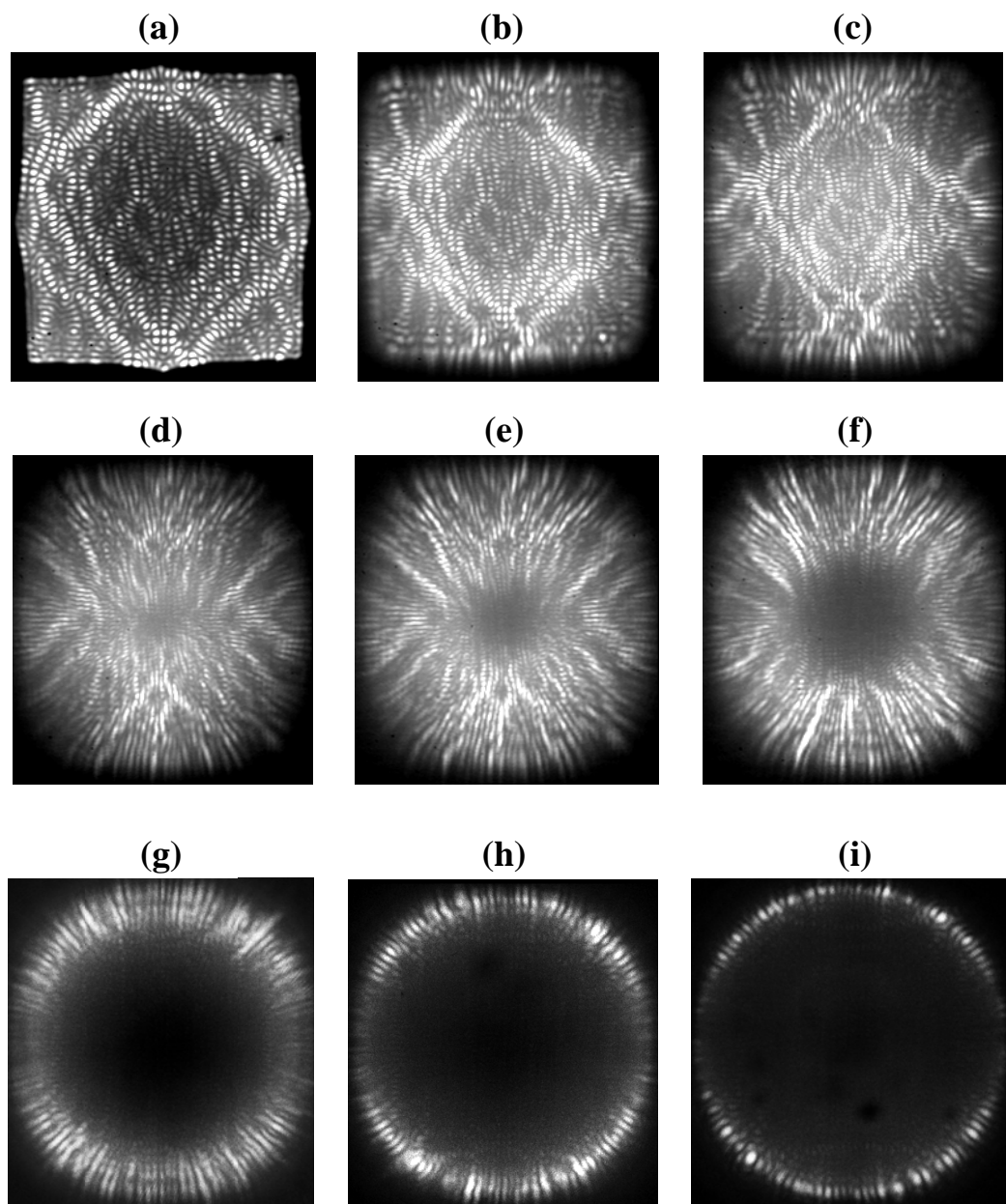


Fig. 4.3-2. Experimental patterns of a chaotic mode with propagation distance at $z =$ (a) $0z_d$, (b) $0.1z_d$, (c) $0.2z_d$, (d) $0.4z_d$, (e) $0.55z_d$, (f) $0.8z_d$, (g) $1.5z_d$, (h) $3.0z_d$, and (i) 20cm , where $z_d \sim 138\mu\text{m}$.

4.4 Probability Current and Angular Momentum Densities of Coherent Waves Released from Quantum Billiard: Optical Vortices Generated by VCSEL

In Sec. 4.1 we first review the free time evolution of a sine function with suddenly removal of the 1-D infinite potential well. Next, the problem is extended to the transient dynamics of various types of coherent waves released from square billiard in second section. In 1-D systems the current flow is monotonous since it is linear and can only flow in two direction, $+x$ or $-x$ axes. However, the 2-D probability current density becomes much complicated because it forms a vector field. As indicated in Sec. 1.3, 2-D current field has three kinds of vector singularities, sink and source, saddle, and vortex, which correspond to the phase minima and maxima, saddle, and singularity, of the wave function. Moreover, angular momentum, which is an important physical quantity both in classical- [GPS02] and quantum-mechanical [BVD65] systems, will naturally arise due to the 2D current flow.

On the other hand, the analogy between transverse modes emitted from VCSEL and wave functions released from quantum billiards has been established and experimentally verified in Sec. 4.3. However, the analogies between paraxial optics and 2-D quantum system are not only restricted to the correspondence between amplitude distribution and wave function. For a non-stationary state, the probability current is defined by the continuity equation of probability density

$$\nabla \cdot \vec{j}(x, y, t) = -\frac{\partial \rho(x, y, t)}{\partial t} \quad (4.4.1)$$

, where $\rho(x, y, t) = |\psi(x, y, t)|^2$. In terms of $\psi(x, y, t)$, $\vec{j}(x, y, t)$ is expressed as

$$\vec{j}(x, y, t) = \frac{\hbar}{m} \text{Im}[\psi^*(x, y, t) \nabla \psi(x, y, t)]. \quad (4.4.2)$$

On the other hand, the transverse linear momentum density of a linearly polarized quasi-TEM wave is related to the amplitude distribution of electric field $u(x, y, z)$ by [ZB07] (See Appendix B for a detailed discussion.)

$$\vec{p}_\perp(x, y, z) = \frac{\epsilon_0}{2\omega} \text{Im}[u^*(x, y, z) \nabla_\perp u(x, y, z)]. \quad (4.4.3)$$

Since the wave function $\psi(x, y, t)$ is analogous to amplitude distribution $u(x, y, z)$, the probability current density $\vec{j}(x, y, t)$ has the similar behavior as the optical momentum density $\vec{p}_\perp(x, y, z)$. Moreover, the orbital angular momentum (OAM) density of the two systems expressed by

$$\vec{l}(x, y, t) = m(\vec{r} - \vec{r}_0) \times \vec{j}(x, y, t) \quad \text{and} \quad \vec{l}_z(x, y, z) = (\vec{r}_\perp - \vec{r}_0) \times \vec{p}_\perp(x, y, z) \quad (4.4.4)$$

, respectively, are also in the same mathematical form.

Recent years have been increased attention being given to optical OAM [ABSW92, FAAP08] for its wide applications in atom trapping [KTS+97], optical tweezers [MRS+99], and optical spanner [SADP97]. Furthermore, OAM of light beam can be encoded as qudit and has great potential applications in quantum information [MVWZ01]. However, the OAM carried by the coherent waves emitted from VCSELs has never been investigated. In this section our aim is to analyze the linear and angular momentum densities of the light beam emitted from VCSELs by analogously calculating the probability current and angular momentum densities of coherent waves released from quantum billiard.

We have to first deal with $\nabla \psi$ in order to obtain \vec{j} . By definition, $\nabla \psi$ is written as

Ch4 Transient Dynamics of Coherent Waves Released from Quantum Billiard:
Analogous Studies on the Propagation of Lasing Modes Emitted from VCSELs

$$\nabla \psi(x, y, t) = \frac{\partial}{\partial x} \psi(x, y, t) \hat{a}_x + \frac{\partial}{\partial y} \psi(x, y, t) \hat{a}_y \quad (4.4.5)$$

Consider the eigenstate of square billiard Eq. (4.2.3), we have

$$\begin{aligned} \frac{\partial}{\partial x} \psi_{n_1, n_2}(x, y, t) = & \frac{e^{-\frac{i}{\hbar} E_{n_1, n_2} t}}{4i^3 a} \left[H(x, t; k_{n_1}, a) - H(x, t; -k_{n_1}, a) \right] \\ & \times \left[G(y, t; k_{n_2}, a) - G(y, t; -k_{n_2}, a) \right] \end{aligned} \quad (4.4.6)$$

and

$$\begin{aligned} \frac{\partial}{\partial y} \psi_{n_1, n_2}(x, y, t) = & \frac{e^{-\frac{i}{\hbar} E_{n_1, n_2} t}}{4i^3 a} \left[G(x, t; k_{n_1}, a) - G(x, t; -k_{n_1}, a) \right] \\ & \times \left[H(y, t; k_{n_2}, a) - H(y, t; -k_{n_2}, a) \right] \end{aligned} \quad (4.4.7)$$

, where $H(x, t; k_{n_1}, a)$ is given by

$$\begin{aligned} H(x, t; k_{n_1}, a) = & \sqrt{\frac{m}{\pi \hbar t}} e^{ik_{n_1}(x+a/2)} \left[e^{i\frac{\pi}{2}\xi^2(x+\frac{a}{2}, t; k_{n_1})} - e^{i\frac{\pi}{2}\xi^2(x-\frac{a}{2}, t; k_{n_1})} \right] \\ & + ik_{n_1} G(x, t; k_{n_1}, a) \end{aligned} \quad (4.4.8)$$

Hence, the probability current density of a eigenstate released from square billiard can be expressed as

$$\vec{j}_{n_1, n_2}(x, y, t) = \frac{\hbar}{m} \text{Im}[\psi_{n_1, n_2}^*(x, y, t) \nabla \psi_{n_1, n_2}(x, y, t)] \quad (4.4.9)$$

Fig. 4.4-1 (a)-(f) depict the vector plots of $\vec{j}_{15,15}(x, y, t)$ with corresponding $\psi_{15,15}(x, y, t)$ as background at $t = 0.1T$, $0.2T$, $0.3T$, $0.4T$, $0.5T$, and $1.0T$, respectively. In the vector plot, the arrows point to the directions of the flow on that

position and the length of the arrows is proportional to the strength of the flow. From equations (4.2.1) and (4.2.4) we can know that the wave function $\psi_{15,15}(x, y, t)$ is purely real at $t=0$ and $t=\infty$ such that we have $\vec{j}_{15,15}(x, y, 0) = 0$ and $\vec{j}_{15,15}(x, y, \infty) = 0$. It can be clearly seen that the motion of the intensity pattern is led by the current flow.

For the eigenstate released from the square billiard, the OAM density is given by $\vec{l}_{n_1, n_2}(x, y, t) = m(\vec{r} - \vec{r}_0) \times \vec{j}_{n_1, n_2}(x, y, t)$. Fig. 4.4-2 (a)-(f) show the density plots of $\vec{l}_{15,15}(x, y, t)$ at $t = 0.1T$, $0.2T$, $0.3T$, $0.4T$, $0.5T$, and $1.0T$, respectively. The scale of the color-coded contour plots are given aside with unit in (\hbar / S^2) , where $S = a + 2 \frac{\hbar k_{n_1}}{m} t$ is the time-dependent spatial range for calculations. The positive (negative) value of angular momentum indicates a counter-clockwise (clockwise) rotation with rotation axis points to $+\hat{a}_z$. We can see that the distribution of OAM is always anti-symmetric and such that the net OAM computed by

$$\langle l_{n_1, n_2}(x, y, t) \rangle = \iint |\vec{l}_{n_1, n_2}(x, y, t)| dx dy \quad (4.4.9)$$

is always zero for any t . A further analysis indicates that the distribution of OAM density depends on the choice of rotation axis, but the net value $\langle l_{n_1, n_2}(x, y, t) \rangle$ does not. The OAM has such an axis-independent net value was said to be intrinsic [CZDV06]. The OAM can be validated to be intrinsic by verifying the relation

$$\iint \vec{j}(x, y, t) dx dy = 0. \quad (4.4.10)$$

One can calculate the OAM spectrum [MTTT02] to further analyze an intrinsic OAM density. The OAM spectrum is defined as follow

$$P(\ell) = \int |a_\ell(r, t)|^2 r dr \quad (4.4.11)$$

, where

$$a_\ell(r, t) = \frac{1}{\sqrt{2\pi}} \int_0^{2\pi} \psi(x, y, t) e^{-i\ell\phi} d\phi. \quad (4.4.12)$$

with $r = \sqrt{x^2 + y^2}$ and $\phi = \tan^{-1}(y/x)$. The wave function should be normalized such that $\sum_{\ell=-\infty}^{\infty} P(\ell) = 1$. The OAM spectrum is experimental measurable [GCP+04]

and has great potential applications in quantum information [MVWZ01]. Although the distribution of OAM density depends on t (or z for a light beam), the OAM is an invariance of t (or z) [MTTT02]. Fig. 4.4-3 shows the OAM spectrum of the eigenstate $\psi_{15,15}(x, y, t)$. Since the eigenstate $\psi_{15,15}(x, y)$ has a $\pi/2$ symmetry (i. e. the wave-function distributions in the four quadrants are identical), the OAM spectrum only has values as ℓ equals to the multiples of four. The net OAM can be alternatively calculated from OAM spectrum by

$$\langle l_{n_1, n_2}(x, y, t) \rangle = \bar{\ell} \hbar = \hbar \sum_{\ell=-\infty}^{\infty} P(\ell) \ell. \quad (4.4.13)$$

Obviously, we have $\bar{\ell} = 0$ for the symmetric OAM spectrum and this result is consistent with the value calculated by Eq. (4.4.9). The OAM spectra of all eigenstates of square billiard are symmetrically distributed and have their peaks centered at $\ell = 0$. Hence, all eigenstates have their net OAM to be zero. As revealed by Zambrini and Barnett, it is more accurate to say that the OAM with axis-independent net value but axis-dependent density distribution is quasi-intrinsic [ZB06]. The indicator of the relevance of the position of rotation axis for calculating OAM density is the dimensionless variance of OAM spectrum [ZB06], which is given by

$$V = \sum_{\ell=-\infty}^{\infty} P(\ell) (\ell - \bar{\ell})^2 = 0. \quad (4.4.14)$$

For the OAM spectrum of eigenstate $\psi_{15,15}(x, y, t)$, the variance V is evaluated to be 158.7. Although the eigenstate $\psi_{15,15}(x, y, t)$ do not exist in our experiments, our analysis may provide useful information for the chessboard-like patterns emitted from phase-coupled VCSEL arrays or photonic resonator crystals [PKM02].

The probability current of coherent state $\Psi_{N,M}^{p,q,\phi}(x, y, t)$ can be expressed as

$$\bar{J}_{N,M}^{p,q,\phi}(x, y, t) = \frac{\hbar}{m} \text{Im}[\Psi_{N,M}^{*p,q,\phi}(x, y, t) \nabla \Psi_{N,M}^{p,q,\phi}(x, y, t)] \quad (4.4.15)$$

Since the partial differential operator is linear, we have

$$\frac{\partial \Psi_{N,M}^{p,q,\phi}(x, y, t)}{\partial x} = \frac{1}{\sqrt{2^M}} \sum_{K=0}^{M-1} \sqrt{C_K^M} e^{iK\phi} \frac{\partial}{\partial x} \psi_{qN+pK, pN+q(M-1-K)}(x, y, t) \quad (4.4.16)$$

and

$$\frac{\partial \Psi_{N,M}^{p,q,\phi}(x, y, t)}{\partial y} = \frac{1}{\sqrt{2^M}} \sum_{K=0}^{M-1} \sqrt{C_K^M} e^{iK\phi} \frac{\partial}{\partial y} \psi_{qN+pK, pN+q(M-1-K)}(x, y, t). \quad (4.4.17)$$

The vector plots of $\bar{J}_{N,M}^{p,q,\phi}(x, y, t)$ with parameters $N = 35$, $M = 6$, and $(p, q, \phi) = (1, 1, 0.6\pi)$ at $t = 0.1T$, $0.2T$, $0.3T$, $0.4T$, $0.5T$, and $1.0T$ are presented in Fig. 4.4-4 (a)-(f), respectively. As expected, the current flux displays high directionality indicated by the motion classical particle. The OAM density distribution of a coherent state is much interesting and can be easily expected from the distribution of current density. The OAM density of superscar can be expressed as

$$\bar{L}_{N,M}^{p,q,\phi}(x, y, t) = m(\bar{r} - \bar{r}_0) \times \bar{J}_{N,M}^{p,q,\phi}(x, y, t). \quad (4.4.18)$$

The density plots of $\bar{L}_{35,13}^{1,1,0.6\pi}(x, y, t)$ at $t = 0.1T$, $0.2T$, $0.3T$, $0.4T$, $0.5T$, and $1.0T$ are presented in Fig. 4.4-5 (a)-(f), respectively. In this case the OAM is still intrinsic and has a large net value $\langle L_{35,13}^{1,1,0.6\pi}(x, y, t) \rangle$ numerically computed to be about $-60\hbar$. It can be seen from the OAM spectrum illustrated in Fig. 4.4-6 that the coherent state $\Psi_{35,13}^{1,1,0.6\pi}(x, y, t)$ has only negative OAM component. Besides, the peak does not center at $\ell = 0$ but shifts to $\ell = -62$. The net OAM calculated from OAM spectrum has the same value as $\langle L_{35,13}^{1,1,0.6\pi}(x, y, t) \rangle$. The OAM variance is evaluated to be 255.7.

It can be seen that there are two small peaks embedded in a big peak. To further understand this phenomenon, we show the OAM spectra of the coherent states $\Psi_{35,13}^{1,1,\phi}(x, y, t)$ with ϕ equals to 0, 0.25π , and 0.5π in Fig. 4.4-7(a')-(c'), respectively. We find that two opposite segments of the superscar will result in one peak in which the OAM spectrum only has values as ℓ is even because of the π symmetry. Since the PO has two pairs of opposite segments, the OAM spectrum generally has two peaks as shown in Fig. 4.4-7(b'). In the critical case of $\phi = 0$, the stationary coherent state becomes a standing wave and has its OAM spectrum to be even. As $\phi = \pi/2$, the two peaks completely overlap and the OAM spectrum only has values as ℓ equals to multiples of four due to the $\pi/2$ symmetry. Hence, there are actually only two partially overlapped peaks in the OAM spectrum shown in Fig. 4.4-6.

The predominant lasing modes in the broad-area square-shaped oxide-confined VCSEL are the superscar modes that are analogously interpreted by the standing-wave representation of stationary coherent state $C_{N,M}^{p,q,\phi}(x, y, t)$. Although $C_{N,M}^{p,q,\phi}(x, y, t)$ is purely real, it becomes complex as soon as the billiard is removed.

The probability current of $C_{N,M}^{p,q,\phi}(x, y, t)$ is given by

$$\bar{J}C_{N,M}^{p,q,\phi}(x, y, t) = \frac{\hbar}{m} \text{Im}[C_{N,M}^{p,q,\phi*}(x, y, t) \nabla C_{N,M}^{p,q,\phi}(x, y, t)] \quad (4.4.19)$$

, where

$$\nabla C_{N,M}^{p,q,\phi}(x, y, t) = \frac{1}{\sqrt{2}} \left[\nabla \Psi_{N,M}^{p,q,\phi}(x, y, t) + \nabla \Psi_{N,M}^{p,q,-\phi}(x, y, t) \right] . \quad (4.4.20)$$

Fig. 4.4-8 (a)-(f) illustrate the vector distributions of $\bar{J}C_{N,M}^{p,q,\phi}(x, y, t)$ at $t = 0.1T$, $0.2T$, $0.3T$, $0.4T$, $0.7T$, and $1.0T$, respectively. At $t = 0T$ the coherent state $C_{N,M}^{p,q,\phi}(x, y, t)$ is a standing wave that is composed by two completely overlapped traveling waves, one ($\Psi_{N,M}^{p,q,\phi}(x, y, t)$) rotates clockwise and the other ($\Psi_{N,M}^{p,q,-\phi}(x, y, t)$) counter-clockwise. Although the two components begin to split as the coherent state $C_{N,M}^{p,q,\phi}(x, y, t)$ is released, they still partially overlap in some regions. In these overlapped regions, the currents of the two traveling-wave components interfere and destroy each other. As the time $t \gg ma^2 / \hbar$, the two components start to merge.

On the other hand, the OAM density of $C_{N,M}^{p,q,\phi}(x, y, t)$ can be expressed as

$$\bar{L}C_{N,M}^{p,q,\phi}(x, y, t) = m(\bar{r} - \bar{r}_0) \times \bar{J}C_{N,M}^{p,q,\phi}(x, y, t) \quad (4.4.21)$$

Fig. 4.4-9 (a)-(f) depict the distribution of $|\bar{L}C_{35,13}^{1,1,0.6\pi}(x, y, t)|$ at $t = 0.1T$, $0.2T$, $0.3T$, $0.4T$, $0.7T$, and $1.0T$, respectively. Since $C_{N,M}^{p,q,\phi}(x, y, t)$ is composed by $\Psi_{N,M}^{p,q,\phi}(x, y, t)$ and $\Psi_{N,M}^{p,q,-\phi}(x, y, t)$, $|\bar{L}C_{35,13}^{1,1,0.6\pi}(x, y, t)|$ will naturally be anti-symmetrically distributed and has a zero net value. As shown in Fig. 4.4-10, the OAM spectrum of $C_{N,M}^{p,q,\phi}(x, y, t)$ is just a combination of OAM spectra of $\Psi_{N,M}^{p,q,\phi}(x, y, t)$ and $\Psi_{N,M}^{p,q,-\phi}(x, y, t)$. However, such a OAM spectrum had a variance

as large as 3718.

The zero net value and large variance of OAM make the lasing modes interpreted by $C_{N,M}^{p,q,\phi}(x,y,t)$ have less applications. However, Zou and Mathis recently proposed a scheme for OAM beam splitter to separate light beams with different OAM component [ZM05]. If such a device can be realized, we can employ it to decompose the standing-wave $C_{N,M}^{p,q,\phi}(x,y,t)$ into two traveling waves $\Psi_{N,M}^{p,q,\phi}(x,y,t)$ and $\Psi_{N,M}^{p,q,-\phi}(x,y,t)$. The light beam with their lasing mode interpreted by $\Psi_{N,M}^{p,q,\phi}(x,y,t)$ has its OAM as shown in Figs. 4.4-5 and 4.4-6 to be more convenient for applications.

In the above three regular cases, the probability currents all flow in definite directions. For the chaotic wave function $\psi_{chaos}(x,y,t)$, the current flux becomes much complicated. We first write down the expression of probability current

$$\vec{j}_{chaos}(x,y,t) = \frac{\hbar}{m} \text{Im}[\psi_{chaos}(x,y,t) \nabla \psi_{chaos}(x,y,t)] \quad (4.4.22)$$

By the principle of superposition, we have

$$\nabla \psi_{chaos}(x,y) = \sum_{n_1} \sum_{n_2} C_{n_1,n_2} \nabla \psi_{n_1,n_2}(x,y). \quad (4.4.23)$$

Fig. 4.4-11 (a)-(f) display the vector plots of $\vec{j}_{chaos}(x,y,t)$ at $t = 0.1T$, $0.2T$, $0.4T$, $0.55T$, $0.8T$, and $1.5T$, respectively. Unlike the regular current flows, the current vectors exhibit randomly distributed flux. In order to make a more explicit visualization of the current, the zoom-in views of three small regions of $\vec{j}_{chaos}(x,y,0.1T)$ are shown in Fig. 4.4-12 (b)-(d). Strikingly, several pronounced vortices are induced in the current flux as the chaotic wave function is released. Such discrete vortices have been widely observed in Bose-Einstein condensate [MAH+99], superfluid [MFDM03] and Type-II superconductor films [MFDM03].

The length of the vectors has been modified by setting $\vec{j}' = \vec{j} / |\vec{j}|^{0.9}$ to enhanced the vortex structures. As discussed in Sec. 1.3, the vortices in probability current essentially correspond to the phase singularities of the complex scalar field. In order to verify the vortices, we draw the contour plots of the phase

$$\theta(x, y, t) = \arg[\psi_{chaos}(x, y, t)] \quad (4.4.24)$$

and show them as backgrounds of the vector plots for a convenient comparison. The contour plot is color-coded with red and purple corresponding to 2π and 0 , respectively. The singularities are at the points where all colors get together. The white and black curves in the contour plots stand for the nodal lines for real and imaginary parts of wave function, respectively. By the definition, the intersections of white and black curves are singularities. This result can help us to find the singularities more quickly and accurately. The red squares and pink triangles point out the singularities with topological charges equal to $+1$ and -1 , respectively. It can be easily checked that the clockwise and counter-clockwise vortices are coincident with the positive and negative singularities. Besides, our analysis well demonstrates the sign rule that the nearest neighbor singularities on any contour of constant phase are required to have opposite signs [Freu95].

The minute feature of vortices and phase singularities in the small regions labeled by “1, 2, and 3” in Fig. 4.4-13(a) of $\vec{j}_{chaos}(x, y, 0.2T)$ are displayed in Fig. 4.4-14(b)-(d), respectively. From the figures, we can find that both the spatial density and size of vortices decreases as the distance from the origin increases. This result arises from the fact that all the currents flow out of originally-confined region in a radial way. Therefore, we suggest that the vortices are formed by interference of the many randomly-oriented currents that is still inside the originally-confined region. This phenomenon becomes more obvious as t increases. Fig. 4.4-14(b)-(d) depict the vector plots of $\vec{j}_{chaos}(x, y, 0.4T)$ in the small regions marked in Fig. 4.4-14(a). It can be seen that there is no vortex in the region shown in Fig. 4.4-14(d). As the wave completely leaves the originally-confined region, all currents are radially

flowing and the vortices become trivial.

For the chaotic wave function released from the billiard, the OAM density is calculated by

$$\bar{l}_{chaos}(x, y, t) = m(\bar{r} - \bar{r}_0) \times \bar{j}_{chaos}(x, y, t). \quad (4.3.21)$$

The density plots of $|\bar{l}_{chaos}(x, y, t)|$ at $t = 0.1T$, $0.2T$, $0.4T$, $0.55T$, $0.8T$, and $1.5T$ are illustrated in Fig. 4.4-15 (a)-(f), respectively. We can see that the chaotic wave function has very complicated OAM density. Such a complex OAM density is validated to be intrinsic and has a zero net value. Since the chaotic wave function $\psi_{chaos}(x, y, t)$ is composed by eigenstates with real expansion coefficient, the OAM spectrum of $\psi_{chaos}(x, y, t)$ is still symmetrically distributed as displayed in Fig. 4.4-16. Due to the intricacy of the OAM spectrum, the OAM variance of $\psi_{chaos}(x, y, t)$ has an extremely large value of 2576. As revealed by the Zambrini and Barnett, this large variance of OAM is probably resulted from the formation of off-axis vortices as those shown in Figs. 4.4-12, 4.4-13, and 4.4-14.

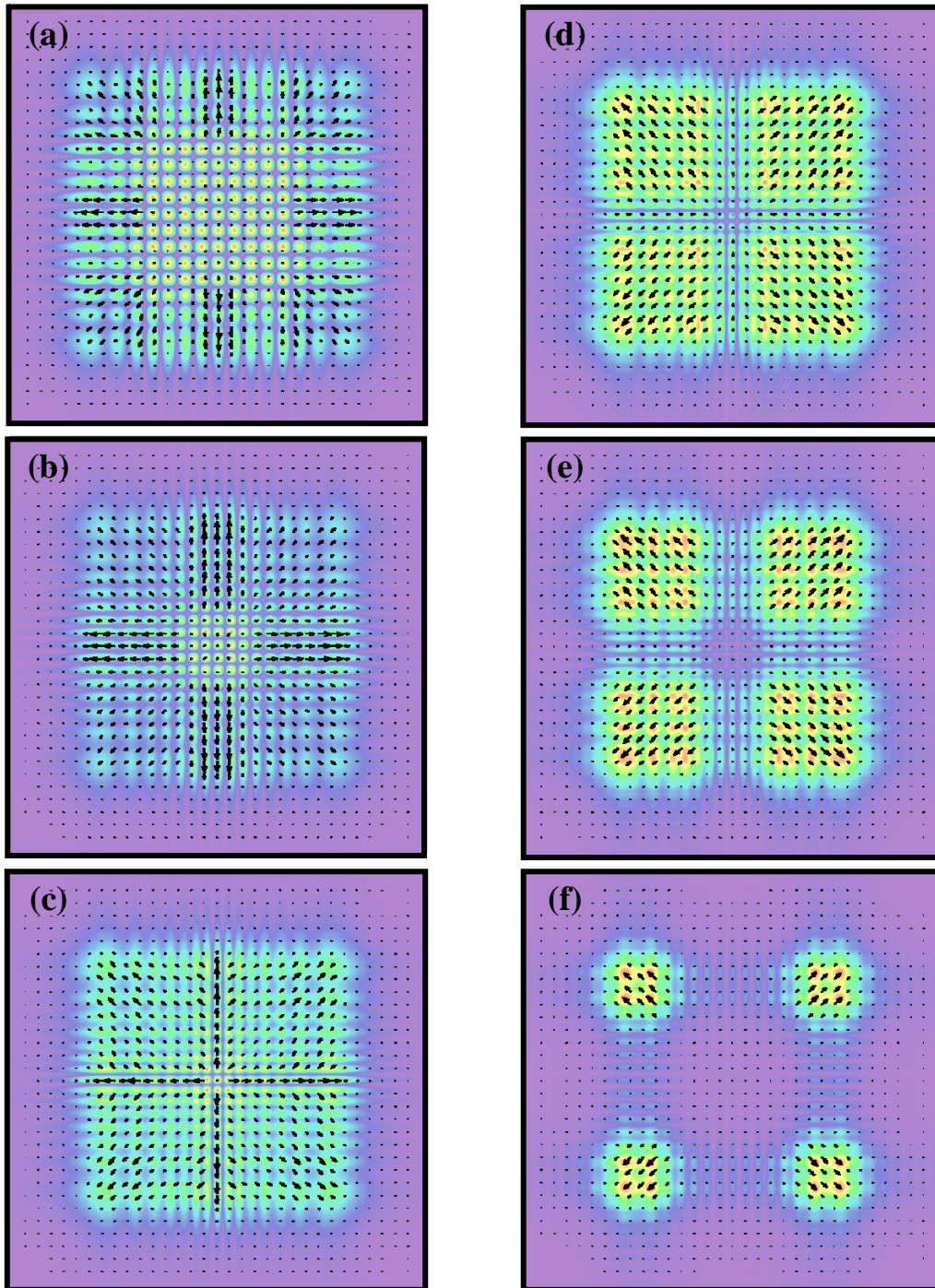


Fig. 4.4-1. (a)-(f) The vector plot of $\vec{j}_{15,15}(x, y, t)$ at $t = 0.1T$, $0.2T$, $0.3T$, $0.4T$, $0.5T$, and $1.0T$, respectively.

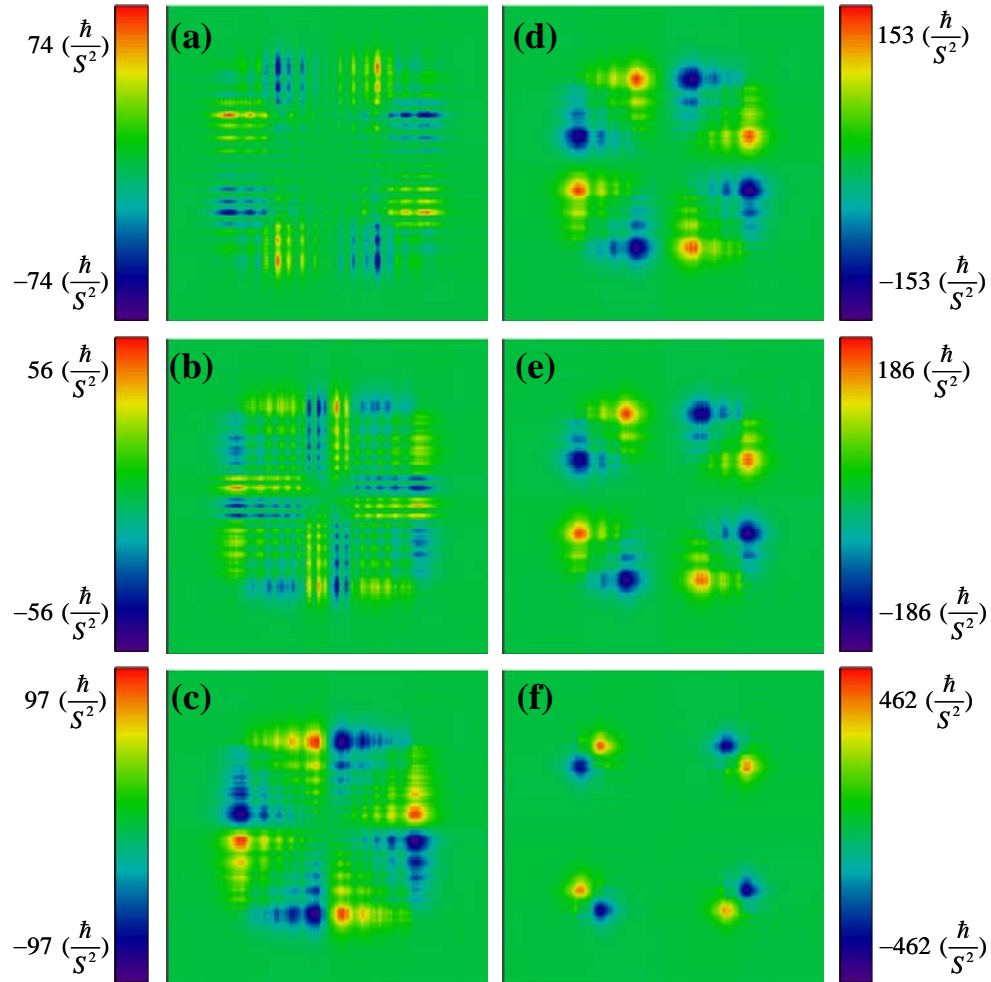


Fig. 4.4-2. (a)-(f) show the density plots of $\bar{l}_{15,15}(x, y, t)$ at $t = 0.1T$, $0.2T$, $0.3T$, $0.4T$, $0.5T$, and $1.0T$, respectively.

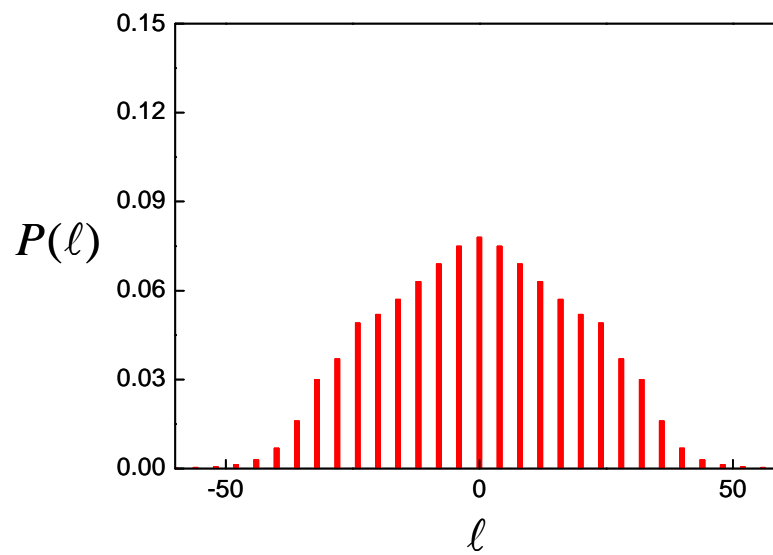


Fig. 4.4-3. The OAM spectrum of $\psi_{15,15}(x, y, t)$.

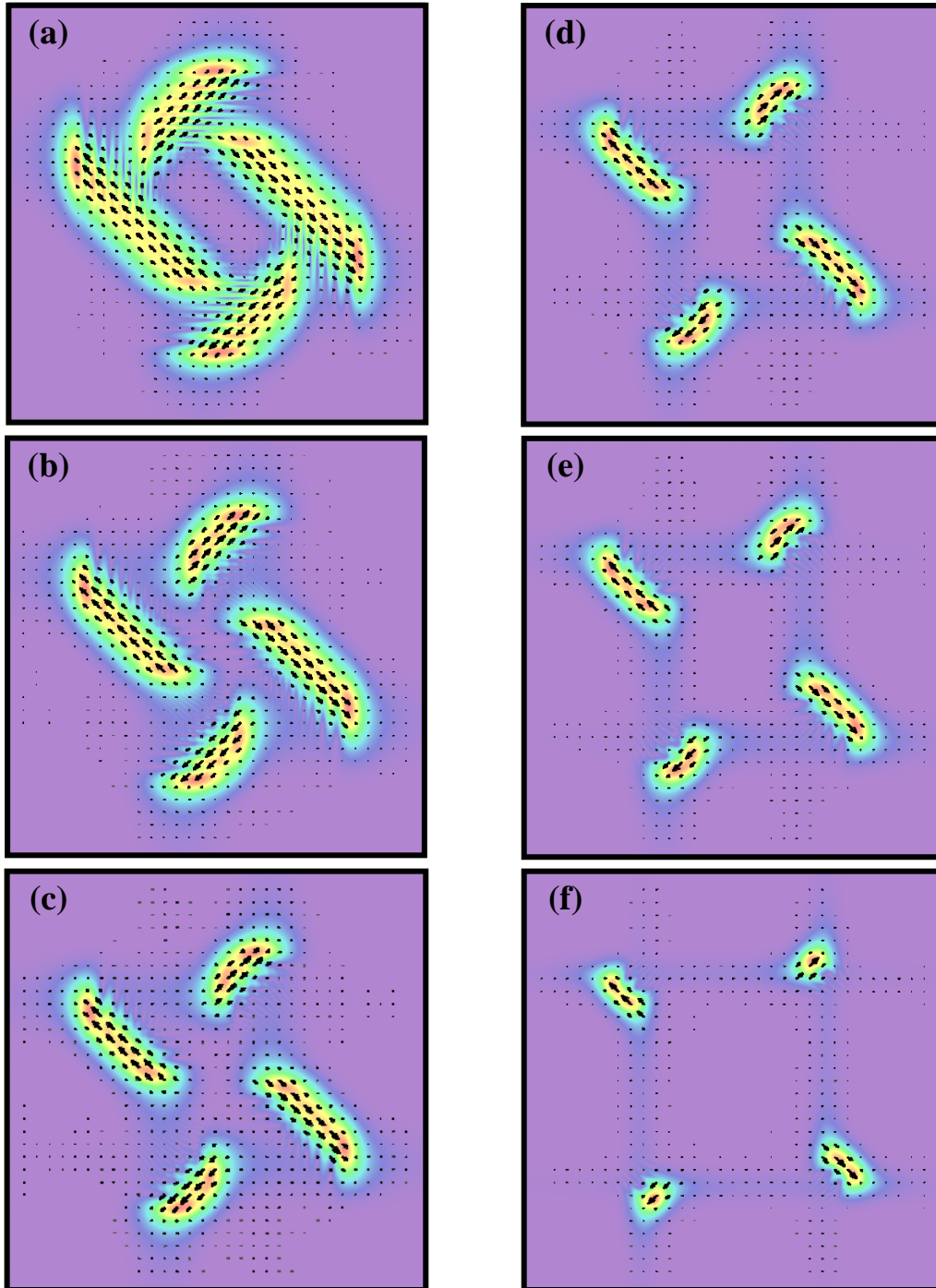


Fig. 4.4-4. (a)-(f) The vector plot of $\bar{J}_{35,13}^{1,0.6\pi}(x, y, t)$ at $t = 0.1T$, $0.2T$, $0.3T$, $0.4T$, $0.5T$, and $1.0T$, respectively.

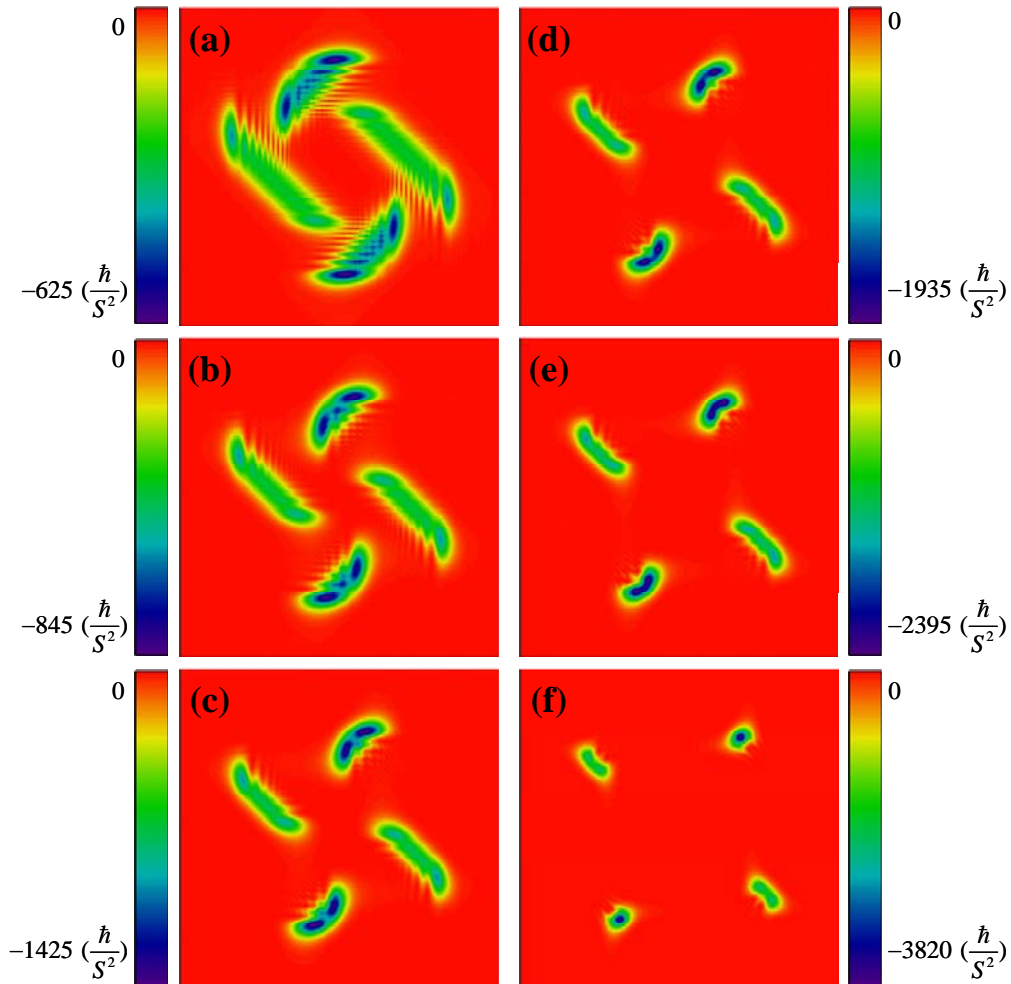


Fig. 4.4-5. (a)-(f) The density plots of $\bar{L}_{35,13}^{1,1,0,6\pi}(x, y, t)$ at $t = 0.1T$, $0.2T$, $0.3T$, $0.4T$, $0.5T$, and $1.0T$ are presented in Fig. 4.3-9 (a)-(f), respectively.

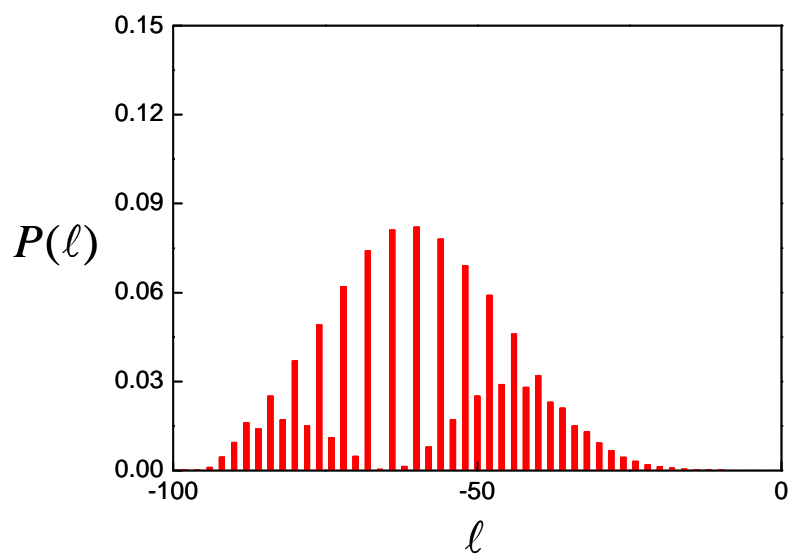


Fig. 4.4-6. The OAM spectrum of $\Psi_{35,13}^{1,1,0,6\pi}(x, y, t)$.

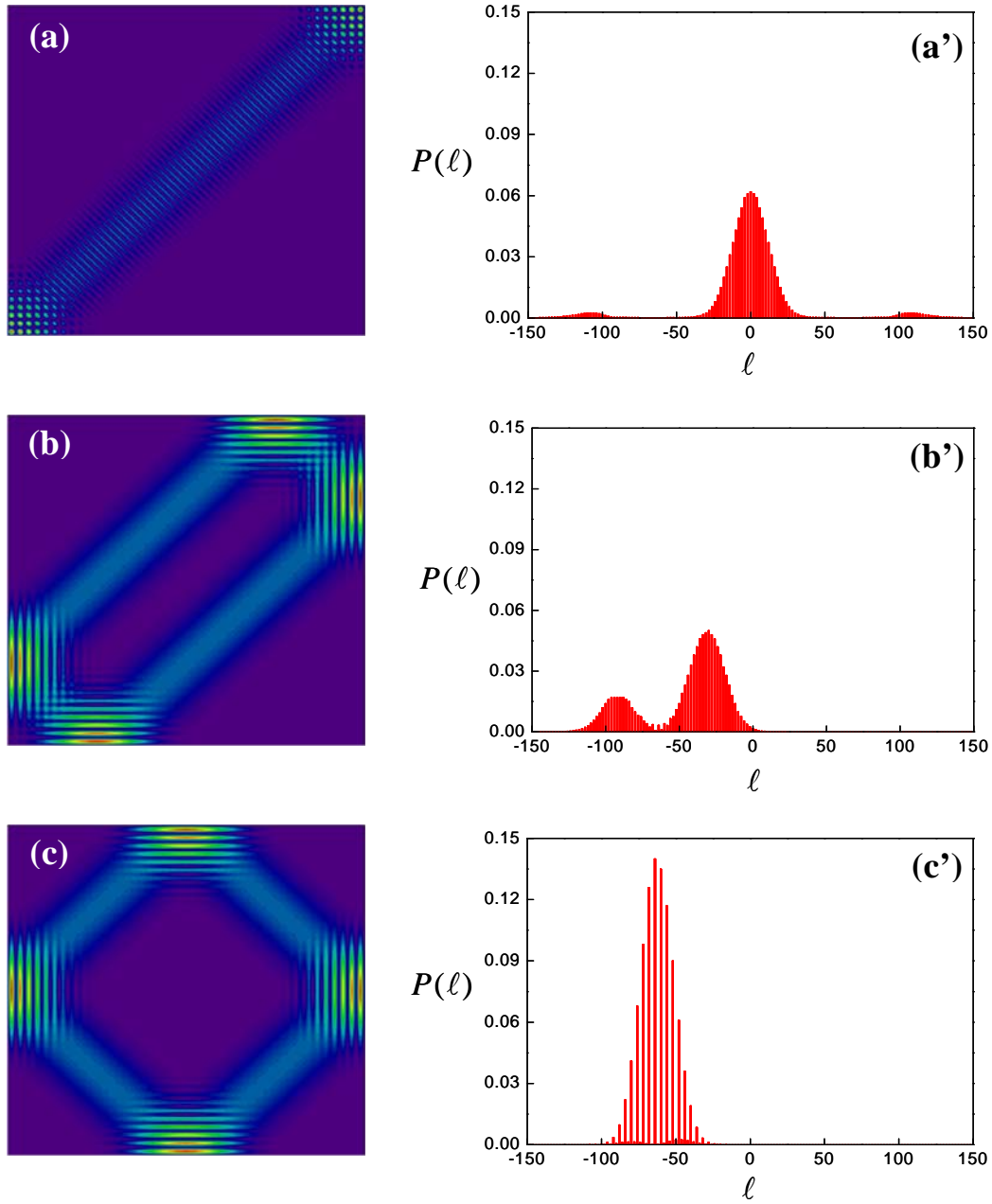


Fig. 4.4-7. (a)-(c) The intensity patterns of $\Psi_{35,13}^{1,1,\phi}(x, y, t)$ with $\phi = 0, 0.25\pi,$ and 0.5π , respectively; (a')-(c') The OAM spectra of the coherent states shown in (a)-(c), respectively.

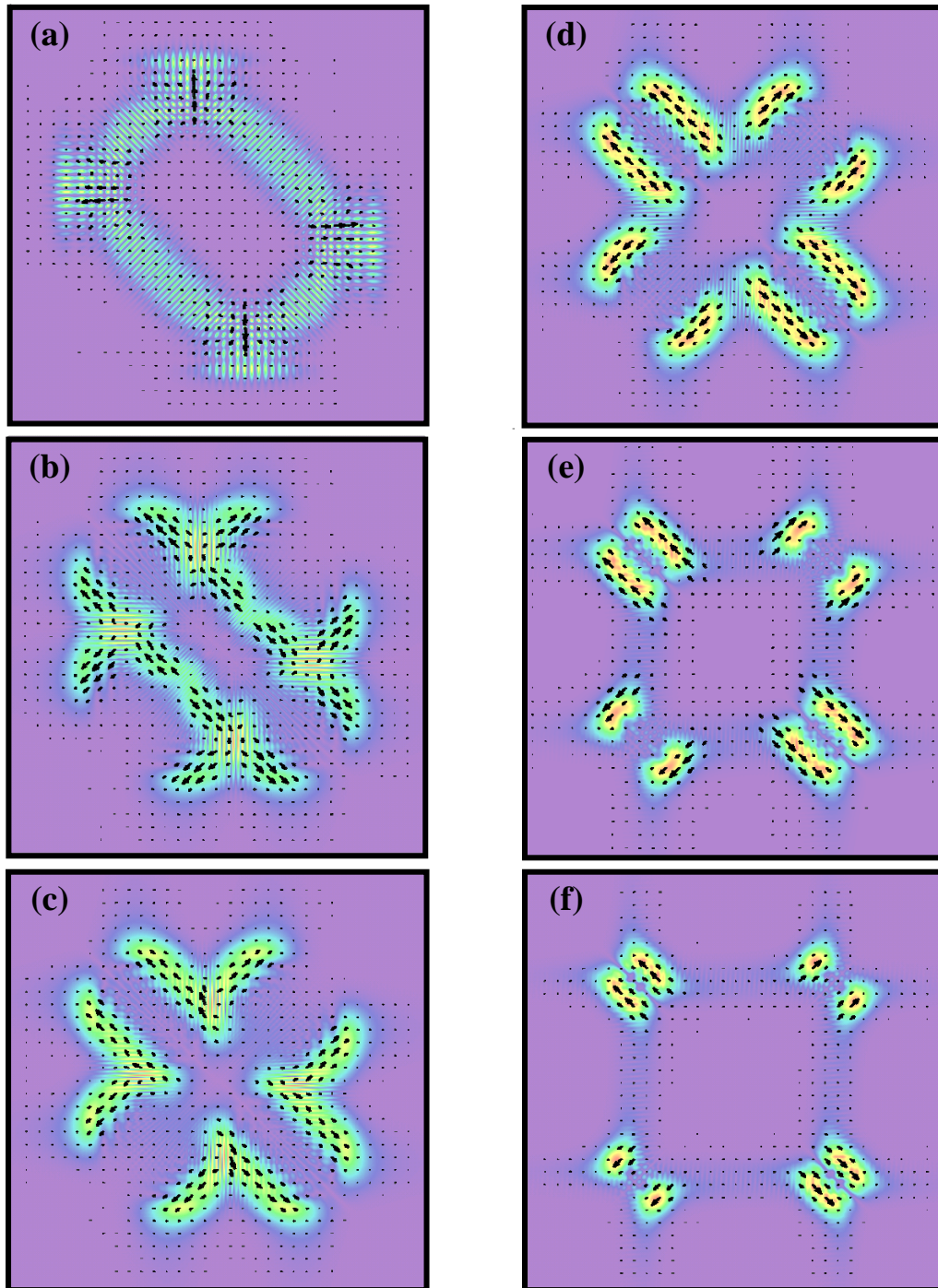


Fig. 4.4-8. (a)-(f)The vector plot of $\bar{J}_C^{1,1,0,6\pi}(x, y, t)$ at $t = 0.1T$, $0.2T$, $0.3T$, $0.4T$, $0.7T$, and $1.0T$, respectively.

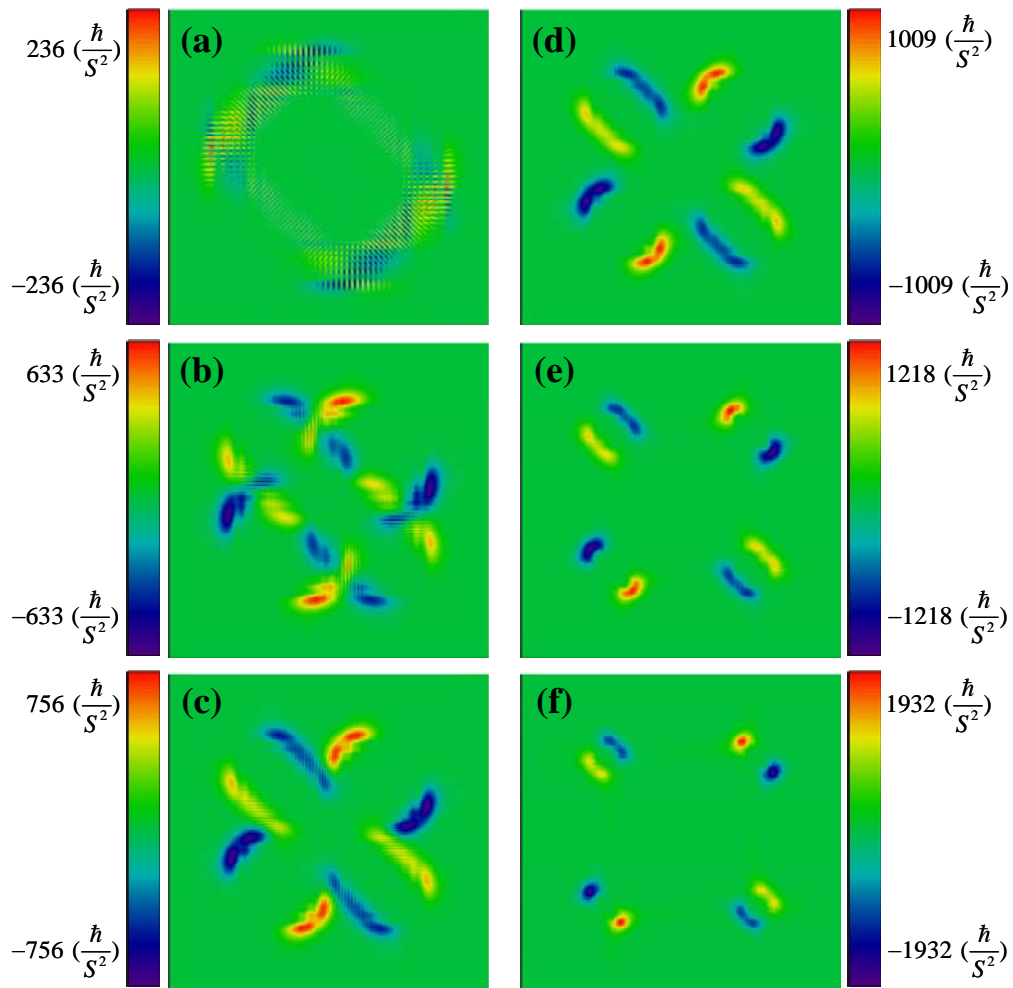


Fig. 4.4-9. (a)-(f) The density plots of $\bar{L}_{35,13}^{1,1,0.6\pi}(x, y, t)$ at $t = 0.1T$, $0.2T$, $0.3T$, $0.4T$, $0.7T$, and $1.0T$, respectively.

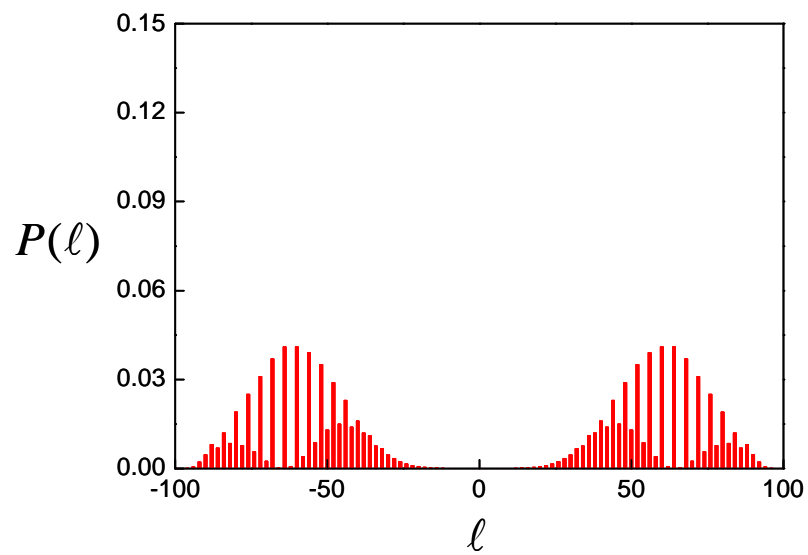


Fig. 4.4-10. The OAM spectrum of $C_{35,13}^{1,1,0,6\pi}(x, y, t)$.

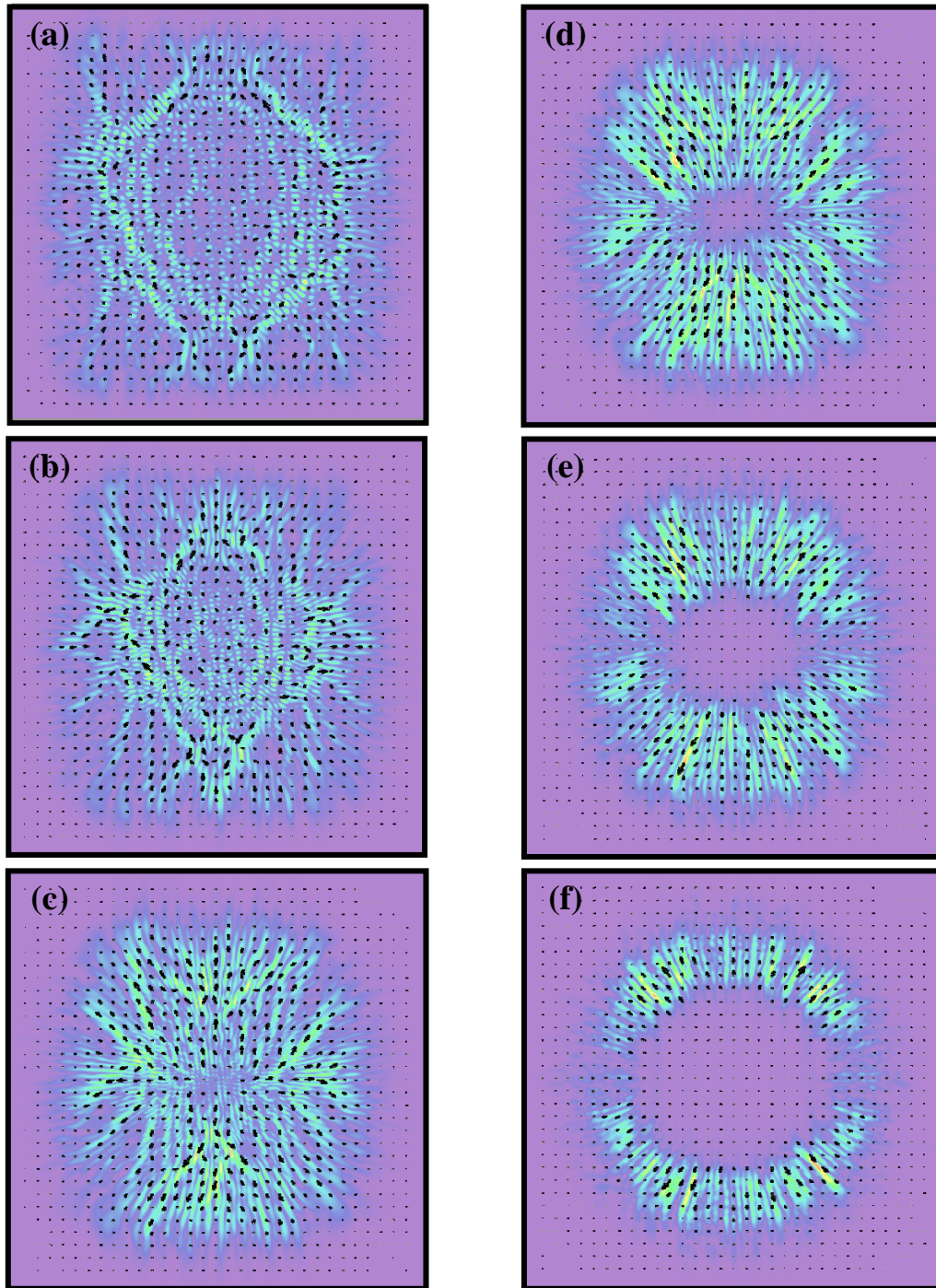


Fig. 4.4-11. (a)-(f) The vector plot of $\vec{j}_{chaos}(x, y, t)$ at $t = 0.1T$, $0.2T$, $0.4T$, $0.55T$, $0.8T$, and $1.55T$, respectively.

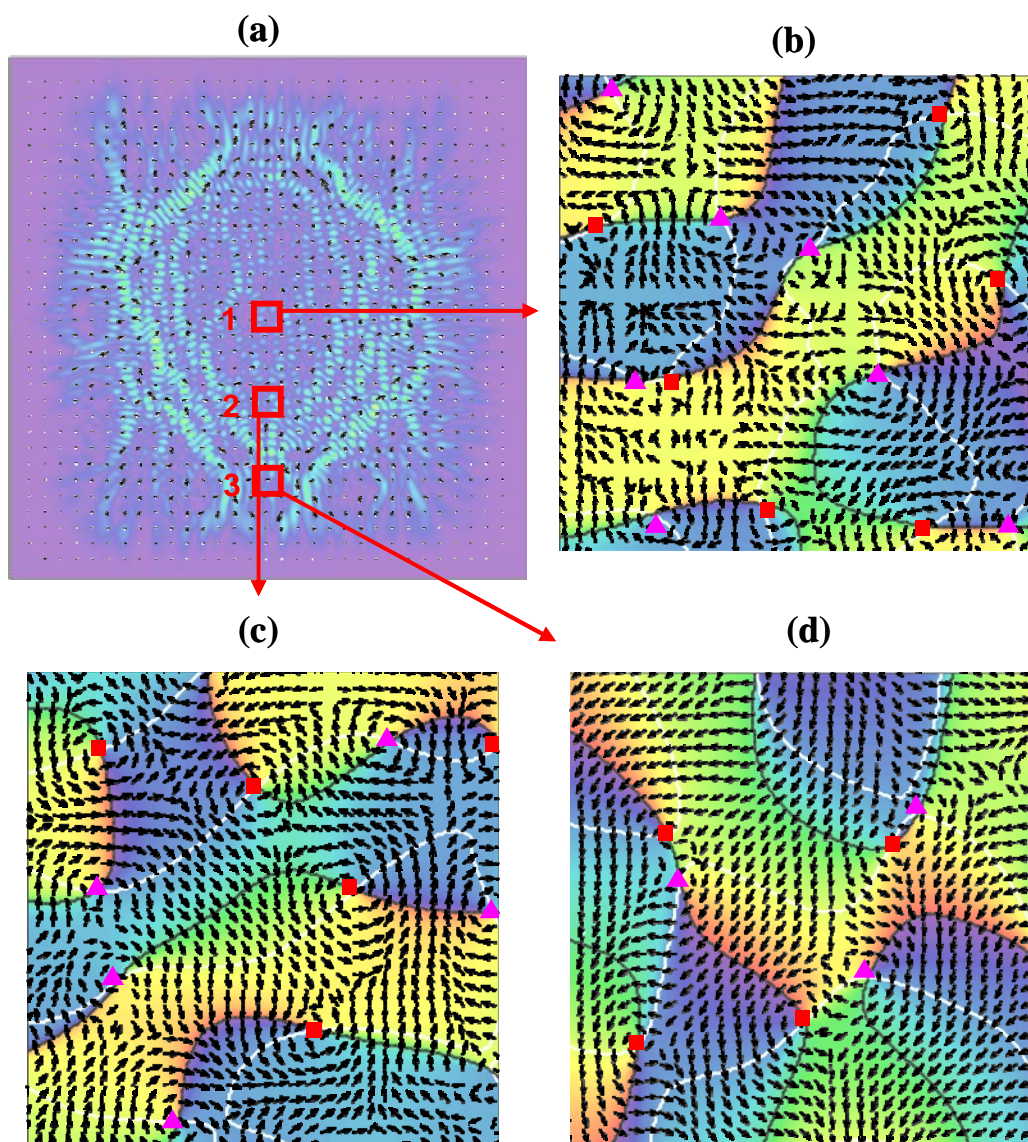


Fig. 4.4-12. (a) The vector plot of $\vec{j}_{chaos}(x, y, 0.1T)$. (b)-(d) Zoom-in views of small regions marked by the hollow squares in (a). Backgrounds are the corresponding contour plots of phase functions.

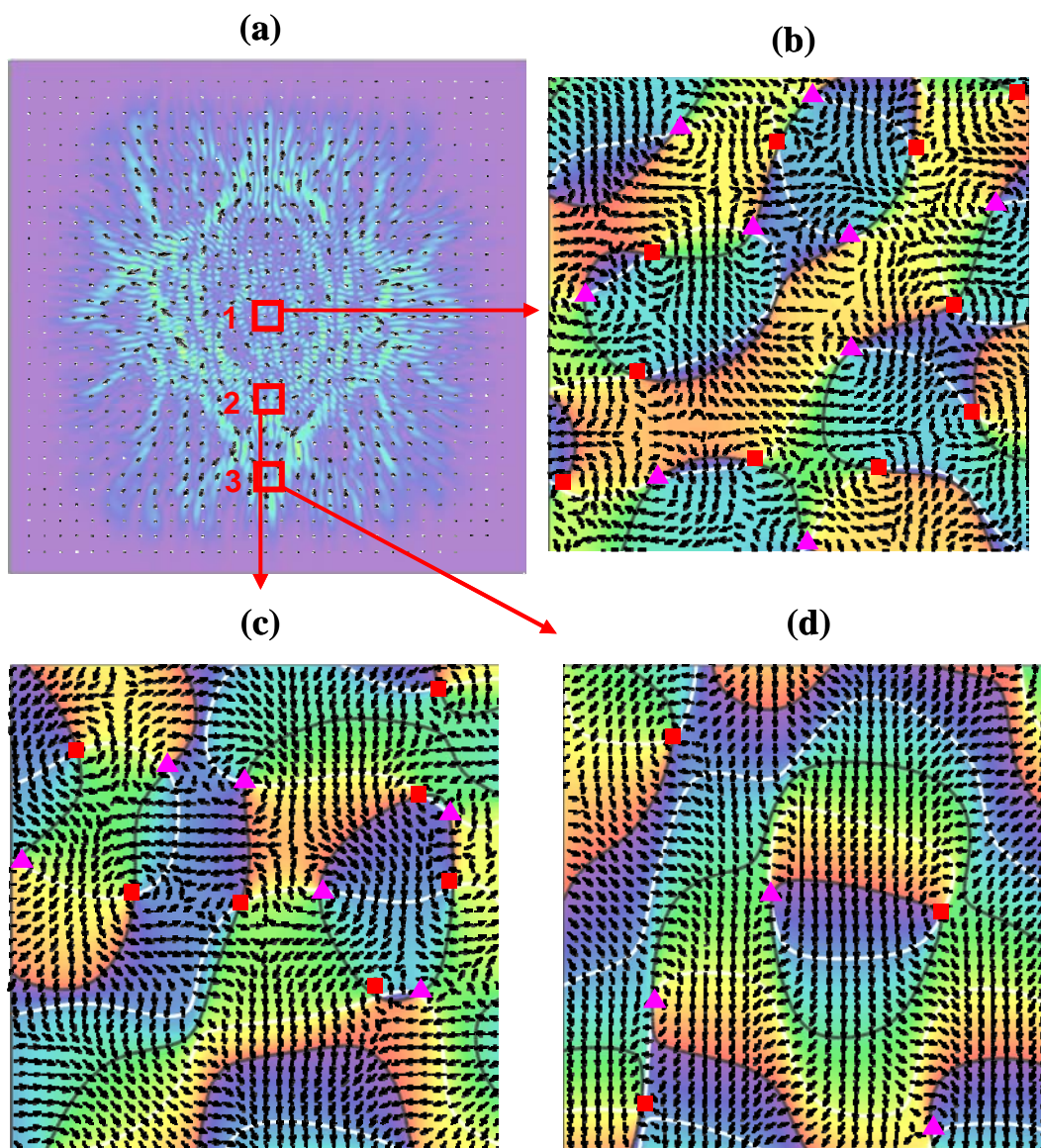


Fig. 4.4-13. (a) The vector plot of $\vec{j}_{chaos}(x, y, 0.2T)$. (b)-(d) Zoom-in views of small regions marked by the hollow squares in (a). Backgrounds are the corresponding contour plots of phase functions.

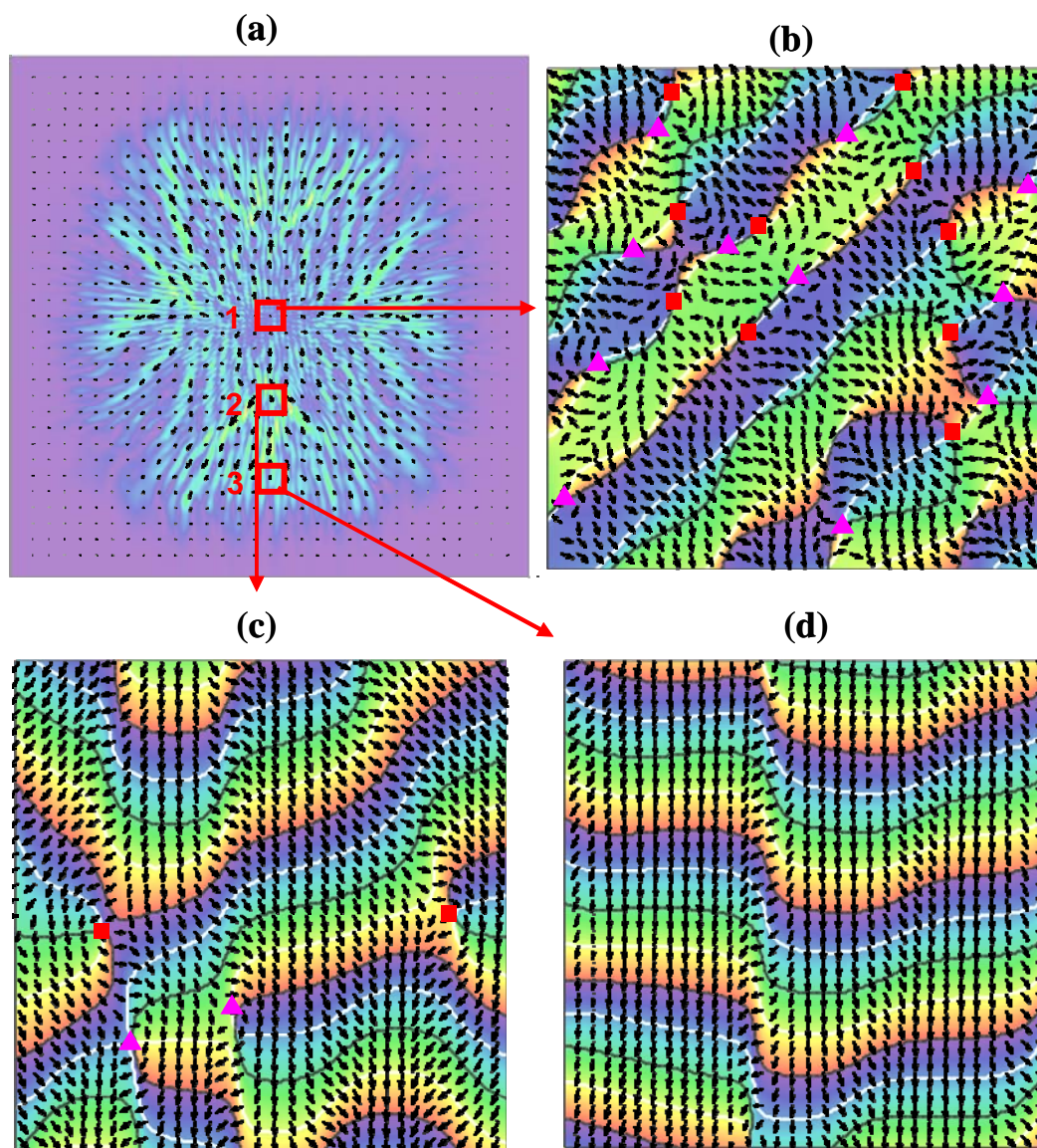


Fig. 4.4-14. (a) The vector plot of $\vec{j}_{chaos}(x, y, 0.4T)$. (b)-(d) Zoom-in views of small regions marked by the hollow squares in (a). Backgrounds are the corresponding contour plots of phase functions.

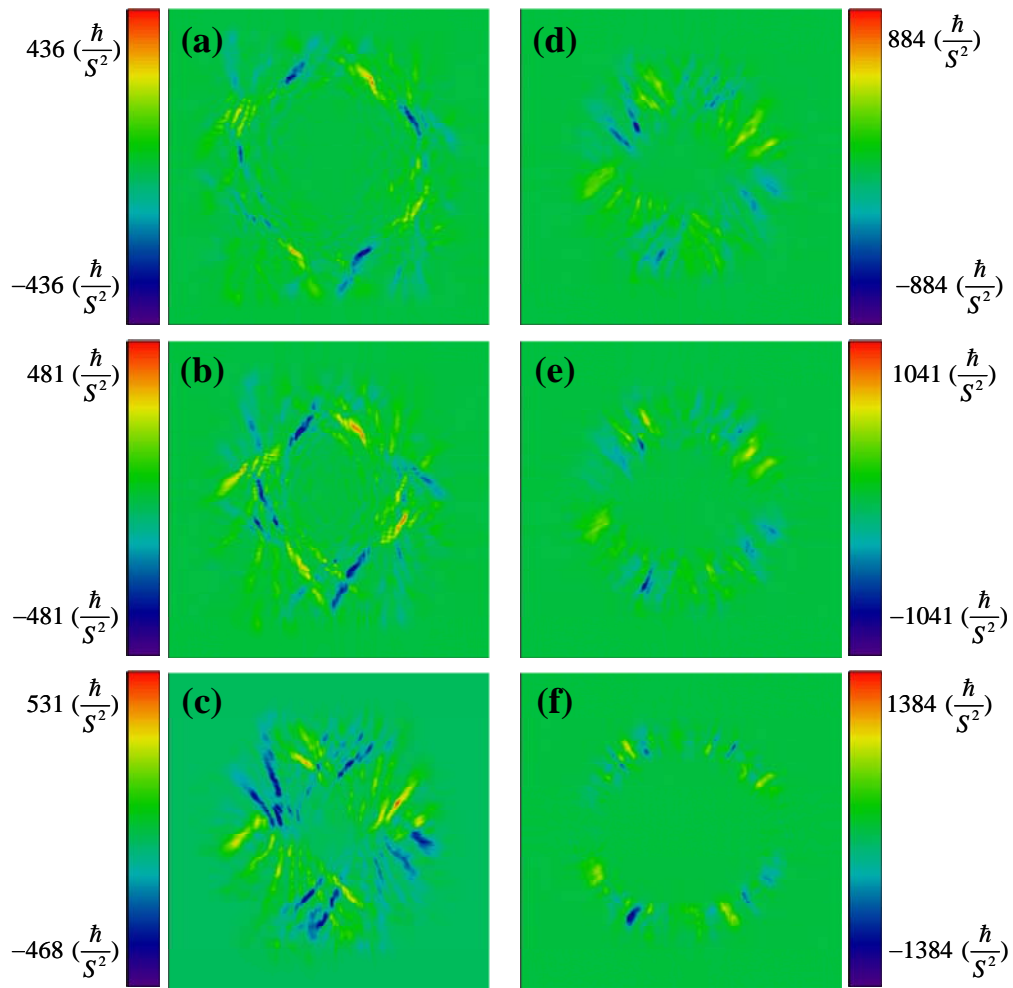


Fig. 4.4-15. (a)-(f) The density plot of $\bar{l}_{chaos}(x, y, t)$ at $t = 0.1T$, $0.2T$, $0.4T$, $0.55T$, $0.8T$, and $1.55T$, respectively.

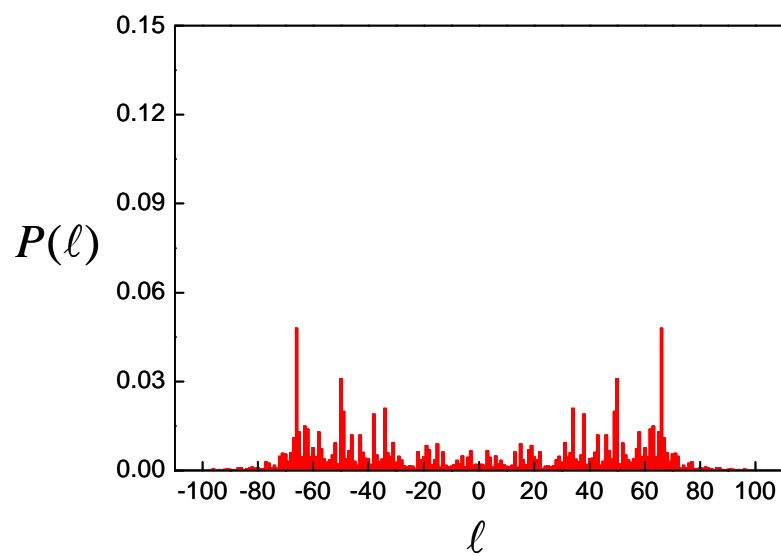


Fig. 4.4-16. The OAM spectrum of $\psi_{chaos}(x, y, t)$.

Chapter 5

Vector Fields and Vector Singularities in VCSELs



In chapter3 we have shown many interesting near-field patterns observed at threshold currents. However, the presented experimental results are restricted to linear polarization. Unlike EEL has unipolarization, VCSEL has a more intriguing polarization state to the birefringence and isotropic gain region. VCSEL typically emits linearly polarized light field in one direction at near-threshold current. As the injection current increases, one common condition is that two orthogonal linear polarization states independently coexist. In this case the wavelengths of two polarization states are different. Besides, this condition is easy to operate in multi-mode lasing that will result in cloudy pattern. Another interesting phenomenon is the polarization switching, the lasing polarization state switches to the perpendicular one [AS01, MFM95, vEWW98] as the injection current increases. Here a third circumstance that has the transverse patterns to be polarization-entangled, i. e. it has different morphology at different polarization angles, is concerned. In fact, this phenomenon corresponds to the formation of vector field which has been widely studied in various laser systems [[Gil93, VKMR01, CLH06, LCH07], as well as in VCSELs [Erdo92, PTMA97, CHLL03b]. Since the near-field pattern that is analogous to quantum-billiard wave function is purely real, VCSELs can be employed to manifest vector singularities. Vector singularities are isolated, stationary points in a plane at which the orientation of the electric field of a real vector field becomes undefined. Vector singularities as well as phase singularities play a vital role in singular optics.

This chapter is organized as follows. In first section we present a polarization-entangled pattern associated with two superscars modes in a square shaped VCSEL. We reconstruct the patterns in two orthogonal polarization states by SU(2) coherent states to manifest the vector field and vector singularities. Similar experimental method as that in Sec. 5.1 is applied to originally generate a chaotic vector. By using the eigenfunction expansion technique, the vector field is reconstructed to unambiguously analyze the vector singularities embedded in a chaotic vector field. Since the polarization of light corresponds to the spin of

quantum wave, the analyses of the vector fields in VCSELs can provide important information for quantum-billiard systems (such as ballistic quantum dots) with consideration on electronic spin.

5.1 Vector Fields in Square VCSEL

As revealed in the introduction of this chapter, the near-threshold lasing modes of VCSELs are usually linearly-polarized and VCSELs can simultaneously lase in two polarizations when injection current increase. However, the increase of injection current tends to lead to multi-mode lasing and result in cloudy pattern. Since the threshold current of VCSEL varies with device temperature, we can alternatively make the lasing thresholds of two orthogonally polarized modes to be nearly the same by means of adjusting the operating temperature. The temperature dependence shown in Fig. 3.3-3 (a) of one square VCSEL has neglected the polarization of the lasing modes. Fig. 5.1-1(b) shows the polarization-resolved temperature dependence of threshold currents of another VCSEL. It can be found that the two polarizations simultaneously lase at temperatures around 295K and 255K. The 0° of the polarization is along the [110] direction of the (001)-GaAs crystal, as illustrated in Fig. 5.2-1(a). Fig. 5.1-2 (a)-(d) present the lasing patterns at temperature of 295K in 0° , 45° , 90° , and -45° , respectively. It can be seen that the patterns in 0° and 90° have different morphology and the patterns in 45° and -45° are just the total intensity pattern that can be observed by removing the polarizer, as shown Fig. 5.2-2(e). Notice that the wave lengths of the two polarizations at 0° and 90° are measured to be different.

To understand this result, we can express the wave amplitude at arbitrary polarization angle θ by the phasor amplitude at 0° and 90°

$$E_{\theta}(x, y, t) = E_0(x, y) \cos \theta e^{i\omega_1 t} + E_{90}(x, y) \sin \theta e^{i\omega_2 t} . \quad (5.1.1)$$

The intensity is then given by

$$\begin{aligned} I_{\theta}(x, y, t) &= |E_{\theta}(x, y, t)|^2 \\ &= |E_0(x, y)|^2 \cos^2 \theta + |E_{90}(x, y)|^2 \sin^2 \theta \\ &\quad + E_0(x, y) E_{90}^*(x, y) \frac{\sin 2\theta}{2} e^{i(\omega_1 - \omega_2)t} + E_{90}^*(x, y) E_0(x, y) \frac{\sin 2\theta}{2} e^{i(\omega_2 - \omega_1)t} \end{aligned} \quad (5.1.2)$$

The experimental patterns are actually time-averaging observations

$$\begin{aligned} \langle I_{\theta}(x, y, t) \rangle &= |E_0(x, y)|^2 \cos^2 \theta + |E_{90}(x, y)|^2 \sin^2 \theta \\ &\quad + E_0(x, y) E_{90}^*(x, y) \frac{\sin 2\theta}{2} \langle e^{i(\omega_1 - \omega_2)t} \rangle \\ &\quad + E_{90}^*(x, y) E_0(x, y) \frac{\sin 2\theta}{2} \langle e^{i(\omega_2 - \omega_1)t} \rangle \end{aligned} \quad (5.1.3)$$

For the condition that $\omega_1 \neq \omega_2$, the time average of the oscillating term $\langle e^{i(\omega_1 - \omega_2)t} \rangle$ results in zero such that the interference term vanishes. Therefore, the observed patterns in 45° and -45° are just the total intensity pattern. However, if $\omega_1 = \omega_2$ then the orthogonally polarized components can mutually interfere to lead to various patterns in other polarizations.

Fig. 5.1-3 (a) and (c) show the polarization resolved near-field patterns in 0° and 90° at operating temperature of $255K$. It can be seen that the patterns in 45° and -45° are no longer the total intensity pattern (Fig.5.1-3(e)) and have greatly different morphologies, as presented in Fig.5.1-3(b) and (d). In other words, the pattern is linearly polarized, but the polarization is not the same for different spatial points. In contrast to the case at $295K$, the measurement of the optical spectrum indicates that the orthogonal polarization modes have the same wavelength. As

mentioned in the previous discussion, the fact that orthogonal polarization modes are phase synchronized to a common frequency is a basic requirement for a polarization-entangled pattern. From Eq. (5.1.1) we can see that, for the two polarization state with the same frequency ($\omega_1 = \omega_2$), the phasor amplitude of the total field can be written in form of vector field

$$\vec{E}(x, y) = E_0(x, y) \hat{a}_x + E_{90}(x, y) \hat{a}_y . \quad (5.1.4)$$

To understand the vector field and manifest vector singularities, we have to find the wave functions of lasing modes in two orthogonal polarizations as basis. In this case the lasing modes in 45° and -45° are easier to reconstruct. Based on thorough numerical analysis, the lasing modes in 45° and -45° can be well reconstructed by the SU(2) coherent states $E_{45}(x, y) = C_{23}^{1,1}(x, y; 11, 0.6\pi)$ and $E_{-45}(x, y) = C_{23}^{1,1}(x, y; 11, 0.3\pi)$, respectively. The reconstructed patterns are displayed in Fig. 5.1-4 (b) and (d). In terms of the two bases, the whole vector field can be expressed as

$$\vec{E}(x, y) = E_{45}(x, y) \hat{a}_{45} + E_{-45}(x, y) \hat{a}_{-45} , \quad (5.1.5)$$

with $\hat{a}_{45} = \frac{\hat{a}_x + \hat{a}_y}{\sqrt{2}}$ and $\hat{a}_{-45} = \frac{\hat{a}_x - \hat{a}_y}{\sqrt{2}}$ to be unit vector in 45° and -45° , respectively. The patterns in 0° and 90° can be obtained by projecting the vector field into x - and y - directions:

$$E_0(x, y) = \vec{E}(x, y) \cdot \hat{a}_x = \frac{1}{\sqrt{2}} [E_{45}(x, y) + E_{-45}(x, y)] ; \quad (5.1.6)$$

$$E_{90}(x, y) = \vec{E}(x, y) \cdot \hat{a}_y = \frac{1}{\sqrt{2}} [E_{45}(x, y) - E_{-45}(x, y)] . \quad (5.1.7)$$

The similarities between Fig. 5.1-3 (a)-(d) and Fig. 5.1-4 (a)-(d) verify our theoretical

reconstruction of the experimental results. Note that the formations of $E_0(x, y)$ and $E_{90}(x, y)$ are critically depended on $E_{45}(x, y)$ and $E_{-45}(x, y)$. Only if $E_{45}(x, y)$ and $E_{-45}(x, y)$ really match the experimental results, one can well reconstruct $E_0(x, y)$ and $E_{90}(x, y)$.

The vector singularities are generally described by the orientation angle function:

$$\Theta(x, y) = \text{angle}[E_0(x, y), E_{90}(x, y)] \quad (5.1.8)$$

The vortices of the angle function $\Theta(x, y)$ correspond to the vector singularities at which the orientation of the electric field vector is undefined. Figure 5.1-5(a) depicts the numerical pattern of the angle function $\Theta(x, y)$ for the experimental vector field. Here the angle is color-coded by hue and the singularities are at the points where all colors get together. A small region highlighted by white square area with edge equal to $a/10$ of the vector field is depicted in Fig. 5.1-5(b) to demonstrate the novel lattice structure of the vector singularities. The white and black curves stand for the nodal lines of $E_0(x, y)$ and $E_{90}(x, y)$, respectively. It can be validated that the crossings of white and black curves coincide with the singularities at which all color get together. Besides, it is of pedagogical importance to confirm the sign rule that the nearest neighbor singularities on any contour of constant phase are required to have opposite signs [Freu95]: The singularities with topological charge $+1$ and -1 are labeled by white squares and black triangles, respectively. Furthermore, the vector field distribution in this region is manifested in Fig. 5.1-5(c). It can be seen that the singularities with topological charge equal to -1 correspond to saddle points of the vector flow and those with topological charge equal to $+1$ are all vortices, no source or sink point are found in our thorough analysis.

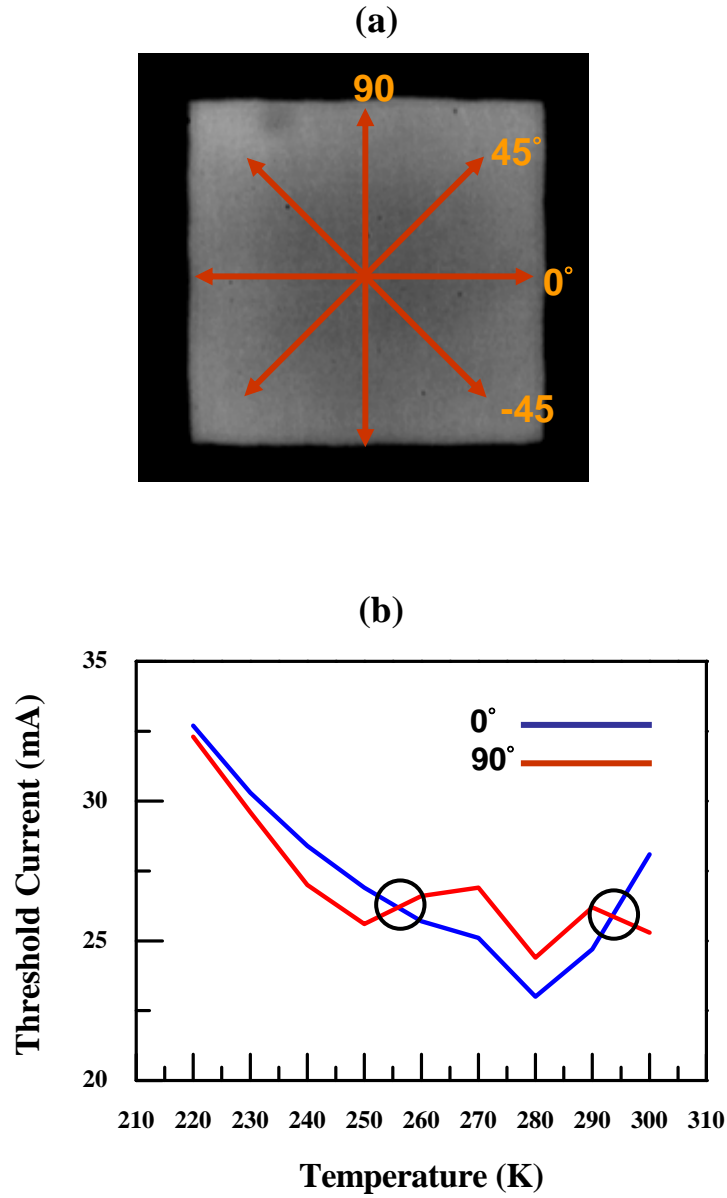


Fig. 5.1-1. (a) Reference of the polarization angle (b) The threshold currents of the two polarizations. Simultaneous lasings occur at temperatures around 295K and 255K.

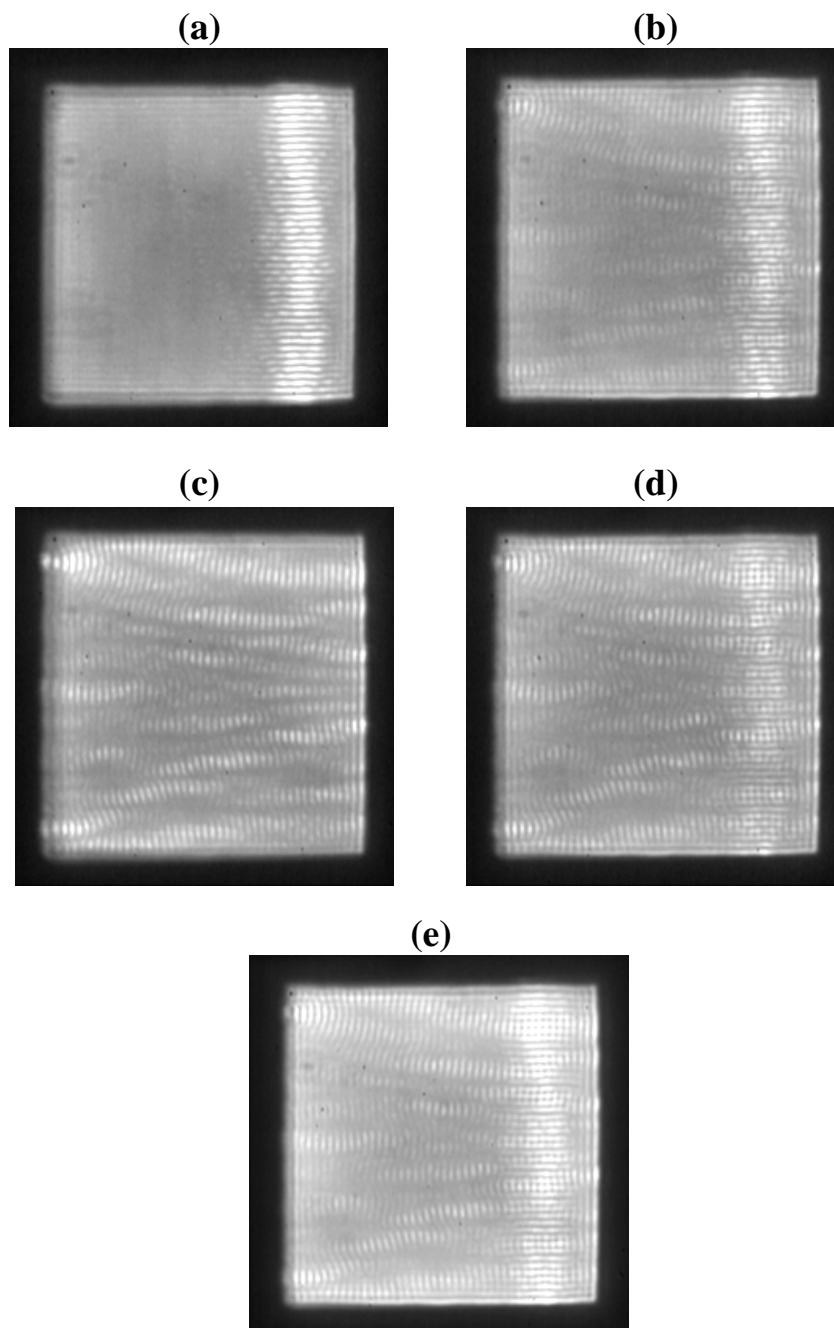


Fig. 5.1-2. (a)-(d) The lasing patterns in 0° , 45° , 90° , and -45° and (e) The total intensity pattern observed at $295K$.

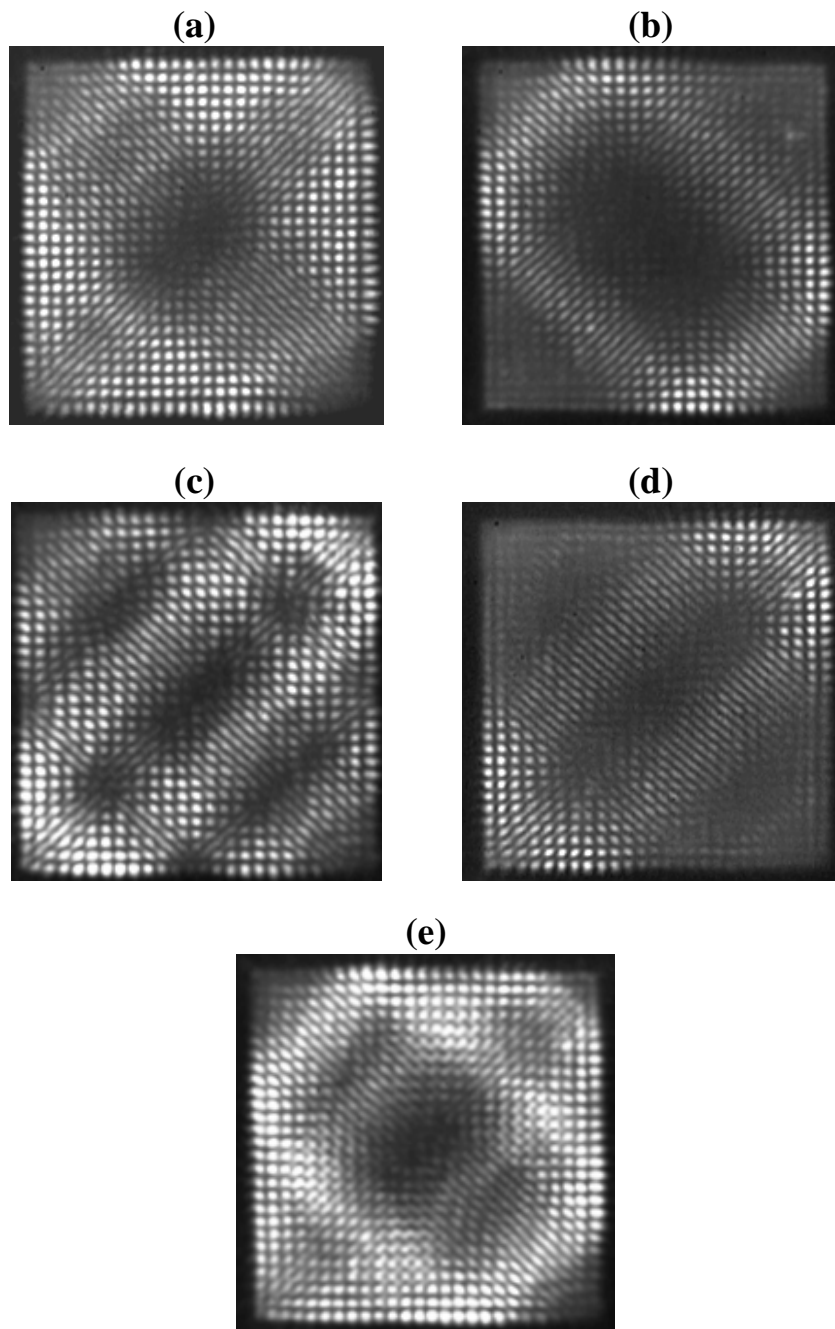


Fig. 5.1-3. (a)-(d) The lasing patterns in 0° , 45° , 90° , and -45° and (e) The total intensity pattern observed at $255K$.

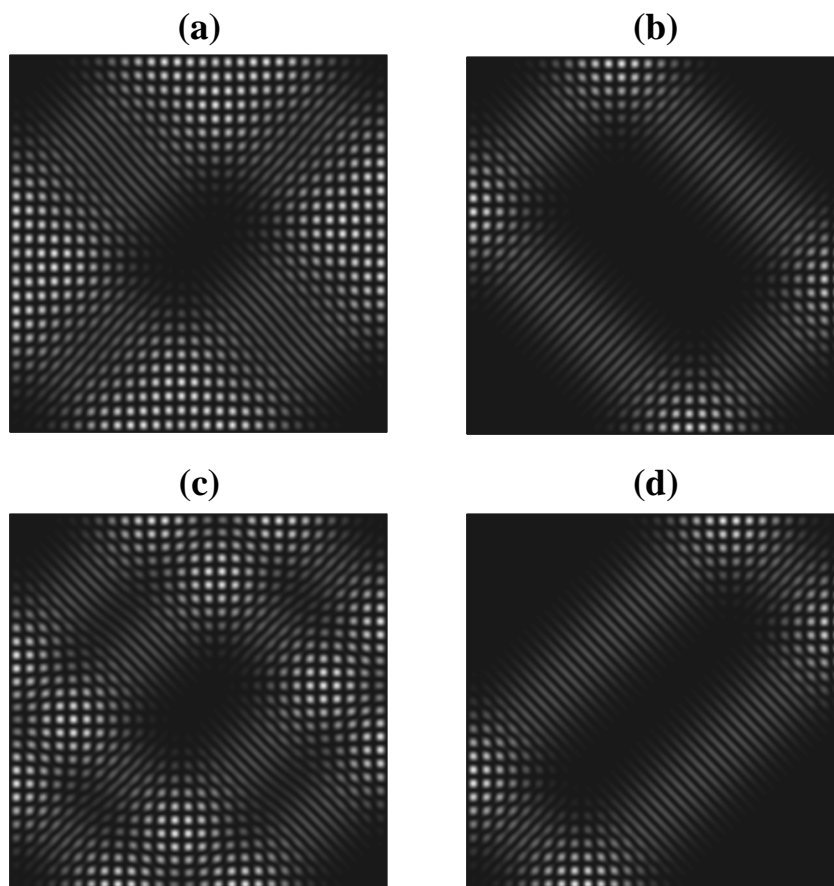


Fig. 5.1-4. (a)-(d) The reconstructed patterns of Fig. 5.2-3(a)-(d), respectively.

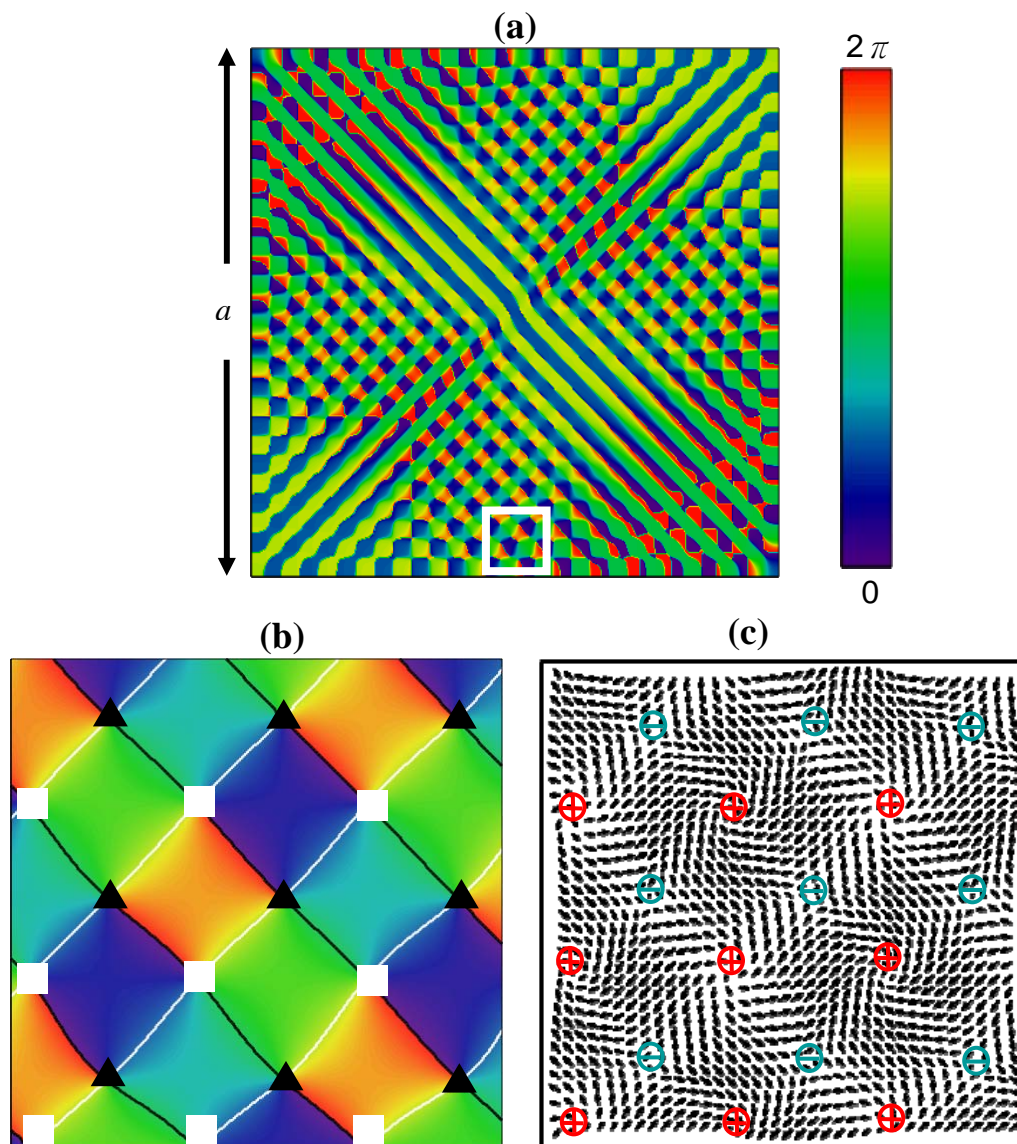


Fig. 5.1-5. (a) The contour plot of the angle function $\Theta(x, y)$. (b) Zoom-in view of the small regions highlighted by the white square. (c) The vector plot of the polarization vector with vortices and saddles labeled by “+” and “-” signs, respectively.

5.2 Chaotic Vector Field in VCSEL

As well as that have been discussed in last section, the features of the vector singularities have been experimentally observed in laser modes with the interrelated behavior of spatial structures and polarization states [Gil93, VKMR01, CLH06, LCH07, Erdo92, PTMA97, CHLL03b]. However, so far all experimental demonstrations were related to the regular lasing modes of integrable optical cavities; no experiments have demonstrated explicitly the entanglement of polarization and spatial structures in chaotic laser resonators. In this section we use the VCSEL that is similar to that used in Sec. 3.4 to generate the 2D chaotic vector fields.

Figures 5.2-1(a) and (b) show the polarization-resolved near-field patterns with operating temperature of $T=265$ K, the threshold current of $I=26.9$ mA, and polarizations in 0° and 90° directions, respectively. The orthogonally polarized modes clearly exhibit to have remarkably distinct chaotic patterns. The measurement of the optical spectrum indicates that the whole experimental wave is phase synchronized to a single frequency at 806.45 nm. As a consequence, the orthogonally polarized components can mutually interfere to lead to a greatly different pattern in the polarization resolved near-field image, as shown in Fig. 5.2-1 (c) for 45° polarization and Fig.5.2-1 (d) for -45° polarization. Explicitly, the entanglement of spatial structures and polarization states lead to the formation of an optical vector field. We investigated the dependence of the 2D chaotic vector field on the operating parameters, and it turns out that the experimental vector field remains unchanged for $262.5 \text{ K} < T < 267.5 \text{ K}$ and for $26.9 \text{ mA} < I < 27.6 \text{ mA}$. The width of these ranges indicates that generation of 2D chaotic vector fields is a robust phenomenon. To our best knowledge, the present result proffers the first experimental realization of 2D chaotic vector fields in a microcavity laser.

Since it is not feasible to measure polarization vector fields in a straightforward way, the reconstruction of the orthogonally polarized wave functions is practically

useful for analyzing the property of vector singularities. We use the same eigenfunctions expansion method as that described in Sec 3.4 to reconstruct the polarization resolved patterns. Figures 5.2-2(a) and 5.2-2(b) depict the patterns of $|\psi_p(x_i, y_j)|$ for two orthogonally polarized modes shown in Fig. 5.2-1(a) and 5.2-1(b), respectively. Figures 5.2-3(a) and 5.2-3(b) show the intensity plots of $|C_{n_1, n_2}|$ obtained from Eq. 3.4-5 for the experimental polarization-resolved modes at 0° and 90° , respectively. Figures 5.2-4(a) and (b) depict the wave patterns of the analytical wave functions corresponding to the experimental polarization-resolved modes at 0° and 90° , respectively. It can be clearly seen that the experimental polarization-resolved patterns are well-reconstructed with the analytical wave functions.

Let $E_0(x, y)$ and $E_{90}(x, y)$ denote the polarization-resolved wave functions at 0° and 90° , respectively. In terms of $E_0(x, y)$ and $E_{90}(x, y)$, the vector field distribution for the experimental pattern is given by

$$\vec{E}(x, y) = E_0(x, y) \hat{a}_x + E_{90}(x, y) \hat{a}_y. \quad (5.2.1)$$

With the vector field \vec{E} the polarization-resolved wave functions at 45° and -45° are given by

$$E_{45}(x, y) = \frac{1}{\sqrt{2}} [E_0(x, y) + E_{90}(x, y)] \quad (5.2.2)$$

and

$$E_{-45}(x, y) = \frac{1}{\sqrt{2}} [E_0(x, y) - E_{90}(x, y)]. \quad (5.2.3)$$

Figures 5.2-4(c) and 5.2-4(d) depict the numerical results for the intensity patterns of $|\psi_{45}(x, y)|^2$ and $|\psi_{-45}(x, y)|^2$, respectively. The good agreement between the numerical and experimental patterns evidences the accuracy of the reconstructed wave function in representing the observed vector field.

To further validate the experimental observation to be a chaotic vector field, we use the reconstructed wave functions to calculate the amplitude and intensity distributions. For the chaotic wave function of Berry's conjecture, the amplitude distribution is a Gaussian function (Eq. 2.3-2) and the intensity distribution is shown to be a Porter-Thomas distribution (Eq. 2.3-3). Figures 5.2-5 (a)-(b) show the amplitude distributions of the reconstructed wave functions with polarizations in 0° , 90° , 45° , and -45° , respectively. In addition, 5.2-6 (a)-(b) illustrate and intensity distributions corresponding to Fig. 5.2-5 (a)-(b), respectively. All amplitude and intensity distributions of the polarization-resolved wave functions are found to be fairly good agreement with the theoretical distributions.

With the reconstructed vector field we can do the similar process as what has been done in last section to analyze the properties of vector singularities in the chaotic case. The angle function is again employed to describe the vector singularities:

$$\Theta_c(x, y) = \text{angle}[E_0(x, y), E_{90}(x, y)]. \quad (5.2.4)$$

Figure 5.2-7(a) depicts the numerical pattern of the angle function $\Theta_c(x, y)$ for the experimental vector field. Different from the lattice structure of regular vector field, the chaotic polarization vector field is clearly seen to reveal a highly sophisticated interlace pattern. Fig. 5.2-7(b) is the zoom-in views of the central region with edge length equal to $a/10$. Although the singularities are randomly distributed, the sign rule of the nearest neighbor singularities is still obeyed. The polarization vectors of the chaotic field as show in Fig. 5.3-7(c) become very intricate. However, one can still find that the singularities with $+1$ topological charge are all vortices.

As mentioned by Freund [Freu95], the phase of a chaotic wave with real and imaginary parts to be $E_0(x, y)$ and $E_{90}(x, y)$ is identical to the orientation phase shown in Fig. 5.3-7(a). In fact such a complex chaotic wave function does exist. The vector field expressed as eq. (5.2.1) can be decomposed into a linear combination of orthogonal circularly-polarized helical modes

$$\bar{E}(x, y) = E_R(x, y) \hat{a}_R + E_L(x, y) \hat{a}_L \quad (5.2.5)$$

, where

$$E_R(x, y) = [E_0(x, y + iE_{90}(x, y))]/\sqrt{2} \quad (5.2.6)$$

, and

$$E_L(x, y) = [E_0(x, y - iE_{90}(x, y))]/\sqrt{2}. \quad (5.2.7)$$

$\hat{a}_R = (\hat{a}_x - i\hat{a}_y)/\sqrt{2}$ and $\hat{a}_L = (\hat{a}_x + i\hat{a}_y)/\sqrt{2}$ are the helical basis unit vectors for the right- and left-handed circular polarizations, respectively. Hence, the phase function of $E_R(x, y)$ is completely the same as $\Theta_c(x, y)$. In addition to singularities, it is also meaningful to analyze the critical points in $\Theta_c(x, y)$. Based on the thorough numerical analysis, it is found that all saddle points are manifestly found to be open saddles with no joined arms. In other words, no phase extrema are observed in the experimentally generated random phase field. This result is consistent with the theoretical analysis that the phase extrema are really rare because there is little room left in the phase field to accommodate them [Freud95]. Since the circular polarization of light corresponds to the spin of quantum wave, the analyses of $\Theta_c(x, y)$ can provide important information for chaotic quantum-billiard systems (such as ballistic quantum dots) with consideration on electronic spin.

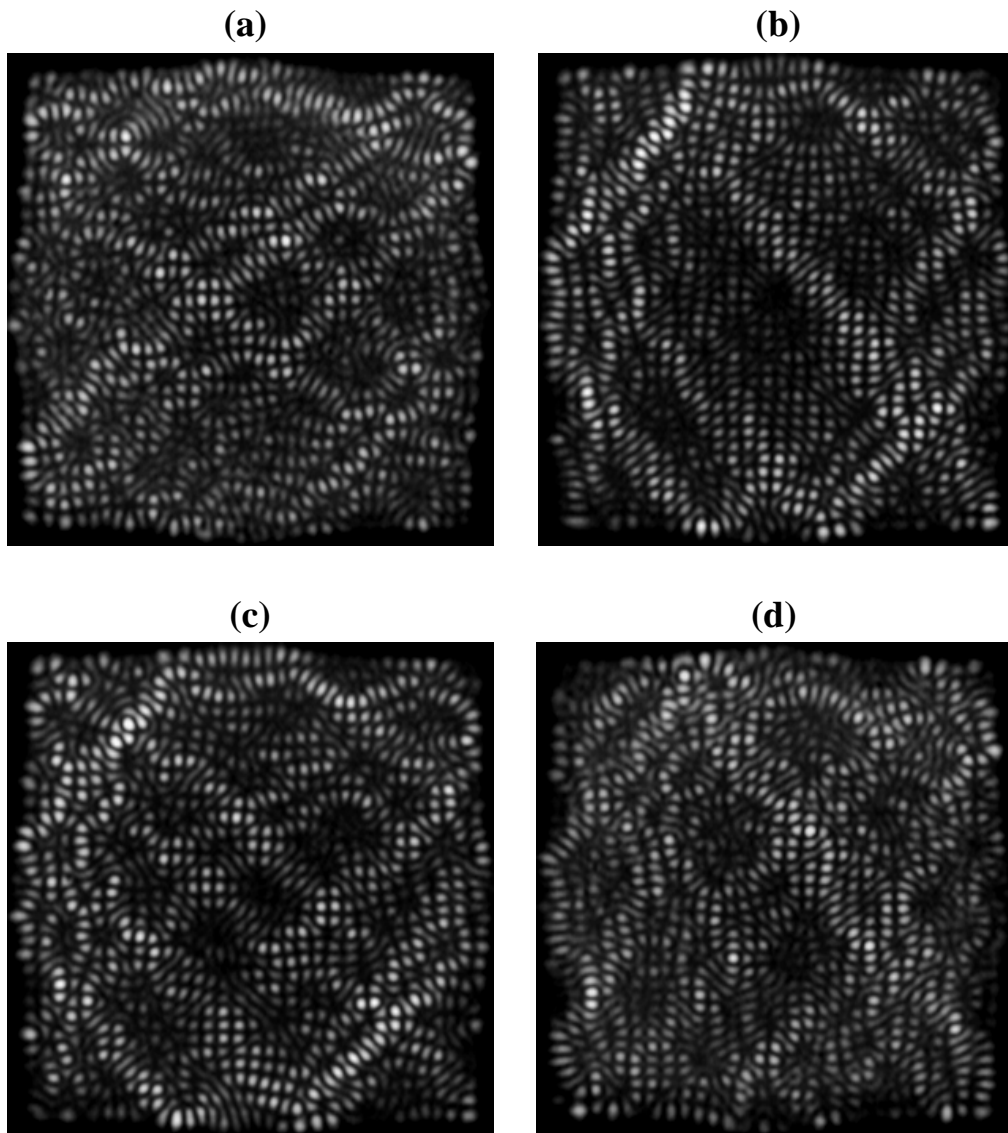


Fig. 5.2-1. Experimental polarization-resolved near-field patterns observed at the operating temperature of $T=265$ K with polarization in (a) 0° (perpendicular) (b) 90° (horizontal) (c) 45° (d) 135° .

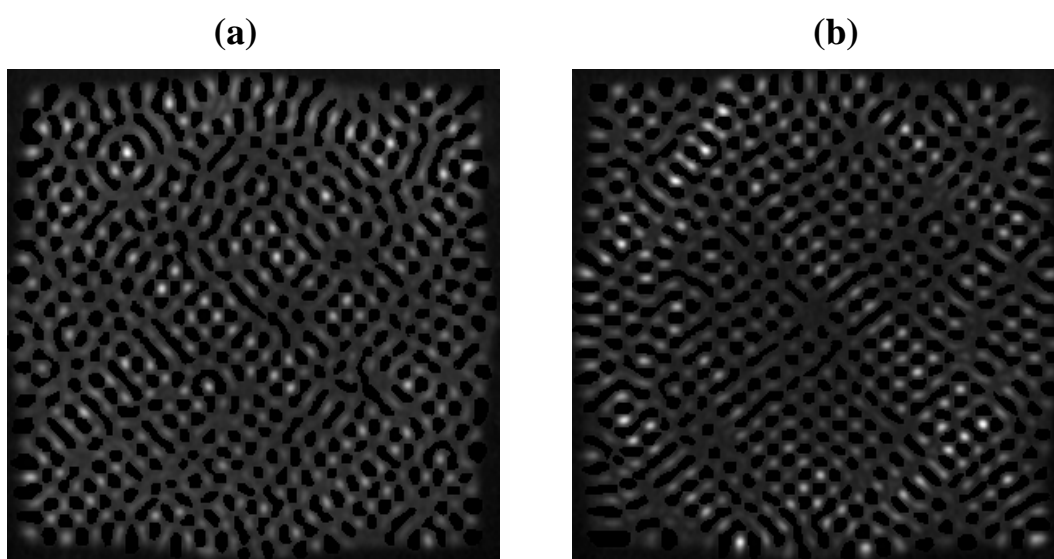


Fig. 5.2-2. (a) and (b) Intensity plots of the positive wave functions $|\psi_p(x_i, y_j)|$ for experimental results shown in Figs. 5.2-1(a) and 5.2-1(b), respectively.

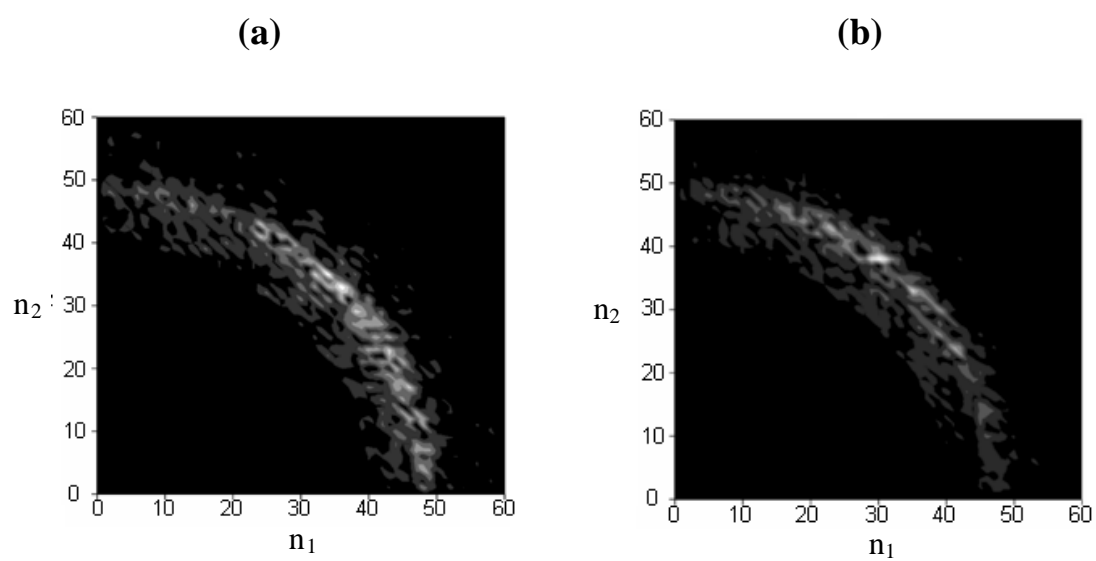


Fig. 5.2-3. (a) and (b) Distribution of the coefficients $|C_{m,n}|$ obtained by Eq. (3.4.6) for experimental results shown in Figs. 5.2-1(a) and (b), respectively.

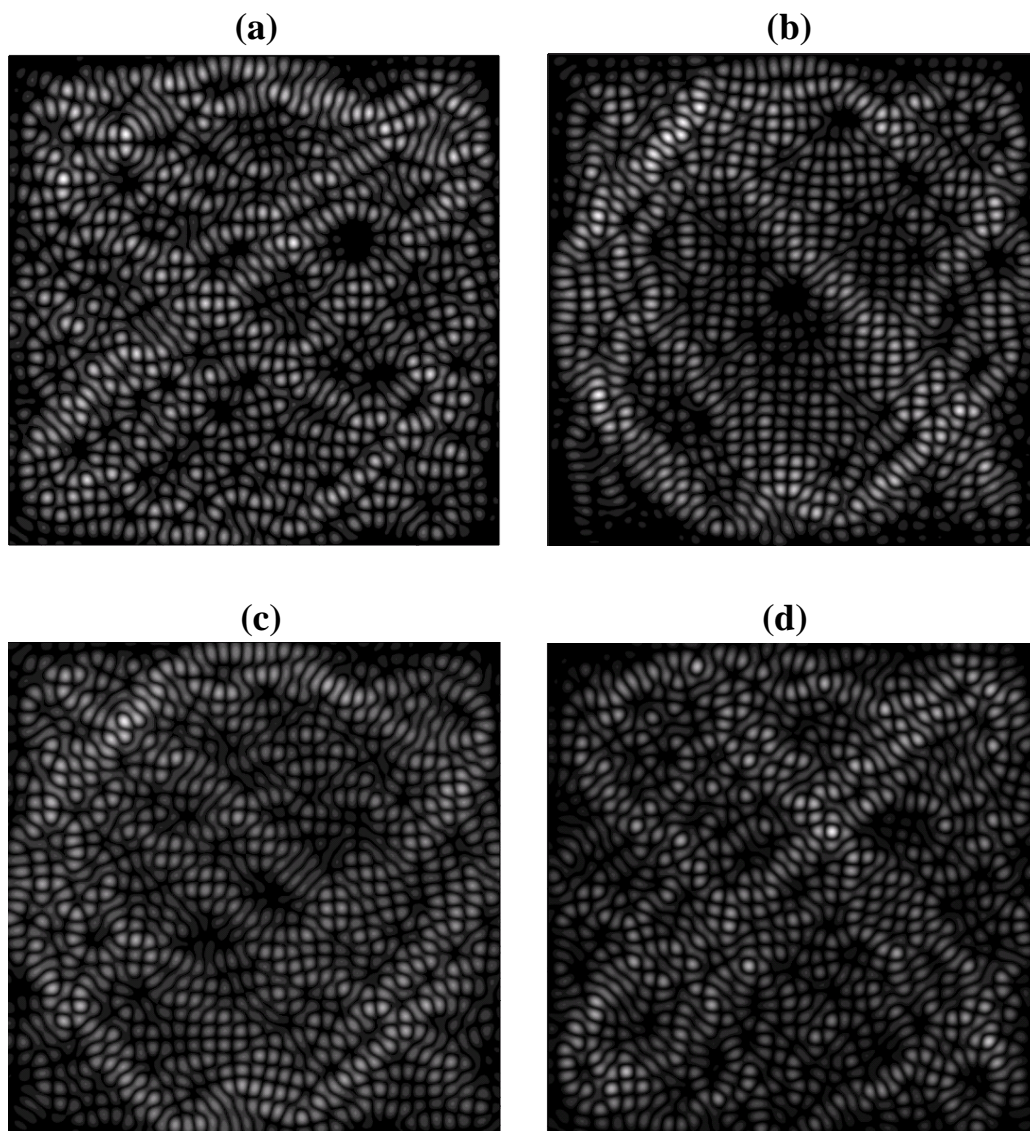


Fig. 5.2-4. (a)-(d): Reconstructed patterns with the eigenfunction expansion method for experimental results shown in Fig. 5.2-1(a)-(d), respectively.

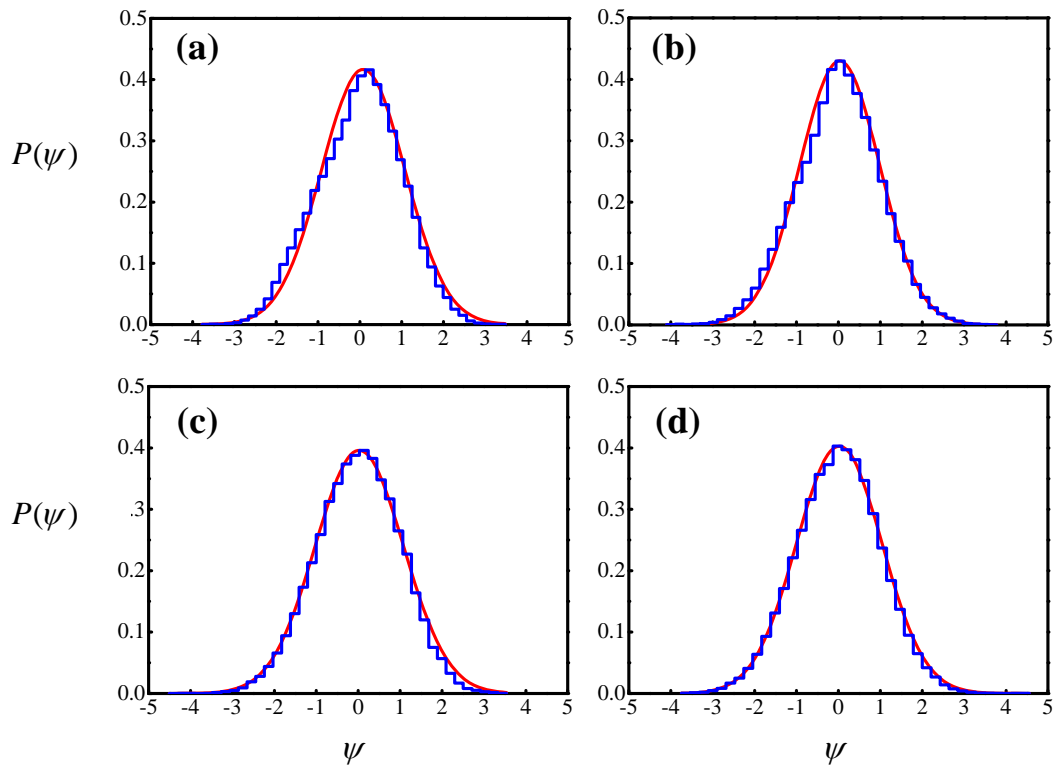


Fig. 5.2-5. Amplitude distributions of the polarization-resolved wave functions (blue step lines) for experimental results shown in Fig. 5.2-1(a)-(d), respectively. Red lines: Gaussian distributions (Eq. (2.3.2)).

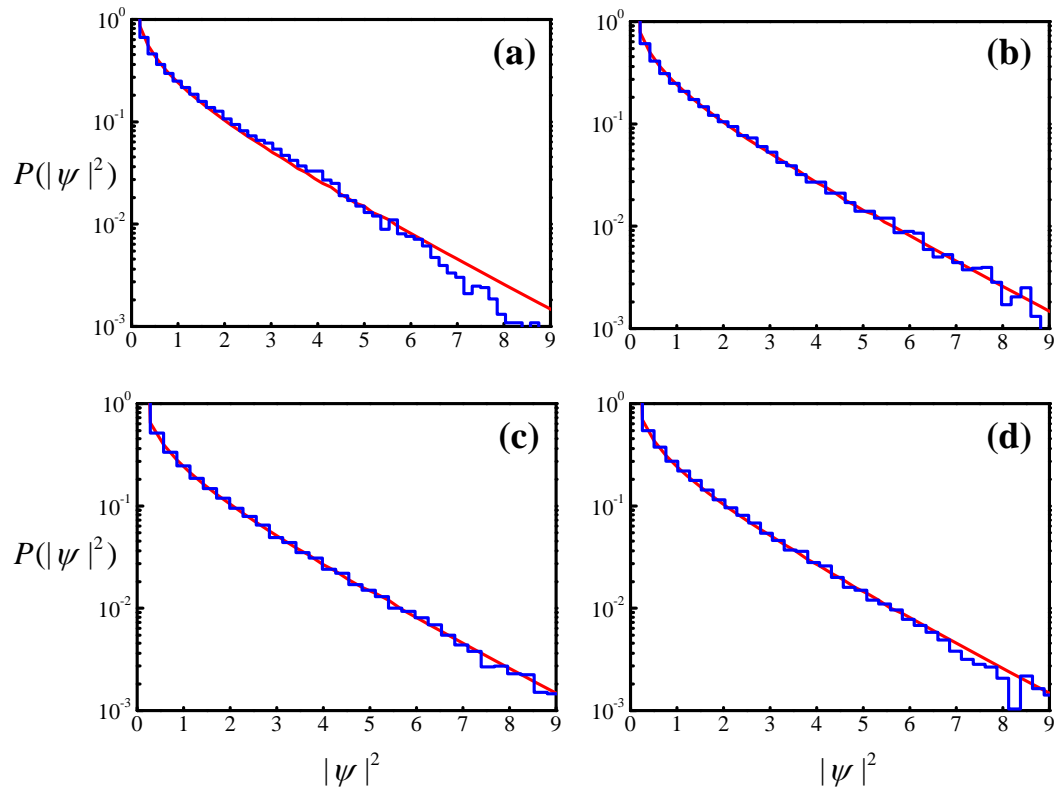


Fig. 5.2-6. Intensity distributions of the polarization-resolved wave functions (blue step lines) for experimental results shown in Fig. 5.2-1(a)-(d), respectively. Red lines: Porter-Thomas distributions (Eq. (2.3.3)).

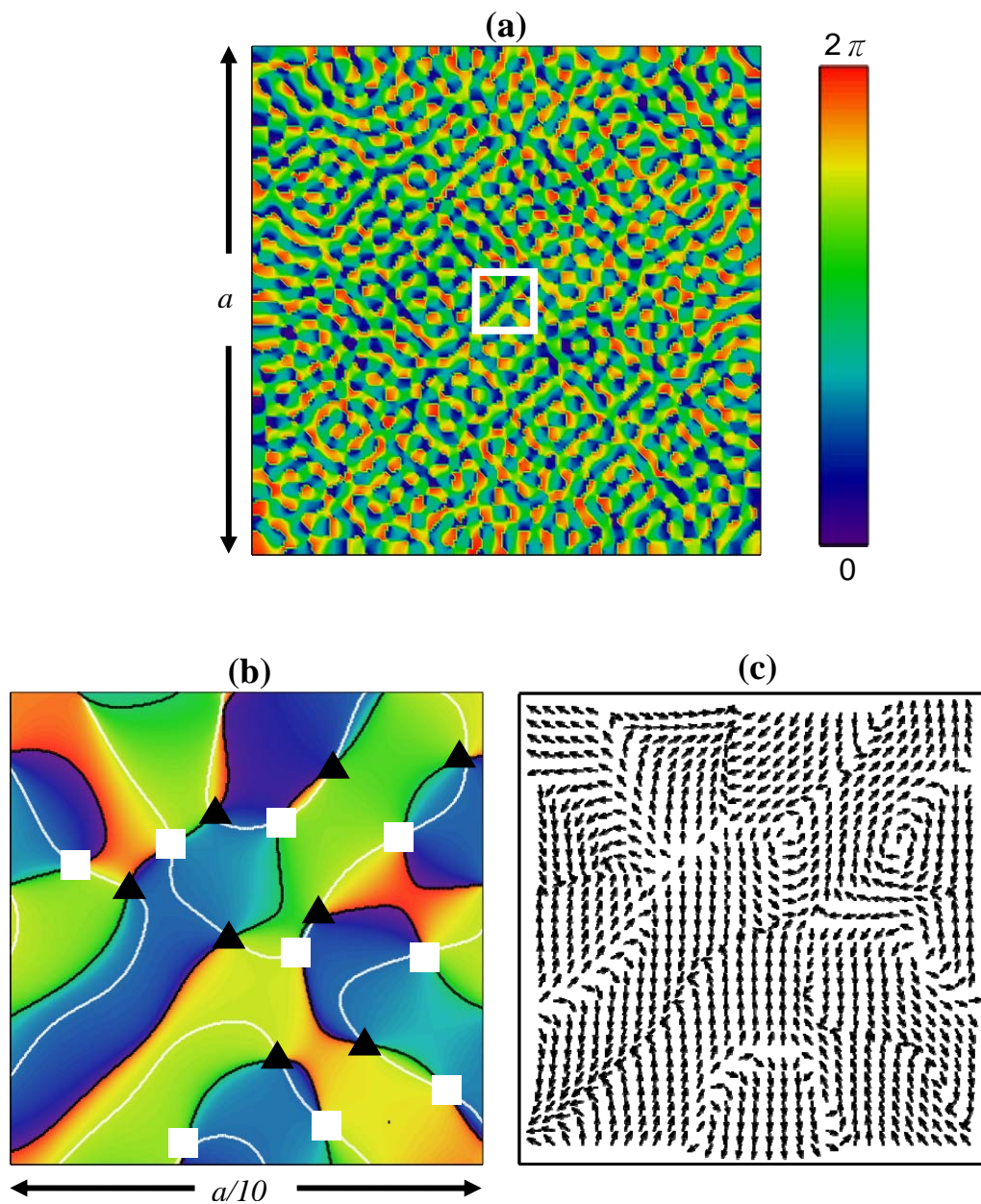
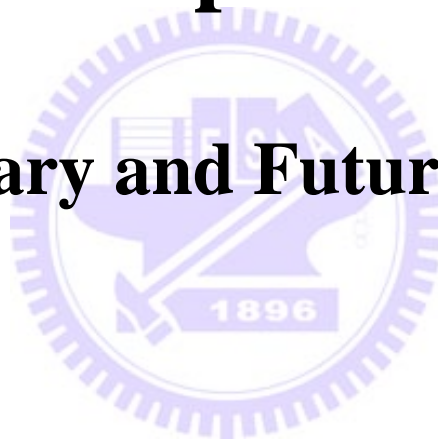


Fig. 5.3-7. (a) The contour plot of the angle function $\Theta_c(x, y)$. (b)-(c) Zoom-in view of the two small regions with the hollow circles on the singularities.

Chapter 6

Summary and Future Work



6.1 Summary

In this work we have studied the analogies between high-order transverse modes of VCSELs and mesoscopic wave functions of quantum billiards in several aspects. In chapter 2 we first introduce the mesoscopic wave functions of square, equilateral-triangular, and chaotic billiards. The properties of chaotic system are demonstrated by means of various eigenstates of stadium billiard. In Sec. 2.3, it can be found that the low-order eigenstates of stadium billiard are just similar to that of rectangular billiard. However, the highly-excited eigenstates can be random patterns or scars. The two kinds of high-order eigenstates correspond to the classical ergodic trajectories and unstable PO, respectively. However, as illustrated in sections 2.1 and 2.2, the eigenstates of regular billiards do not have corresponding classical properties. This inconsistency with Bohr's correspondence for regular eigenstates has long been overlooked. In sections 2.1 and 2.2 we develop the stationary coherent states to generate the so-called superscars, wave functions localized on the stable POs, of square and equilateral-triangular billiards, respectively.

With the analytic expressions of superscars, we can reconstruct the lasing modes observed in VCSEL. Sec. 3.3 presents the typical near-field lasing modes of the square-shaped VCSEL. The agreement between theoretical patterns and experimental results confirm the analogy between near-field transverse modes of VCSELs and mesoscopic wave functions of quantum billiards. We claim that the formation of superscar modes arises from natural imperfection of the real device. In Sec. 3.4 we fabricate a rippled-squared VCSEL that is analogous to the ripple billiard by selective oxidization to generate chaotic modes. Besides, we develop a method of eigenfunction expansion to reconstruct the wave functions of the chaotic lasing modes. With the reconstructed wave functions, we can test the statistical properties of experimentally generated chaotic wave functions. Unlike square VCSEL, in Sec. 3.5

an equilateral-triangular shaped VCSEL are shown to exhibit mixed properties of regular and chaotic systems with no deliberate perturbation. According to this result, we suggest that spontaneous symmetry breaking due to natural imperfection can lead to the emergence of superscar as well as chaotic modes in the integrable but non-separable systems.

The analogies are not only between near-field patterns and stationary wave functions but also between free-space propagation of transverse modes of VCSELs and free time evolution of waves suddenly released from quantum billiards. In Sec. 4.2 we first theoretically investigate the transient dynamics of various wave functions released from square billiard. From our analysis, it can be seen that regular and chaotic wave functions have quite different behaviors. The interesting time evolutions are analogously observed from the free-space propagations of lasing modes emitted from VCSELs. Since the optical OAM density has the same mathematical form as quantum OAM density, we can analyze the OAM carried by the light beams emitted from VCSELs by means of calculating the quantum OAM of abruptly released quantum-billiard wave functions. Although the superscar mode generated by VCSEL is a standing wave and carries zero net OAM, it can be decomposed to two counter-traveling parts which have distinct OAM components and both carry large net OAM. Based on the OAM beam splitter, we propose a scheme to generate light beams carrying large OAM. Besides, temporary vortices formations are found in the time evolution of the chaotic wave function that is suddenly released from quantum billiard. The embedded vortices result in a complex OAM spectrum of chaotic modes and a large OAM variance that is an indicator for the quasi-intrinsic character. Moreover, according to the presented analysis, we suggest that the VCSELs can be employed to generate optical vortices by just slightly defocusing the objective lens.

Due to the isotropic gain region and birefringence, the lasing modes of VCSELs are not necessarily be linearly-polarized as considered in chapter3 and chapter4. The final part of this thesis deal with the near-field transverse modes that form the vector fields, in which the polarization is spatially dependent. In Sec. 5.1, a vector field associated with two superscars is observed in a square VCSEL. With the stationary

coherent states developed in chapter2, we reconstruct the vector field and analyze the vector singularities contained. The vector vortices are shown to locally make up a lattice structure. Quite different from the regular vector field, the orientation phase structure of the vector field comprising two chaotic modes presents a random distribution of vector singularities. However, we do not find any phase extremum in such a complicated phase structure. Since optical polarization corresponds to the electronic spin, the analyses of the vector fields in VCSELs can provide important information for quantum-billiard systems (such as ballistic quantum dots) with consideration on electronic spin.



6.2 Future Works

One of our aims in this thesis is to study the singularities embedded in the lasing modes emitted from VCSELs. Although the near-field amplitude distribution is purely real and contains no singularities, we showed that the amplitude distribution becomes complex scalar field as soon as the light beam propagates out of the laser cavity and carries phase singularities. On the other hand, the vector singularities existing in the real vector field formed by two near-field transverse modes of VCSELs have also been explored. However, the most general state of optical field is the complex vector field which can be achieved by the propagation of the real vector field in near field. In the complex vector field, the light field is generally elliptically-polarized but the polarization is spatially dependent. There are two special conditions of Stokes singularities, C lines and L surfaces [Freu01], in complex vector field. C lines in a light beam are the locations at which the orientation of major and minor axes of the ellipse becomes undefined, i. e. the light field becomes circularly-polarized. On L surfaces the field is linearly-polarized and the handedness of the ellipse is undefined. In the transverse section of a light beam, C lines present as isolated points and L surfaces reduce to continuous lines. Our future researches will be devoted to explore the polarization singularities [Nye83, SDE04, Berr04] in the complex vector fields generated by VCSELs.

Appendix A

Diffraction in Time: Moshinsky's Shutter Problem

Consider the following shutter problem proposed by Moshinsky: A monochromatic non-relativistic particle beam with kinetic energy $E_0 = \hbar^2 k_0^2 / 2m$, moving parallel to the x -axis, incidents on a completely absorbing shutter placed at $x = 0$, as illustrated in Fig. 1.2-1. If the shutter is suddenly opened at $t = 0$, what will be the transient particle current observed at a distance behind the shutter? The problem implies to solve the Schrödinger equation

$$i\hbar \frac{\partial}{\partial t} \psi(x,t) = -\frac{\hbar^2}{2m} \frac{\partial^2}{\partial x^2} \psi(x,t) \quad (\text{A.1})$$

with initial condition

$$\psi(x,0) = \begin{cases} \exp(ik_0 x) & \text{if } x < 0 \\ 0 & \text{otherwise} \end{cases} . \quad (\text{A.2})$$

For a free particle, the time-dependent wave function can be spanned by plane waves

$$\psi(x,t) = \int_{-\infty}^{\infty} \Phi(k) e^{i(kx - \frac{E}{\hbar}t)} dk . \quad (\text{A.3})$$

At $t = 0$ Eq. (A.3) becomes

$$\psi(x,0) = \int_{-\infty}^{\infty} \Phi(k) e^{ikx} dk \quad (\text{A.4})$$

which implies that $\Phi(k)$ is the Fourier component of initial condition and can be obtained by inverse Fourier transform

$$\Phi(k) = \frac{1}{2\pi} \int_{-\infty}^{\infty} \psi(x', 0) e^{-ikx'} dx'. \quad (\text{A.5})$$

To achieve a more general expression we preserve the integral to the final step and first replace the $\Phi(k)$ in Eq. (A.3) by Eq. (A.5)

$$\psi(x, t) = \int_{-\infty}^{\infty} \left[\frac{1}{2\pi} \int_{-\infty}^{\infty} \psi(x', 0) e^{-ikx'} dx' \right] e^{i(kx - \frac{E}{\hbar}t)} dk. \quad (\text{A.6})$$

In this problem we apply the dispersion relation $E = \frac{\hbar^2 k^2}{2m}$ and rearrange the integral

$$\psi(x, t) = \frac{1}{2\pi} \int_{-\infty}^{\infty} \psi(x', 0) \left\{ \int_{-\infty}^{\infty} \exp\left[ik(x-x') - \frac{\hbar k^2}{2m} t \right] dk \right\} dx'. \quad (\text{A.7})$$

After some algebra and a Gaussian integral, Eq. (A.7) becomes

$$\psi(x, t) = \sqrt{\frac{m}{i2\pi\hbar t}} \int_{-\infty}^{\infty} \psi(x', 0) \exp\left[\frac{im(x-x')^2}{2\hbar t} \right] dx'. \quad (\text{A.8})$$

Notice that $\sqrt{\frac{m}{i2\pi\hbar t}} \exp\left[\frac{im(x-x')^2}{2\hbar t} \right]$ is just the propagator of free particle.

Moreover, this equation is similar to the formula of 1D Fresnel diffraction [Good05]

$$\psi(x, z) = \sqrt{\frac{e^{ikz}}{iz\lambda}} \int_{-\infty}^{\infty} \psi(x', 0) \exp\left[\frac{ik(x-x')^2}{2z} \right] dx' \quad (\text{A.9})$$

with the analogies $t \leftrightarrow z$ and $m/\hbar \leftrightarrow k$. We have neglect the phase difference

e^{ikz} in Eq. (A.9) since only probability intensity is concerned.

Inserting the initial condition for the shutter problem Eq. (A.2) into Eq. (A.8), it becomes

$$\psi(x, t) = \sqrt{\frac{m}{i2\pi\hbar t}} \int_{-\infty}^0 e^{ik_0 x'} e^{\frac{im(x-x')^2}{2\hbar t}} dx'. \quad (\text{A.10})$$

Completing the square in the exponent, we obtain

$$\psi(x, t) = \sqrt{\frac{m}{i2\pi\hbar t}} e^{i(k_0 x - \frac{E_0 t}{\hbar})} \int_{-\infty}^0 \exp\{i \frac{m}{2\hbar t} [x' - (x - \frac{\hbar k_0}{m} t)]^2\} dx'. \quad (\text{A.11})$$

Change variable by setting $x' = \sqrt{\frac{\pi\hbar t}{m}} u + (x - \frac{\hbar k_0}{m} t)$ to obtain a more compact expression

$$\psi(x, t) = \sqrt{\frac{1}{2i}} e^{i(k_0 x - \frac{E_0 t}{\hbar})} \sqrt{\frac{m}{\pi\hbar t}} \int_{-\infty}^{\frac{\hbar k_0 t - x}{m}} \exp\{i \frac{\pi}{2} u^2\} du. \quad (\text{A.12})$$

The integral in Eq. (A.12) is associated with the Fresnel integral

$$C(\xi) = \int_0^\xi \cos(\frac{\pi}{2} u^2) du \quad \text{and} \quad S(\xi) = \int_0^\xi \sin(\frac{\pi}{2} u^2) du \quad (\text{A.13})$$

In terms of $C(\xi)$ and $S(\xi)$ the transient wave function of shutter problem is finally given by

$$\psi(x, t) = \sqrt{\frac{1}{2i}} e^{i(k_0 x - \frac{\hbar k_0^2 t}{2m})} \{ [C(\xi(x, t; k_0)) + \frac{1}{2}] + i[S(\xi(x, t; k_0)) + \frac{1}{2}] \} \quad (\text{A.14})$$

, with $\xi(x, t; k_0) = \sqrt{\frac{m}{\pi \hbar t}} \left[\frac{\hbar k_0}{m} t - x \right]$. The red curve in Fig. 1.2-1(b) shows the time variation of the probability density observed at distance d behind the shutter. The blue dotted line indicates the probability of receiving the particles in a classical view. The x – axis has unit in the arrival time T of a classical particle with kinetic energy $E_0 = \frac{\hbar^2 k_0^2}{2m}$ and we have $T = \frac{d}{(\hbar k_0 / m)}$. Notice that in quantum-mechanical aspect one has probability to receive particles before the classical arrival time T . For this deflection into the classically forbidden time zone and temporal interference pattern, which are similar to the behavior of light diffracted by an infinite straight edge, Moshinsky termed the name “diffraction in time [Mosh52].”



Appendix B

Angular Momentum Density of a Light Beam

The electric field and magnetic field for a light beam propagating along z-axis can be expressed as

$$\begin{aligned}\bar{e}(\vec{r}, t) &= \text{Re}[(E_x \hat{a}_x + E_y \hat{a}_y + E_z \hat{a}_z) e^{ikz - i\omega t}] \\ &= \frac{1}{2} \{ [E_x e^{i\phi} + E_x^* e^{-i\phi}] \hat{a}_x + [E_y e^{i\phi} + E_y^* e^{-i\phi}] \hat{a}_y + [E_z e^{i\phi} + E_z^* e^{-i\phi}] \hat{a}_z \}\end{aligned}\quad (\text{B.1})$$

and

$$\begin{aligned}\bar{b}(\vec{r}, t) &= \text{Re}[(B_x \hat{a}_x + B_y \hat{a}_y + B_z \hat{a}_z) e^{ikz - i\omega t}] \\ &= \frac{1}{2} \{ [B_x e^{i\phi} + B_x^* e^{-i\phi}] \hat{a}_x + [B_y e^{i\phi} + B_y^* e^{-i\phi}] \hat{a}_y + [B_z e^{i\phi} + B_z^* e^{-i\phi}] \hat{a}_z \}\end{aligned}\quad (\text{B.2})$$

, where k is wave number, ω is angular frequency, and $\phi = kz - \omega t$. Under paraxial approximation, the amplitudes of electric field are assumed to depends only on (x, y)

$$E_x = E_x(x, y) \quad \text{and} \quad E_y = E_y(x, y). \quad (\text{B.3})$$

From Gauss's law which state that $\nabla \cdot \bar{e} = 0$ for source-free space, we have the relation

$$\nabla \cdot \bar{e} = \frac{\partial E_x}{\partial x} e^{i\phi} + \frac{\partial E_x^*}{\partial x} e^{-i\phi} + \frac{\partial E_y}{\partial y} e^{i\phi} + \frac{\partial E_y^*}{\partial y} e^{-i\phi} + ikE_z e^{i\phi} - ikE_z^* e^{-i\phi} = 0. \quad (\text{B.4})$$

Hence, the longitudinal amplitude can be expressed by transverse amplitudes

$$E_z = \frac{i}{k} \left(\frac{\partial E_x}{\partial x} + \frac{\partial E_y}{\partial y} \right) \quad (\text{B.5})$$

On the other hand, Faraday's Law states that

$$-\frac{\partial \vec{b}}{\partial t} = \nabla \times \vec{e} = \det \begin{pmatrix} \hat{a}_x & \hat{a}_y & \hat{a}_z \\ \frac{\partial}{\partial x} & \frac{\partial}{\partial y} & \frac{\partial}{\partial z} \\ (E_x e^{i\phi} + E_x^* e^{-i\phi}) & (E_y e^{i\phi} + E_y^* e^{-i\phi}) & (E_z e^{i\phi} + E_z^* e^{-i\phi}) \end{pmatrix} \quad (\text{B.6})$$

, we have the following relations:

$$-ikE_y e^{i\phi} + ikE_y^* e^{-i\phi} = i\omega B_x e^{i\phi} - i\omega B_x^* e^{-i\phi} \quad (x\text{-part}); \quad (\text{B.7})$$

$$ikE_x e^{i\phi} - ikE_x^* e^{-i\phi} = i\omega B_y e^{i\phi} - i\omega B_y^* e^{-i\phi} \quad (y\text{-part}); \quad (\text{B.8})$$

$$\left(\frac{\partial E_y}{\partial x} - \frac{\partial E_x}{\partial y} \right) e^{i\phi} + \left(\frac{\partial E_y^*}{\partial x} - \frac{\partial E_x^*}{\partial y} \right) e^{-i\phi} = i\omega B_z e^{i\phi} - i\omega B_z^* e^{-i\phi} \quad (z\text{-part}); \quad (\text{B.9})$$

Then the amplitudes of magnetic field can be also expressed by E_x and E_y :

$$B_x = -\frac{k}{\omega} E_y, \quad B_y = \frac{k}{\omega} E_x, \quad \text{and} \quad B_z = \frac{1}{i\omega} \left(\frac{\partial E_y}{\partial x} - \frac{\partial E_x}{\partial y} \right). \quad (\text{B.10})$$

According to Poynting's theorem, the momentum density $\vec{p}(\vec{r}, t)$ of electromagnetic (EM) waves can be obtained by

$$\vec{p}(\vec{r}, t) = \varepsilon_0 [\vec{e}(\vec{r}, t) \times \vec{b}(\vec{r}, t)]. \quad (\text{B.11})$$

, where ε_0 is the permittivity in vacuum. For a paraxial light beam, the linear

momentum density is then expressed as

$$\bar{p}(\vec{r}, t) = \epsilon_0 \det \begin{pmatrix} \hat{a}_x & \hat{a}_y & \hat{a}_z \\ (E_x e^{i\phi} + E_x^* e^{-i\phi}) & (E_y e^{i\phi} + E_y^* e^{-i\phi}) & (E_z e^{i\phi} + E_z^* e^{-i\phi}) \\ (B_x e^{i\phi} + B_x^* e^{-i\phi}) & (B_y e^{i\phi} + B_y^* e^{-i\phi}) & (B_z e^{i\phi} + B_z^* e^{-i\phi}) \end{pmatrix} \quad (\text{B.12})$$

In the z -part we obtain the relation

$$p_z(\vec{r}, t) = \frac{\epsilon_0}{4} [E_x B_y^* + E_x^* B_y - E_y B_x^* - E_y^* B_x + \text{oscillating terms}] \quad (\text{B.13})$$

In practice, only time-averaging result is concerned

$$\begin{aligned} \langle p_z(\vec{r}, t) \rangle &= \frac{\epsilon_0}{4} [E_x \frac{k}{\omega} E_x^* + E_x^* \frac{k}{\omega} E_x - E_y (-\frac{k}{\omega} E_y^*) - E_y^* (-\frac{k}{\omega} E_y)] \\ &= \frac{\epsilon_0}{2} \frac{k}{\omega} (|E_x|^2 + |E_y|^2) \end{aligned} \quad (\text{B.14})$$

, where $\langle \rangle$ denotes $\frac{\omega}{2\pi} \int_0^{2\pi} dt$. The energy density stored in the EM field is

$W_e = \frac{\epsilon_0}{2} (|E_x|^2 + |E_y|^2)$ and $\langle p_z \rangle = \frac{W_e}{C}$, which means that all the energy stored in

the field all propagates along z -direction.

In the transverse plane, we have

$$\begin{aligned} \langle p_x(\vec{r}, t) \rangle &= \frac{\epsilon_0}{4} [E_y B_z^* + E_y^* B_z - E_z B_y^* - E_z^* B_y] \\ &= \frac{\epsilon_0}{4} \frac{i}{\omega} (E_x \frac{\partial E_x^*}{\partial x} + E_y \frac{\partial E_y^*}{\partial x} - E_y \frac{\partial E_x^*}{\partial y} - E_x^* \frac{\partial E_y}{\partial y} \\ &\quad - E_x^* \frac{\partial E_x}{\partial x} + E_y^* \frac{\partial E_y}{\partial x} - E_y^* \frac{\partial E_x}{\partial y} - E_x \frac{\partial E_y^*}{\partial y}) \end{aligned} \quad (\text{B.15})$$

and

$$\begin{aligned}
 \langle p_y(\vec{r}, t) \rangle &= \frac{\epsilon_0}{4} [E_z B_x^* + E_z^* B_x - E_x B_z^* - E_x^* B_z] \\
 &= \frac{\epsilon_0}{4} \frac{i}{\omega} (E_y \frac{\partial E_y^*}{\partial y} + E_x \frac{\partial E_x^*}{\partial x} + E_x^* \frac{\partial E_x}{\partial y} - E_y \frac{\partial E_x}{\partial x} \\
 &\quad - E_y^* \frac{\partial E_y}{\partial y} + E_x^* \frac{\partial E_x}{\partial x} + E_x \frac{\partial E_x^*}{\partial y} - E_y^* \frac{\partial E_x^*}{\partial x}) .
 \end{aligned} \tag{B.16}$$

It is convenient to define the transverse momentum density by

$$\bar{p}_\perp(x, y, z) = \langle p_x(\vec{r}, t) \rangle \hat{a}_x + \langle p_y(\vec{r}, t) \rangle \hat{a}_y \tag{B.17}$$

and $\bar{p}_\perp(x, y, z)$ can be rearranged as

$$\bar{p}_\perp(x, y, z) = -\frac{\epsilon_0}{2\omega} [\text{Im}(E_x \nabla_\perp E_x^*) + \text{Im}(E_y \nabla_\perp E_y^*) + (\nabla_\perp \times \vec{\sigma})] \tag{B.18}$$

, where $\vec{\sigma} = \text{Im}(E_x^* E_y) \hat{z}$ and $\nabla_\perp = \frac{\partial}{\partial x} \hat{a}_x + \frac{\partial}{\partial y} \hat{a}_y$ is the del operator in the transverse plane. The angular momentum density can then be expressed as

$$\begin{aligned}
 \vec{l}(x, y, z) &= (\vec{r}_\perp - \vec{r}_0) \times \bar{p}_\perp(x, y, z) \\
 &= -\frac{\epsilon_0}{2\omega} \{ \vec{r} \times [\text{Im}(E_x \nabla_\perp E_x^*) + \text{Im}(E_y \nabla_\perp E_y^*)] + \vec{r} \times (\nabla_\perp \times \vec{\sigma}) \}
 \end{aligned} \tag{B.19}$$

, where $\vec{r}_\perp = x \hat{a}_x + y \hat{a}_y$ is the position vector on transverse plane and \vec{r}_0 is location of rotation axis. To further appreciate $\vec{l}(x, y, z)$, we set $\vec{r}_0 = 0$ in Eq. (B.19) and find the following the equality

$$\bar{r}_\perp \times (\nabla_\perp \times \bar{\sigma}) = \nabla_\perp (\bar{r}_\perp \cdot \bar{\sigma}) - (\nabla_\perp \cdot \bar{r}_\perp) \bar{\sigma} = -2\bar{\sigma}. \quad (\text{B.20})$$

In addition expressing the gradient operation in polar coordinate

$$\nabla_\perp = \frac{\partial}{\partial r_\perp} \hat{a}_{r_\perp} + \frac{1}{r_\perp} \frac{\partial}{\partial \phi} \hat{a}_\phi \quad (\text{B.21})$$

and inserting into Eq. (B.19), it can be lead to

$$\bar{r}_\perp \times \text{Im}(E_x \nabla E_x^*) = \text{Im}\{r_\perp \hat{a}_{r_\perp} \times [E_x \frac{\partial E_x^*}{\partial r_\perp} \hat{a}_{r_\perp} + \frac{1}{r_\perp} E_x \frac{\partial E_x^*}{\partial \phi} \hat{\phi}]\} = \text{Im}[E_x \frac{\partial E_x^*}{\partial \phi}] \hat{a}_z \quad (\text{B.22})$$

and

$$\bar{r}_\perp \times \text{Im}(E_y \nabla E_y^*) = \text{Im}\{r_\perp \hat{a}_{r_\perp} \times [E_y \frac{\partial E_y^*}{\partial r_\perp} \hat{a}_{r_\perp} + \frac{1}{r_\perp} E_y \frac{\partial E_y^*}{\partial \phi} \hat{\phi}]\} = \text{Im}[E_y \frac{\partial E_y^*}{\partial \phi}] \hat{a}_z \quad (\text{B.23})$$

Finally, the angular momentum density can be written as

$$\bar{l}(x, y, z) = \left\{ \frac{\varepsilon_0}{2\omega} \text{Im}\left[E_x^* \frac{\partial E_x}{\partial \phi} + E_y^* \frac{\partial E_y}{\partial \phi}\right] + \frac{\varepsilon_0}{\omega} \sigma \right\} \hat{a}_z. \quad (\text{B.24})$$

It can be seen that the angular momentum density $\bar{l}(x, y, z)$ comprises three terms. The first two are in the same form and are essentially the orbital angular momentum (OAM) arose from the variations of x - and y -components of electric field by the polar angle. On the other hand, the third term in Eq. (B.24) is the spin angular momentum (SAM) resulted from the circular polarization of light field. For a light beam to carry angular momentum, the amplitude functions, E_x or E_y , must be complex,.

For a linearly polarized light beam (assuming $E_y = 0$), the transverse linear

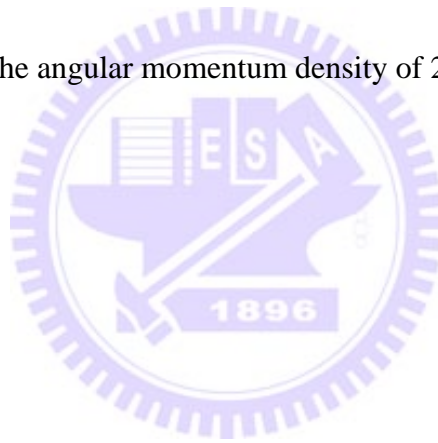
momentum density reduces to

$$\bar{p}_\perp(x, y, z) = \frac{\epsilon_0}{2\omega} [\text{Im}(E_x^* \nabla_\perp E_x)] \quad (\text{B.25})$$

, whose mathematical form is the same as that of probability current density of 2D quantum systems. Moreover, the SAM $\bar{\sigma}$ vanishes and angular momentum density becomes

$$\bar{l}(x, y, z) = \frac{\epsilon_0}{2\omega} \text{Im}(E_x^* \frac{\partial E_x}{\partial \phi}) \quad (\text{B.26})$$

that is also analogous to the angular momentum density of 2D quantum systems.



References

- [ABSW92] L. Allen, M. W. Beijersbergen, R. J. C. Spreeuw, and J. P. Woerdman, “Orbital Angular Momentum of Light and the Transformation of Laguerre-Gaussian Laser Modes,” *Phys. Rev. A* **45**, 8185 (1992).
- [AF99] R. Akis and D. K. Ferry, “Ballistic transport and scarring effects in coupled quantum dots,” *Phys. Rev. B* **59**, 7529 (1999).
- [AS01] T. Ackemann and M. Sondermann, “Characteristics of polarization switching from the low to the high frequency mode in vertical-cavity surface-emitting lasers,” *App. Phys. Lett.* **78**, 3574 (2001).
- [AYL+06] S.-J. An, J. Yoon, J. Lee, and O. Kwon, “Spectral Analysis of a Three-Dimensional Photonic Quantum Ring Laser with a Square Microcavity,” *J. Appl. Phys.* **99**, 033102 (2006).
- [BÅ00] *Quantum Chaos Y2K Proceedings of Nobel Symposium 116*, edited by K. F. Berggren and S. Åberg (World Scientific, Singapore, 2000).
- [BAF+99] J. P. Bird, R. Akis, D. K. Ferry, D. Vasileska, J. Cooper, Y. Aoyagi, and T. Sugano, “Lead-Orientation-Dependent Wave Function Scarring in Open Quantum Dots,” *Phys. Rev. Lett.* **82**, 4691 (1999).
- [BAv+93] M. W. Beijersbergen, L. Allen, H. E. L. O. van der Veen and J. P. Woerdman, “Astigmatic Laser Mode Converters and Transfer of Orbital Angular Momentum,” *Opt. Commun.* **96**, 123 (1993).
- [BB97] M. Brack and R. K. Bhaduri, *Semiclassical Physics* (Addison-Wesley, Reading, MA, 1997), Section 2.7.
- [BBL+91] M. Brambilla, F. Battipede, L. A. Lugiato, V. Penna, F. Prati, C. Tamm, and C. O. Weiss, “Transverse Laser Pattern. I. Phase Singularity Crystals,” *Phys. Rev. A* **43**, 5090 (1991).

- [BCKW94] M. W. Beijersbergen, R. P. C. Coerwinkel, M. Kristensen and J. P. Woerdman, “Helical-wavefront laser beams produced with a spiral phaseplate,” *Opt. Commun.* **112**, 321 (1994).
- [BCSR99] P. Besnard, M. L. Charès, G. M. Stéphan, and F. Robert, “Switching between polarized modes of a vertical-cavity surface-emitting laser by isotropic optical feedback,” *J. Opt. Soc. Am. B* **16**, 1059 (1999).
- [BDF+06] E. Bogomolny, B. Dietz, T. Friedrich, M. Miski-Oglu, A. Richter, F. Schäfer, and C. Schmit, “First Experimental Observation of Superscars in a Pseudointegrable Barrier Billiard,” *Phys. Rev. Lett.* **97**, 254102 (2006).
- [Berr77] M. V. Berry, “Regular and Irregular Semiclassical Wave Functions,” *J. Phys. A: Math. Gen.* **10**, 2083 (1977).
- [Berr80] M.V. Berry, “Some geometric aspects of wave motion: wavefront dislocations, diffraction catastrophes, diffractals,” in *Geometry of the Laplace operator* edited by R. Osserman and A. Weinstein, *Proc. Symp. App. Maths*, AMS, 13 (1980).
- [Berr83] M. V. Berry, “Semiclassical Mechanics of regular and irregular motion,” in *Les Houches Lecture Series Session XXXVI*, edited by G. Iooss, R. H. G. Helleman and R. Stora, North Holland, Amsterdam, 171 (1983).
- [Berr87] M. V. Berry, “Quantum Chaology,” *Proc. R. Soc. Lon. A* **413**, 183 (1987).
- [Berr98] M. V. Berry, “Much ado about nothing: optical dislocation lines (phase singularities, zeros, vortices...),” in *Singular optics*, Edited by M. S. Soskin, Frunzenskoe, Crimea, SPIE, vol.3487, p.1 (1998).
- [Berr04] M.V. Berry, “The electric and magnetic polarization singularities of paraxial waves,” *J. Opt. A: Pure Appl. Opt.* **6**, 475 (2004).
- [BR84] M. V. Berry and M. Robnik, “Semiclassical level spacings when regular and chaotic orbits coexist,” *J. Phys. A: Math. Gen.* **17**, 2413 (1984).

References

- [BS04] E. Bogomolny and C. Schmit, “Structure of Wave Functions of Pseudointegrable Billiards,” *Phys. Rev. Lett.* **92**, 244102 (2004).
- [BSS02] K. F. Berggren, A. F. Sadreev, and A. A. Starikov, “Crossover from Regular to Irregular Behavior in Current Flow through Open Billiards,” *Phys. Rev. E* **66**, 016218 (2002).
- [BTB+02] S. Barland, J. R. Tredicce, M. Brambilla, L. A. Lugiato, S. Balle, M. Giudici, T. Maggipinto, L. Spinelli, G. Tissoni, T. Knödl, M. Miller, and R. Jäger, “Cavity solitons as pixels in semiconductor microcavities,” *Nature* **419**, 699 (2002).
- [BU94] P. Bellomo and T. Uzer, “State Scarring by ‘Ghosts’ of Periodic Orbits,” *Phys. Rev. E* **50**, 1886 (1994).
- [Buni79] L. A. Bunimovich, “On the Ergodic Properties of Nowhere Dispersing Billiards”, *Commun Math Phys* **65**, 295 (1979).
- [BVD65] *Quantum Theory of Angular Momentum*, edited by L. C. Biedenharn and H. Van Dam, (Academic Press, New York, U. S. 1965).
- [BZ97] C. Brukner and A. Zeilinger, “Diffraction of matter waves in space and in time,” *Phys. Rev. A* **56**, 3804 (1997).
- [CC+97] W. W. Chow, K. D. Choquette, M. Haserot-Crowford, K. L. Lear, and Hadley, “Design, Fabrication, and Performance of Infrared and Visible Vertical-Cavity Surface-Emitting Lasers,” *IEEE J. Quantum Electron.* **33**, 1810 (1997).
- [CH96] P. A. Chinnery and V. F. Humphrey, “Experimental visualization of acoustic resonances within a stadium-shaped cavity,” *Phys. Rev. E* **53**, 272 (1996).
- [CH99] M. C. Cross and P. C. Hohenberg, “Pattern formation outside of equilibrium,” *Rev. Mod. Phys.* **65**, 851 (1993).
- [CH03] Y. F. Chen and K. F. Huang, “Vortex Formation of Coherent Waves in Nonseparable Mesoscopic Billiards,” *Phys. Rev. E* **68**, 066207 (2003).
- [CHL02] Y. F. Chen, K. F. Huang, and Y. P. Lan, “Localization of wave

- patterns on classical periodic orbits in a square billiard,” *Phys. Rev. E* **66**, 046215 (2002).
- [CHLL03a] Y. F. Chen, K. F. Huang, H. C. Lai, and Y. P. Lan, “Rules of selection for spontaneous coherent states in mesoscopic systems: Using the microcavity laser as an analog study,” *Phys. Rev. E* **68**, 026210 (2003).
- [CHLL03b] Y. F. Chen, K. F. Huang, H. C. Lai, and Y. P. Lan, “Observation of Vector Vortex Lattices in Polarization States of an Isotropic Microcavity Laser,” *Phys. Rev. Lett.* **90**, 053904 (2003).
- [CKH+00] H. C. Chang, G. Kioseoglou, E. H. Lee, J. Haetty, M. H. Na, Y. Xuan, H. Luo, A. Petrou, and A. N. Cartwright, “Lasing Modes in Equilateral-Triangular Laser Cavities,” *Phys. Rev. A* **62**, 013816 (2000).
- [CL01] Y. F. Chen and Y. P. Lan, “Transverse pattern formation of optical vortices in a microchip laser with a large Fresnel number,” *Phys. Rev. A* **65**, 013802 (2001).
- [CLH06] Y. F. Chen, T. H. Lu, and K. F. Huang, “Observation of spatially coherent polarization vector fields and visualization of vector singularities,” *Phys. Rev. Lett.* **96**, 033901 (2006).
- [CLO+97] L. Christensson, H. Linke, P. Omling, P. E. Lindelof, I. V. Zozoulenko, and K. -F. Berggren, “Classical and Quantum Dynamics of Electrons in Open Equilateral Triangular Billiards,” *Phys. Rev. B* **57**, 12306 (1997).
- [CLS+07] C. C. Chen, C. C. Liu, K. W. Su, T. H. Lu, Y. F. Chen, and K. F. Huang, “Statistical properties of experimental coherent waves in microcavity lasers: Analogous study of quantum billiard wave functions,” *Phys. Rev. E* **75**, 046202 (2007).
- [CMPL05] Y. Colombe, B. Mercier, H. Perrin, and V. Lorent, “Diffraction of a Bose-Einstein condensate in the time domain,” *Phys. Rev. A* **72**, 061601R (2005).

References

- [CSCH08] C. C. Chen, K. W. Su, Y. F. Chen, and K. F. Huang, “Various High-Order Modes in Vertical-Cavity Surface-Emitting Lasers with Equilateral Triangular Lateral Confinement,” *Opt. Lett.* **33**, 509 (2008).
- [CSL+07] C. C. Chen, K. W. Su, T. H. Lu, C. C. Liu, Y. F. Chen, and K. F. Huang, “Generation of two-dimensional chaotic vector fields from a surface-emitting semiconductor laser Analysis of vector singularities,” *Phys. Rev. E* **76**, 026219 (2007).
- [CSG+03] R. Crook, C.G. Smith, A.C. Graham, I. Farrer, H. E. Beere, and D. A. Ritchie, “Imaging Fractal Conductance Fluctuations and Scarred Wave Functions in a Quantum Billiard,” *Phys. Rev. Lett.* **91**, 246803 (2003).
- [CYC+09] C. C. Chen, Y. T. Yu, R. C. C. Chen, Y. J. Huang, K. W. Su, Y. F. Chen, and K. F. Huang, “Transient Dynamics of Coherent Waves Released from Quantum Billiards and Analogous Observation from Free-Space Propagation of Laser Modes,” *Phys. Rev. Lett.* **102**, 044101 (2009).
- [CZDV06] J. Courtial, R. Zambrini, M. R. Dennis, and M. Vasnetsov, “Angular Momentum of Optical Vortex Arrays,” *Opt. Express* **14**, 938 (2006).
- [DAL06] P. Z. Dashti, F. Alhassen, and H. P. Lee, “Observation of Orbital Angular Momentum Transfer between Acoustic and Optical Vortices in Optical Fibers,” *Phys. Rev. Lett.* **96**, 043604 (2006).
- [DCM02] F. Delgado, H. Cruz, and J. G. Muga, “The transient response of a quantum wave to an instantaneous potential step switching,” *J. Phys. A: Math Gen.* **35**, 10377 (2002).
- [DD04] D. Dragoman and M. Dragoman, *Quantum-Classical Analogies* (Springer-Verlag, Berlin Heidelberg, 2004) and references cited therein.
- [Denn01] M. R. Dennis, *Topological Singularities in Wave Fields*, PhD thesis, University of Bristol, 2001.

References

- [dGP93] P. G. de Gennes and J. Prost, *The physics of Liquid crystals* (Oxford University Press, New York, 1993), 2nd Ed.
- [dCMM07] A. del Campo, J. G. Muga, and M. Moshinsky, “Time modulation of atom sources,” *J. Phys. B* **40**, 975 (2007).
- [dCL+08] A. del Campo, I. Lizuain, M. Pons, J. G. Muga, and M. Moshinsky, “Atom laser dynamics in a tight waveguide,” *J. of Phys.: Conference Series* **99**, 012003 (2008).
- [DG27] C. Davisson and L. H. Germer, “Diffraction of Electrons by a Crystal of Nickel,” *Phys. Rev.* **30**, 705 (1927).
- [DG86] D. Delande and J. C. Gay, “Quantum Chaos and Statistical Properties of Energy Levels: Numerical Study of the Hydrogen Atom in a Magnetic Field,” *Phys. Rev. Lett.* **57**, 2006 (1986).
- [DLM01] V. Doya, O. Legrand, and F. Mortessagne, “Light Scarring in an Optical Fiber,” *Phys. Rev. Lett.* **88**, 014102 (2001).
- [DMA+05] F. Delgado, J. G. Muga, D. G. Austing, and G. García-Calderón, “Resonant tunneling transients and decay for a one-dimensional double barrier potential,” *J. Appl. Phys.* **97**, 013705 (2005)
- [dSF01] J. A. de Sales and J. Florencio, “Bohmian quantum trajectories in a square billiard in the bouncing ball regime,” *Physica A* **290**, 101 (2001).
- [DR02] M. A. Doncheski and R. W. Robinett, “Quantum Mechanical Analysis of the Equilateral Triangular Billiard: Periodic Orbit Theory and Wave Packet Revivals,” *Ann. Phys. (N.Y.)* **299**, 208 (2002).
- [EFM+96] K. J. Ebeling, U. Fiedler, R. Michalzik, G. Reiner and B. Weigl, “Efficient vertical cavity surface emitting laser diodes for high bit rate optical data transmission,” *Int. J. Electron. Commun.* **50**, 316 (1996).
- [Enge97] A translation of the paper appears in *The Collected Papers of Albert Einstein*, vol. 6, A. Engel, trans., Princeton U. Press, Princeton, NJ (1997), p. 434.

References

- [Erdo92] T. Erdogan, "Circularly symmetric operation of a concentric-circle-grating, surface-emitting, AlGaAs/GaAs quantum-well semiconductor laser," *Appl. Phys. Lett.* **60**, 1921 (1992).
- [FAAP08] S. Franke-Arnold, L. Allen, and M. Padgett, "Advances in optical angular momentum," *Laser & Photon. Rev.* **2**, 299 (2008).
- [Freu95] I. Freund, "Saddles, singularities, and extrema in random phase fields," *Phys. Rev. E* **52**, 2348 (1995).
- [Freu01] I. Freund, "Polarization Flowers," *Opt. Commun.* **199**, 47 (2001).
- [GAL98] K. S. Giboney, L. B. Aronson, and B. E. Lemoff, "The ideal light source for datanets," *IEEE Spectr.* **2**, 43 (1998).
- [GBF+05] T. Gensty, K. Becker, I. Fischer, W. Elsässer, C. Degen, P. Debernardi, and G. P. Bava, "Wave Chaos in Real-World Vertical-Cavity Surface-Emitting Lasers," *Phys. Rev. Lett.* **94**, 233901 (2005).
- [GCN+98] C. Gmachl, F. Capasso, E. E. Narimanov, J. U. Nöckel, A. D. Stone, J. Faist, D. L. Sivco, A. Y. Cho, "High-Power Directional Emission from Microlasers with Chaotic Resonators," *Science* **280**, 1556 (1998).
- [GCP+04] G. Gibson, J. Courtial, M. J. Padgett, M. Vasnetsov, V. Pas'ko, S. M. Barnett, and S. Franke-Arnold, *Opt. Express* **12**, 5448 (2004).
- [GGK+96] C. Gmachl, A. Golshani, A. Kock, E. Gornik, J. F. Walker, "Vertical-cavity surface-emitting lasers with monolithically integrated modulators," *Microcavities and photonic bandgaps: physics and applications, NATO ASI series, series E, applied science* **324**, 387 (1996).
- [Gil93] L. Gil, "Vector order parameter for an unpolarized laser and its vectorial topological defects," *Phys. Rev. Lett.* **70**, 162 (1993).
- [Godo02] S. Godoy, "Diffraction in Time: Fraunhofer and Fresnel Dispersion by a Slit," *Phys. Rev. A* **65**, 042111 (2002).
- [Godo03] S. Godoy, "Diffraction in time of particles released from spherical traps," *Phys. Rev. A* **67**, 012102 (2003).

References

- [Good05] J. W. Goodman, *Introduction to Fourier Optics 3rd Ed.*, (Roberts & Company, Engle, Colorado, U. S. 2005).
- [GPS02] H. Goldstein, C. P. Poole, and J. L. Safko, *Classical Mechanics 3rd Ed.*, (Addison Wesley, San Francisco, U. S. 2002).
- [GL99] J. P. Gollub and J. S. Langer, "Pattern formation in nonequilibrium physics," *Rev. Mod. Phys.* **71**, S396 (1999).
- [GM05] E. Granot and A. Marchewka, "Generic short-time propagation of sharp-boundaries wave packets," *Europhys. Lett.* **72**, 341 (2005).
- [GMJ+99] M. Grabherr, M. Miller, R. Jäger, R. Michalzik, U. Martin, H. J. Unold, and K. J. Ebeling, "High-Power VCSEL's: Single Devices and Densely Packed 2-D-Arrays," *IEEE J. Selected Topics Quantum Electron.* **5**, 495 (1999).
- [Gutz71] M. C. Gutzwiller, "Periodic Orbits and Classical Quantization Conditions," *J. Math. Phys.* **12**, 343 (1971).
- [Gutz80] M. C. Gutzwiller, "Classical Quantization of a Hamiltonian with Ergodic Behavior," *Phys. Rev. Lett.* **45**, 150 (1980).
- [Gutz90] M. C. Gutzwiller, *Chaos in Classical and Quantum Mechanics* (Springer-Verlag, New York, 1990), and references cited therein.
- [GZT54] J. P. Gordon, H. J. Zeiger, and C. H. Townes, "Molecule Microwave Oscillator and New Hyperfine Structure in the Microwave Spectrum of NH₃," *Phys. Rev.* **95**, 282 (1954).
- [Haak91] F. Haake, *Quantum Signatures of Chaos* (Springer-Verlag, Berlin, 1991), and references cited therein.
- [Haus84] H. A. Haus, *Waves and Fields in Optoelectronics*, (Prentice-Hall, New Jersey, U. S., 1984).
- [HCLL02] K. F. Huang, Y. F. Chen, H. C. Lai, and Y. P. Lan, "Observation of the Wave Function of a Quantum Billiard from the Transverse Patterns of Vertical Cavity Surface Emitting Lasers," *Phys. Rev. Lett.* **89**, 224102 (2002).
- [Hell84] E. J. Heller, "Bound-State Eigenfunctions of Classically Chaotic

- Hamiltonian Systems: Scars of Periodic Orbits,” *Phys. Rev. Lett.* **53**, 1515 (1984).
- [HFG+98] T. Hils, J. Felberg, R. Gähler, W. Gläser, R. Golub, K. Habicht, and P. Wille, “Matter-wave optics in the time domain: Results of a cold-neutron experiment,” *Phys. Rev. A* **58**, 4784 (1998).
- [HFH+95] H. He, M. E. J. Friese, N. R. Heckenberg, and H. Rubinsztein-Dunlop, “Direct Observation of Transfer of Angular Momentum to Absorptive Particles from a Laser Beam with a Phase Singularity,” *Phys. Rev. Lett.* **75**, 826 (1995).
- [HGW00] Y.-Z. Huang, W.-H. Guo, and Q.-M. Wang, “Influence of Output Waveguide on Mode Quality Factor in Semiconductor Microlasers with an Equilateral Triangle Resonator,” *Appl. Phys. Lett.* **77**, 3511 (2000).
- [HGYL01] Y.-Z. Huang, W.-H. Guo, L.-J. Yu, and H.-B. Lei, “Analysis of Semiconductor Microlasers with an Equilateral Triangle Resonator by Rate Equations,” *IEEE J. Quantum Electro.* **37**, 1259 (2001).
- [HHMC99] S. P. Hegarty, G. Huyet, J. G. McInerney, and K. D. Choquette, “Pattern Formation in the Transverse Section of a Laser with a Large Fresnel Number,” *Phys. Rev. Lett.* **82**, 1434 (1999).
- [HHP+99] S. P. Hegarty, G. Huyet, P. Porta, J. G. McInerney, K. D. Choquette, K. M. Geib, and H. Q. Hou, “Transverse-mode structure and pattern formation in oxide-confined vertical-cavity semiconductor lasers,” *J. Opt. Soc. Am. B* **16**, 2060 (1999).
- [HMS+92] N. R. Heckenberg, R. McDuff, C. P. Smith, H. Rubinsztein-Dunlop, and M. J. Wagner, “Laser Beams with Phase Singularities,” *Opt. Quant. Electron.* **24**, 951 (1992).
- [HTW+91] G. Hasnain, K. Tai, Y.H. Wang, J.D. Wynn, K.D. Choquette, B.E. Weir, N.K. Dutta, and A.Y. Cho, “Monolithic integration of photodetector with vertical cavity surface emitting laser,” *IEEE Electro. Lett.* **27**, 1630 (1991).

References

- [JHS+91] J. L. Jewell, J. P. Harbison, A. Scherer, Y. H. Lee, and L. T. Florez, “Vertical-Cavity Surface-Emitting Lasers : Design, Growth, Fabrication, Characterization,” *IEEE J. Quantum Electro.* **27**, 1332 (1991).
- [JHT+89] J. L. Jewell, K. F. Huang, K. Tai, Y. H. Lee, S. L. McCall, and A. Y. Cho, “Vertical cavity single quantum well laser,” *Appl. Phys. Lett.* **55**, 424 (1989).
- [KAG01] A. Kudrolli, M. C. Abraham, and J. P. Gollub, “Scarred patterns in surface waves,” *Phys. Rev. E* **63**, 026208 (2001).
- [KDR+08] I. Kardosh, F. Demaria, F. Rinaldi, S. Menzel, and R. Michalzik, “High-Power Single Transverse Mode Vertical-Cavity Surface-Emitting Lasers With Monolithically Integrated Curved Dielectric Mirrors,” *IEEE Photon. Technol. Lett.* **20**, 2084 (2008).
- [KKI89] F. Koyama, S. Kinoshita, and K. Iga, “Room-temperature continuous wave lasing characteristics of a GaAs vertical cavity surface-emitting laser,” *Appl. Phys. Lett.* **55**, 221 (1989).
- [KKS95] A. Kudrolli, V. Kidambi, and S. Sridhar, “Experimental Studies of Chaos and Localization in Quantum Wave Functions,” *Phys. Rev. Lett.* **75**, 822 (1995).
- [KKS99] D.L. Kaufman, I. Kosztin, and K. Schulten, “Expansion method for stationary states of quantum billiards,” *Am. J. Phys.* **67**, 133 (1999).
- [KKS+07] V. V. Kotlyar, A. A. Kovalev, V. A. Soifer, C. S. Tuvey and J. A. Davis, “Sidelobe Contrast Reduction for Optical Vortex Beams Using a Helical Axicon,” *Opt. Lett.* **32**, 921 (2007).
- [KL91] H. J. Korsch and J. Lang, “A new integrable gravitational billiard,” *J. Phys. A* **24**, 45 (1991).
- [Kroe63] H. Kroemer, “A Proposed Class of Heterojunction Injection Lasers,” *Proc. IEEE* **51**, 1782 (1963).
- [KSL+08] A. M. Kasten, J. D. Sulkin, Paul O. Leisher, David K. McElfresh, David K. McElfresh, and Kent D. Choquette, “Manufacturable

- Photonic Crystal Single-Mode and Fluidic Vertical-Cavity Surface-Emitting Lasers,” *IEEE J. Selected Topics Quantum Electron.* **14**, 1123 (2008).
- [KTS+97] T. Kuga, Y. Torii, N. Shiokawa, T. Hirano, Y. Shimizu, and H. Sasada, “Novel Optical Trap of Atoms with a Doughnut Beam,” *Phys. Rev. Lett.* **78**, 4713 (1997).
- [Lam98] L. Lam, *Nonlinear Physics for Beginners- Fractals, Chaos, Solitons, Pattern Formation, Cellular Automata, and Complex Systems* (World Scientific, Singapore, 1998).
- [LB85] W. K. Li and S. M. Blinder, “Solution of the Schrödinger Equation for a Particle in an Equilateral Triangle,” *J. Math. Phys.* **26**, 2784 (1985).
- [LCG+04] Q.-Y. Lu, X.-H. Chen, W.-H. Guo, L.-J. Yu, Y.-Z. Huang, J. Wang, and Y. Luo, “Mode Characteristics of Semiconductor Equilateral Triangle Microcavities with Side Length of 5-20 μm ,” *IEEE Photon. Technol. Lett.* **16**, 359 (2004).
- [LCH07] T. H. Lu, Y. F. Chen, and K. F. Huang, “Generation of polarization-entangled optical coherent waves and manifestation of vector singularity patterns,” *Phys. Rev. E* **75**, 026614 (2007).
- [LMH+06] A. Löfgren, C. A. Marlow, T. E. Humphrey, I. Shorubalko, R. P. Taylor, P. Omling, R. Newbury, P. E. Lindelof, and H. Linke, “Symmetry of magnetoconductance fluctuations of quantum dots in the nonlinear response regime,” *Phys. Rev. B* **73**, 235321 (2006)
- [LLHZ06] M. Lebental, J. S. Lauret, R. Hierle, and J. Zyss, “Highly Directional Stadium-Shaped Polymer Microlasers,” *Appl. Phys. Lett.* **88**, 031108 (2006).
- [LLM06] R. T. Liu, S. S. Liaw, and P. K. Maini, “Two-stage Turing model for generating pigment patterns on the leopard and the jaguar,” *Phys. Rev. E* **74**, 011914 (2006).
- [LLP+05] H. C. Lin, D. A. Louderback, G. W. Pickrell, M. A. Fish, J. J. Hindi, M. C. Simpson, and P. S. Guilfoyle, “Vertical-Cavity

References

- Surface-Emitting Lasers With Monolithically Integrated Horizontal Waveguides,” *IEEE Photon. Tech. Lett.* **17**, 10 (2005).
- [LLZ+07] M. Leental, J. S. Lauret, J. Zyss, C. Schmit, and E. Bogomolny, “Directional emission of Stadium-Shaped Micro-Lasers,” *Phys. Rev. A* **75**, 033806 (2007).
- [LRW02] W. Li, L. E. Reichl, and B. Wu, “Quantum Chaos in Ripple Billiard,” *Phys. Rev. E* **65**, 056220 (2002).
- [LSW+05] F. Lindner, M. G. Schätzel, H. Walther, A. Baltuška, E. Gouliemakis, F. Krausz, D. B. Milošević, D. Bauer, W. Becker, and G. G. Paaulus, “Attosecond Double-Slit Experiment,” *Phys. Rev. Lett.* **95**, 040401 (2005).
- [MAH+99] M. R. Matthews, B. P. Anderson, P. C. Haljan, D. S. Hall, C. E. Wieman, and E. A. Cornell, “Vortices in a Bose-Einstein Condensate,” *Phys. Rev. Lett.* **83**, 2498 (1999).
- [Maim60] T. H. Maiman, “Stimulated optical radiation in ruby,” *Nature* **187**, 493 (1960).
- [MDLM07] C. Michel, V. Doya, O. Legrand, and F. Mortessagne, “Selective Amplification of Scars in a Chaotic Optical Fiber,” *Phys. Rev. Lett.* **99**, 224101 (2007).
- [MFDM03] V. R. Misko, V. M. Fomin, J. T. Devreese, and V. V. Moshchalkov, “Stable Vortex-Antivortex Molecules in Mesoscopic Superconducting Triangles,” *Phys. Rev. Lett.* **90**, 147003 (2003).
- [MFM95] M. S. Miguel, Q. Feng, and J. V. Moloney, “Light-polarization dynamics in surface-emitting semiconductor lasers,” *Phys. Rev. A* **52**, 1728 (1995).
- [MK79] S. W. McDonald and A. N. Kaufman, “Spectrum and Eigenfunctions for a Hamiltonian with Stochastic Trajectories,” *Phys. Rev. Lett.* **42**, 1189 (1979).
- [MK88] S. W. McDonald and A. N. Kaufman, “Wave chaos in the stadium: Statistical properties of short-wave solutions of the Helmholtz

References

- equation,” *Phys. Rev. A* **37**, 3067 (1988).
- [MMN64] J. C. Marinace, A. E. Michel, and M. I. Nathan, “Triangular injection lasers,” *Proc. IEEE* **52**, 722 (1964).
- [MMS99] V. I. Man’ko, M. Moshinsky, and A. Sharma, “Diffraction in time in terms of Wigner distributions and tomographic probabilities,” *Phys. Rev. A* **59**, 1809 (1999).
- [Mosh52] M. Moshinsky, “Diffraction in Time,” *Phys. Rev.* **88**, 625 (1952).
- [MRS+99] A. D. Mehta, M. Rief, J. A. Spudich, D. A. Smith, and R. M. Simmons, “Single-Molecule Biomechanics with Optical Methods,” *Science* **283**, 1689 (1999).
- [MTTT02] G. Molina-Terriza, J. P. Torres, and L. Torner, “Management of the Angular Momentum of Light: Preparation of Photons in Multidimensional Vector States of Angular Momentum,” *Phys. Rev. Lett.* **88**, 013601 (2002).
- [MVG+99] H. Martinsson, J. A. Vucusić, M. Grabherr, R. Michalzik, R. Jäger, K. J. Ebeling, and A. Larsson, “Transverse Mode Selection in Large-Area Oxide-Confined Vertical-Cavity Surface-Emitting Lasers Using a Shallow Surface Relief,” *IEEE Photon. Technol. Lett.* **11**, 1536 (1999).
- [MVWZ01] A. Mair, A. Vaziri, G. Weihs, and A. Zeilinger, “Entanglement of the Orbital Angular Momentum States of Photons,” *Nature* **412**, 313 (2001).
- [NB74] J. F. Nye and M. V. Berry, “Dislocation in Wave Trains,” *Proc. R. Soc. A* **336**, 165 (1974).
- [NDB+62] M. I. Nathan, W. P. Dumke, G. Burns, F. H. Dill Jr., and G. Lasher, “Stimulated Emission of Radiation from GaAs p-n Junctions,” *App. Phys. Lett.* **1**, 62 (1962).
- [NH04] K. Nagamura and T. Harayama, *Quantum Chaos and Quantum Dots* (Oxford University Press, New York, 2004).
- [NS97] J. U. Nöckel and A. D. Stone, “Ray and Wave Chaos in Asymmetric

- Resonant Optical Cavities,” *Nature* **385**, 45 (1997).
- [NSC94] J. U. Nöckel, A. D. Stone, and R. K. Chang, “Q Spoiling and Directionality in Deformed Ring Cavities,” *Opt. Lett.* **19**, 1693 (1994).
- [Nye83] J. F. Nye, “Polarization effect in the diffraction of electromagnetic waves: the role of disclinations,” *Proc. R. Soc. A* **387**, 105 (1983).
- [Nye99] J. F. Nye, *Natural focusing and fine structure of light : caustics and wave dislocations* (Philadelphia, PA : Institute of Physics Pub., 1999).
- [OC09] K. Otsuka and S. C. Chu, “Generation of vortex array beams from a thin-slice solid-state laser with shaped wide-aperture laser-diode pumping,” *Opt. Lett.* **34**, 10 (2009).
- [OGH87] P. O’Connor, J. Gehlen, E.J. Heller, “Properties of random superpositions of plane waves,” *Phys. Rev. Lett.* **58**, 1296 (1987).
- [OHKY83] M. Ogura, T. Hata, N. J. Kawai, and T. Yao, “GaAs/Al_xGa_{1-x}As multilayer reflector for surface emitting laser diode,” *Japan. J. Appl. Phys.* **22**, L112 (1983).
- [PCC01] A. W. Poon, F. Courvoisier, and R. K. Chang, “Multimode Resonance in Square-Shaped Optical Microcavities,” *Opt. Lett.* **26**, 632 (2001).
- [PKM02] H. Pier, E. Kapon, and M. Moser, “Strain effects and phase transitions in photonic resonator crystals,” *Nature (London)* **407**, 880 (2002).
- [PLW+03] G. G. Paulus, E. Lindner, H. Walther, A. Baltuška, E. Gouliemakis, M. Lezius, and F. Krausz, “Measurement of the Phase of Few-Cycle Laser Pulses,” *Phys. Rev. Lett.* **91**, 253004 (2003).
- [POS97] V. Petrov, Q. Ouyang, H. L. Swinney, “Resonant pattern formation in a chemical system,” *Nature* **388**, 655 (1997).
- [PSF+07] R. Pugatch, M. Shuker, O. Firstenberg, A. Ron, and N. Davidson, “Topological Stability of Stored Optical Vortices,” *Phys. Rev. Lett.* **98**, 203601 (2007).

- [PTMA97] F. Prati, G. Tissoni, M. S. Miguel, and N. B. Abraham, “Vector vortices and polarization state of low-order transverse modes in a VCSEL,” *Opt. Commun.* **143**, 133 (1997).
- [RB81] R. J. Richens and M. V. Berry, “Pseudointegrable Systems in Classical and Quantum Mechanics,” *Physica D* **2**, 495 (1981).
- [Rich01] A. Richter, “Test of Trace Formulas for Spectra of Superconducting Microwave Billiards,” *Foundations of Physics* **31**, 327 (2001).
- [Robi97] R. W. Robinett, “Visualizing classical periodic orbits from the quantum energy spectrum via the Fourier transform: Simple infinite well examples,” *Am. J. Phys.* **65**, 1167 (1997).
- [RTS+02] N. B. Rex, H. E. Tureci, H. G. L. Schwefel, R. K. Chang, and A. D. Stone, “Fresnel Filtering in Lasing Emission from Scarred Modes of Wave-Chaotic Optical Resonators,” *Phys. Rev. Lett.* **88**, 094102 (2002).
- [SADP97] N. B. Simpson, K. Dholakia, L. Allen, and M. J. Padgett, “Mechanical equivalence of spin and orbital angular momentum of light: an optical spanner,” *Opt. Lett.* **22**, 52 (1997).
- [SDE04] M. S. Soskin, V. G. Denisenko, and R. I. Egorov, “Topological networks of paraxial ellipse speckle-fields,” *J. Opt. A: Pure Appl. Opt.* **6**, S281 (2004).
- [SF94] N. Shvartsman and I. Freund, “Vortices in random wave fields: Nearest neighbor anticorrelations,” *Phys. Rev. Lett.* **72**, 1008 (1994).
- [SF01] J. A. de Sales and J. Florencio, “Bohmian quantum trajectories in a square billiard in the bouncing ball regime,” *Physica A* **290**, 101 (2001).
- [SGV+97] M. S. Soskin, V. N. Gorshkov, M. V. Vasnetsov, J. T. Malos, and N. R. Heckenberg, “Topological Charge and Angular Momentum of Light Beams Carrying Optical Vortices,” *Phys. Rev. A* **56**, 4064 (1997).
- [Shaw74] G. B. Shaw, “Degeneracy in the Particle-in-a-Box Problem,” *J. Phys.*

- A **7**, 1537 (1974).
- [ŠHK+97] P. Šeba, F. Haake, M. Kus, M. Barth, U. Kuhl, and H.-J. Stöckmann, “Distribution of the wave function inside chaotic partially open systems,” *Phys. Rev. E* **56**, 2680 (1997).
- [SHS04] N. Savytsky, O. Hul, and L. Sirko, “Experimental investigation of nodal domains in the chaotic microwave rough billiard,” *Phys. Rev. E* **70**, 056209 (2004).
- [Sieg86] A. E. Siegman, *Lasers* (University Science Books, Mill Valley, California 1986).
- [SIKS79] H. Soda, K. Iga, C. Kitahara, and Y. Suematsu, “GaInAsP/InP surface emitting injection lasers,” *Japan. J. Appl. Phys.* **18**, 2329 (1979).
- [Sina70] Y. G. Sinai, “Dynamical systems with elastic reflections: Ergodic properties of dispersing billiards,” *Russ. Math. Surveys* **25**, 141 (1970).
- [ŠKBS99] P. Šeba, U. Kuhl, M. Barth, and H.-J. Stöckmann, “Experimental Verification of topologically induced vortices inside a billiard,” *J. Phys. A: Math. Gen.* **32**, 8225 (1999).
- [SO99] J. Scheuer and M. Orenstein, “Optical Vortices Crystals: Spontaneous Generation in Nonlinear Semiconductor Microcavities,” *Science* **285**, 230 (1999).
- [Srid91] S. Sridhar, “Experimental observation of scarred eigenfunctions of chaotic microwave cavities,” *Phys. Rev. Lett.* **67**, 785 (1991).
- [SS90] H. J. Stöckmann and J. Stein, “Quantum Chaos in Billiards Studied by Microwave Absorption,” *Phys. Rev. Lett.* **64**, 2215 (1990)
- [SS92] J. Stein and H. J. Stöckmann, “Experimental determination of billiard wave functions,” *Phys. Rev. Lett.* **68**, 2867 (1992).
- [SSDD95] A. Steane, P. Szriftgister, P. Desiolles, and J. Dalibard, “Phase Modulation of Atomic de Broglie Waves,” *Phys. Rev. Lett.* **74**, 4972 (1995).
- [ST58] A. L. Schawlow and C. H. Townes, “Infrared and Optical Masers,”

- Phys. Rev. **112**, 1940 (1958).
- [STB+93] G. Shtengel, H. Temki, P. Brusenbach, T. Uchida, M. Kim, C. Parsons, W. E. Quinn, and S. E. Swirhun, “High-speed vertical-cavity surface emitting laser,” *IEEE Photon. Tech. Lett.* **5**, 1359 (1993).
- [Stöc99] H. J. Stöckmann, *Quantum Chaos: An Introduction* (Cambridge University Press, Cambridge, U.K., 1999), and references cited therein.
- [Ston05] A. D. Stone, “Einstein's unknown insight and the problem of quantizing chaos,” *Phys. Today* **58**, 37 (2005).
- [SV01] M. S. Soskin and M. V. Vasnetsov, Chap. 4 of *Progress in Optics* Vol. **42**, edited by E. Wolf (Elsevier, New York, 2001).
- [SWMD48] C. G. Shull, E. O. Wollan, G. A. Morton, and W. L. Davidson, “Neutron Diffraction Studies of NaH and NaD,” *Phys. Rev.* **73**, 842 (1948).
- [TAFJ08] Y. Tanguy, T. Ackemann, W. J. Firth, and R. Jäger, “Realization of a Semiconductor-Based Cavity Soliton Laser,” *Phys. Rev. Lett.* **100**, 013907 (2008).
- [VdS+06] G. Van der Sande, M. Peeters, I. Veretennicoff, J. Danckaert, G. Verschaffelt, and S. Balle, “The Effects of Stress, Temperature, and Spin Flips on Polarization Switching in Vertical-Cavity Surface-Emitting Lasers,” *IEEE J. Quantum Electron.* **42**, 898 (2006).
- [vEWW98] M. P. van Exter, M. B. Willemsen, and J. P. Woerdman, “Polarization fluctuations in vertical-cavity semiconductor lasers,” *Phys. Rev. A* **58**, 4191 (1998).
- [VKMR01] I. V. Veshneva, A. I. Konukhov, L. A. Melnikov, and M. V. Ryabinina, “Vectorial Karhunen-Loeve modes for the description of the polarization transverse pattern dynamics in lasers and their classification based on the characterization of the singular points,” *J. Opt. B* **3**, S209 (2001).

References

- [vonO94] F. von Oppen, “Magnetic susceptibility of ballistic microstructures,” *Phys. Rev. B* **50**, 17151 (1994).
- [VS99] *Optical Vortices* edited by M. V. Vasnetsov and K. Staliunas (Nova Science, New York, 1999).
- [VSF+06] A. Volyar, V. Shvedov, T. Fadeyava, A. S. Desyatnikov, D. N. Neshev, W. Krolikowski, and Y. S. Kivshar, “Generation of Single-Charge Optical Vortices with an Uniaxial Crystal,” *Opt. Express* **14**, 3724 (2006).
- [Wier01] J. Wiersig, “Quantum-classical correspondence in polygonal billiards,” *Phys. Rev. E* **64**, 026212 (2001).
- [Wint87] D. Wintgen, “Connection between Long-Range Correlations in Quantum Spectra and Classical Periodic Orbits,” *Phys. Rev. Lett.* **58**, 1589 (1987).
- [WKL+89] G. R. Welch, M. M. Kash, C. Iu, L. Hsu, and D. Kleppner, “Experimental Study of Energy-Level Statistics in a Regime of Regular Classical Motion,” *Phys. Rev. Lett.* **62**, 893 (1989).
- [WPW99] C. E. Wieman, D. E. Pritchard, and D. J. Wineland, “Atom cooling, trapping, and quantum manipulation,” *Rev. Mod. Phys.* **71**, S253 (1999) and references therein.
- [WS48] E. O. Wollan and C. G. Shull, “The Diffraction of Neutrons by Crystalline Powders,” *Phys. Rev.* **73**, 830 (1948).
- [YAC+07] X.-C. Yuan, B. P. S. Ahluwalia, H. L. Chen, J. Bu, J. Lin, R. E. Burge, X. Peng, and H. B. Niu, “Generation of High-Quality Optical Vortex Beams in Free-Space Propagation by Microfabricated Wedge with Spatial Filtering Technique,” *Appl. Phys. Lett.* **91**, 051103 (2007).
- [YAK+07] J. Yoon, S.-J. An, K. Kim, J. K. Ku, and O. Kwon, “Resonance Spectrum of a Three-Dimensional Photonic Quantum Ring Laser with an Equilateral Triangle Microcavity,” *Appl. Opt.* **46**, 2969 (2007)
- [ZB97] I. V. Zozoulenko and K. -F. Berggren, “Quantum scattering, resonant

References

- states, and conductance fluctuations in an open square electron billiard,” *Phys. Rev. B* **56**, 6931 (1997).
- [ZB06] R. Zambrini and S. M. Barnett, “Quasi-Intrinsic Angular Momentum and the measurement of Its Spectrum,” *Phys. Rev. Lett.* **96**, 113901 (2006).
- [ZB07] R. Zambrini and S. M. Barnett, “Angular momentum of multimode and polarization patterns,” *Opt. Express* **15**, 15214 (2007).
- [ZM05] X. Zou and W. Mathis, “Scheme for optical implementation of orbital angular momentum beam splitter of a light beam and its application in quantum information processing,” *Phys. Rev. A* **71**, 042324 (2005).



Curriculum Vitae

Personal Data

Name: Chien-Cheng Chen

Sex: Male

Birthday: Nov. 13, 1982

Nationality: Taiwan (Republic of China)

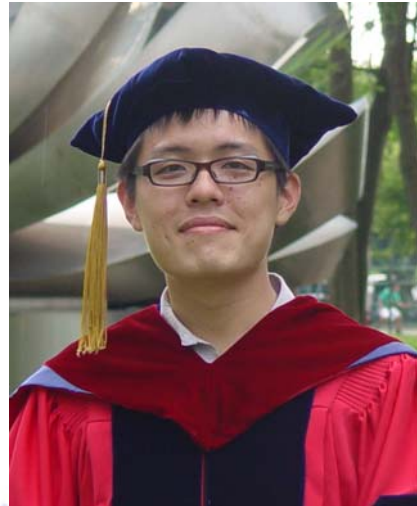
Birthplace: Yilan County

E-mail: makoto.ep94g@nctu.edu.tw

devilscrying@hotmail.com

makotoscorpio@yahoo.com.tw

Mobile Phone: 886-912-297661



Education

2005-2009 Ph.D. in Department of Electrophysics, National Chiao Tung University, Hsinchu, Taiwan.

2001-2005 B.S. in Department of Physics, National Tsing Hua University, Hsinchu, Taiwan.

1998-2001 National Yilan Senior High School, Yilan, Taiwan.

Work Experience

2005-2008 T. A. of General Physics

2008-2009 Pre-PhD T. A. of General Physics

Current Research Interests

Vertical-Cavity Surface-Emitting Lasers

Quantum Billiards

Singular Optics

Publication List

1. **C. C. Chen (陳建誠)**, C. C. Liu (劉春鞠), K. W. Su (蘇冠暉), T. H. Lu (陸亭樺), Y. F. Chen (陳永富), and K. F. Huang (黃凱風), “Statistical properties of experimental coherent waves in microcavity lasers: Analogous study of quantum billiard wave functions,” *Phys. Rev. E* **75**, 046204 (2007).
2. **C. C. Chen (陳建誠)**, K. W. Su (蘇冠暉), T. H. Lu (陸亭樺), C. C. Liu (劉春鞠), Y. F. Chen (陳永富), and K. F. Huang (黃凱風), “Generation of two-dimensional chaotic vector fields from a surface-emitting semiconductor laser Analysis of vector singularities,” *Phys. Rev. E* **76**, 026219 (2007).
3. **C. C. Chen (陳建誠)**, K. W. Su (蘇冠暉), Y. F. Chen (陳永富), and K. F. Huang (黃凱風), “Various high-order modes in vertical-cavity surface-emitting lasers with equilateral triangular lateral confinement,” *Opt. Lett.* **33**, 509 (2008).
4. **C. C. Chen (陳建誠)**, Y. T. Yu (余彥廷), Ross C. C. Chen (陳建至), Y. J. Huang (黃郁仁), K. W. Su (蘇冠暉), Y. F. Chen (陳永富), and K. F. Huang (黃凱風), “Transient Dynamics of Coherent Waves Released from Quantum Billiards and Analogous Observation from Free-Space Propagation of Laser Modes,” *Phys. Rev. Lett.* **102**, 044101 (2009).
5. Ross C. C. Chen (陳建至), Y. T. Yu (余彥廷), Y. J. Huang (黃郁仁), **C. C. Chen (陳建誠)**, Y. F. Chen (陳永富), and K. F. Huang (黃凱風), “Exploring the origin of the directional emission from a microcavity with a large-aperture surface-emitting laser,” *Opt. Lett.* **34**, 1810 (2009).